Author:
Tanner, Hugh R C

Title:
Development of Novel Probes for Correlative Light Electron Microscopy

Development of Novel Probes for Correlative Light Electron Microscopy

Hugh Robert Charles Tanner

April 10, 2020

A dissertation submitted to the University of Bristol in accordance with the requirements for the award of the degree Doctor of Philosophy in the Faculty of Biochemistry

School of Biochemistry

Word count: 50175

Abstract

This thesis covers two separate projects linked by the common theme of correlative light electron microscopy (CLEM) probes. Many imaging modalities can potentially be utilised within a CLEM experiment but for the purposes of this thesis laser scanning confocal microscopy and transmission electron microscopy for the focus. CLEM seeks to gain the positive attributes of both constituent techniques in order to acquire information otherwise unattainable using the same techniques in isolation.

Firstly the development of a previously studied protein ligand binding pair into an affinity based CLEM probe. A dissociation constant between a mutagenic variant of the FK506 binding protein (FKBP) and synthetic ligand of FKBP (SLF') was reported to be 94pM (Clackson et al., 1998). Enhanced green fluorescent protein (EGFP) was endogenously expressed on the protein of interest along with the FKBP(F36V) to produce a chimera. The small molecule SLF' was conjugated with gold nanoparticles in a stoichiometric ratio of 1:1. The tight binding between FKBP(F36V) and SLF' conjugated to AuNP was used to co-localise AuNPs to the protein of interest. This probe was used both *in vivo* and to investigate the putative helical oligomeric structures formed by SNX1 around lipid tubules *in vitro*.

The second project investigated the feasibility of platinum nanoclusters (PtNCs) to be used as CLEM probes. Several atoms in size, the electrons within the structure become discretised which gives rise to a size dependent fluorescence. We discovered PtNCs can be silver enhanced in order to produce more electron density in the electron micrograph. The quantum yield of the PtNCs was shown to be 4.8%. *In vivo* CLEM experiments in HeLa cells produced sufficient fluorescence to be readily detected. Once silver enhanced electron dense punctae were visible that displayed a high correlation with previously acquired fluorescent signals

Declaration

I declare that the work in this dissertation was carried out in accordance with the requirements of the University's *Regulations and Code of Practice for Research Degree Programmes* and that it has not been submitted for any other academic award. Except where indicated by specific reference in the text, the work is the candidate's own work. Work done in collaboration with, or with the assistance of, others, is indicated as such. Any views expressed in the dissertation are those of the author.

SIGNED: ..... DATE:.....

.

Table of Contents

Figure List

Abbreviation List

AOM	Acousto-optical Modulators
APEX	Ascorbate Peroxidase
ATP	Adenine Triphosphate
AuNP	Gold Nanoparticle
BAR	Bin/Amphiphysin/Rvs
BFP	Blue Fluorescent Protein
BSA	Bovine Serum Albumin
CEMOVIS	Cryo Electron Microscopy of Vitreous Sections
CLEM	Correlative Light Electron Microscopy
DAB	3,3'-Diaminobenzidine
DMSO	Dimethyl Sulfoxide
DNA	Deoxyribonucleic Acid
EDX	Electron Dispersive X-ray
EEA1	Early Endosome Associated Protein 1
EELS	Electron Energy Loss Spectroscopy
EFS1	EGFP-FKBP-SNX1
EGF	Epidermal Growth Factor
EGFP	Enhanced Green Fluorescent Protein
EGFR	Epidermal Growth Factor Receptor
EM	Electron Microscopy
ES1	EGFP-SNX1
EwtFS1	EGFP-wtFKBP-SNX1
F-BAR	FCH Bin/Amphiphysin/Rvs
FIB	Focused Ion Beam
FIB-SEM	Focused Ion Beam – Scanning Electron Micrscopy
FKBP	FK Binding Protein (Specifically mutagenic variant (F36V))
FNG	Fluoronanogold
FRET	Forster's Resonance Energy Transfer

GA	Glutaraldehyde
GDP	Guanine Diphosphate
GFP	Green Fluorescent Protein
GTP	Glan-Thompson Polariser
GTP	Guanine Triphosphate
HAADF-STEM	High Angle Annular Dark Field – Scanning Transmission Electron Microscopy
HIV	Human Immunodeficiency Virus
HPF	High Pressure Freezing
I-BAR	Inverse Bin/Amphiphysin/Rvs
ICPM	Interferometric Cross Polarisation Microscopy
ILV	Intraluminal Vesicle
IPTG	Isopropyl β- d-1-thiogalactopyranoside
ITC	Isothermal Titration Calorimetry
LM	Light Microscopy
LOV	Light Oxygen Voltage
LSFM	Light Sheet Fluorescent Microscopy
LSPR	Localised Surface Plasmon Resonance
MCS	Multiple Cloning Site
mSA	Monomeric Streptavidin
MT	Metallothionien
MVB	Multi-Vesicular Body
NA	Numerical Aperture
N-BAR	N-terminal Bin/Amphiphysin/Rvs
NC	Nanocluster
NG	Nanogold
NHS	N-Hydroxysuccinimide
NSET	Nanometal Surface Energy Transfer
PALM	Photo-activated Localisation Microscopy
PAMAM	Polyamidoamine(pamam) Dendrimer
PBS	Phosphate Buffered Saline
PEI	Polyethylene Imine

PFA	Paraformaldehyde
PI(3)P	Phosphoinositol 3 phosphate
PMT	Photomultiplier Tube
PSF	Point Spread Function
PX-domain	Phox Homology Domain
QD	Quantum Dot
QS	Quinine Sulfate
RESOLFT	Reversible Saturable Optical Fluorescence Transitions
RFP	Red Fluorescent Protein
SADP	Selected Area Diffraction Pattern
SBF-SEM	Serial Block Face – Scanning Electron Microscopy
SDS-PAGE	Sodium Dodecyl Sulfate Polyacrylamide Gel Electrophoresis
SEM	Scanning Electron Microscopy
SLF'	Synthetic Ligand of FKBP
SNX	Sorting Nexin
STED	Stimulated Emission Depletion Microscopy
STEM	Scanning Transmission Electron Microscopy
STORM	Stochastic Optical Reconstruction Microscopy
TEM	Transmission Electron Microscopy
TGN	Trans Golgi Network
UA	Uranyl Acetate
YFP	Yellow Fluorescent Protein

Chapter 1

A Brief Introduction to Light and Electron Microscopy Techniques for the Life Sciences

1.1 Green Fluorescent Protein

In 2008, Osamu Shimomura, Martin Chalfie and Roger Y. Tsien were awarded the Nobel Prize for the discovery and development of green fluorescent protein (GFP) (Ormö et al., 1996) (Yang et al., 1996a). GFP was discovered and isolated from *Aequorea victoria* and has since been utilised in an immense number of applications within the field of biological science. Moreover, it has also revolutionised the way biological samples are imaged and thrust techniques such as fluorescence/confocal microscopy to the fore. Proteins and bio-molecules not typically visible by light microscopy (LM) could now readily be visualised when expressed as part of a in a GFP construct. Since GFP is a protein, genetic engineering allows the expression of GFP chimera proteins, ensuring GFP is always co-localised to the protein of interest with a very high specificity. This has enabled researchers to observe protein expression, distribution and trafficking in whole organisms such as rabbits (Yang et al., 2009), frogs, (Gross et al., 2006) zebrafish (Berretta et al., 2016) and down to the single cell level (Kukulski et al., 2011).

First extracted and purified by Shimomura in 1962, the structure of GFP determined by X-ray crystallography was published in 1996 by two separate groups one month apart (Ormö et al., 1996) (Yang et al., 1996a). GFP was found to be a stable β-can structure consisting of 11 parallel β-barrel structures surrounding a single alpha helix. The fluorophore is contained at the centre of the protein and formed when serine65, tyrosine66 and glycine67 undergo an auto-cyclisation reaction followed by an oxidation (Figure 1.1). The β-can structure surrounding these residues provide a favourable environment for these reactions to take place. The final π-conjugated system gives rise to the characteristic GFP fluorescence.

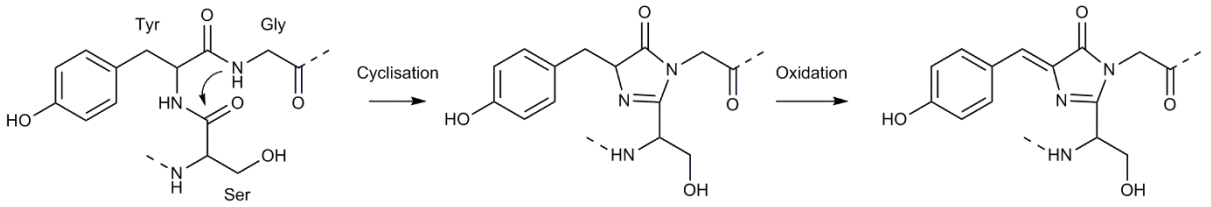

Figure 1.1: Internal reaction between serine 65, tyrosine 66 and glycine 67 to produce the fluorescent chromophore within the GFP protein.

The first iterations of GFP were found to be fluorescent at room temperature without the need of exogenous cofactors required for function in jellyfish. It had several drawbacks including: poor

photo-stability, poor quantum yield, chloride sensitivity, pH sensitivity, dual peaked excitation spectra and poor folding at 37°C. The development of GFP for use as a probe has seen 190 silent mutations to create an open reading frame of exclusively mammalian codons (Yang et al., 1996b). GFP's attributes specific to fluorescent labelling were improved by the development of a larger protein EGFP. This GFP variant also contained two point mutations Ser65 to Thr and Phe64 to Leu, boasting a 35 times increase in brightness, lower aggregation and improved protein folding. The beta-can structure of GFP protects the fluorophore from bleaching while providing an optimal environment for fluorescence generation. GFP subsequently sparked the discovery of a whole family of fluorescent proteins with varying excitation and emission spectra: BFP, YFP, mCherry, RFP, etc. The robust nature of the modern GFP/EGFP labels, including the huge array of other fluorescent proteins, has seen a concomitant rise in epifluorescence microscopy techniques which seek to take advantage of these labels.

1.2 Light Microscopy

Light microscopy is a straightforward and non-destructive method allowing live cells to be imaged. This technique lends itself well to studying dynamic and transient cellular events. However due to visible spectra existing between 380-750nm the resolution is inherently limited. Spatial resolution is defined as the minimum distance two objects can be separated by and remain discrete. Two points separated by a distance less than the resolution of a piece of imaging apparatus will appear as a single point or a merging of two point spread functions. Using standard optics the theoretical maximum resolution for light would be 200nm, around half of the illumination wavelength. This is referred to as the Abbe diffraction limit.

Focal plan (x, y)

$$\frac{\lambda}{2nsin\alpha}$$

Optical axis (z)

$$\frac{2}{nsin^2\alpha}$$

Where α is the diameter of the aperture, λ is wavelength and *n* is the refractive index of the media directly surrounding object. The wavelength of light and the numerical aperture of the lens suggests a maximum resolution for any light microscope at around 200nm. This limit assumes the use of

violet light (400nm) and a numerical aperture of >1.5. The Airy disc describes the point spread function as observed through a perfect microscope free of aberrations and close to the optimal optical plane. Objects resolvable by this system would appear as the true image convoluted with the point spread function (PSF) which would appear as a blur. PSF could be thought of as a predictable and calculable blur which is a combination of imaging artefacts induced by the microscope and dispersion of light from the optical plane. Epifluorescence techniques share the same restricted resolution as their LM counterparts due to their reliance on light and the accompanying fundamental limitations. However fluorescent labelling allows the vicarious visualisation of objects far smaller than the maximal resolution of the optics.

1.2.1 Fluorescence Microscopy

Fluorescence microscopy (FM) shares many similarities with standard light microscopy except the epifluorescence signal of the sample is used to form images. A monochromatic light source incident on the sample excites fluorophores with a complimentary excitation spectra. Before hitting the detector the light collected from the sample passes through a spectral emission filter. The much brighter reflected or scattered light with the same wavelength as the incident beam is separated from the much weaker fluorescent signal which passes through to the detector. Fluorophores are small molecules capable of absorbing light around a peak excitation value followed by the electrons within the structure being promoted to an excited state. Upon de-excitation of these electrons back to ground state via smaller energy levels, the light re-radiated out is at a lower energy. The relationship between energy and wavelength is:

$$E = \frac{hc}{\lambda}$$

Where *E* is energy, *h* is Planck's constant, *c* is the speed of light in a vacuum, and λ is the wavelength. Both *h* and *c* are constants and so E is proportional to the inverse of λ. Therefore as the energy decreases the wavelength must increase, red-shifting any re-radiated light. The presence of a fluorescently labelled biomolecule of interest can be rapidly identified by this colour change.

1.2.1.1 Laser Scanning Confocal Microscopy

One of the most commonly used and versatile types of fluorescence microscopy is laser scanning confocal microscopy. This method allows the visualisation of fluorescently labelled bio-molecules within relatively thin biological samples ≈ 50µm with a higher end resolution of 200nm in the optical plane. In addition, confocal microscopy is able to optically section, acquiring data at specific z-planes throughout the sample by means of a pin hole. This also effectively removes fluorescent signal from other axial planes creating a clearer image. Its robust nature and the ability to generate insight into protein localisation, protein expression levels, structural biology, and cellular mechanics have resulted in a widespread adoption of the technique.

1.2.2 Super Resolution Fluorescence Microscopy

In 2014 Eric Betzig, Stefan W. Hell and William E. Moerner were awarded the Nobel Prize in chemistry for the development of super-resolution light microscopy. Abbe's fundamental laws are essentially circumvented by means of specialist methods: stimulated emission and single-molecule microscopy. These techniques are still relatively new and at the current time laser scanning confocal microscopy remains the workhorse of fluorescent imaging. Super resolution techniques are under constant development with new techniques such as MINFLUX only recently coming to the fore (Balzarotti et al., 2017). As the techniques are developed and become more robust it is likely their usage will supersede currently established fluorescence microscopes. Super resolution techniques are the future of FM and will also be/continue to be beneficial to correlative workflows.

1.2.2.1 Stimulated Emission Depletion Microscopy

Stimulated Emission Depletion Microscopy (STED) functions by essentially shrinking the point spread function of the incident light used to excite a fluorescent sample. The smaller incident beam excites fewer neighbouring fluorophores producing far greater lateral resolution. This is usually achieved by using a separate depletion laser that illuminates a "doughnut" shape, where the centre has an intensity of zero, around the primary excitation laser. Under normal circumstances a fluorophore that has been promoted to an excited state will undergo spontaneous emission. This process is stochastic and the emitted photon will have a relatively narrow emission wavelength but will have a random phase and direction. However an excited photon positioned in the electromagnetic field of

the depletion laser will undergo stimulated emission. As the excited electron transitions from an excited state to the ground state, it behaves like a small electric dipole and is therefore influenced by the depletion field. This interaction produces coherent photons with identical phases, wavelength and direction to the incident photon. Theoretically STED has the resolution to resolve individual molecules but is limited by the signal to noise ratio (Tortarolo et al., 2018) but has managed to generate data with 20nm resolution (Göttfert et al., 2013). Complex microscope architecture and the high depletion laser intensity used can cause fluorophores to photo-bleach and cause photo-toxicity. This has hindered widespread adoption of STED in biological fields.

1.2.2.2 PALM/STORM

Photo-activated Localisation Microscopy (PALM) and Stochastic Optical Reconstruction Microscopy (STORM) both use a similar principle in order to achieve super resolution. Both these techniques exploit fluorophores ability to be in a bright (ON) state or dark (OFF) state. PALM photo-bleaches fluorophores while STORM utilises blinking in order to more accurately localise the origin of the fluorescent signal. Blinking or bleaching enables multiple proximal fluorophores to be individually identified and resolved. Once individual fluorophores are identified, deconvolution can be used to reduce the point spread function to a centroid. Fluorescent emitters can be localised to an accuracy of 1.5nm (Yildiz et al., 2003), further improving the resolution another order of magnitude and thus achieving super resolution.

These stochastic imaging modalities however do rely heavily on photo-bleaching or blinking. Photo-bleaching has the obvious drawback of being irreversible and any given sample can only be imaged once. The alternative is to use photo-switchable fluorophores. The on-off contrast state is characterised by the ratio between the signal intensity of the fluorophore in the on and off state. If the contrast between on and off low, the fluorophores in the off state produce a large competing signal that masks any meaningful measurements. Each fluorophore is only capable of switching between an on and off state before irreversibly bleaching. Techniques such as RESOLFT or psSIM require a fluorophore to photo-switch many times in order for a single super resolution image to be generated. A single photo-switch cycle is sufficient for PALM/STORM to be able to generate a super resolution image, although additional cycles reduce errors and improve resolution (Dempsey etal., 2011).

The buffers used in super resolution techniques are also paramount to their efficacy. Using an oil immersion lens with high NA produces a tight focus and high photon collection efficiency. However physiological buffers routinely used to image biological samples have a lower refractive index than immersion oil. This mismatch causes spherical aberration and a shift in the observed axial position of the fluorophore (Huang et al., 2008). Furthermore dependent on which fluorophore is used, specific buffers containing oxygen scavengers and reducing agents may be necessary for optimal photo-switching (Olivier et al., 2013).

1.2.2.3 Light Sheet

Light sheet fluorescence microscopy (LSFM) is a super resolution technique capable of attaining a maximum optical resolution of approximately 100nm but with increased optical sectioning compared with a laser scanning confocal microscope. A thin laser light sheet a few hundred nanometres thick is created by focusing a laser through a cylindrical lens, illuminating the sample through the focal plane perpendicular to the detector. Illumination of the sample with interfering Bessel beams to produce structured/lattice light sheets are also used. Regularly spaced regions of destructive interference create nodes at periodic intervals and therefore reduce fluorophore photo-bleaching. Coupled with the rapid sampling rate of these systems enable long exposure times to capture videos without loss of clarity (Chen et al., 2014). Bessel waves do not diffract or spread out, they can also reform further down the propagation axis of the beam if obstructed. The combination of rapid data acquisition and light propagation through the sample means LSFM is well suited to imaging larger transparent structures such as embryos (Keller et al., 2008) (Chen et al., 2014).

1.3 Electron Microscopy

With the epoch of GFP and organic fluorescent dyes, relatively straight forward sample preparation and the ability to image cells live, FM has become the workhorse of biological imaging. Despite the myriad strengths of FM, it does possess a number of shortcomings. Firstly, its resolution is limited and at present even super resolution techniques are yet to supersede electron microscopy. Furthermore, the technique is only able to visualise fluorescent signals and is incapable of imaging the majority of the cellular ultrastructure. Therefore, the ultrastructural context where a given fluorescent signal originated from can be uncertain. For example, two discrete signals of a similar

size and intensity may be visible but located in two separate cellular organelles which would not be identified by fluorescence alone. This niche, for a high resolution imaging technique capable of capturing a holistic view of the cellular ultrastructure is still primarily occupied by electron microscopy techniques.

In 1923 de Broglie proposed the idea of wave-particle duality and hypothesised that electrons, classically considered particles, could possess the properties of waves (Aspect and Villain, 2017). The de Broglie wavelength equation used to describe an electrons behaviour:

$$\lambda = \frac{h}{mv}$$

Where λ is the wavelength, *h* is Planck's constant, *m* is the mass of the particle and *v* is the velocity. Both *h* and *m* are constants which leaves an inverse proportionality between λ and *v*. Therefore by accelerating electrons to high velocities it is possible to attain an electron beam with a very short

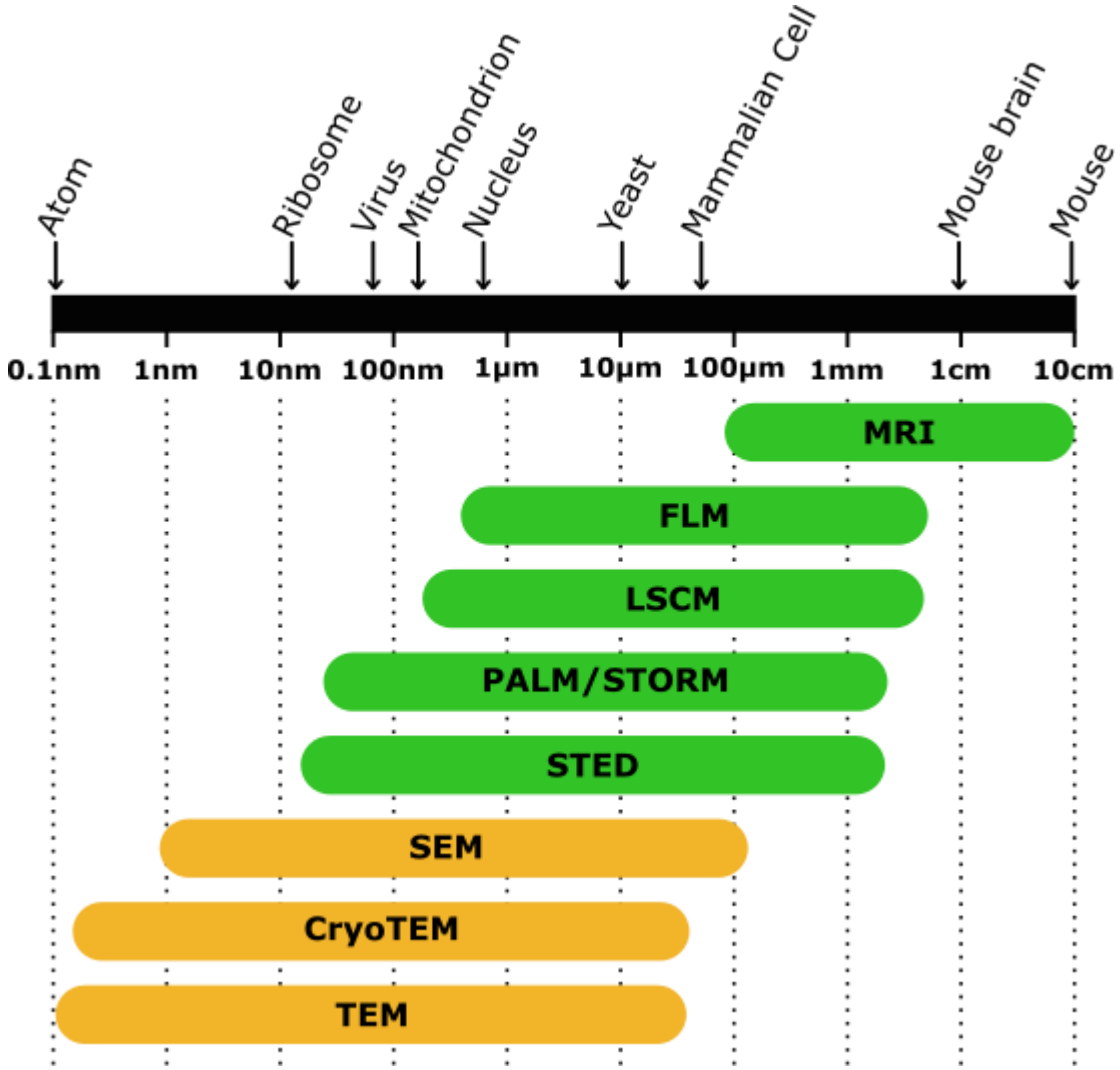

Figure 1.2: Diagram to show the comparative resolutions of several imaging modalities. Techniques in green rely on signal from the electromagnetic spectra mainly light while orange utilise electrons.

wavelength. The aforementioned Abbe's equation states that the maximal resolution is determined by half the wavelength. At high enough velocities this potentially affords an electron beam incredible resolving power, with the de Broglie wavelength much shorter than the distance between covalently bonded atoms. The subsequent observation by Busch in 1926 of the similarity between light passing through a convex lens and the effect of using a magnetic focussing coil on an electron beam provided the practical basis for the development of the electron microscope (Freundlich, 1963).

The high resolution garnered by electron microscopy does inevitably come with limitations due to its reliance on an electron beam. Electrons in comparison to a photon, are large particles with significant mass and charge. Electrons experience strong coulombic interactions with other electrons and nuclei present in the air causing the beam to be scattered and severely hindering beam propagation. To minimize this scattering effect, the electron beam in an electron microscope is propagated through a very high vacuum. For some samples (crystals inorganic materials etc.) the vacuum is of negligible consequence but does present some significant issues for samples of a biological nature. To avoid biological samples desiccating and potentially bursting as a result of pressure differentials it is important these samples are correctly prepared (preservation methods are discussed in more detail in section 1.3.3). These preservation methods nullify live cell imaging, negating the ability to observe dynamic cellular events. Since the electron beam is sensitive to coulombic forces, samples are limited to a ≈300nm thickness (not in SEM (Scanning Electron Microscopy)) in order for electrons to transmit through the sample, reach the detector, and generate an image. Therefore thick cells and tissues must be sectioned prior to imaging. This thesis is primarily concerned with TEM (Transmission Electron Microscopy) and its associated methods. Several EM techniques including SEM will be discussed in section 1.3.4.

Electron microscopes rely on variance of the electron density throughout the sample to generate contrast. Since the electron beam within a TEM can pass through a thin section of biological material and experience minimal coulombic interaction, native biological samples (with the exception of modern cryo-EM techniques) would essentially be invisible to the electron beam. This necessitates the usage of contrast generating agents, the most common of which are heavy metal stains. Once fixed, biological samples are incubated with solutions containing heavy metal ions which preferentially localise to specific subcellular regions: uranyl acetate to proteins and lipids, lead citrate to proteins and glycogens and osmium tetroxide to lipids. The aforementioned are the most routinely used stains, many others exist but are often limited to niche usage.

1.3.1 Lens Defects and Resolution

There are three main lens defects that limit the resolving power of electron microscopy. The first of which originate from the magnetic lenses used to focus the electron beam. Glass lenses used in LM also suffer from spherical aberration but can be somewhat mitigated by the use of compound lenses. Magnetic lenses are heterogeneous in their deflecting power from the optical axis outward. Essentially causing electrons travelling down the optical axis to be deflected far less than those travelling further from the centre. Therefore several images of varying defocus can overlay one another at the focal plane which can severely limit the resolution.

Chromatic aberrations are attributed to the electron source. A perfect electron source would be an infinitely small point emitter that would produce electrons of identical energy, velocity and phase. However, in reality electrons leaving the source have an energy spread and leave the source with different velocities and energies. Higher energy/velocity electrons are deflected less by the magnetic lenses and will be focused at a point further down the optical axis. The effect of chromatic aberration is proportional to the half opening angle of the beam. The closer the sample is to the condenser lens, the larger the focussing angle and the larger the chromatic aberration.

Astigmatism is another lens defect which can limit the resolution of an electron microscope. An astigmatism arises when a non-uniform magnetic field deflects the beam and causes the image to become warped and stretched in a single direction. Astigmatisms can be minimised with the use of stigmators which are variable electromagnets which compensate for the defects in the magnetic lens. They are most commonly octopoles that produce a magnetic field perpendicular to the electron beam correcting any heterogeneity in the magnetic field of the objective and condenser lens systems.

1.3.2 Transmission Electron Microscopy

The fundamental principles and layout of a TEM are reminiscent of a standard LM. Both share an objective lens, condenser lens, illumination source, and detector/eye piece. Similar to LM contrast in an image is defined by a measureable change in the amplitude before and after transmission through a sample. As electrons pass through and elastically collide with the sample, the amplitude of the de Broglie wavelength is altered. These elastic collisions can alter the amplitude of electrons while conserving their velocity and momentum which is then used to generate contrast in the

electron micrographs. During inelastic collisions the amplitude, velocity and momentum are not conserved and are primarily used by analytical electron microscopy techniques such as electron energy loss spectroscopy (EELS) and energy dispersive X-ray (EDX). Furthermore due to momentum not being conserved in inelastic collisions, the electrons can be scattered at acute angles. Therefore detectors can be positioned accordingly to only capture these inelastically scattered electrons. However in standard TEM these inelastically scattered electrons cause noise in the final image and are blocked out by the objective aperture. Electron dense regions within a sample will naturally scatter more electrons inelastically. The objective aperture will therefore block relatively more electrons from these regions which can further increase contrast, making these areas appear darker. This is particularly useful for imaging biological samples that would not ordinarily produce high contrast. This thesis is chiefly concerned with the use and application of transmission electron microscopy (TEM) and a limited number of variations thereof. Other electron microscopy techniques will be outlined briefly in section 1.3.4.

1.3.3 Electron Microscopy Sample Preparation

The ultra-high vacuum environment of a TEM presents potential challenges for biological samples. Cellular structures, particularly membrane bound structures containing fluid would explode as a result of the pressure differential when exposed to the high vacuum. Fixation preserves native cellular ultrastructure in a robust form that also protects the sample from the high vacuum environment. Freezing and/or chemical fixation are the two most widely used methods.

1.3.3.1 Negative Stain

Negative stain is the most straightforward method to preserve and visualise smaller objects such as proteins and vesicles. After depositing the structure/protein/object of interest on to a TEM grid, the negative stain is applied which stains the background. The stain is occluded by the object of interest leaving a negative impression, hence negative stain. Negative stains can act as fixatives (such as uranyl acetate) but also contain electron dense metals to produce contrast when imaged with the TEM. An electron dense outline is observed where the negative stain has been occluded by a biomolecule/structure. Negative stain is not the most precise technique often producing high background and can mask finer structural details of the sample. Due to their ease of use and rapid sample preparation times, negative stains continue to be used regularly. Each negative stain has a niche but uranyl acetate (UA) is the most ubiquitous. Containing uranium atoms confers it with a

high electron density while also readily staining nucleic acids and to a lesser extent lipids (Maunsbach and Afzelius, 2001).

1.3.3.2 Chemical Fixation

Chemical fixation is a straightforward method that provides adequate ultrastructural preservation for electron microscopy. Aldehyde fixatives: paraformaldehyde (PFA) and glutaraldehyde (GA), are the preferred fixatives for EM. Chemical fixation for EM aims to preserve the cellular ultrastructure and fine detail of the sample as close to natively as possible. Therefore many chemical fixation methods are not suitable for TEM e.g. cold methanol fixation, mecurials, and picrates as they provide poor ultrastructural preservation and/or introduce artefacts. The aldehyde groups contained within PFA and GA when in aqueous conditions react primarily with the nitrogen atoms of proteins. If two atoms are sufficiently proximal the aldehyde can crosslink the two forming a methylene bridge. Proteins become bound to one another and the cytoskeleton immobilising the cellular machinery and preserving the cellular architecture. GA contains two reactive aldehyde groups producing a stronger fixation than PFA but its increased molecular size does decrease its diffusivity. Despite this GA remains the preferred chemical fix for TEM sample preparation but it should be noted that glutaraldehyde is not compatible with FM except at very low concentrations. GA reacts with and crosslinks primary and secondary amines contained within cellular proteins. This process can form fluorescent cyclic molecules containing conjugated π-electron structures leading to a high auto fluorescent background when imaged with FM (Lee et al., 2013). Low concentrations of GA can be used to improve ultrastructural preservation of fluorescent samples without creating an overly high background but PFA is the preferred fixative for FM. Fixative attaching to and crosslinking proteins has a positive impact on ultrastructural preservation but deleteriously affects some antibodies epitope recognition. Therefore fixation must be carefully considered for a given protocol, as there is a trade-off between optimal ultrastructural preservation and antigenicity.

GA and PFA both primarily act to crosslink amine groups leaving other cellular structures in an unstable state. In electron micrographs the cellular ultrastructure is also visible so additional fixation steps are necessary to preserve the rest of the ultrastructure, in particular, lipid membranes. Standard sample preparation for EM will routinely use other fixatives such as osmium tetroxide and uranyl acetate. These heavy metals crosslink proteins and lipids while simultaneously staining the sample. For example, UA preferentially reacts and crosslinks phosphate groups together. The phospholipid bilayer contains a large concentration of phosphate head groups which the UA reacts

with, inducing cross linkages and incorporating large amounts of uranium into the membrane. This drastically increases the overall electron density of the lipid membrane which in the TEM can then be observed with a much higher contrast.

1.3.3.3 High Pressure Freezing and Plunge Freezing

An alternative method of fixation utilizes rapid sample freezing to form vitreous ice. Vitreous ice is formed so rapidly the atoms are not afforded sufficient time to orient themselves into ordered crystals. Therefore ice crystals do not propagate through or penetrate cellular structures. Additionally as the water changes states the same volume is retained which helps to retain a native sample structure. This is advantageous for two main reasons: firstly the formation of ice crystals can damage and puncture cellular structures particularly lipid membranes. Secondly, for Cryo-EM methods vitreous ice produces very low contrast allowing objects of interest embedded within to be visualised. Two primary methods are used to form vitreous ice: plunge freezing in liquid ethane and high pressure freezing.

Plunge freezing samples contained in an aqueous solution are dropped cast onto holey carbon films. The sample is blotted to produce a thin lamella of water suspended across the holes in the film before being plunged into liquid ethane. A significantly higher heat transfer is possible with liquid ethane over liquid nitrogen due to the lack of Leidenfrost effect, freezing the sample far more rapidly, creating vitreous ice. Samples thicker than ≈1µm are too thick for vitreous ice to form uniformly through the whole sample. Thick samples such as whole cells can be prepared in this manner, however nuclear and perinuclear regions of a eukaryotic cell for example will not be vitrified. The thin cellular extremities will become vitrified and can subsequently be imaged.

High pressure freezing is the second method used to generate samples preserved in vitrified ice. At pressures of 204.5 MPa the temperature required to form vitreous ice rises to -22°C enabling much wider samples ≈6mm to be processed (200µm thick). Two main high pressure freezing methods are routinely used to produce samples for TEM. The method chosen will be determined by the thickness of sample and the speed at which transfer between LM and HPF (high pressure freezing) needs to take place. The standard HPF systems include: HPM 010 (ABRA), Compact HPF 01 (Wohlend) and the EM HP 100 (Leica). However if transfer speed is paramount then the EMPACT2 HPF (Leica) rapid loading system is likely to be more suitable. Despite being able to only freeze small samples that fit into specialised carriers (200µm thick) the transfer time between imaging and freezing is around 4-5

seconds. This system is particularly complementary with live cell imaging as the EMPACT2 is portable so can be placed directly adjacent to the microscope allowing ephemeral events to be imaged and fixed with relative ease. More recently HPF systems with integrated fluorescent microscope have been developed allowing even more rapid transfer ≈2s (Heiligenstein et al., 2017).

1.3.3.4 Processing Vitreous Frozen Samples

Once a thick vitreous frozen sample has been acquired it may be processed in a number of ways including: freeze substitution, direct to Cryo-EM and cryo-microscopy of vitreous sections (CEMOVIS). CEMOVIS is a very technical demanding sample preparation step. Samples undergo HPF but are immediately sectioned at cryogenic temperatures to retain the vitreous ice and the cellular environment as close to the native structure as possible. Using a diamond knife on an ultramicrotome, ultra-thin 50nm cryosections are collected. Ultra-thin cyrosections can exploit the superior antigen preservation of HPF when used in conjunction with immunostaining (Hagen and Grünewald, 2008). Despite its many advantages CEMOVIS can introduce very technique specific artefacts including chattering, compression and knife marks. However these artefacts can be somewhat reduced by using a vibratome where the diamond knife rapidly oscillates (Al-Almoudi et al., 2003).

While CEMOVIS opts for a mechanical means to produce thin sections, focused ion beams (FIBs) offer a more delicate and automated alternative. FIBs fire a high powered and very precise beam of ions at a substrate. The collision of these ions with the substrate is able to extract material in an exact and intentional manner. FIB-SEM (focused ion beam – scanning electron microscopy) is a technique that has been developed to compliment serial block face scanning electron microscopy (SBF-SEM) techniques. While SBF-SEM can progress through a greater thickness and process larger sample areas, the FIB enables much finer progression through the sample with minimal artefacts effectively increasing the axial resolution of SBF-SEM. FIB-SEM can mill through a block until a specific area of interest is discovered. The FIB can then mill away at an angle to produce a thin vitreous lamella. This can be followed by a technically demanding method called cryo lift-out where thin vitreous sections can be transferred into the TEM. The FIB is therefore a useful tool to prepare both SEM and TEM samples.

1.3.3.5 Freeze Substitution

Freeze substitution is a technique performed at cryogenic temperatures that replaces the vitreous ice with a polymer resin. Firstly the frozen sample is dehydrated by replacing it with solvent which often contains a fixative such as OsO_4 and/or UA. The solvent is then replaced by a polymer resin which when fully infiltrated is typically polymerised at low temperatures under a UV light. Freeze substitution avoids many of the common artefacts introduced from chemical fixation achieving a more native cellular ultrastructure. Substituting the vitreous ice for hydrophilic resins while retaining a small percentage of water ≈5% in the freeze substitution mix enables fluorophores to remain functional when embedded (Nixon et al., 2009). In-resin fluorescence is a powerful tool in the correlative light electron microscopy (CLEM) workflow. It streamlines many CLEM workflows and enables much greater resolution and control in the z/optical-axis when compared to FM. The optical section resolution of a typical confocal is around 500nm, however it is possible to create sections of a thickness of 50-70nm drastically increasing the axial resolution. In the context of a CLEM protocol, in resin fluorescence removes uncertainty between FM and TEM data in the z-axis, enabling more straightforward correlation.

1.3.4 Scanning Electron Microscopy and Analytical Electron Microscopy Techniques

1.3.4.1 Scanning Electron Microscopy

Scanning electron microscopy (SEM) utilises a focused electron beam which is scanned over the surface of a sample in a raster system. Samples imaged with an SEM do not necessarily require sectioning, this limits SEM to the analysis of surface topography as electrons are unable to transmit through thicker samples. Since electrons are unable to transmit through thick samples they are captured leading to charging effects. Sputter coating, most commonly with silver, gold and platinum are used to combat this. These heavy metals reduce surface charging effects by dissipating/conducting excess electrons away while providing an electron dense layer to scatter electrons back to the detector and increase the signal/resolution.

Although EM exceeds the resolution offered by both diffraction limited and super resolution light microscopy techniques, photons allow imaging depths from hundreds of microns (Helmchen and Denk, 2015) to millimetres (Chung et al., 2013). Electron beams are routinely used to image 300nm thick sections but at most can only reach depths of several microns (Kanaya and Okayama, 1972). Initially 3D EM was limited to serial section TEM (Birch-Andersen, 1955) which could acquire 3 dimensional information but its low throughput dissuaded the acquisition of large 3-D data sets.

Volume SEM techniques such as serial block face SEM (SBF-SEM) and focused ion beam SEM (FIB-SEM) use automated systems to iteratively remove surface material between image capture producing large 3-D data sets. SBF-SEM consists of a diamond knife microtome mounted within a vacuum chamber. The sample is aligned similarly to a standard microtome before imaging the surface. Between each image the sample is moved up toward the knife in 25-200nm increments (Titze and Genoud, 2016). The whole surface is then mechanically removed with the diamond knife before the process repeats. The automation of this process enables high throughput large 3-D datasets with high resolution to be acquired. FIB-SEM functions in a similar manner but utilises a FIB to carefully and deliberately remove material from the surface of the sample. The FIB-SEM system can be adapted with a cryotransfer unit to process cryogenically preserved samples. The FIB can also progress through the sample in far finer increments than the SBF-SEM, reliably removing several nanometres of material at a time. The improved axial resolution of the technique enables acquisition of data sets with isotropic voxels in the size regime of 3-5nm^3 (Wei et al., 2012).

1.3.4.2 High Angle Annular Dark Field Scanning Transmission Electron Microscopy

STEM was developed initially as a bright field technique where electrons with no or very small angular scatter were collected on a circular detector placed in a conjugate plane to the diffraction pattern. Microscope users became interested in the electrons scattered with even higher angles which led to the development of dedicated annular dark field detectors. Scanning transmission electron microscopy (STEM) focuses the electron beam to a very small spot size <0.2nm in diameter. The beam is then rastered over the sample to create an image. The technique can be used in a number of ways to acquire additional resolution and/or information.

High angle annular dark field scanning transmission electron microscopy (HAADF-STEM) takes advantage of the inelastic scattering of electrons interacting with a sample. In standard TEM objective lenses block electrons scattered at high angles to generate additional contrast in electron dense regions. Blocking these high angle electrons makes these regions appear far darker. HAADF-STEM collects scattered electrons with an annular detector, which are displayed as bright regions within the image. In standard TEM, the objective aperture excludes these electrons, making them appear darker. Thus if the HAADF signal is inverted it appears similar but not identical to a bright field TEM image of the same region. Since a HAADF-STEM collects electrons from high scattering regions it is very sensitive to the atomic number (Z) of elements in the sample (Figure 1.3). As the Z number increases so too does the electron density of the element producing more inelastic collisions and higher frequency of electrons detected by the annular detector. In the biological sciences, HAADF-STEM lends itself well to the identification of electron dense crystalline objects in a cellular/tissue context. The additional contrast of heavier elements afforded by STEM has enabled the identification of endogenously synthesised magnetite nanocrystals within intact magnetotactic bacteria (Woehl et al., 2014). Furthermore HAADF-STEM has been utilised to aid in the identification of QD (Quantum Dot) labels within endosomal structures (van Weering et al., 2010b)

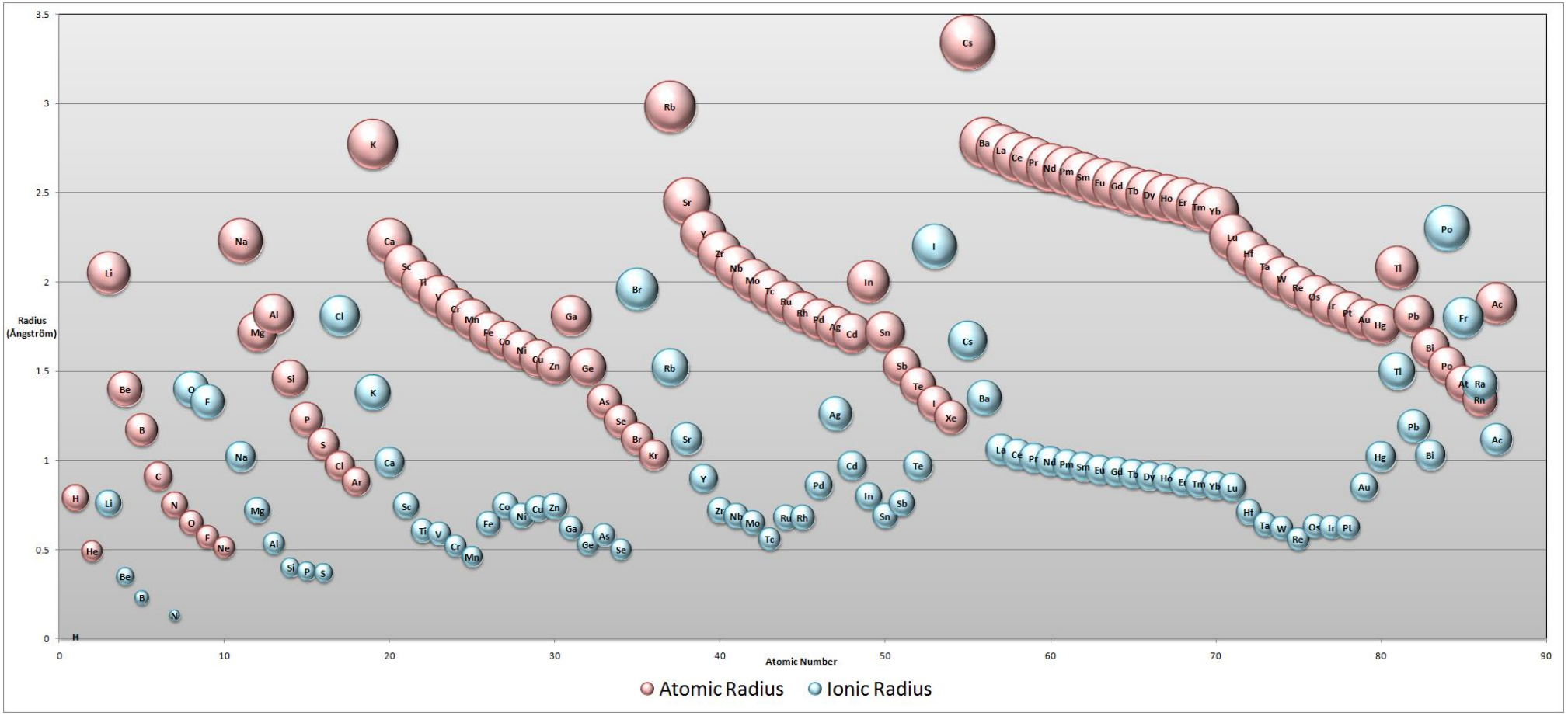

Figure 1.3: A diagram of a select number of elements ordered in size of their atomic and ionic radii. Elements increase in atomic number along the x-axis. However the coulombic force exerted on an incident electron is likely to increase as the ionic radius decreases/down the y-axis. As the values of x increases and the value for y decreases the scattering these elements produce in a STEM-HAADF will also increase. Adapted from Hatteland.

1.3.4.3 Electron Energy Loss Spectroscopy

EELS can be used in wide field as a spectroscopic technique or STEM mode to enhance resolution and generate spectral maps. Electrons incident upon the sample will transmit through but not all will retain the same amplitude/energy upon exit. For accurate results the electron beam must have a very narrow spread of energies. The vast majority will travel through the sample unaffected and are termed zero loss electrons. A smaller subset of electrons will lose energy or have their paths deflected which is measured by an electron spectrometer. Energy loss tends to be discretised phonon/plasmon excitations, inter/intra-band transitions, inner shell ionisations and Cherenkov radiation. Inner shell ionisations are particularly useful energy transitions for analysing the elemental content of a sample. Electrons losing energy at a discrete peak around 285eV would likely be measuring the inner shell ionisation of a carbon atom. EELS niche is identifying the elemental composition of relatively light elements from around carbon up to zinc. The increased electrostatic interactions from heavier elements results in greater energy losses and very weak signals which can be difficult to interpret. Although only a limited range of elements can be analysed, EELS is capable of gleaning information regarding atomic composition, chemical bonding/grain boundaries (Fallon and Brown, 1993) and, valence/oxidation states (Riedl et al., 2007). EELS has proven an effective tool for mapping elemental distribution throughout cells. Phosphorus has been detected within a 1-2nm resolution in complex with both DNA (Bazette-Jones et al., 1999) and proteins (Leapman and Rizzo, 1999).

1.3.4.4 Energy Dispersive X-ray

EDX shares some similarities with the aforementioned EELS. Also a spectroscopic technique, it can be used in STEM mode to map out the elemental content of a sample. In some respects EDX is less flexible than EELS being limited to purely elemental analysis, however EDX is not limited to the analysis of light elements. Electrons from the STEM beam can transfer energy to inner shell electrons present in the sample, ejecting them, ionising atoms in the sample. The ejected electron leaves behind an electron hole which is filled by an electron orbiting in a higher energy orbital. This process releases an X-ray whose energy values are both discrete and element specific. Each element will release X-rays with characteristic energy values which can be interpreted by the detector. It is not uncommon for a given element to have multiple energy signatures dependent upon which orbital the initial electron is ejected from. EDX excels in mapping the distribution of heavier elements within

biological and inorganic samples alike. Unlike EELS, EDX is particularly apt at identifying heavier elements within biological samples. For example EDX has been used to study the distribution and concentrations of Cu, Zn and Fe within red blood cells (Wu et al., 2013).

1.4 Correlative Light Electron Microscopy

Correlative imaging techniques are highly varied and can include any number of different techniques depending on the sample and information required. Multiple imaging techniques are used in tandem to examine the same sample. Complimentary techniques used correlatively, can provide more information than the same techniques used in isolation of one another. More often than not one technique is used to gain spatial information or used to acquire regions of interest within a sample while the complimentary method extracts useful data from the previously identified areas. This is not always the case and the strength of correlative approaches revolves around the combination of many different methods dependent upon the sample being analysed.

CLEM is a technique that seeks to use light and electron microscopy techniques in tandem to reap the benefits of both. The constituent techniques, electron microscopy and fluorescence microscopy, are both well-established techniques used to investigate the structural characteristics of biological samples. CLEM seeks to redress the disadvantages of FM: lower resolution, lack of ultrastructural context and poor optical sectioning by imaging the same cell/location again with electron microscopy. While the inclusion of FM into a CLEM workflow simultaneously overcome EMs reliance on fixed samples so dynamic cellular events can be tracked. A CLEM experiment relies on being able to find the same cell/location in both techniques so that images and data generated in each imaging modality can be correlated. To do this effectively the probes must be visible in each technique. Therefore an ideal probes must have a fluorescent and electron dense component. This thesis will focus primarily on the combination of confocal microscopy and transmission electron microscopy for its light and electron components respectively.

1.5 CLEM Probes

CLEM probes are specialist labels that are visible in multiple imaging modalities. Probes must generate a fluorescent signal observable with FM and be electron dense enough to generate contrast in an electron micrograph. Individual structures that possess both these attributes are rare. More commonly two or more individual components are assembled together in a proximal manner for optimal signal colocalisation (Brown et al., 2012).

1.5.1 CLEM Probes with an Endogenously Expressed Element

With the popularity of GFP and its many variations, genetic modification of a hosts DNA or transformation/transfection with plasmid DNA to produce fluorescent fusion proteins is a method widely used in LM to label a protein of interest. Fusion proteins display excellent colocalisation of signal and target as only a small peptide linker is present between the two and does not rely on binding affinity. Since the discovery of GFP a whole family of fluorescent proteins from far-red (Rodriguez et al., 2016) through to blue fluorescent proteins (Subach et al., 2011) have been developed for use as FM probes.

The creation of endogenously expressed electron density for use as an EM label which would confer the great attributes/advantages GFP (and other fluorescent proteins) has bestowed to FM is not a trivial task. However the strong colocalisation protein constructs confer would be particularly beneficial in conjunction with the high resolution of TEM. Consider a standard immunolabelling protocol for TEM using a primary antibody followed by a secondary conjugated to a suitable EM label. An uncertainty of 20-30nm between the target and the label is introduced due to the additional elements required to co-localise the label (Lee et al., 2008). In LM this small distance is negligible but severely restricts the maximum resolution achievable with TEM. Therefore encoding electron density into a gene is highly desirable for this reason.

1.5.1.1 Horseradish Peroxidase

Horseradish peroxidase (HRP) is one such enzyme capable of generating sufficient singlet oxygen species to trigger the polymerization of Diaminobenzidine (DAB) into an osmiophilic precipitate. Subsequent OsO_4 staining forms an electron dense precipitate. However due to the reducing

environment of mammalian cytosol, inactivating the enzyme, HRP can only be used to label proteins within the secretory route (Li, 2010). The loss of function could be attributed to four disulphide bonds that are unlikely to form in a low Ca^{2+}, reducing environment.

1.5.1.2 APEX

An alternative enzyme, ascorbate peroxidase, has been utilized for the same purpose but overcomes some of the shortfalls of HRP. The ascorbate peroxidase (APEX) used was a class I cytosolic plant peroxidase derived from peas (Patterson and Poulos, 1995). The enzyme does not contain disulphide bonds or require calcium ions and is therefore active in the reducing environment of the cytosol. APEX is only 28kDa in size, approximately 40% smaller than HRP. The enzyme had to be modified in two major ways to create an effective EM probe. Firstly the active site was modified to accommodate DAB as a substrate. Secondly the ability of wild type enzyme to dimerize was removed, as dimerization can cause incorrect trafficking or localisation of the target protein. The crystal structure was used as a reference to induce point mutations at the dimer interface (Martell et al., 2012). APEX remains active after membrane-preserving cell fixation and generates a minimally diffusive reaction product that does not cross membranes. Therefore this particular genetic probe is well suited to study membrane proteins. The authors elegantly showed which side of the inner mitochondrial membrane a specific protein terminus was located by observing which side of the membrane the electron dense precipitate formed (Martell et al., 2012).

1.5.1.3 Metallothionein

Metallothionein (MT) is a small 61 amino acid protein capable of binding heavy metal ions. A third of its residues are cysteine which enable the protein to chelate a wide variety of metal ions. Upon binding ions the initially amorphous protein forms a bi-lobed structure separated by a short flexible hinge region. The two lobes create a nearly spherical cavity 1.5-2nm lined with the cysteine residues. In physiological conditions MT is involved in chelating ions such as selenium, zinc and copper (Kägi and Schäffer, 1988). However MT has a high binding affinity for xenobiotic ions such as gold, silver, mercury and cadmium (Nielson et al., 1995). More recently Morphew et al. have developed protocols to more readily include the MT probe into sample preparation for EM. The authors performed genomic editing on the SPC42 gene which codes for spc42 protein, which is a component of the spindle pole body in yeast. The gene was edited to express a protein construct with 2xMT peptides attached to the C-terminus of spc42. Cells expressing this tag at wild-type levels did not see

a decrease in growth rates when compared to a control, suggesting that protein function was not impaired. The cells were high pressure frozen and freeze substituted in acetone and diglyme. Au(III)Cl_3 gold salts were added to the freeze substitution mixture and subsequently silver enhanced. This method produced punctate particles easily visualised by TEM with negligible noise. Furthermore this protocol removes the need to individually stain sections with gold salts which increases through-put significantly (Morphew et al., 2015).

The aforementioned clonable EM tags do not provide a concomitant fluorescent signal which would be required for use in a CLEM workflow. Combinatorial probes such as FLIPPER use two or more well characterised proteins to produce the desired characteristics of a CLEM probe. FLIPPER uses both a fluorescent protein (either: mTurquoise2, EGFP, mOrange2, or mCherry) and an HRP in a single tag (Kuipers et al., 2015). However, Mini Singlet Oxygen Generator (MiniSOG) is a small protein tag 106 amino acids in length engineered from Arabidopsis phototropin II that is both inherently fluorescent and capable of generating electron density. MiniSOG's quantum yield of 0.37 is relatively low compared with the widely used GFP/EGFP but it is also capable of enzymatically polymerising DAB when exposed to blue light (Shu et al., 2011). Similar to both HRP and APEX, this precipitate is osmiophilic and when stained generates strong contrast in the electron micrographs. MiniSOG is a very close to a true combinatorial probe in the respect that this single protein that can be visualised in both LM and EM.

1.5.2 Affinity Based CLEM Probes

Unlike endogenously expressed tags which are inescapably linked to the protein of interest, exogenous probes require a mechanism to reach and co-localise with the target. Affinity based probes rely on specific complementary ligand-target binding to deliver and co-localise a probe to the protein of interest. The cell membrane poses a significant barrier of entry for exogenous probes to enter and additional steps are required to bypass it. Most commonly cells are permeabilised in some way to disrupt the cell membrane. This process can cause ultrastructural damage and the cellular contents to extract. Alternatively labelling cell surface proteins that are retained on the surface or are internalised is an elegant way to avoid this but limits the number of proteins one can label.

The majority of affinity probes rely on the avidity of antibodies to co-localise the label to the target while AuNPs are the most commonly used label. AuNPs have long been used as labels to mark proteins in TEM (Takizawa and Robinson, 1994). This is due to the superior contrast they produce in

the TEM compared with other less dense metals, their low cytotoxicity (Connor et al., 2005) and their ease of synthesis and surface functionalisation. The diversity of potential surface functionalisation means gold nanoparticles can be conjugated to a wide variety of biomolecules which vicariously binds the gold to a specific target. One of the first and most widely cited examples was by Robinson and Takizawa who showed the efficacy of 1.4nm gold nanoparticles conjugated to antibodies termed nanogold (NG) as a TEM probe. The probe was shown to effectively label Human neutrophil granules, lactoferrin and myeloperoxidase positive (Takizawa and Robinson, 1994). NG displays better sample penetration and labelling efficiency than colloidal gold due to its smaller size (Robinson et al., 2000). Additionally antibody fragments can be functionalised with NG without the need for macromolecule stabilisation which keeps the probe compact retaining high diffusivity (Takizawa et al., 2015).

1.5.2.1 Gold Nanoparticles

Fluoronanogold (FNG) combines its predecessor, NG, with an organic fluorophore in a single probe for use in CLEM workflows. The fluorescence and NG can be conjugated to a Fab' fragment, IgG or streptavidin depending on which mode of colocalisation is most suitable. The 1.4nm AuNP is conjugated to a thiol in the hinge region of the Fab' via a maleimido derivative and to the streptavidin using a sulfo-N-hydroxysuccinimide derivative. The organic fluorophores are attached to the Fab' and streptavidin with either an N-hydroxysuccinimide or a sulfo-N-hydroxysuccinimide linker. The AuNP and fluorophore are attached in a region removed from both the target binding site and each other to minimize steric hindrance and fluorescence quenching respectively (Takizawa et al., 2015). FNG labelling on ultrathin cryosections was the first example of the exact same structures imaged with both FM and TEM (Robinson et al, 2001). FNG has been shown to be a very robust and versatile probe capable of labelling samples pre-embedded in polymer resins (Fabig et al., 2012), endogenous proteins within cells (Olmos, 2015) and tissues (Takizawa et al., 2015).

Alternatively, one can opt to endogenously express the fluorescent component (such as GFP) as part of a construct with the protein of interest. This ensures a strong correlation between the target protein and the fluorescent signal. Antibodies raised against GFP can then be used to colocalise a second label to this protein. The aforementioned NG is used widely for this purpose. A single antibody can therefore label a plethora of protein targets so long as it is in a construct containing the relevant fluorescent protein. However due to the lack of a direct interaction with the target protein

this method cannot be used to label specifically modified proteins for example a phosphorylated/dephosphorylated protein.

Not all affinity based probes rely on antibodies to deliver the label to the target. Native binding pairs can be utilized *in vivo* to deliver a label. The trafficking of the epidermal growth factor receptor (EGFR) was studied vicariously by attaching a fluorescent AuNP to its ligand epidermal growth factor (EGF). EGFR translocates to the cell surface membrane where it binds the extracellular ligand before being endocytosed. This method takes advantage of a natural uptake mechanism and removes the requirement of cell permeabilisation for the probe to traverse the cell membrane (Brown and Verkade, 2010). More commonly probes based on streptavidin are used to label proteins *in vivo*. The probes success stems from the incredibly tight binding of streptavidin to its ligand, biotin, which is on the order of $\approx 10^{-14}$ mol/L. Methods of biotinylating proteins *in vivo* can be used to label targets (Han et al., 2017) or alternatively streptavidin can be endogenously expressed as a chimera protein for labelled biotin to attach (Arribillaga et al., 2013). Streptavidin labelling does present some complications which are more thoroughly discussed in section 1.5.2.1 but its high binding affinity and robust nature has seen it become widely used in the field.

1.5.2.2 Quantum Dots

QDs are nanoparticles composed of semiconducting materials most commonly cadmium and selenium. QDs display size-tuneable fluorescent emission due to electron confinement, resist photo-bleaching and give high signal brightness. These inherently fluorescent and electron dense nanoparticles displays very desirable attributes for use as a CLEM probe. Giepmans et al. explored the feasibility of using QDs as CLEM probes with moderate success. With size specific and narrow emission peaks the authors demonstrated triple labelling resolvable in both FM and EM using solely QDs. Proteins were first labelled with a primary antibody, followed by a secondary antibody biotin conjugate and finally streptavidin functionalised QDs. Despite appearing to be an efficient and effective labels there were several key drawbacks. Cells labelled with QDs could not be fixed with either paraformaldehyde/glutaraldehyde or osmium tetroxide. Instead the cells had to be dehydrated and triple stained with UA after being embedded and sectioned. This method of sample preparation is likely to have a deleterious effect on the ultrastructure of the cell and therefore not be wholly representative of its natural state (Giepmans et al., 2005). Furthermore, QDs must be composed of a semi-conducting metal such as cadmium, selenium or tellurium. These metals are significantly less electron dense than the silver, gold and platinum commonly used in other probes

which results in less straight forward label identification in electron micrographs (and tomograms) (van Weering et al., 2010b). QDs are also less straightforward to surface functionalise than AuNPs. Consequently, the surface of a quantum dot can become densely packed with ligands. Multiple proteins are likely to bind to the QD surface, become aggregated or interact with one another due to their increased and sustained proximity. This can result in either non-physiological effects or undesirable natural signalling pathways which deviate from the expected native pathways. Cell surface receptors are one ubiquitous example of ligand binding inducing multiple proteins to move proximal to one another triggering a transduction pathway. EphA3 is a cell surface receptor with tyrosine kinase activity found in neuronal synapses. Using quantum dots to label this protein has been shown to activate this protein's transduction pathway. Howarth et al used monovalent quantum dots with a single binding site for EphA3 and was able to avoid proximity induced phosphorylation and pathway activation (Howarth et al., 2008).

1.6 Application of CLEM to the Endosomal Network

Membrane bound proteins contained within endocytosed intracellular vesicles will be processed by the cell in one of two ways. Some proteins will remain in the endosomal membrane as it matures leading to degradation. Other proteins not fated for degradation can be rescued and recycled back to a membrane bound organelle or cell membrane. Proteins to be rescued from the degradative pathway are removed via tubulo-vesicular carriers that transfer them to specific targeted locations. Proteins capable of forming these tubulo-vesicular structures can either directly bind the cargo protein or vicariously via an accessory protein. Membrane bound proteins fated for degradation will remain associated with the late endosome and will be sequestered in smaller vesicles that pinch off in to the endosomal lumen. This process forms cargo rich multi-vesicular bodies (MVB). Finally the MVB will fuse with a lysosome and the contents of the endosome will be degraded by a myriad of acid hydrolyses. CLEM is well suited to investigating these processes and has been used successfully to shed light onto key processes of endosomal trafficking. Fluorescently marking specific protein events and then scrutinising these areas in high resolution with EM enables small structures crucial to this network's function to be identified and imaged efficiently. A robust example of this was into endosomal pit formation in yeast where Cryo-CLEM techniques were employed. The pit formation process was caught at different time points as identified by TEM. The concurrent fluorescent signal generated from labelled key regulatory proteins interacting with the endosomal pit provided temporal insight. Fluorescent signal colocalisation showed the order in which proteins became

bound and unbound and the length of time each one of these steps took (Kukulski et al., 2011). Similar techniques to identify function and form have been applied to: caveolin-1 (Ariotti et al., 2020) and caveolin-3 (Nixon et al., 2009) both involved in caveolae formation, and LCa (Kirchhausen, 2009) part of the clathrin dependent pathway have also been investigates using CLEM techniques. However, we are only beginning to place mechanistic understanding of endosomal machinery into a whole cell context. The further development of CLEM methodologies will help us further elucidate these processes further.

The next stage of endocytosis, after intracellular vesicle formation, is to traffick cargo from them to relevant areas of the cell. Sorting Nexin (SNX) proteins play a major role in the formation of tubulo-vesicular structures. In order to manipulate lipid vesicles into a tubular structure requires SNX proteins to undergo higher order oligomerisation. This forms a putative helical array which supports the lipid tubule. Using the novel FKBP-SLF' probe system we aim to improve on previous attempts in infer these structures. Firstly, it is unknown whether these helical protein arrays are continuous or occupy discrete regions along the tubule. Secondly, we would aim to visualise the helical pitch of the SNX protein array. Potentially the FKBP-SLF' probe's size and high binding affinity may be able to label these structures with minimal steric hindrance and high labelling efficiency.

1.6.1 Endosomal Maturation

Endosomes having just budded into the cell and still containing contents from the extracellular environment are termed early endosomes. At this stage the early endosomes lipid composition is thought to be similar to the cell membrane it originated from. Relatively high levels of both cholesterol and phosphatidyl serine are present. However specific lipid concentrations are elevated in the early endosome. For example phosphatidyl inositol 3 phosphate (PI(3)P) is responsible for enabling many cargo sorting proteins to bind, including the PX-domain contained within the SNX-BAR family of proteins (Kutateladze et al., 2010).

Although changes occurring during the process of maturation are not discrete, endosomes are often considered to either be in an early or late stage. These stages can be defined by several morphological changes occurring as an endosome matures. Initially endosomes are small, around 100nm in diameter (Van Meel and Klumperman, 2008), and located at the cell periphery. As they

mature they typically migrate towards the perinuclear region of the cell. This process is mediated by Myosin 6 which traverses actin filaments toward the minus end (Aschenbrenner et al., 2003). The lumen of early endosomes is slightly acidic causing ligands bound to receptor proteins to dissociate. Membrane remodelling proteins bind to the endosome, and with the addition of certain accessory proteins, recycle these receptor proteins by means of tubulo-vesicular structures. Any proteins that are unable to dissociate from their ligands or are fated for degradation bud inwards and become sequestered on intraluminal vesicles (ILVs). As the process of maturation progresses endosomes generate more ILVs (Figure 1.4), increase in size due to homotypic fusion events (Gruenberg et al., 1989) and adopt a rounded or ovular morphology. In addition the luminal cavity of the endosomedrops in pH from 5.9-6.8 to 4.9-5.9 over the course of the maturation process (Yamashiro et al., 1987). Vacuolar adenosine triphosphate trans-membrane protein pumps are responsible for this luminal acidification (Kane, 2006). They share a significant homology with the ATP synthase enzymes found in the mitochondria.

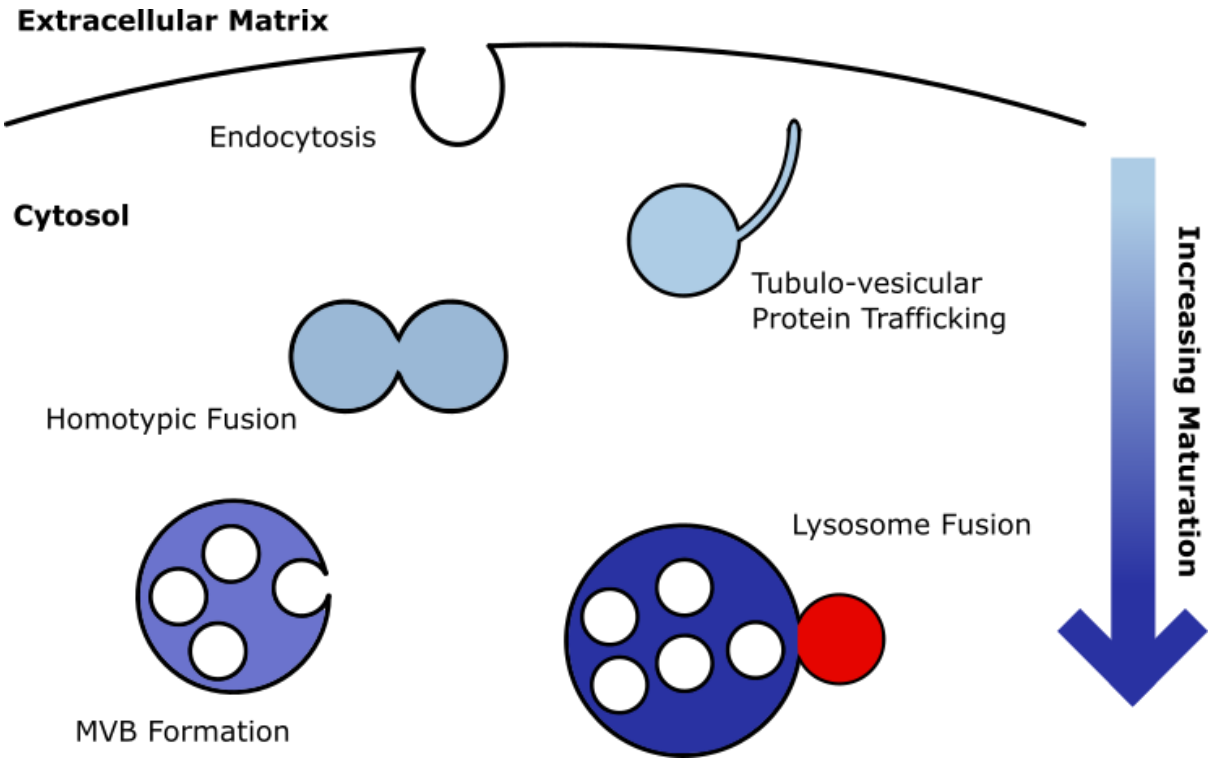

Figure 1.4: Diagram depicting the typical process an endosome would experience as it matures and traverses the endosomal network. The colour gradient indicates endosome maturation.

The lowered pH present in the endosomal lumen is reduced following endosomal fusion with a lysosome. In the TGN (trans golgi network), sorting receptor proteins are packaged on the luminal

side with acid hydrolyse enzymes. Vesicles containing these enzymes bud from the TGN and are most commonly delivered to the lysosomal/endosomal network by mannose-6-phosphate pathway. The acid hydrolyses are not active while in this bound state but upon fusion with the late endosome are exposed to the low pH present in the endosomal lumen. This triggers the dissociation and activation of the acid hydrolyse cargo (Luzio et al., 2007) (Coutinho et al., 2012). The sorting receptor proteins once vacant can then be recycled back to the TGN.

1.6.1.1 Membrane Marker Changes During Endosomal Maturation

Two prominent markers of the early endosomal membrane are Rab5 and PI(3)P (Jovic et al., 2010). Ras associated binding proteins (Rab) are a family of small GTP binding proteins. They cycle between an active GTP bound state and an inactive GDP bound state. This process is in turn mediated by GDP-GTP exchange factors (GEF) which determine the Rab protein's activation state and how long they remain in any given configuration (Barr and Lambright, 2010). Rabex-5 is a protein that also promotes GDP/GTP exchange in Rab5. Rabaptin-5 is a protein which binds Rab5 in a GTP dependent manner and slows the GTP hydrolysis enabling Rab5 to remain active longer. When all three are complexed Rab5:Rabaptin-5:Rabex-5, they promote further Rab-5 effector recruitment, creating a positive feedback loop and activating more Rab-5 molecules in the vicinity (Horiuchi et al., 1997). While in their active state they are able to bind to intracellular membranes and recruit a myriad of proteins termed Rab effector proteins. These Rab effectors are then able to orchestrate several functions including: fusion, tethering, delivery and budding. The active Rab5 platform is also responsible for the recruitment of Class III PI 3-kinases, VPS34 and PI3Kβ. PI 3-kinases are of particular interest as they are responsible for the catalytic generation of PI(3)P lipids on the endocytic membrane. Two well characterised domains: Phox homology (PX) domain and the FYVE finger (which is a zinc finger originally observed in Fab1p, YOTB, Vac1p and EEA1) are able to interact with this phosphorylated lipid (Gaullier et al., 1999). The interaction between the PI(3)P lipid and the PX domain is pertinent as the SNX1 protein also contains a PX domain. This interaction is one of the key triggers for tubulo-vesicular structure formation enabling protein recycling from endosomes.

At a certain stage of maturation there is a sudden and large shift in the biochemical make-up of the early endosome leading to biomarkers for the late endosome rising to prominence: Rab7 and PI(3,5)P (Meresse et al., 1995). Rab5, which was previously driving many pathways characteristic of the early endosome also aids in recruitment of and activation of Rab7 and its guanine nucleotide

exchange factor. At a critical concentration of Rab7 a cut-off switch mechanism takes place where Rab7 begins to deactivate Rab5. In addition the Mon1-Ccz1 complex (which is the guanine exchange factor for Rab7) is able to bind Rab7 promoting its activation and further Rab7 accumulation (Nordmann et al., 2010).

The enzyme phosphatidylinositol 5-kinase (PIKfyve) binds via association between its FYVE domain and PI(3)P lipids which exist on the early endosomal membrane. PIKfyve then catalyses the conversion of existing PI(3)P to PI(3,5)P_2 which is tightly regulated by a myriad of PIKfyve associated protein complexes including: VAC14 and FIG4 (Rudge et al., 2004) (Sbrissa and Shisheva, 2005) (Botelho et al., 2008) (Jin et al., 2016). PI(3,5)P_2 is then able to recruit a wide variety of effectors. Chiefly among these are effectors controlling retrograde vacuole transport and anterograde protein trafficking via MVBs. The majority of proteins destined for the MVB are tagged with mono-ubiquitin regulated by the FYVE domain containing protein Hrs/Vps27p and ESCRT (endosomal sorting complexes required for protein transport)-1, ESCRT-2 and ESCRT-3. In cells unable to generate PI(3,5)P_2 protein trafficking to the MVB is compromised. Constitutive N-terminal tagging these cargo proteins with monoubiquitin does rescue MVB trafficking but via a PI(3,5)P_2 independent pathway (Michell et al., 2006).

1.7 SNX-BAR Family of Proteins

Sorting Nexin proteins are characterised by their PX-domain which mediates binding primarily to PI(3)P enriched membranes of the endocytic network. Their function is fairly diverse, spanning endocytosis, endosomal sorting and endosomal signalling (Cullen, 2008). Sorting Nexin - Bin/Amphiphysin/Rvs (SNX-BARs) are a subset of SNXs and as the name suggests contain a BAR domain. A fairly large portion of SNX proteins belong to this subset: SNX1, SNX2, SNX5, SNX6, SNX8, SNX30 and SNX32. SNX9, SNX18 and SNX33 all of which contain an N-terminal Src-homology-3 domain (van Weering et al., 2010). The primary function of most SNX-BAR proteins can be summarised by dimerization, localisation to specific lipid sub-domains, tubule formation and the subsequent trafficking of cargo along the tubule to specific subcellular location/organelle. Cargo trafficking to different subcellular locations is mediated by different SNX-BAR proteins with a certain degree of degeneracy. A huge number of other accessory proteins also interact with SNX-BAR proteins including: retromer (Seaman, 2012), Retriever complex (McNally et al., 2017) WASH complex (Helfer et al., 2013) which go beyond the scope of this thesis.

SNX1 has been shown to regulate the trafficking of various protein cargoes. Knocking down the SNX1 gene decreased the concentration of sortilin and mannose 6-phosphate receptors measured in the trans-golgi network and an increase in their lysosomal degradation (Mari et al., 2008). SNX1 has also been shown to traffic cation independent mannose 6-phosphate receptors from endosomes to the TGN. This process has recently been shown to be retromer independent which suggests SNX-BAR proteins may play a larger role in endosomal trafficking than previously assumed (Simonetti et al., 2017). Additionally, SNX-BAR proteins are also capable of downregulating protein trafficking in certain circumstances. In the absence of SNX1, both Shiga toxin and ricin are sorted and trafficked from endosomes to the TGN via the SNX8 tubules. Upon knocking down the SNX8 gene, significantly higher concentrations of Shiga toxin was trafficked from endosomes. Therefore, the authors suggest that in some circumstances SNX8 may act to downregulate the trafficking of certain cargoes (ricin was more or less unaffected) (Dyve et al., 2009).

1.7.1 Subdomains of SNX-BAR Proteins

BAR domains are a highly conserved family of three α-helices and come in four flavours: BAR, N-terminal amphipathic helix BAR (N-BAR), FCH-BAR (F-BAR) and Inverse Bar (I-BAR). All of these BAR domains act on lipid membranes to induce or stabilise a positive curvature with the exception of the I-BAR. Despite the sequence homology of SNX-BARs not closely resembling that of other BAR domains, they are most closely related to N-BARs such as endophilin (Pylypenko et al., 2007). In order for a BAR-domain to become a functional subunit it must dimerise with another BAR-domain containing protein in an antiparallel manner. As a result, there is a strong correlation between the ability of a BAR-domain containing protein to form homodimers and its ability to form tubules in *in vitro* conditions. Although not an exhaustive list: SNX1, SNX2, SNX4, SNX9, SNX18, and SNX33 all predominantly form homodimers in *in vitro* test conditions (van Weering et al., 2012). In turn this is determined by the presence of specific amino acids located at the SNX dimerization site ultimately determines a SNX-BARs proclivity toward homo or hetero-dimerisation (Dislich et al., 2011).

In the absence of any other functional protein region, BAR domains are capable of sensing membrane curvature. This can be demonstrated by BAR domains binding with increasing affinity for membranes that most closely match their own intrinsic curvature (Peter et al., 2004). Upon binding

to a membrane with pre-existing curvature, BAR domains are able to further stabilize this configuration, however in isolation are not capable of inducing membrane curvature or forming tubulo-vesicular structures. BAR domains in isolation are able to sense membrane curvature. However, in conjunction with other functional protein regions, including phox homology domains (PX-domains) and N-terminal amphipathic helices, enable BAR domains to also induce membrane curvature (discussed in more detail in section 1.7.2).

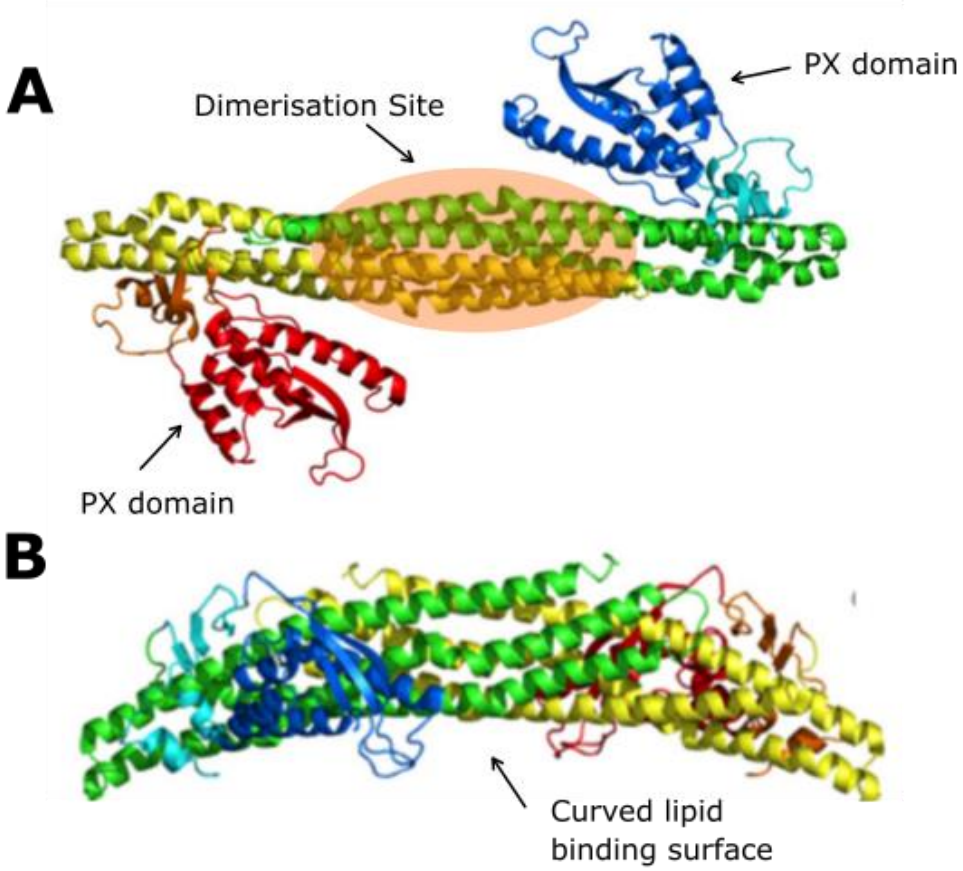

Figure 1.5: Both images A and B show the crystal structure of a SNX9 dimer. Image A is a top down view of the SNX9 dimer with the dimersation site and PX domains clearly shown. The curved lipid binding site can be seen in image B.

There are 49 genes of mammalian origin that code for PX-domains. They are composed of four α-helices and three β-sheets arranged into a “baseball glove” like conformation. Their primary function is to bind to phosphorylated inositide lipids which fit into the pocket formed by the β1, β2, α2 and their linking loops. PX-domains are well conserved but can vary slightly generating specificity towards different phosphoinsoitides. For example the PX-domain of SNX9 preferentially binds $PI(4,5)P_2$ while the PX-domain of SNX1 is specific to PI(3)P and $PI(3,5)P_2$ (van Weering and Cullen, 2014). PX-domain binding plays an important role in localising SNX proteins to relevant lipid membranes.

N-terminal amphipathic helices are an invariable component of the SNX-BAR structure. These amphipathic helices insert into a single leaflet of a lipid bilayer. The insertion is favourable into the disordered regions of highly curved lipid domains (Bhatia et al., 2009) aiding in the specific targeting of the SNX-BAR to endosomal micro-domains. The literature seems in strong agreement that the amphipathic helix is important in SNX-BAR function and membrane binding discussed further in section 1.7.2.

SNX-BAR proteins cycle between the cytosol and various organelles of the endocytic network. This is mediated by the relative binding affinity for particular membrane curvatures, protein cargo and lipid composition of the membrane. A variety of functional protein domains regulate this process, in particular BAR domains, PX domains and N-terminal helices. SNX1 and SNX2 possess all three structures and therefore occupy many of the same functional niches within a cell, often being degenerate. In isolation the binding affinity of the PX and BAR domains for the lipid membrane is relatively weak. However, the summation of the two enable these proteins to utilize co-incident detection to selectively associate with the high curvature, phosphatidylinositol enriched, endosomal membranes. This association of SNX-BARs is not generic, SNX1 has been shown to localise to specific micro-domains of the endosomal membrane characterised by high curvature and PI(3)P and $Pi(3,5)P_2$ enrichment (Carlton et al., 2004). Electrostatic interactions between the acid residues of the BAR domain and the negative lipid head groups may also be a contributing factor for sensing membrane curvature. Similarly, to the previously discussed membrane sensing mechanisms, in isolation it is insufficient to be the sole cause of this behaviour. Rather the combination of these electrostatic interactions and the insertion of an amphipathic helix in to packing defects contained within highly curved lipid membranes may also play a key role in curvature sensing (Bhatia et al., 2009).

1.7.2 Tubule Formation

Large concentrations of SNX-BAR proteins congregate in micro-domains characterised by high membrane curvature and the presence of phosphoinositides including PI(3)P and PI(3,5)P_2. High localised concentrations of SNX-BAR dimers promote higher order oligomerisation forming helical arrays (Cullen and Korswagen, 2012). As a result of biophysical, crystallographic and theoretical work, two potential mechanisms have been put forward to explain the BAR domain's ability to impose curvature on lipid membranes and form tubules. The first of which is the "scaffolding" hypothesis. It states that BAR-domains bend membranes via electrostatic interactions on their concave surface (Mattila et al., 2007) (Shimada et al., 2007). This is supported by observations that the concavity in the quaternary structure of the BAR-domain containing proteins correlates with the diameter of the tubules they form *in vitro*. Classical BAR-domains generate narrower tubules <100nm (Farsad et al., 2001) (Peter et al., 2004) while F-BARs with their more subtle curved surface produce tubules with a wider diameter (Henne et al., 2007) (Shimada et al., 2007). It has been demonstrated that many other proteins use clusters of basic residues to anchor to positively charged lipids within a membrane, phosphatidylserine and phosphatidylinositol bisphosphate, by primarily electrostatic interaction (Zimmerberg and McLaughlin, 2004). It is argued that the BAR domain behaves in a similar manner and primarily interacts via electrostatic interaction and the acidic residues located on its concave surface bind the negative head groups of phospholipids, notably PI(3)P (Frost et al., 2008).

The second proposed mechanism is the "buckling" response induced by the insertion of an amphipathic helix into the cytosolic leaflet of a lipid bilayer. The penetration of a single lipid layer is thought to act like a wedge that induces positive membrane curvature. An example of this type of curvature induction is already well established in Epsin. A small 150 amino acid protein containing an amphipathic helix without a BAR-domain was shown to be capable of generating lipid tubules with an average diameter of 15nm. Mutagenic studies introducing polar residues (replacing hydrophobic residues) into the amphipathic helix abolished this tubulating behaviour (Ford et al., 2002). Even in endophiln, an N-BAR-domain containing protein, point mutations introduced in to the amphipathic helix (hydrophobic to polar residues) was observed to abolish membrane binding and tubulation. However, more conservative mutations (hydrophobic to hydrophobic) had no significant impact on protein function (Farsad et al., 2001). Other studies introducing mutations into this amphipathic

helix with FCHo2 and amphiphysin show a reduced binding affinity for lipid membranes but an increased sensitivity to curvature (Henne et al., 2007), presumably because without a functional helix these proteins can no longer induce curvature complimentary for binding. Spectroscopic data also support these observations with the BAR domain directly above the lipid bilayer with the amphipathic helix inserted into the membrane which can occur independent of the BAR domain (Gallop et al., 2006). It may transpire that both these models have merit and all of the aforementioned factors: acidic residues on the BAR-domain, BAR domain curvature, amphipathic helix insertion and PX-domain binding all play a role in maintaining a specific and balanced protein function.

I-BARs are proteins characterised by their ability to induce negative membrane curvature. Considering a subset of these proteins do not contain an amphipathic helical domain (Linkner et al., 2014), the “buckling” hypothesis seems unlikely to provide a comprehensive explanation of tubule formation. There is also a subset of I-BARs that do contain amphipathic helicies (such as MIM). This inclusion would appear counter-productive to the function of an I-BAR if the helix was inducing a positive curvature. Furthermore mutagenic studies of the N-terminal amphipathic helix on endophilin showed the tubulating phenotype and helicity of the protein was preserved in the case of both point mutations and truncations. However, severely truncated amphipathic helices did not produce a tubulating phenotype due to a huge reduction in binding affinity for the membrane (Chen et al., 2016).

1.7.2.1 Tubule Structure

It has been proposed that the SNX-BAR dimers arrange themselves into a helical array along the length of the tubule. The fundamental building block of these large helical arrays are SNX-BAR dimers. In the context of an *in vitro* experiment with purified protein, homodimerisation is the primary indicator as to whether a given SNX-BAR protein is able to tubulate lipids (van Weering et al., 2012). Although in nature heterodimers between inherently tubulating SNX-BARs and other SNX proteins are common place. SNX-BAR dimers form in an anti-parallel manner, bringing together their BAR domains to form a concave binding surface. The concave surface preferentially binds to positively curved lipids which senses and stabilises curved lipid membranes. Upon the initial SNX-

BAR dimer binding and stabilising the curvature of the membrane, this increases the likelihood further binding events will occur. Large numbers of SNX-BAR homodimers bind at a single site and arrange themselves into a large helical super structure via tip-to-tip interactions. These lateral contact points between dimers are likely mediated by the loop between the first and second β-strands and the beginning of the second α-helix of the PX domain (Kovtun et al., 2018). However at the current time a holistic model of an *in vivo* SNX-BAR mediated lipid tubule has yet to be acquired. This is not surprising considering the vast variety, complexity and heterogeneity of these structures.

Thus far, methods to elucidate tubulo-vesicular structures mainly focus on *in vitro* tubulation assays utilizing purified protein incubated with liposomes and cryo-EM modelling. Some of the earliest studies using tubulation assays to glean insight into tubule structure co-incubated a BAR containing protein with dynamin. Amphiphysin and dynamin co-incubated with liposomes formed tubules with regularly spaced electron dense “fingers” along their lengths (Takei et al., 1999). In a similar study liposomes incubated with dynamin and endophilin again produced tubular structures with well-defined electron dense rings regularly spaced approximately every 132nm around the tubule (Farsad et al., 2001). This was the first direct evidence of periodic structures concomitant with BAR-domain mediated lipid tubules.

More recent studies using single particle analysis were able to generate a 17Å model of an F-BAR mediated helix (Figure 1.5). This model had sufficient resolution to unambiguously discern individual protein subunits adsorbed onto the underlying lipid membrane (Frost et al., 2008). The pitch of the helix was 26Å which is very tight and may be the result of an artefact of the reductionist experimental conditions. Similar studies (Mim et al., 2012) (Pang et al., 2014) generating similar models were also generated from highly charged lipids and very high protein concentrations. This distance between helical repetitions is questionable as it leaves very limited space for accessory proteins to bind and cargo to be trafficked. Despite this, there is validity to these assays regarding their ability to produce biological relevant structures in *in vitro* conditions. The diameter of F-BAR tubules and N-BAR tubules generated *in vivo* and analysed by thin-section electron microscopy were three times larger. This observation is mirrored in data obtained by *in vitro* tubulation assays (Frost et al., 2008).

Some progress has also been made toward including functional accessory proteins to the SNX-BAR tubule structure. Retromer is a heterotrimeric protein complex (Vps26p- Vps29p- Vps35p) in mammalian cells that interacts closely with SNX-BAR dimers *in vivo*. In yeast cells the complex exists as a hetero-pentameric structure: Vps5p (a yeast analogue of SNX1/2), Vps17p (yeast analogue of SNX5/6), Vps26p, Vps29p, and Vps35p. High resolution cryo tomography of lipid tubules *in vitro* were processed using sub-tomogram averaging of 17 tubules successfully modelled part of this pentameric structure in situ. X-ray crystallographic data of Vps26p, Vps29p, and Vps35p were fitted to the electron density maps generated by the cryo-EM model. Unfortunately Vps5p and Vps17p could not be mapped to the cryo-EM model as the area proximal to the lipid membrane did not have sufficient resolution (Kovtun et al., 2018).

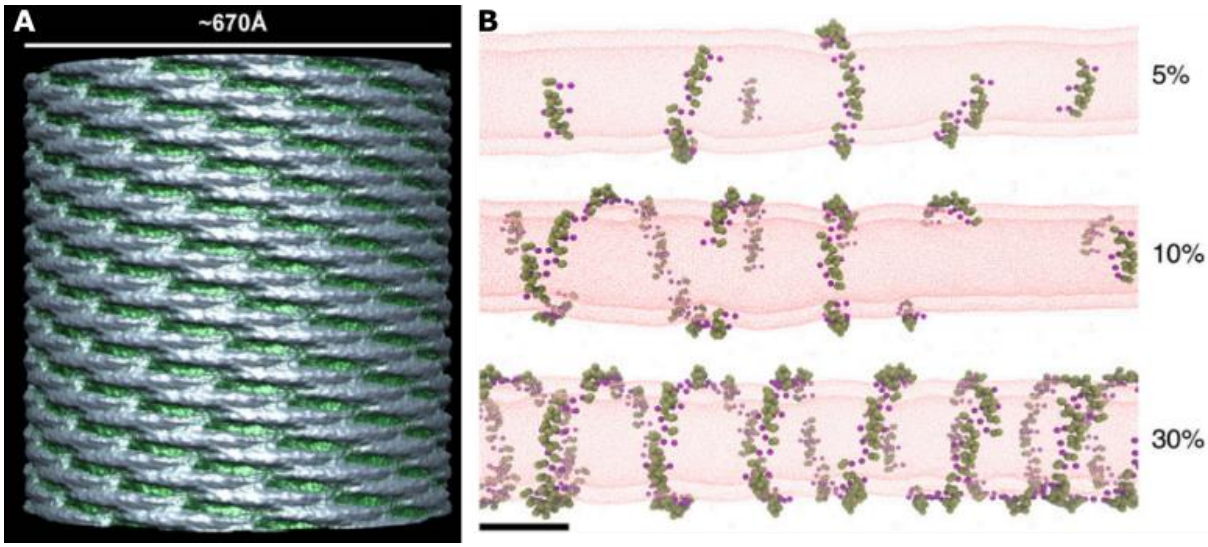

Figure 1.6: Image A is a **h**elical real space reconstruction of an *in vitro* CIP4 F-BAR tubule adapted from (Frost et al., 2008). The protein is coloured blue-grey and the underlying membrane is green. Image B adapted from (Simunovic et al., 2016) shows N-BAR protein coverage based on coarse grain molecular dynamic simulations.

1.7.2.2 Protein Coverage of BAR-domain Induced Tubules

Contrary to the previously discussed models of lipid tubules where they are depicted as tight helical arrays running the entire length of the tubule, compelling evidence suggesting much lower protein concentration can induce and support tubulo-vesicular structures. Giant unilamellar vesicles (GUVs) were manipulated with optical tweezers to form nanotube protrusions. The lipid nanotube was then exposed to human amiphiphysin 1 functionalised with an AlexaFluor 488 reporter molecule. Using quantitative fluorescence microscopy, it was shown that the diameter of the tubule becomes

independent of the optical tweezers external tension once the GUV has greater than 5% protein coverage (assuming the size of the protein is 50nm^2) (Sorre et al., 2012). Enrichment of the protein was observed on the highly curved nanotube surface in comparison to the GUV with a coverage measured between 20-30%. A more recent study using similar methodology as the above measured percentage protein coverage on tubules of two other BAR-domain containing proteins: β2 centaurin and endophilin. The surface density of proteins on the tubule portion of the structure was measured to be 35% and 43% with a GUV coverage of 18% and 8% respectively (Simunovic et al., 2016) (Figure 1.5). *In silico* approaches using coarse grain molecular dynamics appear to support this non-continuous protein coverage to induce and support tubule growth. In simulation with N-BAR proteins, once a tubule reaches 30-40% coverage proteins no longer exchange neighbours and the structure becomes fairly stable and quasistatic (Simunovic et al., 2016).

As previously discussed the in vitro methods used to form BAR protein mediated lipid tubules may not be free from artefacts. These approaches tend to favour highly charged lipids accompanied by high concentrations of BAR protein to form tubules. These methods result in compressed helical arrays which may not be representative of the native structure within cells. This chapter will investigate *in vitro* systems which more closely resemble native conditions and *in vivo* models to acquire data. With the use of the novel FKBP-SLF' CLEM probe it is hoped that helical density and percentage protein coverage on lipid tubules can be investigated.

Chapter 2

Materials and Methods

2.1 Cell Culture

2.1.1 E.coli Strains

XL1-Blue competent cells: E.coli (Stratgene, 200130)

BL21-DE3 One Shot chemically competent (Invitrogen, C600003)

DH5α (Sigma, CMC0001)

2.1.2 Prokaryotic Cells

Bacterial cultures, DH5α, XL1-Blue and BL21(DE3) cells, were cultured in Luria Bertani (LB) broth at 37°C while shaking at 180 rpm. DH5α and XL1-Blue cells were used to maintain and amplify vectors. BL21(DE3) cells were used to produce proteins at high concentrations before subsequent purification. Bacteria were streaked onto 9cm diameter LB agar plates containing antibiotic specific to the vector being used. Working concentrations of antibiotic were: Ampicillin (50µg/ml) or Kanamycin (30µg/ml). All bacterial work was conducted under a Bunsen flame to reduce contamination risk.

During IPTG induction and protein expression, BL21(DE3) cells were cultured at 25°C to maximise protein yield. Otherwise all cells were cultured at 37°C. Glycerol stocks were prepared with 30% glycerol and LB and were stored at -80°C.

2.1.3 Transformation of Chemically Competent Bacterial Cells

5-10ng of plasmid DNA in a volume of 1-5µl was added to 50µl aliquots of cells. 50µl of competent cells were placed on ice in a 5ml Eppendorf. 50ng of plasmid DNA was added to the cells and left to incubate on ice for a further 20 minutes. The cells were then heat shocked at 42°C for 45 seconds in a water bath before being placed back on ice for 2 minutes. 500µl of SOCS media was added and cells were incubated for 1 hour at 37°C while being shaken at 180rpm. Cells were then streaked on

selective agar media to ensure resulting colonies were derived from single cells. Mini preps (outlined in section 2.2.2) were then performed on randomly selected colonies and plasmid DNA was cut with restriction enzymes. Restriction digest followed by an agarose gel was performed to select colonies most likely to contain the desired plasmid DNA. Finally samples were sequenced to confirm no undesirable mutations had occurred.

2.1.4 Eukaryotic Cells

HEK-293, HeLa and RPE1 cell lines were all utilized over the course of this project. Dulbecco Modified Eagle's Media (DMEM) supplemented with 10% fetal bovine serum and 1% penicillin-streptomycin was used to culture all three cell lines at 37°C and 5% CO_2. At around 80% cell confluence cells were passaged. Cells were gently washed in an excess of phosphate buffered saline (PBS) before being incubated with trypsin at 37°C and 5% CO_2 for 2-3 minutes. Once the cells were visibly detaching from the culture flask they were gently agitated to fully dislodge them. The trypsin reaction was then halted by diluting 1 in 5 with supplemented DMEM. Cells were then diluted a further 1 in 5 in supplemented DMEM to a total volume of 10ml and further cultured at 37°C and 5% CO_2.

2.1.5 Mammalian Cell Transfection – Polyethylene Imine

HEK293T cells were grown to a confluency of around 70% on 15cm diameter plate. 15µg DNA was resuspended in 5ml of Optimem media and a separate tube of 5ml Optimem and 10mM of average weight 25kDa branched PEI (polyethylene imine) (Sigma, 408727) was made up and filtered with a 0.2µm filter. The two optimum solutions were combined, mixed by pipette and left to incubate at room temperature for 20 minutes. HEK293T cells were cultured in serum containing media. The media was removed and the cells washed with PBS before adding the combined Optimem solution containg both DNA and PEI. Cells were then left to incubate for 4 hours at 37°C in 5% CO_2. Cells were washed twice in warm PBS. Serum containing cell media was added to the cells and they were left to incubate for 24-48 hours. This method of PEI transfection was only used in conjunction with GFP-trap beads and immunoblotting.

2.1.6 Mammalian Cell Transfection – FuGene HD

FuGENE HD (Promega, E2311) causes fewer changes in cell physiology and morphology lending itself to samples that were to be imaged with confocal or electron microscopy. Both HeLa and RPE1 cell lines were transfected using FuGENE HD. Cells were grown in 6 well plates, MatTek etched dishes or 35mm dishes to a confluency of around 80%. 2.75µg of DNA suspended in 125µl of Optimem was mixed before adding 8µl of FuGENE HD. The solution was thoroughly mixed by piptetting and incubated at room temperature for 5-10 minutes. This solution was then added gently to a 35mm plate containing 2ml of growth media. When using varying sized plates or wells, the ratio of these reagents were varied accordingly. Cells were then cultured in an incubator for 48 hours before being imaged.

2.2 Molecular Biology Methods and Genomics

2.2.1 Agarose Gels

Agarose gels were used to visualise and purify samples. All DNA gels were prepared using 1% agarose (w/v) dissolved in TAE buffer. The agarose was stained with SYBR Safe (Invitrogen) to enable DNA visualisation when illuminated with UV light. 0.5g of agarose was added to 50ml of TAE buffer and was heated with a microwave for 1 minute until the agarose had dissolved. The TAE was cooled for 2 minutes before pouring the solution into a gel mould that had been streaked with 5µl of SYBR Safe and thoroughly mixed. While still liquid, different sized combs were inserted into the gel depending on how many samples or how much DNA needed to be loaded. Once set, gels were transferred into an electrophoresis cell containing TAE buffer. DNA was combined with a commercial loading dye (New England Biolabs, 7025) and added to the wells formed by the comb. A DNA ladder (New England Biolabs, N3200) was also loaded into the furthest left well. A voltage of 100V was then applied to the electrophoresis cell until the dye front approached the bottom of the gel. The gel was then immediately visualised using Di-Digit Gel Scanner (Licor).

2.2.2 DNA Purification and Quantitation

DNA from small trimmed sections of agarose gel or PCR products were purified using Illustra GFX PCR DNA and Gel Band Purification Kit (GE Healthcare, 28903470). The purification was performed as per the manufacturer's protocol. The concentration of double stranded DNA samples was then measured using the NanoDrop ND-1000 (Thermo Fisher) and stored at -20°C.

Plasmid DNA was also purified using "QIAprep Spin MiniPrep and MaxiPrep Kits". DNA was purified from 5ml and 500ml liquid bacterial cultures performed according to the manufacturer's instructions.

2.2.3 Polymerase Chain Reaction

Polymerase chain reaction (PCR) was used to amplify a gene of interest from either purified plasmid DNA or picked bacterial colonies. The T100 Thermal Cycler (Bio-Rad) was used to carry out all PCR reactions. Each reaction used the following reagents: 25µl of Q5 PCR Master Mix x2 (New England Biolabs, M0515), 1µl of forward primer at 10µM, 1µl of reverse primer at 10µM, 100ng of DNA template and finally nuclease free water for a total volume of 50µl.

The typical thermocycler settings for a standard PCR reaction began with a hot start at 98°C for 30 seconds. The denaturation step was 10 seconds at 98°C, followed by the annealing step at 60°C for 30 seconds and finally the extension step at 72°C for 30 seconds plus an additional 30 seconds for every 1kb of DNA being amplified. The denaturation, annealing and extension steps were cycled 32 times before a final extension at 72°C for 5 minutes. The temperature of the annealing step was sometimes variable based on the melting temperature of the primers being used. Furthermore a temperature gradient between 55-70°C was used for the annealing step to troubleshoot problematic reactions.

2.2.4 Gibson Assembly

Gibson assemblies can be used for a variety of applications but in this study the technique was utilized to create genes to express chimera proteins. Primers were designed that were complimentary to the template with an additional flanking portion that was complimentary to the gene being inserted. The first step of the process was to amplify the insert by PCR. The reaction mixture comprised of: 25µl of Q5 PCR master mix (New England Biolabs, M0515), 1µl of forward primer at 10µM, 1µl of reverse primer at 10µM, 20ng of template DNA and nuclease free water for a final volume of 50µl. The thermocycler settings were identical to that of the standard PCR reaction outlined above in the polymerase chain reaction section.

The PCR product was then run on an agarose gel and the relevant bands excised and purified. The Gibson assembly was then performed using 0.02-0.5pmols of plasmid DNA and a 2-3 fold excess of the purified PCR product. 10µl of Gibson Assembly Master Mix x2 (New England Biolabs, E2611S), template DNA, vector and nuclease free water up to a total volume of 20µl. The assembly mixture was then placed in the thermocycler for 15 minutes for 50°C. The resulting mixture was then diluted 1:4 in nuclease free water before transforming bacterial cells with 3µl.

2.2.5 Site Directed Mutagenesis

PCR was used to introduce point mutations at specific locations in target genes. Primers with single base pair mismatches at specific sites within a gene were used in the PCR reaction. The mismatched base was placed in the centre of the primer with the two flanking sides being complimentary and binding to the template DNA. The mismatched base pair would then be present in the resulting daughter plasmid.

The PCR reaction conditions used 25µl of Q5 PCR Master Mix x2 (NEB), 1.5ul of forward primer at 10µM, 1.5µl of reverse primer at 10µM, 25ng of template DNA and nuclease free water for a total volume of 50µl.

The thermocycler settings started at 95°C for 30 seconds. The denaturation step was for 50 seconds at 95°C, followed by the annealing step at 50°C for 50 seconds and an extension step at 68°C for 1 minute plus an additional minute for every kilobase being transcribed before a final extension step at 68°C for 7 minutes. The denaturation, annealing and extension steps were repeated 18 times in total before the final extension.

The PCR reaction mixture was then treated with Dpn1. This enzyme specifically targets the methylated template DNA and reduces the background in transformed colonies. The digestion was carried out by the addition of 1µl of Dpn1 restriction enzyme (New England Biolabs, R0176) to the PCR reaction and incubated at 37°C for 1 hour. This DNA was then transformed into competent bacterial cells.

2.2.6 Pull-Down Assay

15µl of GFP trap beads (Chromotek, gta-10) were washed in 500µl of lysis buffer (500µl of Tris 1M 7.4pH, 500µl 10% NP40, protease inhibitor tablet (Thermo Fisher, A32963) 8890µl of ddH_2O). GFP trap beads were then centrifuged at 2.5g and the supernatant removed. This was repeated three times. Cell media was removed from adherent cells (HEK) grown on dishes overnight and washed twice in 10ml of PBS. 500µl of lysis buffer was added to the cell dishes and the cells were scrapped and collected into eppendorfs. From this point onward all steps were done at 4°C or on ice. Cells were centrifuged for 10 minutes at 23000g at 4°C. 50µl of cell lysate was removed at this point. The rest of the supernatant was added to the GFP trap beads in eppendorfs. These were subsequently incubated on a roller at 4°C for 1 hour. GFP trap beads were then washed twice with wash buffer (500µl of Tris 1M 7.4pH, 250µl 10% NP40, protease inhibitor tablet and 9140µl of ddH_2O). Then washed a final time with the wash buffer containing no NP40 detergent. Beads were resuspended in 30µl of gel loading buffer (Fischer, BP637-1) and the whole cell lysate supernatant into 50µl. Samples were loaded into eppendorfs and incubated on a hot plate at 95°C for 5-10 minutes. 20µl of solution was loaded into 4-12% Bis-Tris Protein gel (Invitrogen – NP0332BOX) with a suitable protein ladder (BioRad, 1610374). The gel was run at 100V in running buffer until the stain front approached the bottom of the gel.

2.2.7 Gel Transfer

After the gel has run, the gel is placed in a gel clamp with a sponge and two layers of filter paper on either side, all soaked in transfer buffer (800ml ddH_2O, 100ml transfer buffer (25mM Tris, 192mM glycine) and 100ml methanol). The transfer membrane (Immobilon-FL Membrane Millipore, IPFL00010), after having been soaked in methanol for 5 minutes, is placed in the blotting cassette with ice and run in a mini-Trans Blot Cell (Bio-Rad) for 90 minutes at 100V.

2.2.8 Immunostaining Transfer Membrane

The transfer membrane was washed in blocking buffer (5-10% BSA (Bovine Serum Albumin) dependent on antibody avidity in TBST) for 30 minutes. This blocking step helped prevent non-specific antibody binding. Primary antibody was diluted to manufacture's specifications in 2% (w/v) BSA in TBST. The transfer membrane was then incubated in the primary antibody solution at 4°C overnight. The antibody solution was then removed and washed 3 times for 5 minutes in TBST. Next the membranes were incubated in a solution of fluorescence conjugated secondary antibody diluted in 5% (w/v) powdered milk and 0.1% (w/v) sodium dodecyl sulphate in TBST. The membrane was then washed a further 3 times for 5 minutes in TBST supplemented with 0.1% (w/v) TBST. Fluorescent antibody binding to the membrane was detected using a LI-COR Odyssey scanner. The Odyssey scanner was capable of imaging two separate proteins labelled with discrete spectral fluorescent secondary antibodies on a single blot.

2.2.9 Protein Expression

BL21 cells were transfected with pET45b(+) vectors by the standard heat shock procedure recommended by the manufacturer. Colonies were then picked and cultured at 37°C in a starter culture overnight in 10ml of LB supplemented with ampicillin 50μg/ml. This starter culture is then added to 1 litre of LB supplemented with ampicillin and grown to an OD of 600-800. The culture is then induced with 1mM IPTG and incubated overnight at 25°C.

2.2.10 Protein Purification

Cells cultures were centrifuged at 6000g for 15 minutes at 4°C. The supernatant was removed and the cell pellet could be stored at -20°C or immediately resuspended in 40ml of lysis buffer at 7.5pH. The basis of all buffers used for protein purification consisted of 20mM Tris HCl, 2mM β-mercaptoethanol, 200mM NaCl and protease inhibitor tablets. For this first step 50 units/µl of benzonase nuclease (Millipore, E1014) was added to the buffer. Cells in lysis buffer were then placed on a roller at 4°C for 20 minutes. Cells were then placed on ice and mechanically lysed using a probe sonicator. Samples were pulsed at 70% amplitude over 40 second intervals. During each interval the sonicator is on for 10 seconds and off for 30 seconds with a total on time of 3 minutes. The cell lysate is then centrifuged at 20000g for an hour at 4°C. During the study two different purification columns were used, a cobalt column (GE Life Sciences, 29000594) and a nickel column (GE Life Sciences, 17524701). The nickel column was the preferred option as it bound the specific his-tagged proteins used in this study far more effectively and the concentration of protein in the final elute was far greater. The following steps were performed with all solutions and buffers on ice or in a cold room at 4°C. The nickel column was stored in ethanol which was washed out by pumping through water followed by buffer. The protein solution was then pumped over the nickel column at a speed of 1ml per minute, washed with a wash buffer containing 20mM imidazole and eluted in 9ml of elution buffer containing 200mM imidazole. The 9ml of eluted protein solution was then dialysed overnight in snakeskin dialysis tubing (Thermo Fisher, 68100) with 200ml of buffer at 4°C to dilute out the imidazole.

At this stage the protein gels showed a small amount of the protein of interest had become unconjugated from the EGFP tag. To ensure that these unconjugated proteins were not responsible for the formation, or lack, of tubulo-vesicular structures in later experiments a further purification step was used. The dialysis retentate was run through a size exclusion column (GE Life Sciences, 28989335) connected to an ÄKTA system. The buffer used to run through the size exclusion column was identical to the lysis buffer without the benzonase.

2.3 Fluorescence Microscopy

2.3.1 Immuno-fluorescence

Cells were transfected with plasmid DNA containing relevant protein constructs. Cells were left to incubate for 48 hours to allow constructs to be well expressed (2.1.5 and 2.1.6). Growth media was removed from cells grown on glass coverslips and washed in PBS. The PBS was removed and replaced with 4% v/v paraformaldehyde (PFA) in PBS for 20 minutes. Cells were washed twice more in PBS before permeabilising with 0.1% Triton X100 (Sigma, T8787) (v/v) in PBS. The permeabilised cells were blocked in 1% BSA for 30 minutes. Coverslips were removed from wells and excess blocking buffer removed by blotting. 50µl of primary antibody solution (primary antibody diluted 1:200 in 1% BSA (w/v) PBS) was spotted onto parafilm and the coverslip placed cells down on top ensuring the antibody solution evenly covers the coverslip with no air bubbles. The antibody was left to incubate at room temperature for 30 minutes. A secondary antibody solution containing DAPI was then prepared. Secondary antibody diluted 1:400 in 1% BSA (w/v) PBS and 30nM DAPI was spotted onto parafilm. The coverslips were washed once in PBS and then placed onto the secondary antibody solution and left to incubate at room temperature for 30 minutes. Coverslips were washed in PBS, the excess blotted off and mounting onto coverslip with 6µ of Mowiol (eBioscience, 00495802). Mounting media was gently compressed to remove any air bubbles and left for several hours to dry before imaging.

2.3.2 Confocal Microscopy – Image Acquisition

The immunofluorescence workflow utilized a DMI6000 (Thermo Fisher) inverted epifluorescent microscope with an attached laser scanning microscope (Leica Microsystems, SP5 AOBS). The 63x oil immersion objective lens with NA 1.4 was used with a zoom factor of 3. The default SP5 Leica software and PMT detectors with Gallium Arsenide Phosphide photocathode were used to acquire images in an environmental chamber at 21°C. Images were captured using Leica Application Suite AF software (Leica, version 2.7.3.9723).

Due to the significantly lower quantum yield of PtNCs relative to the fluorophores used in the immunofluorescence workflow more sensitive detectors were necessary. The DMI6000 epifluorescence microscope was again used but with an SP8 confocal laser scanning microscope. The Gallium Arsenide Phosphide hybrid detectors were far more sensitive and able to pick up the weaker fluorescent signal generated by the PtNCs. To further increase signal strength the x40 oil immersion objective lens with NA 1.3 was used. The software used was Leica Application Suite AF version 2.7.3.9723.

2.3.3 Image Analysis – Fluorescence Microscopy

Images were analysed and processed using the Fiji software. Colocalisation processing was performed using the in-built Fiji plugin Coloc2 (Curits et al., 2017). The ROI manager was used to mask off the background of cells being analysed. This ensured the low signal background in the images was not included in the colocalisation calculation, artificially increasing the colocalisation quantitation. Coloc2 was used to calculate the Pearson's correlation coefficient which is a measure of variation between two input channels. The measurements were taken using the Costes auto-thresholds and data reported was the Pearson's correlation above this threshold.

2.4 Pre-Embedded Labelling CLEM

2.4.1 Cell Seeding

Mammalian cells were seeded into MatTek (MatTek, P35G-1.5-14-CGRD) dishes at a density of 100000 cells per well in fully supplemented growth media. Cells were counted with a haemocytometer to ensure a low enough confluency for specific cells or small groups of cells to be readily identified. Once seeded, cells were incubated overnight at 37°C and 5% CO_2. The cell media was then removed and replaced with a serum free media and incubated for a further two hours.

2.4.2 Labelling with PtNCs

For experiments using PtNCs as the probe, cells were washed in PBS before being incubated with probes. PtNCs at a concentration of 0.65-1.3mg/ml suspended in PBS were incubated with cells at 37°C and 5% CO_2 for 30 minutes. Once the time had elapsed cells were immediately washed in PBS and fixed with 4% PFA in PBS for 15 minutes. The PFA was then removed and replaced with PBS before imaging on the confocal microscope. After imaging the fluorescence, cells were washed for three minutes three times in 0.1M phosphate buffer (PB). Cells were then fixed in 2% Glutaraldehyde in PB for 15 minutes. At this stage samples were silver enhanced. Cells were washed for five minutes three times in water before incubating the samples in silver enhancing solution made up to the manufacturer's instructions (outlined in 2.4.5). Cells were then washed for ten minutes three times in water before osmification in 1% OsO_4 in PB for 15 minutes. Three more washes in water for 10 minutes each were performed to remove the majority of the phosphate present before Uranyl acetate. A solution of 3% Uranyl Acetate in water was added to the cells for 20 minutes while being kept in the dark. A further three washes in water for ten minutes was performed before dehydrating the cells in an ethanol gradient. Cells were treated with 70%, 80%, 90%, 96% and 100% for ten minutes each. A final incubation with 100% was performed before adding resin to the cells. Epon was introduced slowly firstly in a solution containing epon 1:2 ethanol, then epon 2:1 ethanol and finally 100% epon. Each solution was left to infiltrate on a rocker for 1 hour before removing the epon and replacing it with fresh 100% epon and baking at 60°C for 48 hours.

2.4.3 Labelling with FKBP-SLF' Probe

Cells destined to be labelled with the FKBP-SLF' probe system were seeded at 50000 cells per dish and transfected with the relevant protein construct. Cells were incubated for 48 hours in order for protein expression to reach adequate levels. Cells were fixed in 4% PFA in PBS for 15 minutes before being replaced with PBS before confocal imaging. Cells were permeabilised in 0.1% (w/v) saponin in 0.1M phosphate buffer (PB) for 5 minutes. The reaction was then quenched with 30mM glycine, 0.1% saponin PB for 3 minutes. Samples were blocked for 30 minutes in 0.1% saponin 0.1M PB. SLF' conjugated to 2nm AuNP were then added at a concentration of 2µM in 3% BSA in 0.1M PB and left

to incubate for one hour. Samples were washed three times for five minutes each in water before silver enhancement. The protocol for embedding samples is the same from here on as outlined above for PtNCs.

2.4.4 Post Embedded Labelling CLEM

HeLa cells were seeded in 35mm dishes with 60000 cells per dish. Cells were then transfected with EGFP-FKBP12(F36V)-SNX1 and EGFP-SNX1 as a control using the FuGene HD protocol detailed in section 2.1.6. Cells were cultured at 37°C and 5% CO_2 for 48 hours to allow the inserted gene to express. Cells were washed in PBS and trypsinised before being pelleted at 100g for 2 minutes. The supernatant was removed before the pellet was then resuspended in 20µl of 20% BSA w/v in PBS before pelleting again. 1µl of cell pellet was loaded into gold coated membrane carriers to be high pressure frozen (Leica, Empact2). Frozen samples were then loaded into the Leica EM AFS2 and freeze substituted into lowicryl resin. Frozen membrane carriers were transferred into 1ml of freeze substitution media contain (0,1% uranyl acetate and 5% water in acetone). The AFS (AFS2, Leica) was held at -90°C for 5 hours. Samples were warmed to -45°C at a rate of 5°C per hour before being held at -45°C for 2 hours. The automatic reagent exchange apparatus was used to automatically wash the samples in acetone followed by ethanol for 30 minutes each. Samples were then infiltrated with a lowicryl HM20 resin gradient of 25%, 50%, 75% dilutions for 3 hours each before infiltrating with 100% resin overnight. This was followed by 3 more 100% lowicryl resin exchanges for 2 hours each before polymerising the resin with UV light for 48 hours. Samples were retained at -45°C for a further 16 hours before warming up to 0°C at a rate of 5°C per hour. After a final hold at 0°C the samples could be removed and processed. The gold carrier was removed from the lowicryl blocks with a razor blade before sectioning. Lowicryl blocks could be screened for fluorescence using a Leica fluorescence stereomicroscope (Leica, M205 FA) to check for both the presence and depth of fluorescent signals. The lowicryl blocks were then sectioned with a diamond knife on an Ultramicrotome to a thickness of 300nm and collected on carbon coated formvar finder pattern grids (Agar Scientific, AGS138). Sections were washed twice by floating on PBS briefly before finally floating them onto a 2nM Hoechst solution (Thermo Fisher, 62249) for 5-10 minutes. Sections were washed twice more for 2 minutes each in PBS before being mounted between a slide and a coverslip in 6µl in a 50:50 v/v solution of glycerol and PBS. The cells could then be imaged with a Leica fluorescence widefield and a 63x NA 1.4 lens.

Sections were then released from the coverslip by gently flooding the perimeter with water until the coverslip floated up. The freed section was then washed in water three times for 2 minutes each to remove excess glycerol. The sections were left to dry before being imaged in the TEM. Grids were imaged using the Tecnai 12 120kV Bio Twin Spirit transmission electron microscope attached with a FEI Ceta 4k x 4k camera.

2.4.5 Silver Enhancement

Silver enhancement is performed on noble metal probes contained within a sample that would not ordinarily provide enough electron density to be readily visualised in TEM. The Aurion silver enhancement kit SE-EM (Aurion, 500.033) was used as the manufacturer instructed. One drop of developer compound was added to 40 drops of enhancer solution and thoroughly vortexed. To each 35mm dish, 500µl of final solution was added and left to incubate at room temperature in the dark for 1.5 hours. Samples already sectioned were floated on drops of silver enhancement solution before washing thoroughly in buffer.

2.4.6 Transmission Electron Microscopy

TEM imaging was performed using an FEI Tecnai 12 BioTWIN Transmission Electron Microscope operating at 120kV. Images were acquired on a FEI CETA 16M CMOS camera.

2.4.7 Cryo Transmission Electron Microscopy

Lacy carbon film grids were glow discharged for 30 seconds in a Leica ACE 600 Coater system. 5uL of sample were pipetted onto these grids and plunge frozen in liquid ethane using a Leica GP Plunge freezing device. The grids were then transferred under liquid nitrogen into a Gatan 626 Cryotransfer system. Samples were imaged using low dose conditions at ≤ -170 °C in a FEI Tecnai 20 Scanning Transmission Electron Microscope operating at 200kV. Images were acquired on a FEI CETA 16M CMOS camera.

2.4.8 Electron Dispersive X-ray Spectroscopy

Samples were loaded into a JEOL 2100F Field Emission Scanning Transmission Electron Microscope, operating at 200kV. Energy loss spectra and maps were acquired with a GATAN Parallel Electron Energy Loss Spectrometer. EDX spectra and maps were acquired using an Oxford Instruments AZTEC system. HAADF images used to correlate with the EDX were collected on a JEOL BF/HAADF STEM detector and TEM images on a Gatan Ultrascan camera.

2.4.9 Correlation of Light Microscope Images and Electron Micrographs

The ICY software was used to correlate images taken of the same area of a sample using the two different imaging modalities of confocal and TEM. The ec-CLEM plugin was used to accurately correlate sets of images by the manual addition of common reference points (Paul-Gilloteaux, 2017). The software was set to use the electron micrograph as the reference image and any warping or reorientation was applied to the fluorescence image.

2.5 Synthesis and Characterisation

2.5.1 Liposome Synthesis

Liposomes were composed of three component parts. Folch Bovine Brain Lipid Extract (Sigma B1502 (0.5mg) and Avanti Polar Lipids 131101C (0.5mg)) in a 50:50 ratio. This was then supplemented with protonated PI(3)P (Avanti Polar Lipids LM-1900 (3µg)). This lipid composition was dissolved in chloroform and made up to a concentration of 1mg/ml. The individual aliquots were then stored at -20°C.

Before use lipids were warmed to room temperature and placed in a round bottom flask. Lipid cakes were formed by constantly rotating the flask under a gentle stream of nitrogen gas. If the lipid cake

was not smooth, the lipids were re-dissolved in chloroform and the process was repeated until a homogenous lipid cake was formed. Care was taken to not allow the temperature drop too much due to excessive chloroform evaporation as this causes the lipids to clump. The smooth lipid cakes were then left to full dry under a nitrogen flow for 30 minutes. The lipids were then rehydrated in 20mM HEPES (7.4pH), 150nM NaCl, 1mM DTT at 37°C on a shaker for 1 hour. Lipids were then sonicated at room temperature for 5-15 minutes in a water bath sonicator until the solution becomes turbid. The lipid solution then underwent a series of 10 freeze thaw cycles in liquid nitrogen and warm water (60°C). Lipids were placed in liquid nitrogen until the solution was completely frozen (30 seconds – 2 minutes). The container was then placed in warm water until the solution completely thawed. Finally the liposomes were sized via extrusion through a 200nm filter (Whatman, WHA10417031).

2.5.1.1 Liposome Negative Staining

Liposomes must be negatively stained in order for them to be visualised and sized using transmission electron microscopy. Freshly glow discharged carbon coated TEM copper grids were held in reverse forceps. 5µl of stock liposome solution (1mg/ml) was added to the grid and incubated at room temperature for 1 minute. The excess solution was then wicked off with filter paper and 5µl of 3% Uranyl acetate in water was added to the grid and incubated for 30 seconds at room temperature before being wicked off and allowed to dry.

2.5.2 Platinum Nanocluster Synthesis

60mg of Polyethyleneimine, branched M.W. ≈ 10000 (Alfa Aesar, 40331) was vortexed in 400µl of ddH_2O until resuspended. 400µl of this PEI solution was then added to a glass screw top vial with magnetic stir bar and 2.52ml of ddH_2O while stirring. The pH of this solution was then measured and adjusted as the final fluorescent excitation/emission wavelength is dependent on the pH of the solution. The solution used to synthesise the clusters in this thesis was pH 10.8. Next 80µl of hydrogen hexachloroplatinate (IV) hexahydrate at a concentration of 10mg/ml (0.8mg per 80µl) was added dropwise while stirring and immediately. This was left to stir for 1.5 hours in the dark. Finally 80µl of 110mg/ml (8.8mg in 80µl) L-Ascorbic Acid (Sigma-Aldrich, 255564) dissolved in water was

added. The reaction was left to reduce for 1 week while being stirred in a 95°C water bath in the dark.

2.5.2.1 UV-Vis Spectroscopy and Quantum Yield of PtNCs

Quantum yields were obtained using a quinine sulfate standard and platinum cluster sample both suspended in PBS. Fluorescence excitation/emission spectra and quantum yield were acquired on a Cary UV-Vis 50 spectrophotometer and a Perkin-Elmer LS45 using a 700µl quartz cuvette (ThorLabs).

2.5.3 Synthesising the SLF' Molecule

All reagents used for the synthesis of SLF' were acquired from Sigma unless otherwise stated. All reactions were performed in a fumehood.

Flash Columns

Flash columns were loaded with a 1cm depth of sand. A small amount of petroleum ether (all petroleum ether used was 40-60°C) was added to the sand covering it by an approximate depth of 10cm. This removed air bubbles from the sand and ensured the sand was flat. Enough SiO_2 to fill the column 10-15cm is suspended in petroleum ether and gently poured into the column ensuring the sand remains level. Bellows were used to force through petroleum ether and compress the SiO_2. Another 1cm layer of sand is added to the top again ensuring it is level. The level of petroleum ether was always kept above the SiO_2 but should be level with the sand when loading compound. Compound was added to the flash column drop wise and allowed to settle. Usually the compounds were coloured and formed a visible layer at the top of the SiO_2. Solvents can then be added dropwise as to not disturb the compound layer until a deep enough covering allows solvents to be poured. The columns were then run and fractions collected. The concentration of EtOAc was gradually increased until the compound was eluted.

Reaction 1

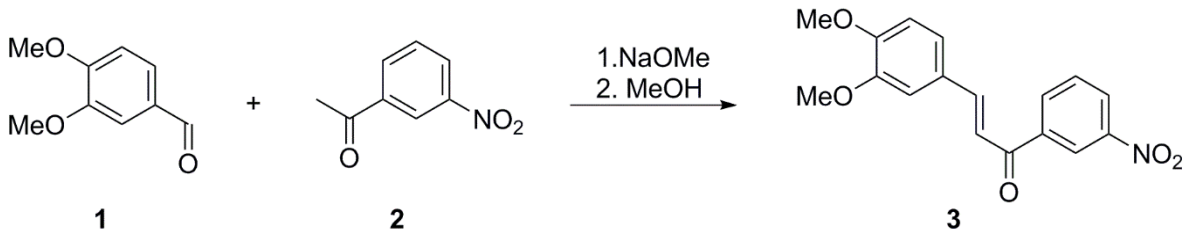

1 2 3

Compound 1, 3,4-dimethyloxybenzaldehyde (4.69g, 28mmol) was added to a round bottom flask with a stir bar. Sodium methoxide (6.09g, 113mmol) was dissolved in 100ml of MeOH and added to the round bottom flask. The solution was stirred until all solute had dissolved. In a separate flask compound 2, 3-nitroacetophenone (4.66g, 28mmol) was fully dissolved in 150ml of MeOH before being added dropwise to the other reagents while stirring. This was left stirring overnight under ambient conditions. The reaction mixture was concentrated *in vacuo* before dissolving in 1M NaOH. The mixture was extracted using Et_2O (2 x 50ml) before acidifying the aqueous phase with 12M HCl at 0°C in an ice bath. The aqueous phase was extracted once more with EtOAc (4 x 100ml). The organic phase was then washed with a saturated solution of $NaHCO_3$ and brine. The organic phase was dried using $MgSO_4$, filtered and concentrated *in vacuo*.

Reaction 2

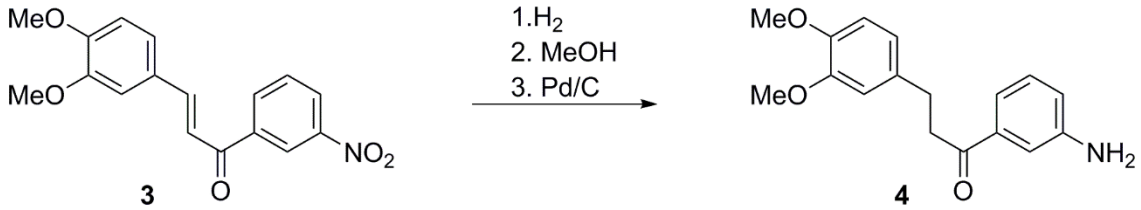

3 4

Compound 3 (10g, 32mmol) was added to a round bottom flask with a stir bar. 250ml of MeOH was added to the flask before degassing the flask for 5 minutes. 0.6g of palladium on activated carbon was added to the flask before degassing again for a further 5 minutes. The reaction was then stirred under one atmosphere of H_2(g) overnight. The reaction mixture was filtered through a Celite plate and concentrated *in vacuo*. The product was purified using a SiO_2 flash column.

Reaction 3

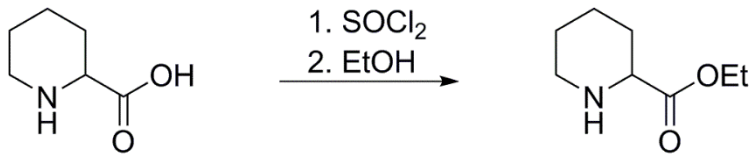

5 **6**

This reaction require anhydrous conditions. The round bottom flask used for this reaction was dried thoroughly by heating with a Bunsen burner and cooled using a flow of nitrogen. (s)-pipecolic acid (0.6g, 4.65mmol) was added to the dry flask with a stir bar. Dry ethanol (30ml) was added to the round bottom flask and cooled to -10°C. $SOCl_2$ (0.5ml) was then added dropwise while stirring and stirred for a further 30 minutes until the solutions temperature returned to room temperature. The solution was heated to 40°C for one hour and then to 60°C for five hours all while being stirred. The product was then concentrated *in vacuo.*

Reaction 4

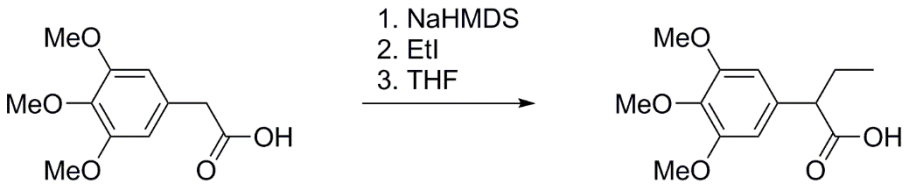

7 **8**

Like reaction 3, this reaction also required anhydrous conditions and was dried as described above. Acetic acid (1.7g) was added to a flame dried flask with a stir bar. Dry THF (11.2ml) was added to the flask and cooled to 0°C. 1M NaHMDS (11.8ml) was added dropwise and stirred for 15 minutes. Next Iodoethane (0.47ml, 5.3mmol) was added dropwise and stirred at room temperature for 16 hours. The reaction mixture was diluted with EtOAc and quenched with 1M HCl. The product was extracted with EtOAc and washed with brine. The solution was dried with $MgSO_4$, filtered and concentrated *in vacuo*. The product was purified with a flash column.

Reaction 5

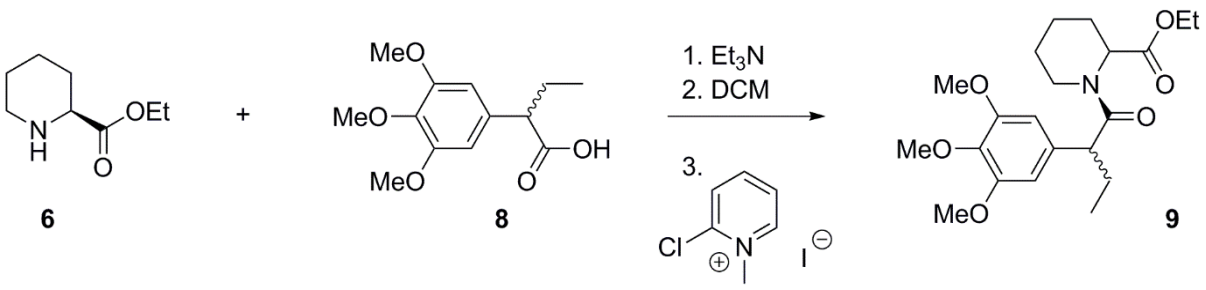

Compound 8 (1g, 3.9mmol) and compound 6 (0.56g, 3.9mmol) were added to a dried flask with a stir bar. Dry DCM (74ml) was then added to the flask under an atmosphere of nitrogen. Et_3N (1.8ml, 13mmol) was added dropwise followed by 2-chloro-1-methyl pyridinium (1.5g, 5.9mmol). Water was added to the reaction (60ml) and was stirred for 4 hours before being extracted with DCM (5 x 60ml). The organic layer was dried with $MgSO_4$, filtered and concentrated *in vacuo*. The crude product was purified using a flash column.

Reaction 6

In order to proceed with further reactions the primary amine on compound 4 needed to be protected. Compound 4 (1.12g, 3.9mmol) was added to a round bottom flask with a stir bar. Anhydrous DCM (26ml) was added under nitrogen. Di-*tert*-butyl dicarbonate (1g, 4.1mmol) was also added under nitrogen followed by DIPEA (0.92ml). The reaction was stirred for 2 days in order for the reaction to progress as far as possible. The crude oil product was purified using flash chromatography.

Reaction 7

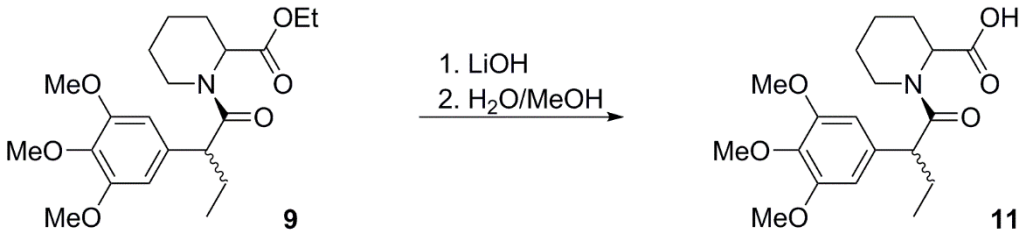

Compound 9 (1.37g, 3.6mmol) was added to a round bottom flask with a stir bar. Methanol (22ml) and water (1.05ml) was added to the flask and stirred until the solute dissolved. LiOH monohydrate (1.515g, 36.1mmol) was added and left to stir at room temperature overnight. The reaction was acidified using 1M HCl at 0°C and placed *in vacuo* to remove volatiles in particular any dissolved MeOH. The remaining aqueous phase was extracted with DCM (5 x 30ml). The organic phase was dried with $MgSO_4$, filtered and concentrated *in vacuo*.

Reaction 8

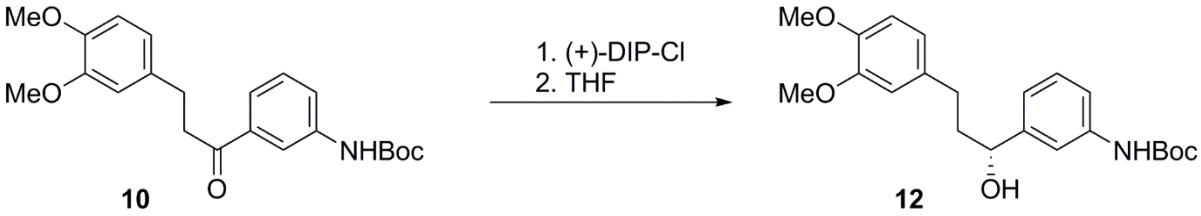

Compound 10 was added to a dried round bottom flask with a stir bar. Dry THF (21ml) was added to the flask and cooled to -20°C while under a nitrogen atmosphere. (+)-DIP-Cl was dissolved in THF (10.5ml) under nitrogen and added dropwise to the flask containing compound 10. This was stirred for six hours at -20°C under nitrogen. The volatiles were removed *in vacuo* before adding Et_2O (42ml) and diethanolamine (4.2ml) and stirring for a further 16 hours. The crude product was concentrated *in vacuo* and purified with a flash column.

Reaction 9

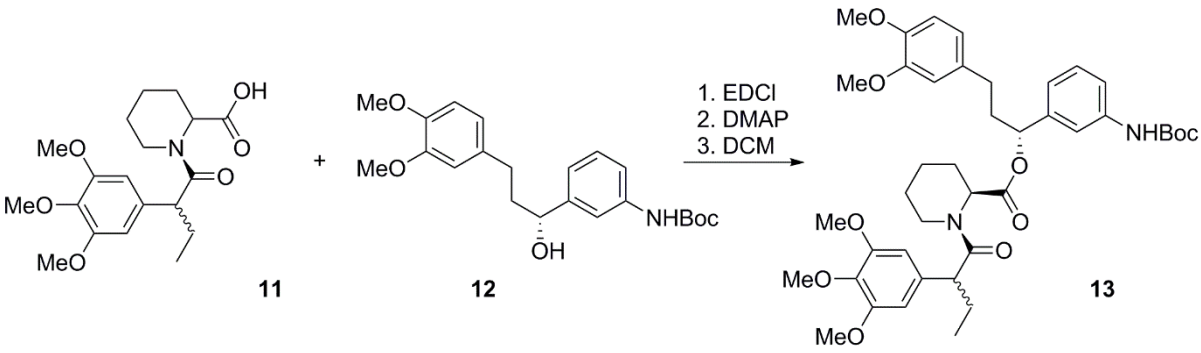

Previously synthesised acid 11 (0.46g, 1.3mmol) and alcohol 12 (0.4g, 1.3mmol) were added to a round bottom flask with a stir bar. The flask was purged using a Schlenk line. Anhydrous DCM (6ml) was added to the flask under a nitrogen atmosphere. EDCI (0.32g, 1.7mmol) and DMAP (0.015g, 0.13mmol) were then also added. The reaction was stirred for 20 hours at room temperature in a nitrogen atmosphere after which saturated NH_4Cl (3ml) was added to the reaction. The aqueous phase was extracted with DCM (3 x 20ml). The organic phase was dried with $MgSO_4$, filtered and concentrated *in vacuo*. The crude product was then purified by flash chromatography.

Reaction 10

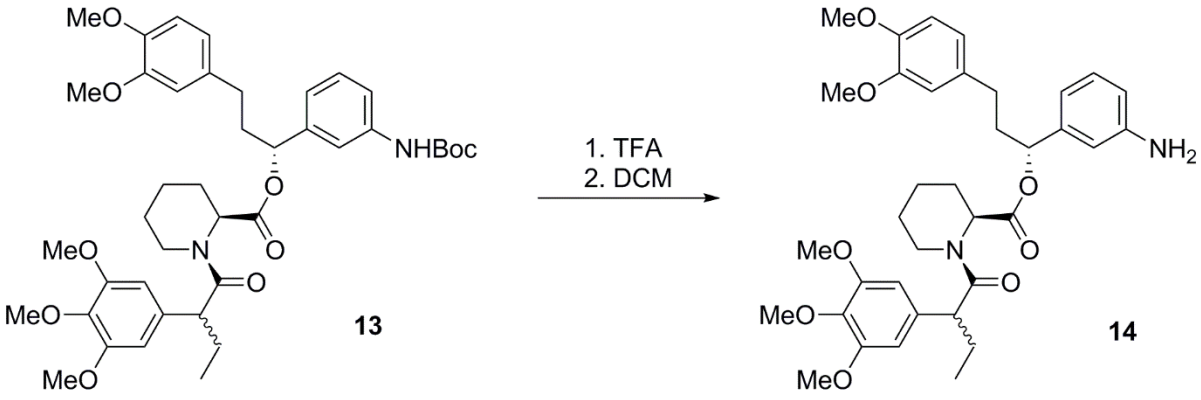

Compound 13 (0.6g, 0.9mmol) was added to a round bottom flask and purged using the Schlenk line. Anhydrous DCM (20ml) was added to the flask under a nitrogen atmosphere followed by TFA (4ml). The reaction was stirred under a nitrogen atmosphere at room temperature for two hours before concentrating *in vacuo*. The crude product was the purified using flash chromatography.

2.5.4 Binding Affinity of FKBP and SLF'

Binding affinity experiments were performed in NUNC black 96 well plates (ThermoFisher Scientific, 137101) and the fluorescent signal measured using a ClarioStar fluorescent plate reader (BMG LABTECH). All conditions were repeated in quadruplicate including a blank containing the EGFP protein construct and buffer only. Dissociation constants can only be accurately calculated to half the concentration of protein used. Therefore, concentrations of various reagents and ligand excesses were variable, they are shown in the table below:

Protein Construct	Protein Concentration	AuNP Size	SLF' Excess
EGFP-FKBP-SNX1	5nM	2nm	1-100
EGFP-FKBP-SNX1	25nM	6nm	0.1-12*
EGFP-wtFKBP-SNX1	10nM	2nm	1-100

In the case of the SLF' conjugated to 6nm AuNP the * indicates that the binding curve was not saturated. This was due to a lack of material at this size range.

2.6.1 Gifted Plasmids

Finally, the eukaryotic expression vectors were kind gifts from other colleges. The pEGFP vector containing EGFP-FKBP-SNX1 was donated by Thom Sharp. While the pEGFP vector containing EGFP-SNX1 was donated by Boris Simonetti. All plasmids used were sequenced using Eurofins tube sequencing service to ensure no detrimental mutations had occurred. Both pEGFP EGFP-SNX1 and pET EGFP-FKBP-SNX1 were both found to contain silent mutations in the SNX1 gene. (Sequences in the appendix)

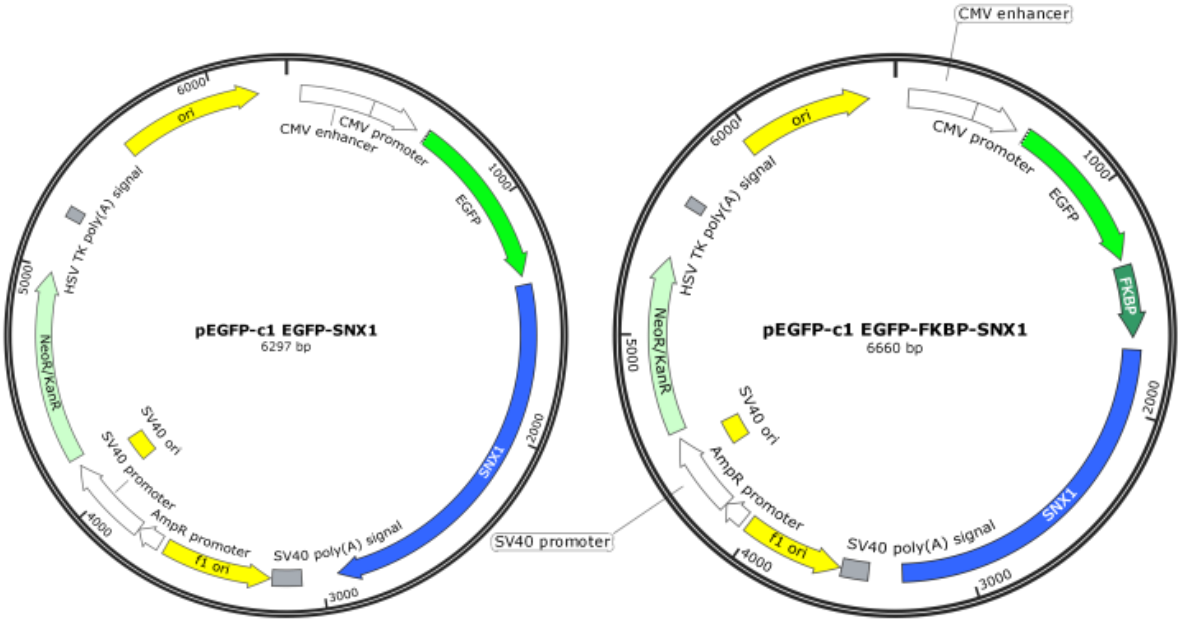

Figure 2.1: Two pEGFP plasmid maps: EGFP-SNX1 gifted from Boris Simonetti (left) and EGFP-FKBP-SNX1 gifted by Thom Sharp (right).

2.6.2 Primer Sequences

Primers for Gibson Assemblies

Primer Name	5’-3’ Sequence
pET fwd	ggagctcgtgtacacggc
pET rev	caattgggatccggactcttg
EFS1 fwd	aagagtccggatcccaattggatggtgagcaagggcgag
EFS1 rev	gcgccgtgtacacgagctccttaggagatggcctttgcc

Primers for Site Directed Mutagenesis

Primer Name	5’-3’ Sequence
EFS1 SDM fwd	atggaaagaaatttgattcctcccg
EFS1 SDM rev	cttcaagcatcccggtgt

Chapter 3

Development of the SLF' Ligand and FKBP12 Protein as a CLEM Probe

3.1 Introduction

Since the discovery of GFP, clonable reporter molecules have become a powerful tool in the microscopist's toolbox. Both transient expression and genome editing with tools like CRISPR-Cas9 enable the production of chimera proteins containing both the target protein and reporter as a single entity. Epifluorescence techniques can subsequently be employed to track, localise and quantify target proteins with precision. While this labelling method has proven very successful for FM techniques, no endogenously expressed electron dense label has been developed/discovered for use in EM. Generating *in vivo endogenously expressed* electron density in order to visualise targets in EM has proven to be less straight forward than the fluorescent counterparts. One of the first methods to generate electron density in this way was the polymerisation of 3,3-diaminobenzide (DAB) by a horseradish peroxidase enzyme (HRP). In the presence of H_2O_2, HRP catalyses the polymerisation of DAB into a highly insoluble brown precipitate. If the reaction is left to proceed long enough the precipitate can be visualised by standard wide field microscopy. However for the purposes of EM the precipitate is not inherently electron dense and therefore does not generate contrast in the micrograph. The contrast is generated due to the osmiophilic characteristic of the DAB precipitate. During standard osmification, OsO_4 preferentially binds to the precipitate generating contrast between itself and the surrounding tissue. An early example of this system was labelling the endocytic lumen of l-cells to study pinocytotic flux (Steinman et al., 1974). Since a variety of endogenously expressed labels that precipitate DAB have been developed (HRP (Valnes and Brandtzaeg, 1984), APEX (Martell et al.,2012), MiniSOG (Shu et al., 2011)).

In the absence of a perfect CLEM tag, a purely endogenously expressed, robust multimodal probe producing accurately aligned correlative images, avidity based probes are ubiquitously used. While antibody based probes including FNG (Takizawa et al.,2015) have been successfully used to localise antigens in EM for decades, they do present major drawbacks. Firstly, they necessitate the use of cell permeabilisation if labelling endogenous targets. This process can cause ultrastructural damage and cellular content extraction. Secondly, their large size limits sample penetration and access to their intended targets. Finally, in some cases antibody avidity is low resulting in low labelling efficiencies. Elegant alternatives in order to avoid reliance upon affinity based probes have been developed in an effort to combat these disadvantages.

In conventional EM sample preparation methods, fluorophore activity is abolished by OsO_4 staining and preservation in hydrophobic resins. In-resin fluorescence can be achieved with hydrophilic resins containing a small percentage of water while using minimal heavy metal stain (Nixon et al., 2009). In niche circumstances these embedded fluorescent reporter proteins have been used as dual modality probes in conjunction with integrated light and electron microscopes. These systems contain both EM and FM imaging systems, with aligned optical axes within a single apparatus. High vacuum environments within EM systems extinguish fluorescence via dehydration. Decreasing vacuum pressure with the introduction of water vapour restores fluorescent signals which enables imaging. The vacuum pressure can be increased once again in order to image the same specimen again with the electron beam (Brama et al., 2015). In this way the fluorescence informs the user which regions to image with EM.

Alternatively, the well-established UA stain, previously considered purely for contrast generation in EM has been investigated as dual modality probe. At cryogenic temperatures UA exhibits a bright fluorescence which using Cryo-Fluorescence Microscopy can be readily visualised. UA was excited with the 405nm laser which produced a broad fluorescent emission with peaks at 493, 538, 564 and, 591nm. This broad emission would likely occlude or frustrate accurate identification of other fluorescent molecules present in the sample. Therefore in order to effectively utilise this phenomenon, low concentrations of UA are used in order to retain other fluorescent labels in the sample. Standard fluorescence imaging is then performed at ambient temperatures before cooling to cryogenic temperatures to register the UA fluorescence. Since the UA is prominently featured in both imaging modalities, the accuracy in image alignment is improved 2-fold over conventional fiducial beads (Tuijtel et al., 2017).

3.1.1 DAB Precipitation

HRP contains four disulphide bridges and two calcium binding sites that are essential for catalytic function. In reducing or low Ca^{2+} environments, such as the cytosol, these structures do not form and disables enzymatic function. Therefore, labelling endogenous cytosolic proteins is not possible with HRP. HRP is also a relatively large protein (44kDa) for use as a label. Typically, larger proteins are disadvantageous as they are more likely to negatively impact the labelled proteins native function and trafficking. In an effort to address these shortcomings research lead by Ellisman and Ting developed a novel protein based on a class I cytosolic ascorbate peroxidase (APEX). APEX is active in the reducing environment of the cytosol as it does not contain any disulphide bridges. It is also approximately 40% the size of HRP (28kDa) which is similar to the widely used GFP and enhanced-GFP (EGFP) weighing 27kDa and 32kDa respectively. Mutagenic work was undertaken to increase the promiscuity of the active site for aromatic substrates to be accommodated and inhibiting the formation of homodimers enables APEX to be successfully used as a TEM probe (Martell et al., 2012).

MiniSOG is a compact protein (106 residues in length) based CLEM probe that is capable of generating fluorescence and singlet oxygen species without the addition of any exogenous cofactors. However, to convert the singlet oxygen species into an electron dense signal, similar to both HRP and APEX, DAB is required. MiniSOG is based on the light, oxygen and voltage (LOV) domain of phototropin. This domain's native function is to bind flavin mononucleotide in its excited form and transform this energy into a covalent bond to a cysteine residue (Cys 426). Saturation mutagenesis was performed to perturb bond formation and increase energy availability for singlet oxygen species generation. The same technique was also employed around the chromophore binding site, which altered the native blue emission of phototropin for a peak emission between 500-528nm (Shu et al., 2011). MiniSOG is the closest example of an entirely endogenous CLEM probe capable of generating fluorescence and electron density. Although DAB incubation is required to form the osmiophilic precipitate, DAB labelling is far more specific with greater diffusibility than the majority of antibodies. DAB precipitate has been shown to localise within 25nm of the target by Cryo-EM. This low diffusivity means DAB precipitate to rival immunogold labelling with respect to precision of the label to the target (Mihelc et al., 2020).

Finally two other methods of producing CLEM probes where the majority of it is endogenously expressed within a cell is tetracysteine based tags such as ReAsH/FlAsH and metallothionein. Metallothionein (MT) has a large number of cysteine residues not involved in disulphide bridge formation contained within a bi-lobed binding pocket. The free thiol groups readily chelate both divalent and monovalent metal ions for the purpose of detoxification, homeostasis and metal ion donation. This binding pocket is promiscuous and has been shown to bind non-native metal ions such as cadmium and gold. Incubating samples labelled with MT with an electron dense metal ion source generates an electron density at the target site. Compelling examples of this probe in use has been demonstrated *in vitro* labelling maltose binding protein (Mercogliano and DeRosier, 2007) and in yeast (Morphew et al., 2015). Other demonstrations of the MT probe used AuCl, which formed electron dense particles at the target location and was corroborated by subsequent immunolabelling (Diesta et al., 2009a), (Diestra et al., 2009b). However AuCl is not soluble in the aqueous media which the cells were incubated in (Gammons et al., 1997), (Lu et al., 2008). This raises a number of questions with regard to the particles formed and whether the probe is working as intended.

3.1.2 Endogenously Expressed Electron Dense Probes

ReAsH/FlAsH has an endogenously expressed component which is six amino acids in length Cys-Cys-Xaa-Xaa-Cys-Cys. Where Xaa represents any non-cysteine amino acid. This short motif has a high binding affinity and specificity for non-fluorescent biarsenical derivatives of fluorescein: ReAsH and FlAsH. Upon binding to the tetra cysteine motif, the previously non-fluorescent molecules generate a strong green fluorescence. To form target localised electron density, photo-conversion is required. This process entails embedded samples being illuminated with an intense light in the presence of oxygen. The fluorescent label under these conditions catalyses the process of singlet oxygen generation which in turn precipitates DAB. Unfortunately the arsenic containing molecules induce cytotoxicity unless treated with antidotes such as 1,2 ethanedithiol (Gaietta et al., 2002). Subsequent papers have also highlighted the issue of non-specific interactions between the probe and off-site targets which produces a high background signal (Machleidt et al., 2007).

3.1.3 Streptavidin Biotin

Having discussed the various methods of endogenous electron density generation, it has been established that the currently available probes are not without issue. Furthermore none of the aforementioned endogenous probes are capable of generating electron density with as much contrast and precision as an AuNP label. Therefore exploring binding partners able to colocalise an AuNP, or other electron dense label, to a specific site of interest could address some of these issues. Biotin and Streptavidin are a ubiquitous binding pair with an incredibly high binding affinity (dissociation constant ≈$4x10^{-14}$M) (Holmberg et al., 2005). Furthermore the increased diffusive capacity of the biotin molecule due to its relatively small size in comparison to antibodies would also be advantageous for use as a probe. However tetrameric structure of streptavidin does not lend itself well for use as a probe. The binding pocket is highly dependent on the tetramer formation as it is composed of residues from multiple adjacent subunits. A stoichiometric ratio of 1:1 between probe and target would be ideal for clear labelling and to preserve native protein function/trafficking. Thus far the reproduction of this binding pocket in a single domain protein for biotechnology applications has yet to be achieved. Protein engineering has had partial success in this endeavour producing a stable monomeric version of streptavidin (mSA) but with a significantly reduced binding affinity (K(d) = 2.8nM) (Lim et al., 2013). A separate group has also reported the formation of mSA with a dissociation constant of 3nM. Cell surface biotinylation was performed before labelling the biotinylated proteins with a streptavidin-Alexa 488 conjugate which displayed specific localisation to the cell surface. However it seems counter-intuitive to use the biotin as the target and the streptavidin as the probe. Streptavidin can be endogenously expressed in chimera proteins creating a very precise target, while the smaller biotin molecule displays greater diffusive capacity to penetrate the sample and bind to the streptavidin. However molecular dynamics modelling suggest that the binding pocket of streptavidin electrostatically interacts with all potential ligand modification sites of the biotin molecule (Liu et al., 2016). Therefore covalent attachment of an electron dense probe to this ligand would likely have a detrimental impact on binding affinity.

3.1.4 Development of FKBP-SLF' as a CLEM Probe

The design of the CLEM probe discussed in this thesis will revolve around the very high binding affinity between a mutant of FKBP12 and a synthetic ligand: synthetic ligand of FKBP (SLF'). The quenching associated with fluorophore and AuNP propinquity will be avoided by binding the AuNP

after fluorescence imaging. Additionally the binding site (FKBP) will also be endogenously expressed to ensure a tight colocalisation with the protein of interest. The FKBP protein is derived from human FKBP12 sometimes referred to as FK506 binding protein. However the FKBP used has a point mutation at the 36th residue where the native phenylalanine is replaced with a valine. For clarity I will refer to the point mutant FKBP(F36V) used in this study as FKBP and wild type FKBP protein as wtFKBP. The dissociation constant reported in the literature for FKBP and SLF' is 94pM (Clackson et al., 1998). This binding affinity competes with many antibodies commonly used to label specific proteins *in vivo* with the added advantage of being far smaller. (Landry et al., 2015). This probe would also avoid some of the issues of the streptavidin-biotin binding model. Firstly, SLF' does not completely occupy the binding site of FKBP in the same way that biotin does for Streptavidin (Clackson et al., 1998). Therefore the SLF' can be functionalised and in theory should have a negligible impact on the binding affinity assuming the site of modification is chosen carefully. Secondly, FKBP is inherently a monomeric protein and does not suffer from the complications of forming higher order structures like streptavidin.

The size of SLF' (634.77 Au) relative to an antibody may also confer the probe with additional advantages. The congested nature of the cytoplasm can sterically hinder an antibody's progression and deny or reduce access to its target. This effect is particularly pronounced when labelling samples pre-embedded in resin. It is hoped that the size of the SLF' ligand will aid in sample penetration in both resin pre-embedded and live/fixed tissue samples. Furthermore, the hydrophobic nature of the ligand may aid in bilayer traversal and resin penetration, particularly in hydrophobic resins such as epon.

Considering the purpose of this research is to explore the generation of localised electron density where some component is expressed endogenously, the fluorescent component chosen was EGFP. EGFP is a robust well characterised and widely used fluorophore. Choosing a well-defined fluorophore enables any data generated from this aspect of the probe to be accurate/more easily interpreted, enabling more straightforward troubling shooting of the electron dense component. The tag was designed as follows: EGFP – FKBP – Protein of interest (SNX1). The FKBP protein is located directly adjacent to the protein of interest to decrease spatial separation between protein of interest and electron density. While the EGFP is further separated from the true target. This was done to reflect the relative resolving powers of each imaging modality the probe was designed for. Expressing the majority of the CLEM probe endogenously requires minimal diffusive entities to

traverse the cytoplasm and reach a target. This should confer a higher specificity and lower background. This probe also has the flexibility to be fluorescently imaged in the absence of the electron dense component of the probe. This avoids fluorescent quenching effects when a fluorophore is proximal to an electron dense object discussed in section 3.2.

3.1.5 Objectives

The work in this chapter will focus on creating the individual components required for the FKBP-SLF' probe system to be viable. Firstly, the FKBP protein will be sub-cloned into relevant vectors for protein expression in both eukaryotes and prokaryotes. The SNX1 protein was chosen as the protein of interest as it allows the efficacy of the probe to be scrutinised in both an *in vivo* and *in vitro* model. Using confocal microscopy *in vivo* tests will investigate native SNX1 tubule formation and native colocalisation with other well established heterodimeric proteins. EGFP-FKBP-SNX1 trafficking, localisation, function and colocalisation/binding with other known well established heterodimer partner (SNX6) will be investigated. Western blots will act as a complimentary technique to quantify the ability of the chimera protein to form native heterodimers.

In vitro studies revolving around tubulation assays will be employed to ascertain whether the ability of SNX1 to tubulate lipid vesicles *in vitro* is preserved with the addition of EGFP-FKBP. The assays will also be used to assess the labelling efficiency of the FKBP-SLF' probe as tubules will provide readily identifiable markers for the presence of SNX1 construct. Large concentrations of SNX1 are required for higher order oligomerisation and tubule formation, and one would expect significantly denser AuNP labelling in these areas assuming the probe functions as intended.

Finally the SLF' ligand will also need to be synthesised from scratch. The synthetic pathway was designed by Li-Chen Han and reported in his PhD thesis (Han, 2012). A method of covalently attaching an AuNP to the primary amine of the SLF' ligand will also be investigated.

3.2 Interferometric Cross Polarisation Microscopy

Currently the most ubiquitous CLEM probes consist of an AuNP favoured for their electron density, low cytotoxicity, straight forward synthesis and functionalisation. The fluorescent aspect is commonly derived from a fluorescent organic dye which is attached to the AuNP directly or in some other proximal location. The motivation for the development of novel CLEM probes came about as a result of work between myself and colleagues in physics. Henkjan Gersen's group developed a novel method of microscopy, able to visualise gold nanoparticles using a light microscope. The technique is termed interferometric cross-polarisation microscopy (ICPM). The system functions in a similar manner to a laser scanning confocal microscope with an epifluorescence and ICPM mode. A laser is scanned across the focal plane to create a raster image and also contains a pinhole to filter out of plane signal.

The ICPM system starts with a coherent light source is passed through a 50:50 beam splitter into a reference and signal beam. The reference beam is passed through two acouto-optical modulators (AOMs) and a Glan-Thompson polariser (GTP). The AOMs induce a frequency offset and the GTP orthogonally polarises the beam. The signal beam then passes through a GTP which generates a coherent x-polarised light source which is focused through a 1.45NA objective lens and on to the sample. The strong focusing effect of the high NA lens on the linearly polarised beam projects it across all three axis (parallel, perpendicular and axial). The presence of small scattering objects (smaller than the diffraction limit) in the focal plane cause these components to be scattered to the far field. Assuming no particles are present in the sample, the field is re-linearized by the collection objective. Assuming scattering particles were present in the focal plane, the collected beam is now comprised of two signals: linearly polarised light that passed through the sample without scattering and an orthogonally polarised portion that interacted with scattering particles in the sample (Figure 3.1). The sample and reference beams are then brought together before hitting the detector. The portion of the sample beam that has become orthogonally polarised is amplified via a heterodyne interaction with the reference beam. This method lends itself well to imaging biological samples only requiring low laser power (around 9μW hitting the sample) and has a high signal to noise ratio (Miles et al. 2015). The images generated by the ICPM imaging modality show the scattering particles to be small four lobed clover shapes. Boundaries such as the cell membrane and to a lesser extent the nuclear envelope can be visualised by a very small amount of scattering that occurs effectively forming a bright field/phase contrast image.

The ICPM system was used to evaluate the colocalisation between the AuNP scattering centres and associated fluorophores of a CLEM probe synthesised by Aurion. The CLEM probes were comprised of a 10nm AuNP surface functionalised with Alex 633 fluorophore. Our prediction was that the conjugated electron system in the fluorophore, when excited, would not decay and release fluorescence due to the close proximity of the AuNP. Instead the excited electrons would decay via the smaller energy intervals of the AuNP and radiate away the energy as lower energy emissions. This process would effectively quench any fluorophore in close proximity to the AuNP. Therefore the two signals would never co-localise rendering this labelling system ineffective for use as a CLEM probe. In order to visualise some residual fluorescence in close proximity to the AuNP Alexa 633 dye was chosen as the emission from this fluorophore had the least overlap with the AuNP absorption spectra of the AuNP but was still quenched by >95% (Miles et al., 2017).

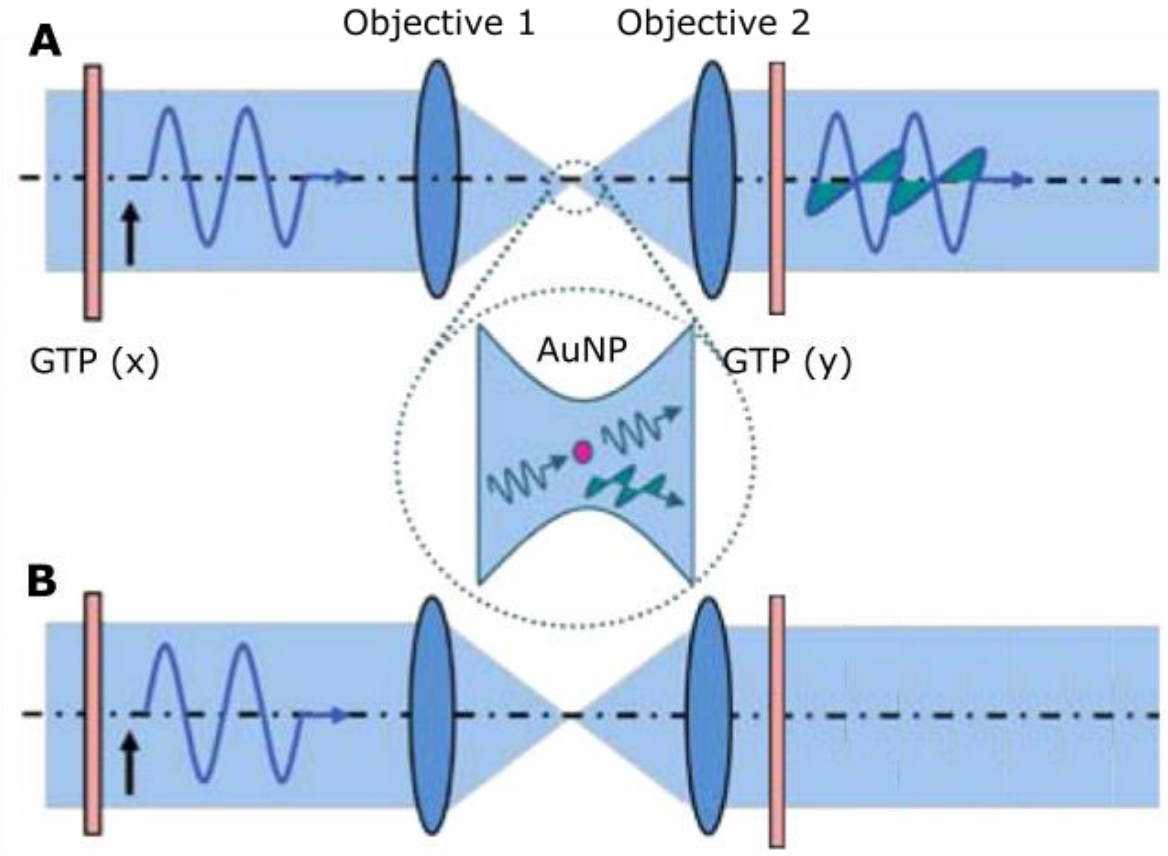

Figure 3.1: Schematic of the ICPM's optical path through a sample. The x-polarised incident beam formed by the Glan-Thompson Polariser (GTP (x)) is strongly focused by objective 1. The beam passes through objective plane before passing through the second objective. Image A shows signal propagation through the GPT (y) as a result of scattering particles present in the sample. Image B shows the light propagation in the absence of scattering particles in the sample. Negligible signal can pass through the GTP (y) without being orthogonally polarised.

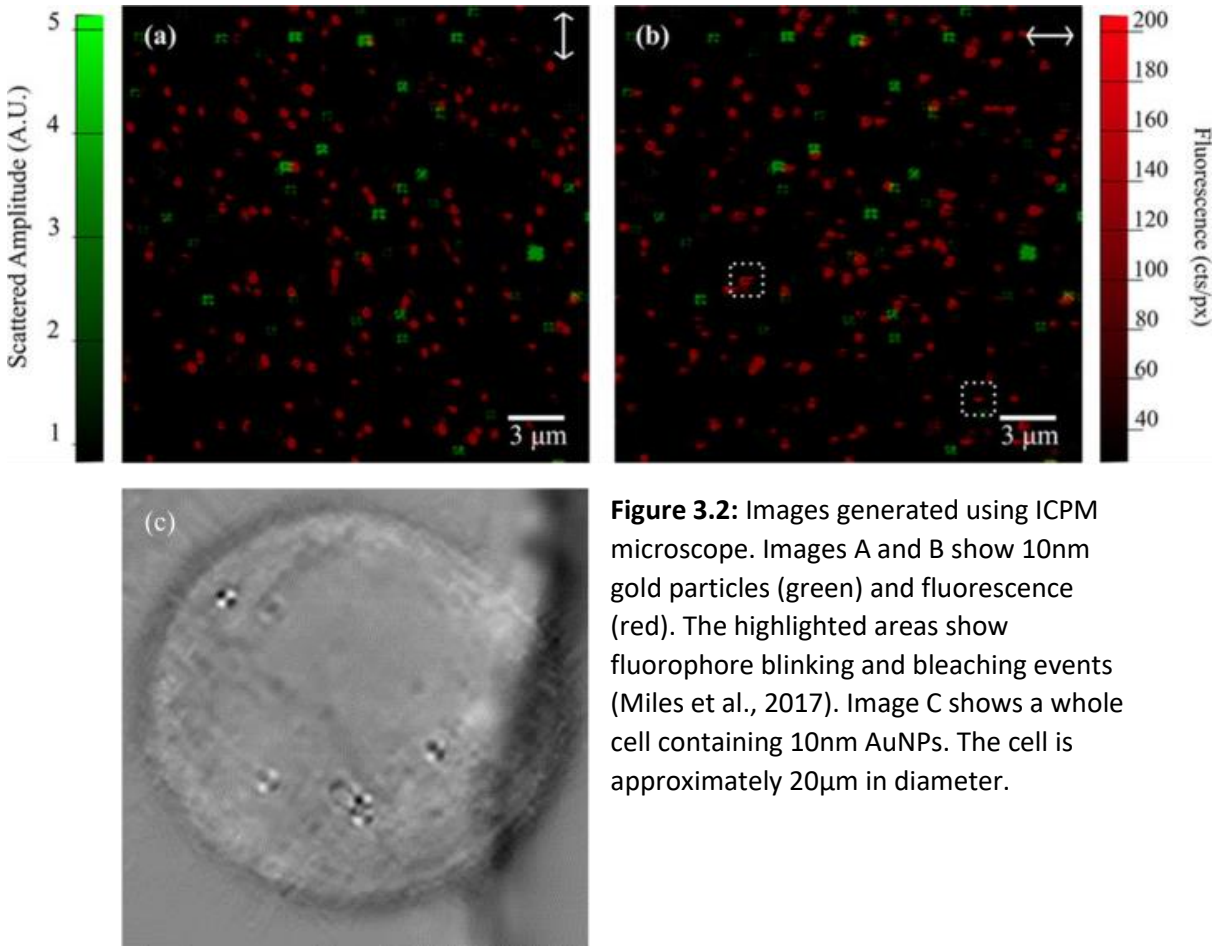

Figure 3.2: Images generated using ICPM microscope. Images A and B show 10nm gold particles (green) and fluorescence (red). The highlighted areas show fluorophore blinking and bleaching events (Miles et al., 2017). Image C shows a whole cell containing 10nm AuNPs. The cell is approximately 20µm in diameter.

Any quenching effects generated by proximity to an AuNP could be masked in a sample containing significant quantities of unconjugated fluorophore or naked AuNPs. A large excess of unconjugated fluorophore was present in the sample which was removed via a centrifugation step. The sample was subsequently analysed via DOSY NMR which generates separate spectra for each diffusive population. The DOSY data showed a single diffusive population of AuNPs bound to Alexa 633 with a small quantity of the citrate stabilising agent. Finally, this purified sample was drop-deposited onto coverslips at a concentration to ensure single AuNPs with an even distribution across the surface. Images A and B (Figure 3.2) shows the overlay of scattering centres (green) and fluorescence (red). The centre of the four lobed cloverleaf structures highlighting scattering particles are never seen to overlap with a fluorescent signal. Quantifying these data showed that 10nm AuNPs were able to quench fluorescence by >95%. This is a significant level of quenching which would at best seriously hinder accurate co-localisation and at worst render it near impossible. Further investigation of this quenching effect for smaller AuNP would allow the ubiquitous fluoronanogold to be evaluated. However, in its current iteration, the scattering cross-section of AuNPs below 5nm do not produce enough signal for the ICPM system to resolve. This thesis shows that 2nm AuNP still illicit detectable

fluorescent quenching (Section 4.2). Although fluoronanogold uses 1.4nm AuNPs, the fluorescent signal may still be significantly quenched. This reduced fluorescent intensity could compromise the accuracy of correlation with the AuNP portion of the label.

3.3 Overview of the SLF' FKBP CLEM Probe

These initial findings were the motivation for the development of novel CLEM probes. The first probe developed was based on the high binding affinity between a protein FKBP(F36V) and a synthetic ligand, SLF'. More specifically FKBP12 (FKBP1a gene) is a peptidyl-prolyl cis-trans isomerase which has been identified to have a number of roles within the cell. FKBP12 suppresses the activation of TGFBR1, a TGF-beta type I serine/threonine kinase receptor, preventing non-specific activation of the TGF-beta receptor in the absence of the ligand. It also recruits SMAD7 to ACVR1B which blocks activin signalling by preventing association of SMAD2 and SMAD3 with the activin receptor complex. In addition to these native functions Clackson et al. showed that the FKBP12 protein displayed a strong binding with tacrolimus (FK506) which was subsequently used as a method to induce dimerization between protein targets (Clackson et al., 1998). They also explored

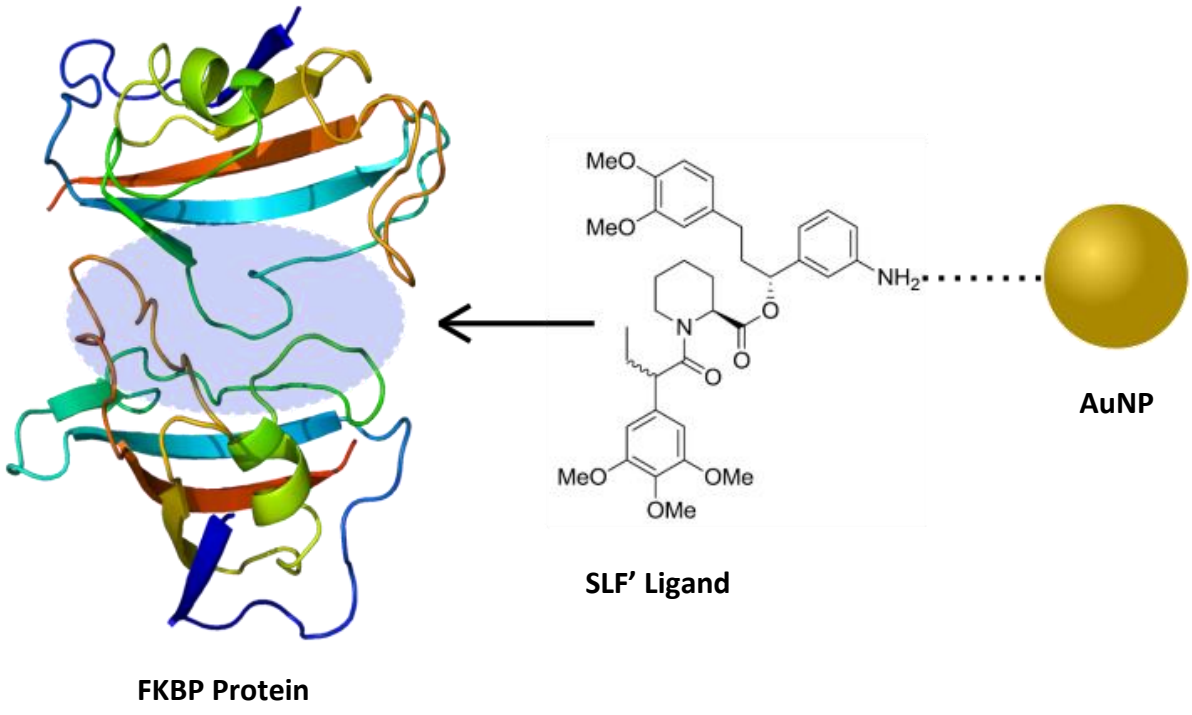

Figure 3.3: Overview of a CLEM probe based on the binding of SLF' and FKBP protein. The pale blue oval on the FKBP Protein indicates the binding site for the SLF' molecule. The dissociation constant for this binding has been reported to be 94pM. The dotted line between the primary amine and the AuNP represents a linker that covalently attaches the two.

modifying the protein and ligand further to increase binding affinity. The highest dissociation constant reported in the paper was 94pM between the designed synthetic ligand SLF' and the modified FKBP(F36V) (Clackson et al., 1998).

Colocalising an electron dense label to a protein of interest could be achieved by taking advantage of the tight binding between SLF' and FKBP (Figure 3.3). In the same manner antibodies are used to deliver an electron dense label to a protein of interest, SLF' conjugated to an AuNP could be used in a similar manner. For this system to work, the gene for the protein of interest must be edited forming a chimera protein: protein of interest-FKBP-EGFP or EGFP-FKBP-protein of interest. Therefore, a cell expressing a chimera protein-FKBP-EGFP, either transiently or via genome editing could be fluorescently imaged before subsequent incubation with SLF'-AuNP. This would allow accurate registration of the fluorescent signals and avoid any quenching effects which may arise from AuNP proximity. Furthermore, the SLF'-AuNP binding affinity is far higher than the vast majority of antibodies, increasing the percentage of proteins labelled and with greater specificity. The SLF'-AuNP would also be far smaller in size than even antibody fragments affording it greater sample penetration. This is particularly relevant when considering the highly crosslinked and reduced diffusibility in the context of a cell treated with strong fixatives for an optimally preserved ultrastructure. Despite these advantages expression of chimera proteins for use as labelling systems can potentially present drawbacks: additional protein subunits can negatively impact on protein function, affect protein trafficking and the probe cannot be used to visualise unmodified native proteins.

3.4 Plasmid Synthesis and Construct Design

The CLEM probe system essentially consisted of two distinct constituent parts. The modified chimera protein containing FKBP and the SLF' ligand with conjugated AuNP. The first step of this process was to design plasmids in order to begin the synthesis of proteins. Furthermore, it was also necessary for certain proteins to be sub-cloned into prokaryotic and eukaryotic expression vectors. The commercially available pET-45b(+) plasmid (Figure 3.4) was the chosen vector for prokaryotic expression. It contained: a multiple cloning site (MTS), T7 promoter, lacI, lacI promoter and an amplicillin resistance gene. In addition, it also contained a hexahistidine tag upstream of the MTS which could be subsequently cleaved off the purified protein using the enterokinase site. An S-tag was also present downstream of the MTS which could be used as a back-up purification method, if the gene were to be added without a stop codon.

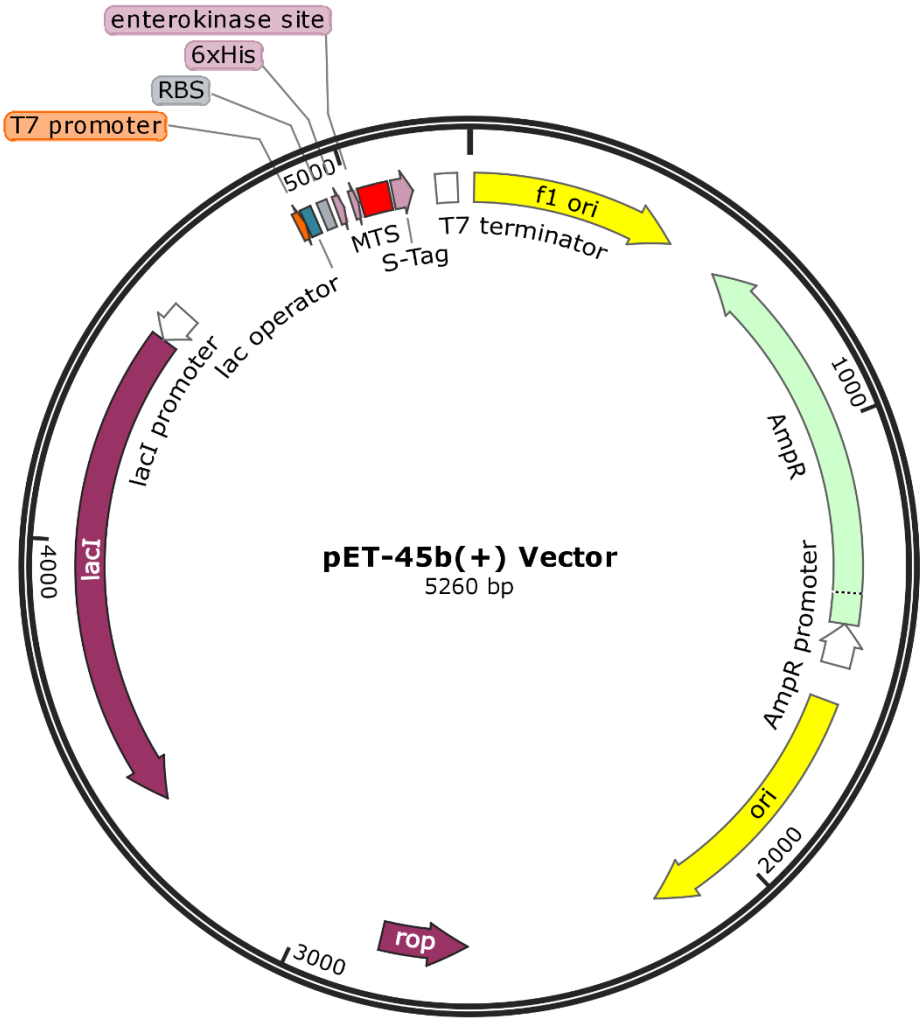

Figure 3.4: Commercially available pET45b(+) plasmid map used for prokaryotic expression of chimera proteins

3.4.1 Gibson Assembly

A kind donation from Thom Sharp already contained the EGFP-FKBP-SNX1 chimera gene in a eukaryotic expression vector. Therefore, acquiring the genes from cDNA was not necessary and sub-cloning could immediately begin. Initially, sub-cloning into the MTS was attempted using standard restriction enzyme cloning methods. Two different restriction enzymes were chosen that appear in the insert DNA and vector DNA just once. These restriction sites must flank the insert gene and appear in the MTS of the vector DNA (ensuring the gene will be inserted the correct way). Both insert and vector DNA were digested with these restriction enzymes to form sticky ends which were not complimentary with one another to stop the DNA from reannealing. The lysed insert DNA and vector DNA were combined with DNA ligase and the two pairs of complimentary sticky ends were annealed. Despite the robust nature of this cloning method, no colonies grew on ampicillin selective media after transformation so an alternative method was used.

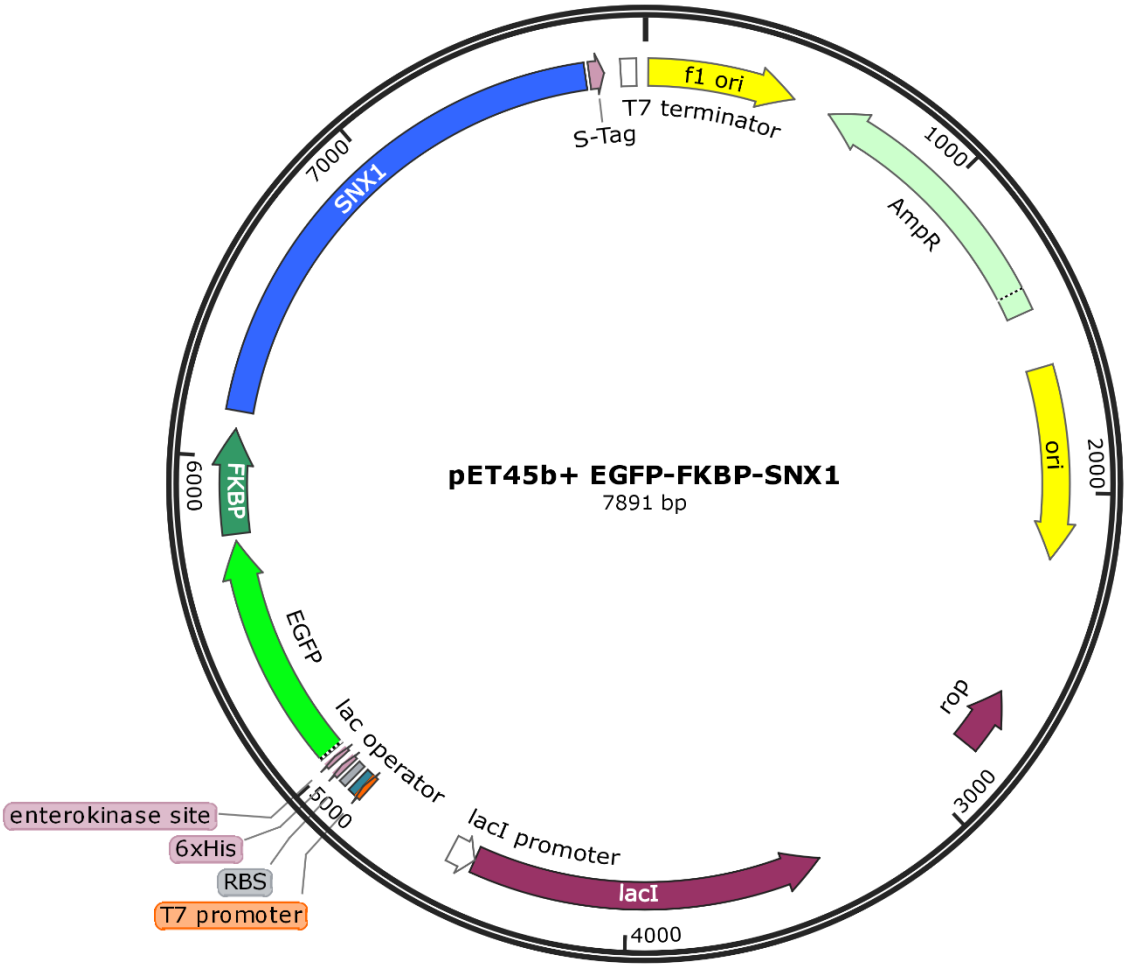

Figure 3.5: pET45b(+) vector sub-cloned with EGFP-FKBP-SNX1

The advantage of using the Gibson assembly is it does not require the use of restriction enzymes allowing genes to be placed very precisely within a vector. Furthermore, with careful primer design DNA inserts can be used to replace existing vector DNA with the insert in a single step. With this method the EGFP-FKBP-SNX1 gene was inserted into MTS of the pET45b(+) vector (Figure 3.5). For use as a control in various experiments, sub-cloning of EGFP-SNX1 into the same vector was attempted with both the aforementioned techniques (restriction cloning and Gibson assembly). In addition, a third method with Gibson assembly primers containing restriction sites was also tried but all were unsuccessful in generating colonies on selective media. Diagnostic gels showed the correct sized fragments were generated so the issue occurred during either the ligation or transformation step.

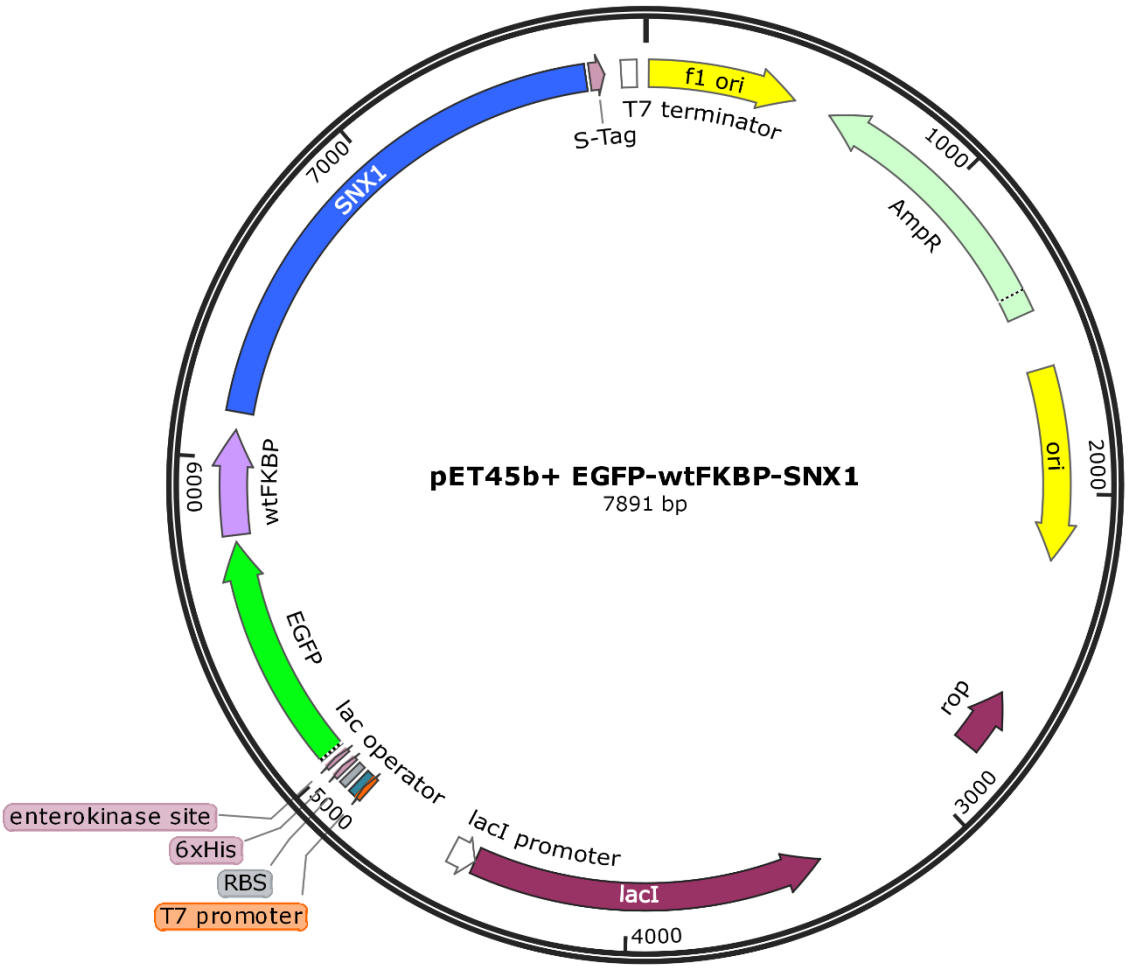

Figure 3.6: pET45b+ vector with EGFP-wtFKBP-SNX1 after site directed mutagenesis

Especially for further studies concerning binding affinity between SLF' and the EGFP-FKBP-SNX1 chimera protein it was imperative to have a control. Due to the aforementioned issues with sub-cloning EGFP-SNX1 into the pET45b(+) vector, site directed mutagenesis was used to compromise the binding site of the FKBP protein within the construct. The FKBP protein used in the EGFP-FKBP-SNX1 construct has a single point mutation which deviates from the wild type protein: phenylalanine to valine in the 36th position (FKBP(F36V)). SDM was used to introduce a single point mutation to convert this valine (gtt) back to a phenylalanine (ttt) essentially restoring the protein back to wild type (Figure 3.6). This residue is in a prominent position of the SLF' binding site and paramount in the ability of SLF' to bind tightly. According to the literature the wtFKBP displays weaker binding by two orders of magnitude (Clackson et al., 1998).

3.5 FKBP Protein Construct Function

Constituent protein markers within a chimera have the potential to have a detrimental impact on native protein function. Additional peptides added to a fusion protein can hinder binding sites via unfavourable electrostatic interactions or steric hindrance. Modifying the protein structure in this way could impact protein organisation and higher order oligomerisation which at worst can render the protein non-functional. In some circumstances the opposite can occur, where addition of fusion proteins induces aggregation and homodimerisation resulting in inclusion body formation and/or redirection of protein trafficking toward the degradative pathway. Avoiding these artefacts is paramount for a probe's success, otherwise observations made using it are likely to be non-representative and misleading. Therefore, to be suitable for use as a protein label, the FKBP protein must not significantly impact the protein of interest's function or trafficking when expressed as a chimera protein.

3.5.1 Fluorescence Colocalisation

To ensure the addition of both EGFP and FKBP to the SNX1 proteins N-terminus did not affect protein function a series of experiments were performed. Firstly confocal microscopy was used to gain a global overview of the distribution of EGFP-FKBP-SNX1 compared to a control of EGFP-SNX1. EGFP-SNX1 was used as the control in this study as its native function is not impaired and has been used in interactome studies (Simonetti et al., 2017). SNX1 is responsible for retrograde trafficking of

various protein cargoes between the endocytic network and trans-golgi network. Expected native protein subcellular localisation would primarily occur on intracellular vesicles with a lesser amount distributed throughout the cytosol. Antibody staining of early endosome associated protein 1 (EEA1) showing a strong colocalisation with EGFP-FKBP-SNX1 (data not shown). To further confirm SNX1 native function *in vivo*, SNX1s ability to bind cargo adapters must be retained and provides an alternative method to test protein function. As well as being able to form homodimers, SNX1 is well known to heterodimerise with SNX6, a cargo selective element (Kvainickas et al., 2017). Laser scanning confocal microscopy was used to investigate the colocalisation between the two proteins at a whole cell level.

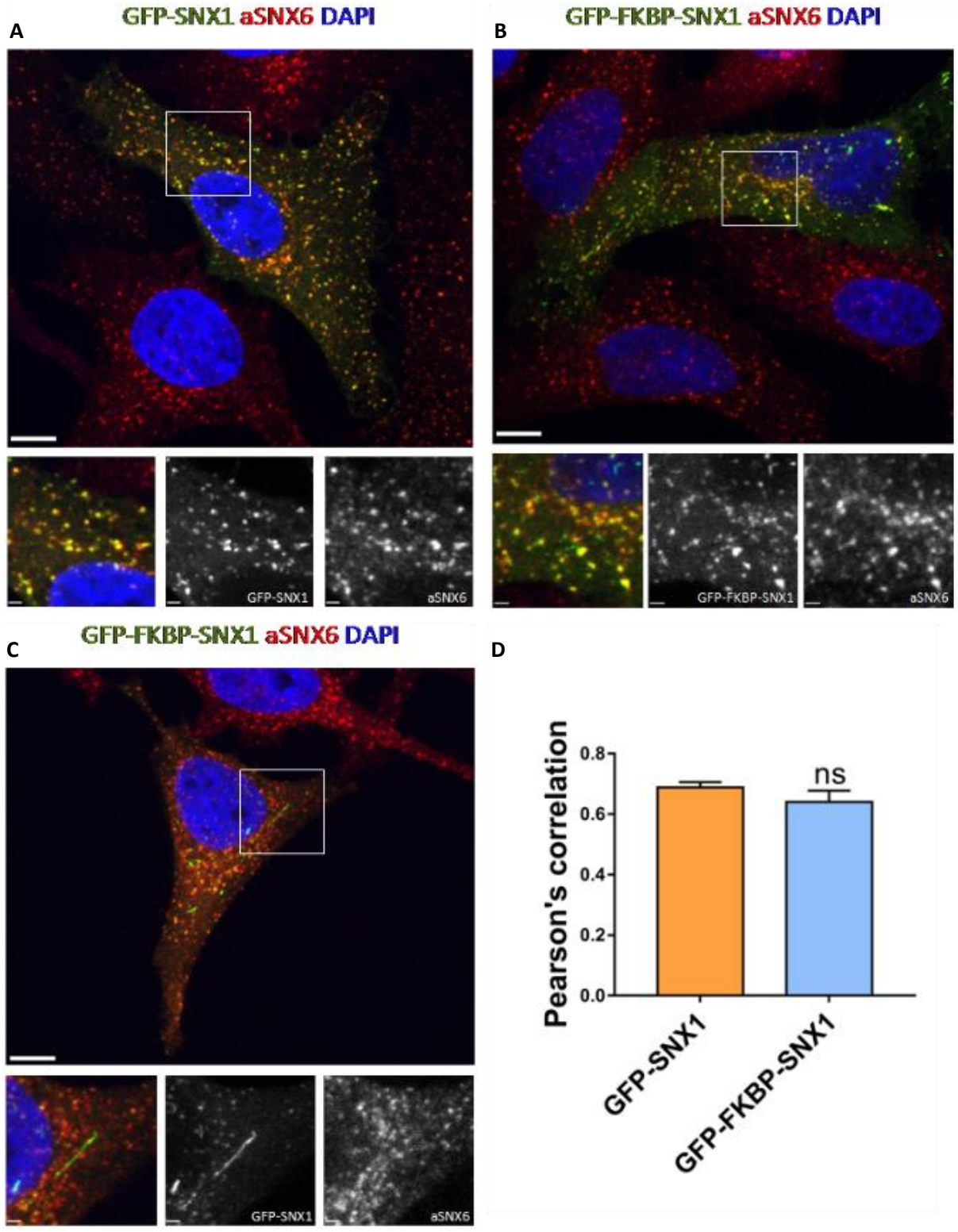

Figure 3.7: Images A and B show HeLa cells with fluorescent antibody labelling against SNX6 (red) while also transiently expressing EGFP-SNX1 and EGFP-FKBP-SNX1 (green) respectively. Nuclei are labelled with DAPI (blue). Image C is labelled in an identical manner as B but shows that the chimera protein is still capable of forming *in vivo* SNX1 tubules. Image D is a graph displaying the colocalisation of SNX6 with EGFP-SNX1 and EGFP-FKBP-SNX1 with the error bars representing the standard error of the mean. Scale bars in the large images represent 10µm and in the smaller images represent 1.6µm.

RPE1 cells were transfected with EGFP-SNX1 and EGFP-FKBP-SNX1 and cultured for 48 hours until sufficient protein expression was achieved. Cells were then fixed in 4% PFA and permeabilised with Triton X100 before labelling with primary antibodies against SNX6. Cells were washed before incubating with a fluorescently labelled secondary antibody. Cells were then imaged using a laser scanning confocal microscope with a x63 oil immersion lens. Cells chosen for imaging were specifically chosen based on the expression levels of SNX1. Cells imaged for the purpose of colocalisation quantification could not be chosen at random. Typically, a random approach is preferred to ensure bias is removed from the selection process. However, the level of protein expression can vary greatly in transient expression. Some cells did not have detectable levels of EGFP containing protein. However, cells overexpressing SNX1 display a non-native phenotype characterised by dense networks of stacked SNX1 positive tubules. Imaging these highly expressing cells is not a typical representation of a healthy cell and a large discrepancy between transient SNX1 chimera expression and native SNX6 expression would produce any quantitation of colocalisation inaccurate.

Cells selected for lower level expression of EGFP-SNX1 and immunolabelled SNX6 were imaged with a scanning laser confocal microscope. Z-stacks were collected and converted to maximum intensity projections. All measurements were performed in triplicate and ten cells were imaged in each experiment. Using Coloc2 plugin for ImageJ the background was masked off so only cellular contents were quantified. The Pearson's correlation was calculated using the Costes threshold. The colocalisation of SNX6 with EGFP-SNX1 and EGFP-FKBP-SNX1 was 0.69 and 0.64 respectively (Figure 3.7). The Pearson's correlation between these two conditions was not statistically significant suggesting that the addition of the FKBP to the chimera protein did not perturb native SNX1 binding to SNX6.

While collecting images for colocalisation SNX1 positive tubules were also observed *in vivo*. These tubules appeared to be composed primarily of SNX1 chimera homodimers (Figure 3.7). These tubules did not appear with a high enough frequency to perform quantitative studies on, however qualitatively this is further evidence that the addition of EGFP-FKBP to the N-terminus of SNX1 does not perturb native function evidenced by the labelled SNX1s ability to form higher order oligomerisation and tubulate lipid membranes.

3.5.2 Coimmunoprecipitation of SNX5 and SNX6

To further investigate whether the FKBP label to the chimera protein affected SNX1 function pulldown assays were performed. HEK293T cells were transiently transfected with EGFP-SNX1 and EGFP-FKBP-SNX1 before being lysed. The whole cell lysate was then incubated with GFP-trap beads immobilising any EGFP containing proteins (EGFP-SNX1 and EGFP-FKBP-SNX1). EGFP containing proteins immobilised by the beads were then washed to remove any non-specifically bound molecules. Proteins coimmunoprecipitated with the immobilised EGFP chimeras were combined and resolved with SDS-PAGE before Western Blotting. SNX5 and SNX6 are well characterised heterodimeric partners for SNX1 and so were selected for immunoblotting. Blots were incubated with SNX5 and SNX6 primary antibodies, washed and incubated with a fluorescent secondary antibody. The blots showed that EGFP-SNX1 and EGFP-FKBP-SNX1 were still both capable of pulling down SNX5 and SNX6 (Figure 3.8). Furthermore, no significant difference in binding was observed between EGFP-SNX1 and EGFP-FKBP-SNX1 for either SNX5 or SNX6.

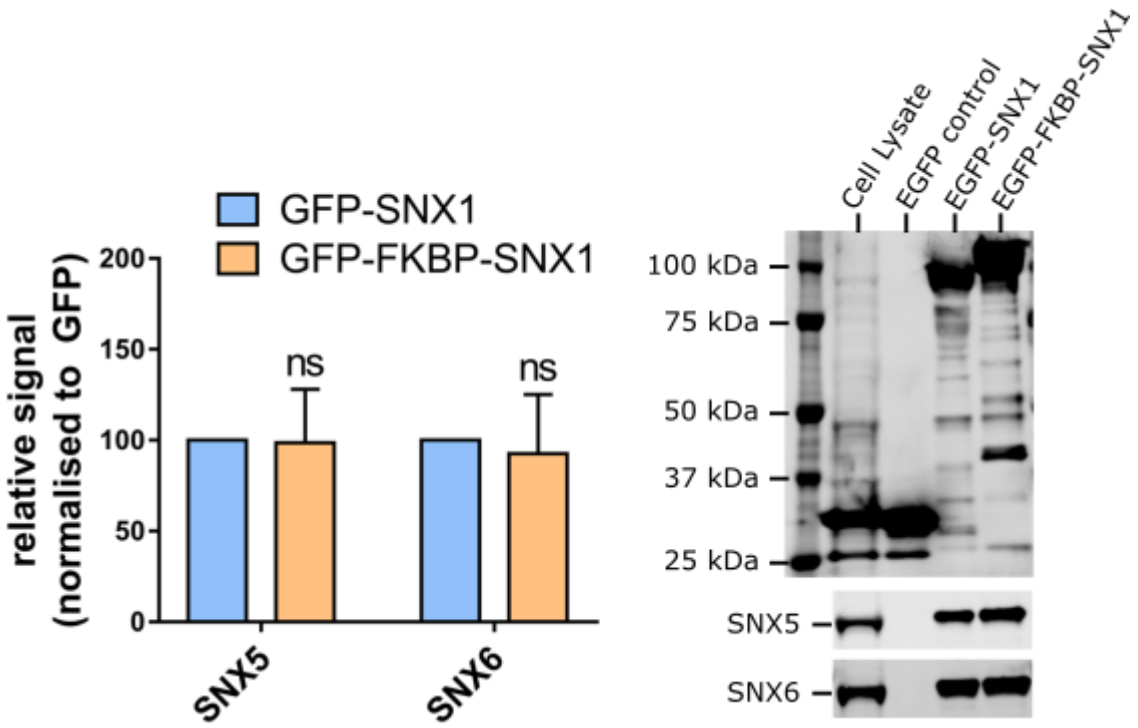

Figure 3.8: Western blot of proteins coimmunoprecipitated with EGFP containing proteins: EGFP, EGFP-SNX1 and EGFP-FKBP-SNX1. The gels show relatively similar expression of all EGFP containing proteins. The graph shows the result of the quantification and averages of three western blots.

3.6 Protein Purification

BL21(DE3) cells transformed with plasmid DNA were used to produce various chimera proteins for use in both tubulation and binding assays. Cells were transformed via the cell distributor's heat shock protocol before growing on selective media to ensure only transformants were cultivated. A starter culture was grown overnight in a shaking incubator at 37°C before transferring into 1L of LB Broth. The cells were then grown to an optical density of 0.6 before inducing with IPTG and incubating in a shaking incubator overnight at 25°C. This temperature was determined to give maximal yield without the formation of excessive misfolded protein or aggregates.

Crude protein purification was achieved utilising the hexahistidine tag with cobalt and nickel based chelation columns. The cobalt columns produced a cleaner final product (≈100kDa) with only minor protein bands of contamination. However the final concentration of protein eluted from the cobalt column was approximately three times more dilute than the nickel and more of the product was lost during wash steps. Dialysis was performed to remove excess imidazole (contained within wash and elution buffers) from the protein solution to reduce any effect it may have had on subsequent experiments.

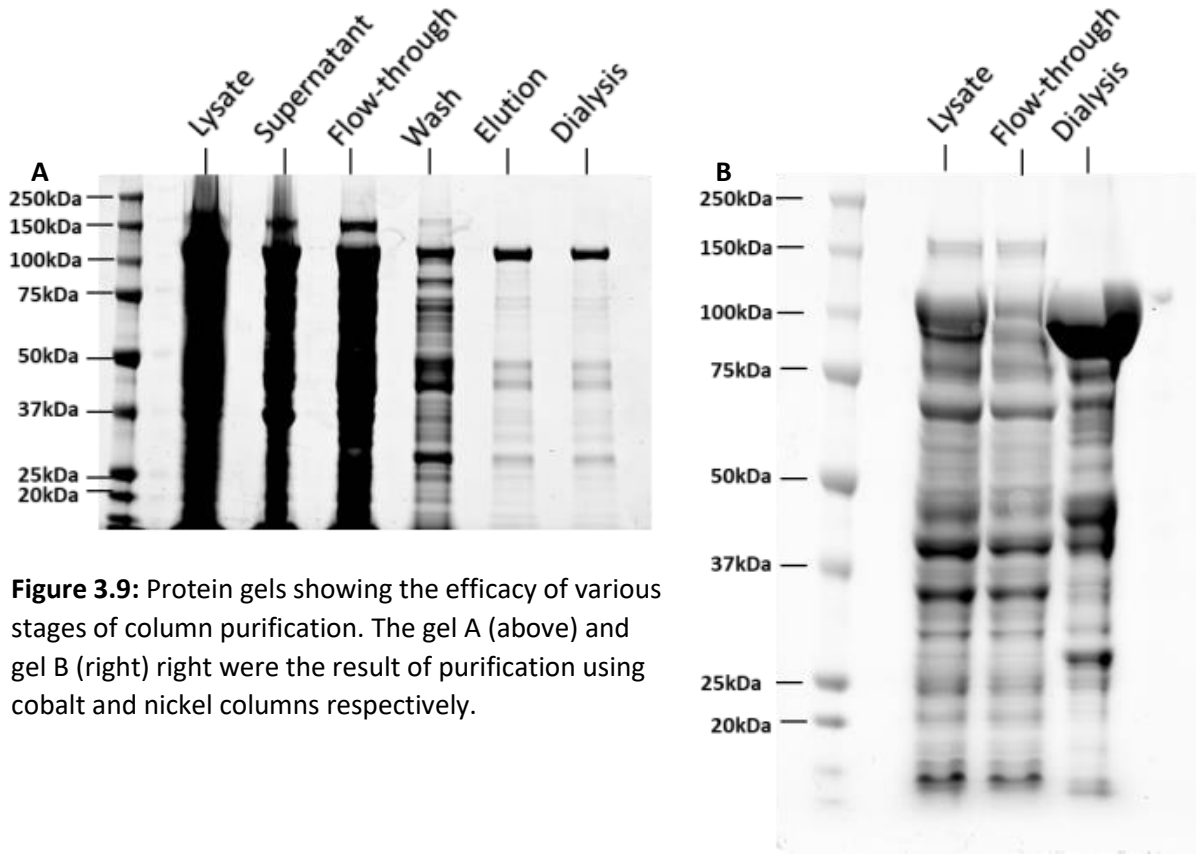

Figure 3.9: Protein gels showing the efficacy of various stages of column purification. The gel A (above) and gel B (right) right were the result of purification using cobalt and nickel columns respectively.

The initial purification step using columns produced a relatively high protein concentration with minimal contamination. However further inspection of the protein gels reveals evidence that the chimera proteins may have been degrading into constituent parts most clearly seen on the cobalt gel (Figure 3.9). Bands just above 25kDa and slightly below 50kDa may have been EGFP and SNX1 respectively. In order to be confident when performing tubulation assays that the chimera protein was responsible for any effects observed, it was paramount to remove as much of this contamination as possible. To achieve this a size exclusion column was used to further purify the crude product.

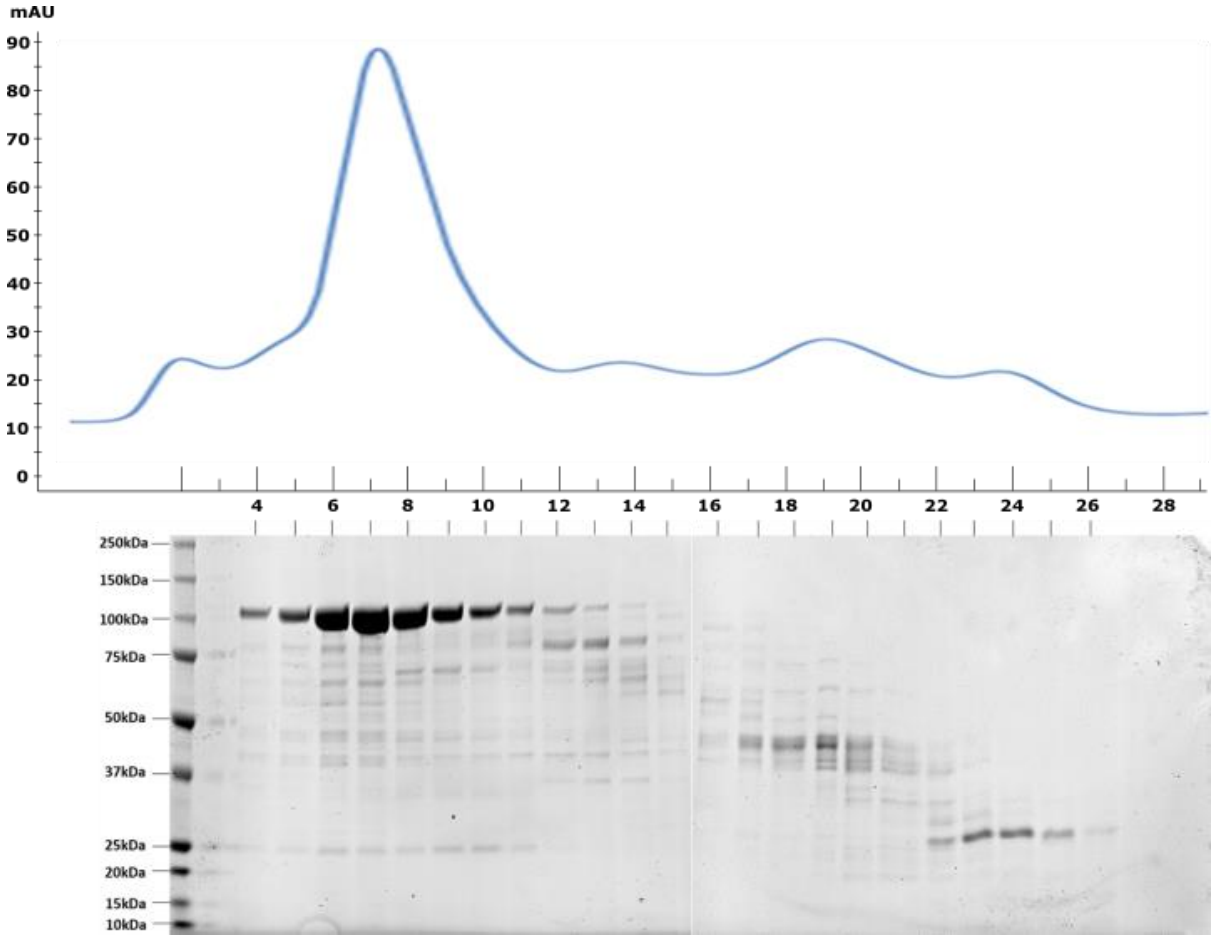

Figure 3.10: Protein purification on an ACTA system. The graph maps the UV-vis absorbance of each fraction. The gel underneath was produced by running each fraction acquired from the ACTA to confirm the presence of the protein of interest, in this case the band at approximately 100kDa.

Although a small amount of protein contaminants are visible in the gel (Figure 3.10) the relative intensities of product to contamination is much improved. Furthermore, from fraction 15 to 27 it is possible to see the contaminants removed from the purified product. The presence of contaminants

still in the presence of the purified product may suggest the protein is delicate and prone to degradation.

3.7 Synthetic Pathway of SLF'

This section details each individual reaction within the synthetic pathway of the SLF' ligand. This synthetic pathway was based previous work reported by Li-Chen Han (Han, 2012).

SLF' Synthesis 1 – 1-(3-Nitrophenyl)-3-(3,4-dimethoxyphenyl)-1-propanone

The first step of this synthesis used commercially available molecules: 3,4 dimethoxybenzaldehyde (**1**) and 3-nitroacetphenone (**2**). The two molecules were conjugated together using a condensation reaction. The crude product was a yellow solid that was highly insoluble in polar solvents. This step had a relatively low yield of 20%.

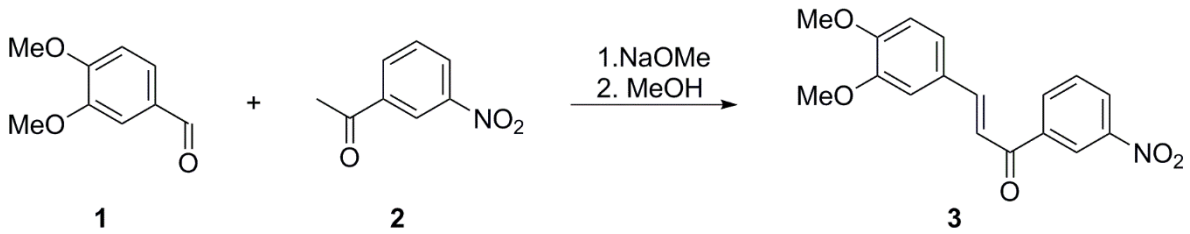

1 **2** **3**

Scheme 1: Condensation conjugation of aldehyde **1** and ketone **2** with sodium methoxide

δ_H(400Hz, $CDCl_3$) 3.94 and 3.97 (both 3H, both s, 2 x OCH_3), 6.93 (1H, d, J=8.4, ArH), 7.18 (1H, d, J=2.0, 2.0, ArH), 7.27 (1H, dd, J=8.3, 2.0, ArH), 7.38 (1H, d J=15.5, 2-H), 7.71 (1H, t, J=8.0, ArH), 7.84 (1H, d, J=15.5, 3-H), 8.34 (1H, ddd, J=8.1, 2.0, 1.0, ArH), 8.43 (1H, ddd, J=8.1, 2.0, 1.0, ArH), 8.82 (1H, t, J=2.2, ArH)

SLF' Synthesis 2 – 1-(3-Aminophenyl)-3-(3,4-dimethoxyphenyl)-1-propanone

The crude product (**3**) from scheme 1 was then stirred under an atmosphere of hydrogen with Pd/C to reduce both the unsaturated double bond and reduce the nitro group to a primary amine. The yield of this step was 48% and the purified product had the appearance of a yellow solid.

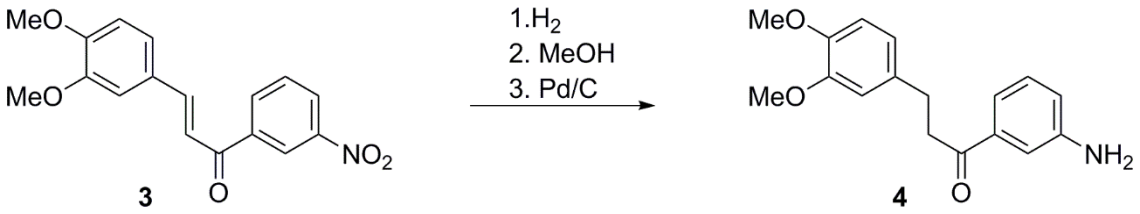

Scheme 2: Reduction of (**3**) to form a saturated ketone and primary amine

δ_H(400Hz, $CDCl_3$) 3.00 (2H, t, J=7.5, 3-H_2), 3.23 (2H, t, J=7.5, 2-H_2), 3.85 and 3.87 (both 3H, both s, 2 x OCH_3), 6.77-6.81 (3H, m, ArH), 6.86 (1H, ddd, J=8.0, 2.0, 1.0, ArH), 7.22 (1H, t, J=8.0, ArH), 7.27 (1H, m, ArH), 7.33 (1H, ddd, J=8.0, 1.0, 1.0, ArH).

SLF' Synthesis 3 – *N*-(*tert*-Butoxycarbonyl)-1-(3-aminophenyl)-3-(3,4-dimethoxyphenyl)-1-propanone

The primary amine of (**4**) had to be protected for subsequent reactions and was treated with $(Boc)_2O$. This protection reaction produced a colourless oil with a yield of 87%.

Scheme 3: Primary amine protection with Boc

δ_H(400Hz, $CDCl_3$) 1.52 (9H, s, $OC(CH_3)_3$), 3.02 (2H, t, J=7.2, 2-H_2), 3.28 (2H, t, J=7.2, 2-H_2), 3.85 and 3.86 (each 3H, each s, 2 x OCH_3), 6.68 (1H, br s, NH), 6.76-6.82 (3H, m, ArH), 7.36 (1H, t, J=8.0, ArH), 7.59-7.63 (2H, m, ArH) 7.94 (1H, t, J=2.0, ArH).

SLF' Synthesis 4 – (1R)-*N*-(*tert*-Butoxycarbonyl)-1-(3aminophenyl)-3-(3,4-dimethoxyphenyl)propan-1-ol

Ketone (**10**) was reacted with (+)-DIP-chloride to reduce the ketone to produce an asymmetric alcohol (**12**). This reaction had a yield of 95% and the purified product was a colourless oil.

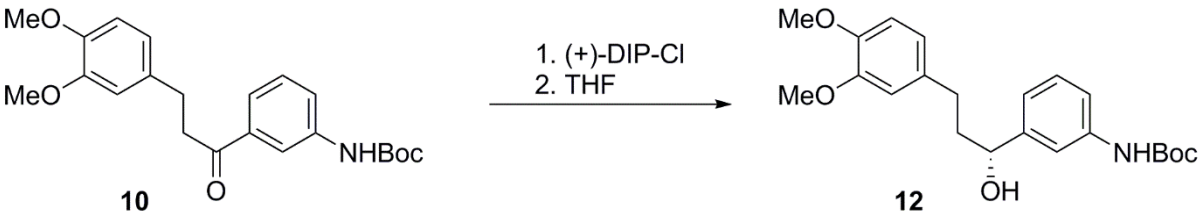

10 **12**

Scheme 4: Production of an asymmetric alcohol by reaction with (+)-DIP-chloride

δ_H(400Hz, $CDCl_3$) 1.49 (9H, s, $OC(CH_3)_3$), 1.89-2.08 (2H, m, 2-H_2), 2.21 (1H, br s, OH), 2.53-2.68 (2H, m, 3-H_2), 3.85 and 3.87 (both 3H, each s, 2 x OCH_3), 4.60 (1H, dd, J=7.4, 5.4, 1-H), 6.68-6.78 (3H, m, ArH), 7.05 (1H, br s, ArH), 7.22 (1H, ddd, J=7.8, 2.1, 1.2, ArH), 7.26 (1H, br d, J=7.6, ArH).

SLF' Synthesis 5 – (*S*)-Pipecolic methyl ester

Reduction of the carboxylic acid (**5**) with ethanol to produce an ethyl ester (**6**). The purified product was a white solid. The reaction had a yield of 97%.

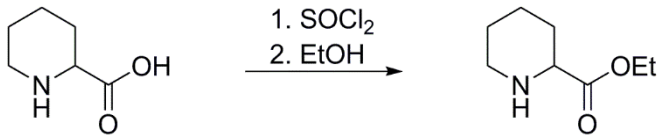

5 **6**

Scheme 5: Reaction between ethanol and carboxylic acid to form an ethyl ester

δH(400Hz, $CDCl_3$) 1.40-1.81 (5H, m, 3-*H*H, 4-H_2 and 5-H_2), 2.11-2.21 (1H, m, 3-H*H*), 2.92 (1H, m, 6-*H*H), 3.35, m, 6-H*H*), 3.89 (1H, m, 2-H), 4.17 (2H, q, CH_2).

SLF' Synthesis 6 – 2-(3, 4, 5-Trimethoxyphenyl)butanoic acid

A symmetric ethyl group was to the second carbon of carboxylic acid (**7**). The yield of this reaction was 98% and when purified produced a white powder.

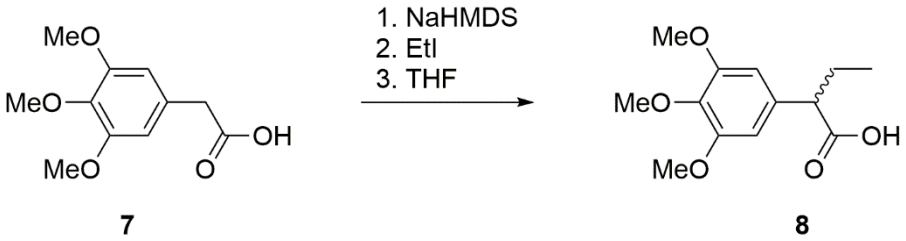

7 **8**

Scheme 6: Addition of an asymmetric ethyl group

δH(400Hz, $CDCl_3$) 0.92 (3H, t,J=7.4, 2''-H_3), 1.74-1.84 (1H, m, 1''-*H*H), 2.02-2.12 (1H, m, 1''-H*H*), 3.37 (1H, t, J=7.6, 2-H), 3.82 (3H, s, OCH_3), 3.85 (6H, s, OCH_3), 6.53 (2H, s, ArH).

SLF' Synthesis 7 – Ethyl (2*S*)-1-(2-(3, 4, 5-Trimethoxyphenyl)butanoyl)piperidine-2-carboxylate

The two separately synthesised molecules (**6**) and (**8**) were conjugated together using 2-chloro-1-methylpyridinium. The purified product was a colourless oil and the reaction had a yield of 88%.

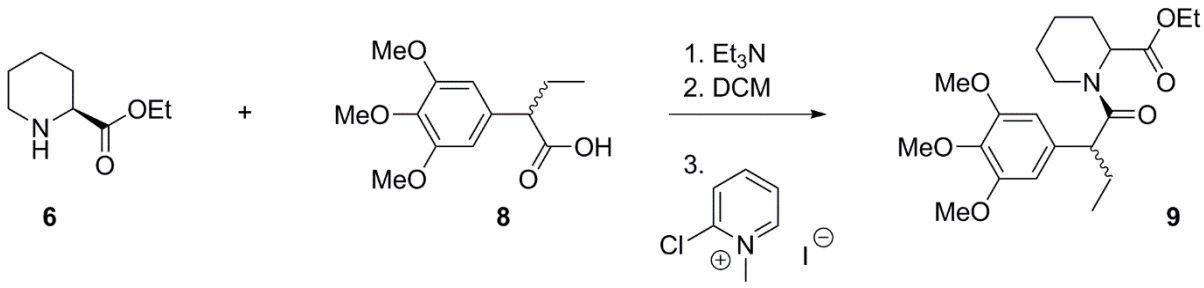

6 **8** **9**

Scheme 7: Conjugation of molecule **6** with carboxylic acid **8** via a condensation reaction

No NMR data available

SLF' Synthesis 8 – (2*S*)-1-(2-(3, 4, 5-Trimethoxyphenyl)butanoyl)piperidine-2-carboxylate

The Ethyl ester (**9**) was converted into a carboxylic acid in preparation for a subsequent conjugation reaction (scheme 9). The product was a white solid and pure enough to proceed without any further purification.

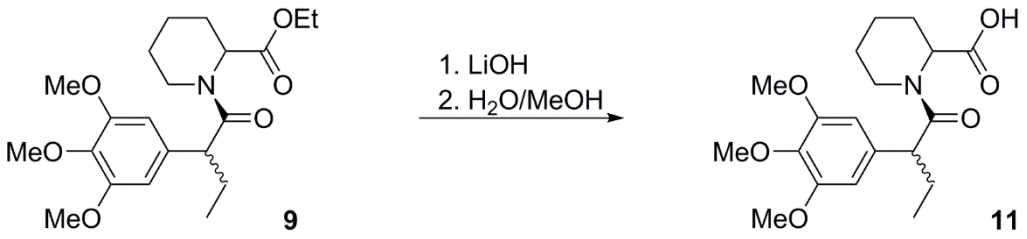

9 **11**

Scheme 8: Conversation of ethyl ester **9** into a carboxylic acid **10**

δH(400Hz, CDCl3) 0.81-0.95 (4H, m 5-*H*H and 2''-H_3), 1.29-1.82 (5H, m, 3-*H*H, 4-H_2, 5-H*H* and 1''-*H*H), 2.00-2.14 (1H, m, 1''-H*H*), 2.16-2.31 (1H, m, 3-H*H*), 3.18 (1H, app. dt, J=13.2, 6-*H*H), 3.57 (1H, t, J=7.0, 2'-H), 3.73-3.89 (10H, m, 6-H*H* and 3 x OCH_3), 5.49, (1H, br d, J=4.2, 2-H), 6.38-6.55 (2H, m, ArH).

SLF' Synthesis 9 – (1*R*)-1-(3-(*N*-(*tert*-Butoxycarbonyl)aminophenyl)-3-(3, 4-dimethoxyphenyl)-1-propanyl) (2*S*)-1-(2-(3, 4, 5-trimethoxyphenyl)butanoyl)piperidine-2-carboxylate

The penultimate synthetic step and the final assembly of the previously synthesised constituent molecules. Product was a thick colourless oil with a yield of 68%.

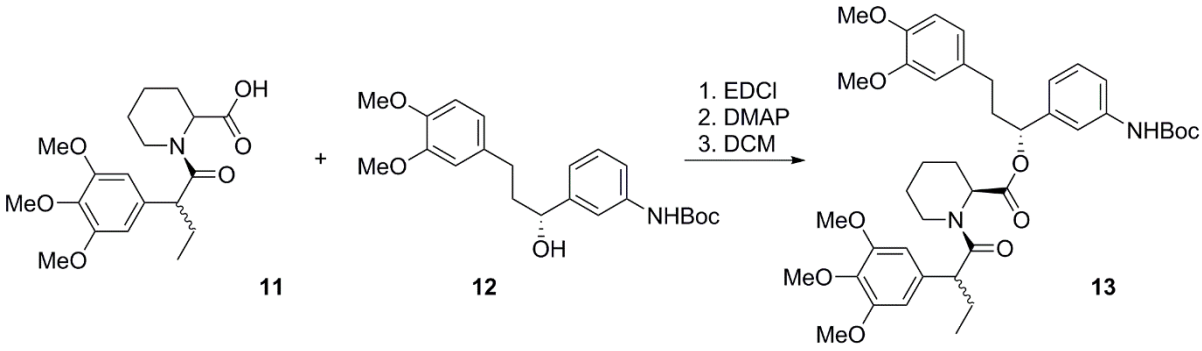

11 **12** **13**

Scheme 9: Final assembly of all individually synthesised molecular components

δ_H(400Hz, $CDCl_3$) 0.78-0.94 (4H, m, 5-*H*H and 2''-H_3), 1.28-1.45 (11H, m, 4-*H*H, 5-H*H* and $OC(CH_3)_3$), 1.49-1.77 (3H, m, 3-*H*H, 4-H*H* and 1''-*H*H), 1.87-2.28 (4H, m, 3-H*H*, 1''-H*H* and 3'''-H_2), 2.33-2.79 (2H, m, 2'''-H_2), 3.02 (1H, m, 6-*H*H), 3.59 (1H, t, J=7.1, 2'-H), 3.69-3.89 (16H, m, 6H*H* (16H, m, 6-H*H* and 5 x OCH_3), 5.54 (1H, br d, J=4.9, 2-H), 5.79 (1H, m, 1'''-H), 6.36-6.81 (5H, m, ArH), 7.09-7.42 (4H, m, ArH).

SLF' Synthesis 10 – (1*R*)-1-(3-Aminophenyl)-3-(3, 4-dimethoxyphenyl)-1-propanyl (2*S*)-1-(2-(3, 4, 5-trimethoxyphenyl)butanoyl)piperidine-2-carboxylate

The final reaction required the removal of the Boc protection group from the primary amine. The product was an incredibly viscous yellow oil. This final reaction step had a high yield of 98%.

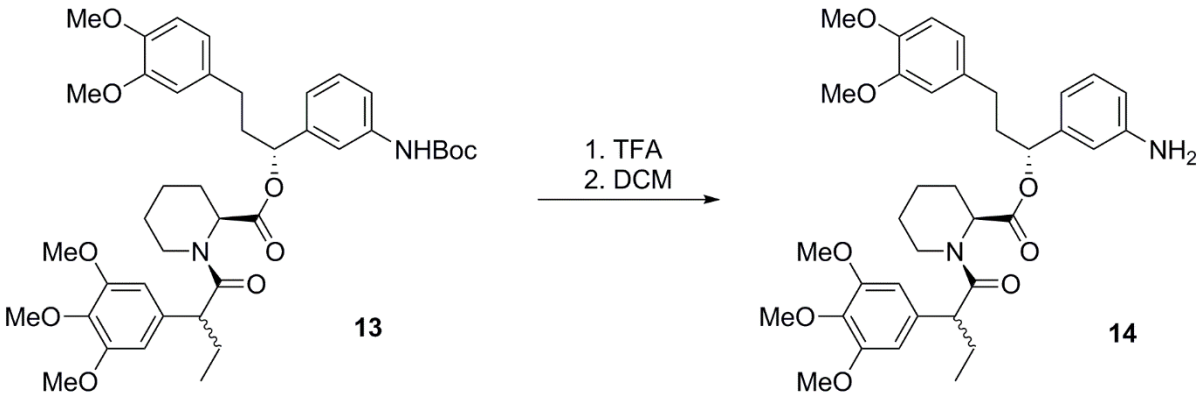

Scheme 10: Final de-protection reaction of the primary amine

δ_H(400Hz, $CDCl_3$) 0.79-0.95 (4H, m, 5-*H*H and 2''-H_3), 1.35-1.80 (5H, m, 3-*H*H, 4-H_2, 5-H*H* and 1''-*H*H), 1.94-2.68 (6H, m, 3-H*H*, 1''-H*H*, 2'''-H_2 and 2''-H_3), 2.75 (1H, app. td, J=13.3, 2.9, 6-*H*H), 3.55-3.92 (17H, 6-H*H*, 2'-H and 5 x OCH_3), 5.46-5.81 (2H, m, 2-H and 1'''-H), 6.38-7.18 (9H, m, ArH).

3.7.1 Covalent attachment of an AuNP to the SLF' molecule

For the SLF' molecule to be visible and identified when imaged in a TEM some form of electron density must accompany it. Commercially available 1.4nm AuNPs functionalised with a monovalent N-hydroxysuccinimide (NHS) ester were initially proposed to conjugate to the SLF'. The reaction between a primary amine and an NHS-ester is well characterised and ubiquitously used to label the N-termini of peptides. The reaction does not require extreme conditions and can be performed at ambient temperature and pressure in an aqueous medium.

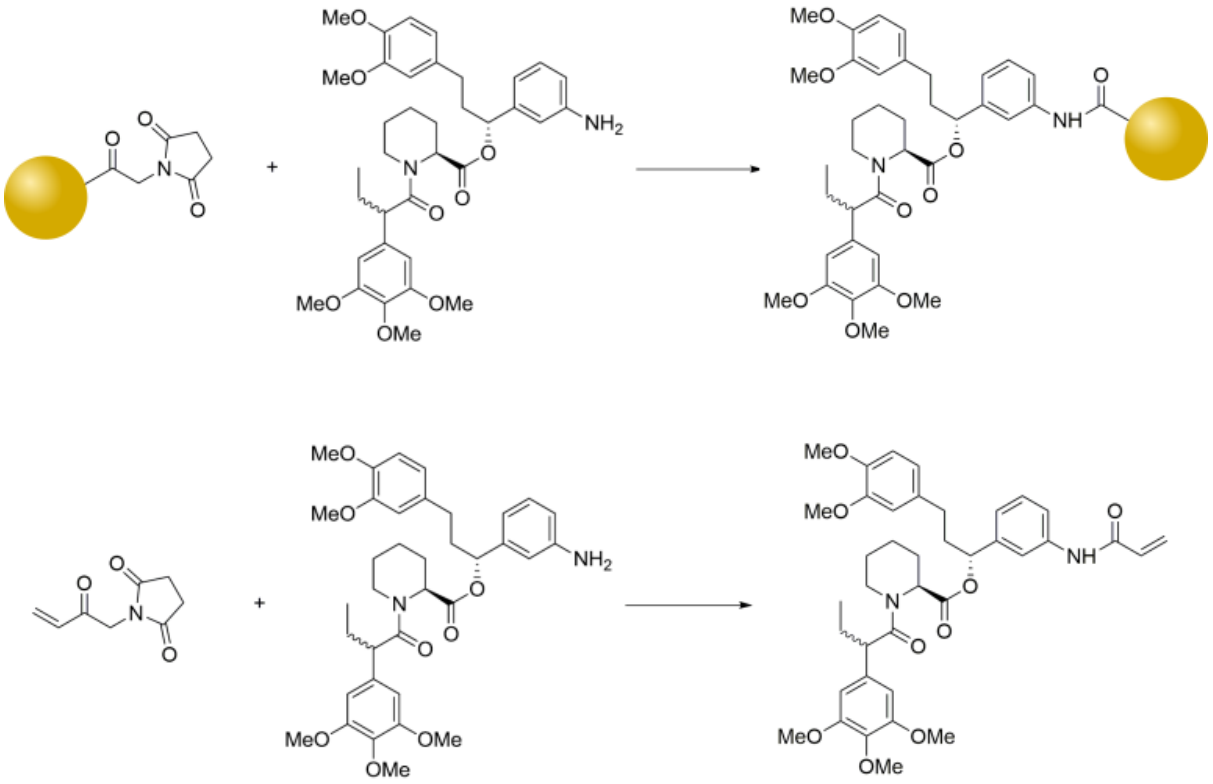

Scheme 11: Functionalisation of the primary amine on the SLF' molecule with an monovalent NHS-ester AuNP and an NHS-ester acrylic acid analog

The commercial monovalent NHS-ester AuNPs in theory would have been ideal for this probe. The monovalent functionalisation ensures a stoichiometric ratio of 1:1 between the AuNP and SLF' molecule. Each FKBP molecule has a one binding site, which can be occupied by one SLF' molecule which is in turn functionalised with a single AuNP. Therefore, the presence of a protein of interest should be reported with the colocalisation of a single AuNP. This monovalent AuNP would also reduce the likelihood of unwanted protein dimerization and aggregation preserving native protein

trafficking and function. Only very small quantities of monovalent NHS-ester AuNP could be purchased and so to optimise reaction conditions an analogue molecule (NHS-ester acrylic acid) was used (shown in scheme 11). This allowed reaction conditions to be optimised and investigated before using the far scarcer AuNPs.

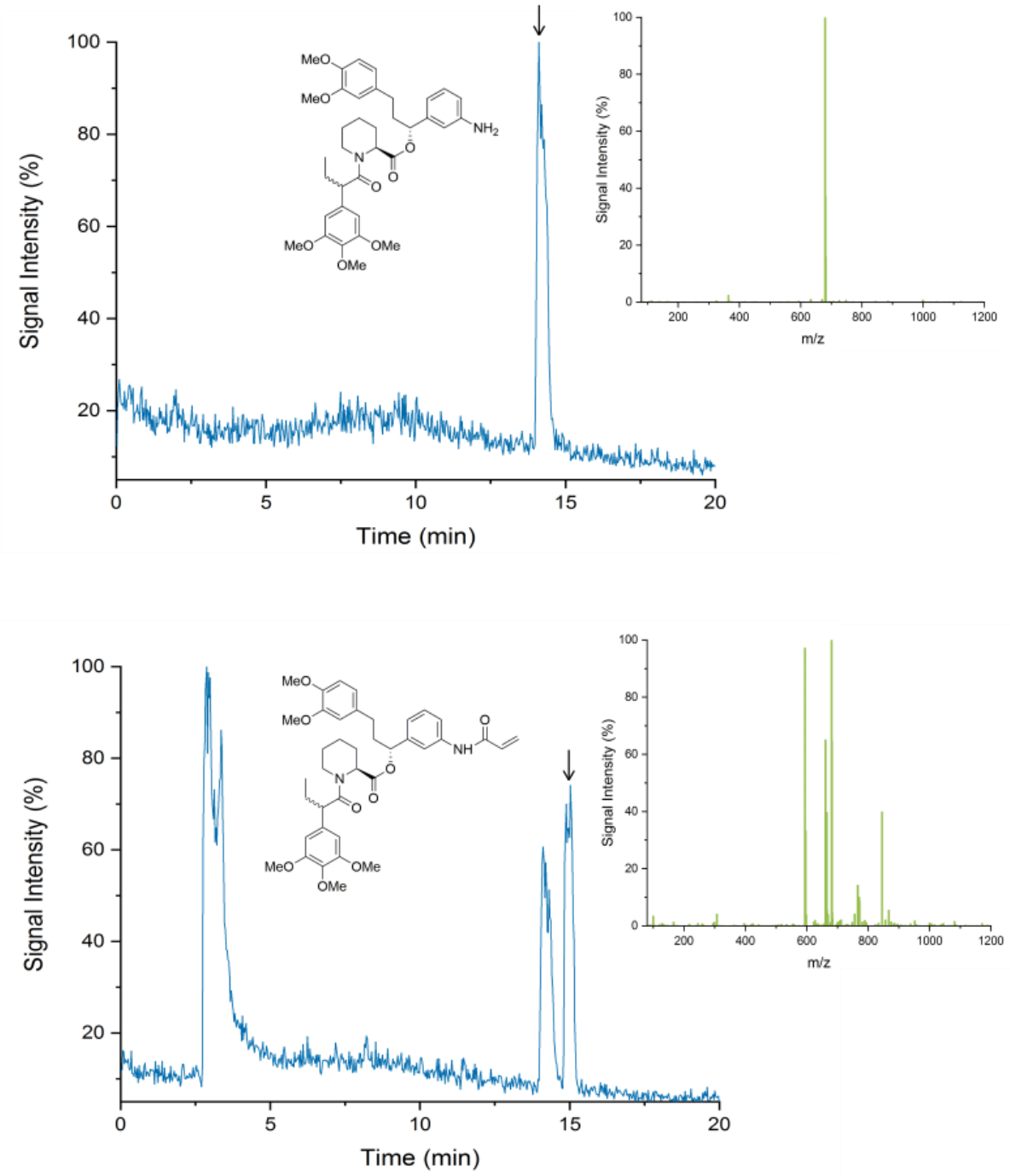

Figure 3.11: Graphs (blue) depict the signal intensity from UV-vis spectrometer attached to HPLC for the SLF' molecule before and after conjugation with an excess of NHS-ester acrylic acid. Peaks on these graphs highlighted with an arrow are accompanied by complimentary MS data (green) and the chemical structure of the molecule.

SLF' is very hydrophobic and did not appear to dissolve in any aqueous solutions or buffers. However it was very soluble in DMSO as was the NHS-ester forms of the acrylic acid and AuNP. However DMSO is not particularly biocompatible and is difficult to remove from the end product. The SLF' would precipitate if the aqueous buffer exceeded 50%. The reaction (Figure 3.11) was performed at 37°C in 40% 20mM HEPES buffer (7.4pH) and 60% DMSO for 2 hours while stirring. The crude product was investigated with high performance liquid chromatography (HPLC) mass spectrometry (MS). Fractions were automatically transferred from the HPLC to an integrated electron spray ionisation chamber to be subsequently analysed by MS. The fraction responsible for the large peak at 2.5 minutes is unreacted acrylic acid, followed by two smaller peaks at around 14 minutes. The first of these smaller peaks contains a molecule with an m/z of 633 which is in strong agreement with the molecular mass of the SLF' ligand. The other contains several mass peaks, the largest of which has an m/z of 686 which is likely to be the conjugated product of the acrylic acid and SLF' molecule.

The yield of this conjugation reaction was ≈60% even in a large excess of NHS-ester acrylic acid. This reaction was used as an analogue for the reaction between SLF' and the commercially available monovalent NHS-ester AuNP. These commercially available AuNPs can only be purchased in very small quantities. Consequently NMR and HPLC-MS were both unsuccessful in measuring whether the reaction had occurred. The NHS-ester acrylic acid was used as a proof of concept that the SLF' ligand could react and coupling could take place via this pathway. Unfortunately the cost and small scale of the monovalent NHS-ester AuNPs was prohibitive for use as a probe. It was not possible to synthesise sufficient quantities of material to adequately characterise the probe or perform experiments (particularly binding affinity experiments which required multiple concentrations in quadruplicate). Therefore the conjugation of the SLF' molecule to AuNPs was outsourced to an external company, Aurion. To protect their own intellectual property, Aurion could only give me limited information regarding their product and the procedure. The AuNPs are coated in a stabilising polymer which the SLF' molecule is conjugated to via the same aforementioned NHS-ester reaction. To ensure the AuNP does not sterically hinder the binding of SLF' with FKBP a 5nm linker between the two was included. The reactions were performed to maximise the likelihood that each AuNP was functionalised with a single SLF' molecule.

3.8 Liposome Synthesis

To test the efficacy of the FKBP-SLF' probe and interrogate the structure of SNX1 lipid tubules a reductionist *in vitro* model was utilized. These *in vitro* tubulation assays were based on the published work of van Weering (van Weering et al., 2012). Choosing to utilize tubulation assays had two main advantages, firstly using a single purified protein enables a more straightforward analysis of the structure formed by the protein. *In vivo* experiments regarding tubule structure are likely to contain a wide variety of other proteins. Secondly, it provides a robust model by which to elucidate the efficacy of the FKBP-SLF' probe. Lipid tubules highlight areas of protein density. If the probe is working correctly, these areas should also have an increased coincident presence of AuNPs.

The tubulation assays essentially had two constituent parts: liposomes and purified protein. The liposomes were made to mimic endosomes as closely as possible. The primary lipid content of the liposomes was derived from bovine brain extract to attempt to recreate a native mammalian lipid environment. These lipids were then doped with 3µg of PI(3)P for every 1mg of bovine extract. PI(3)P is a lipid found ubiquitously in early endosomal membranes which SNX1 uses to bind to lipid membranes via PX domain interaction. The lipids were premixed, aliquoted and stored in chloroform at -20°C. Thin lipid films were formed in a round bottom flask by evaporating the chloroform under a stream of nitrogen gas while continuously rotating the flask. Lipid aliquots were warmed to room temperature before forming lipid films to stop lipid aggregates forming. The thin film was then left under a stream of nitrogen for 20-30 minutes to remove any residual chloroform (a vacuum pump can also be used to achieve the same result). The lipid film was then rehydrated with buffer at 37°C in a shaking incubator, before water bath sonication to fully disperse any lipid aggregates. A freeze-thaw process was used to reduce the formation of multi-vesicular structures before being extruded through a 200nm filter. The high surface energy of the smaller liposomes was reduced by fusion events resulting in the majority of liposomal diameters to be slightly larger than the filter size ≈400nm (figure 3.12). As endosomes progress from an early stage to a later one, their size tends to increase from around 100nm and can reach in excess of 0.6µm (Shearer and Petersen, 2019). The SNX1 protein naturally senses and binds to lipid membranes within this size and curvature range. So although the diameter of these synthesised liposomes was not particularly homogenous, with respect to mimicking the size range of naturally occurring structures, the method was successful.

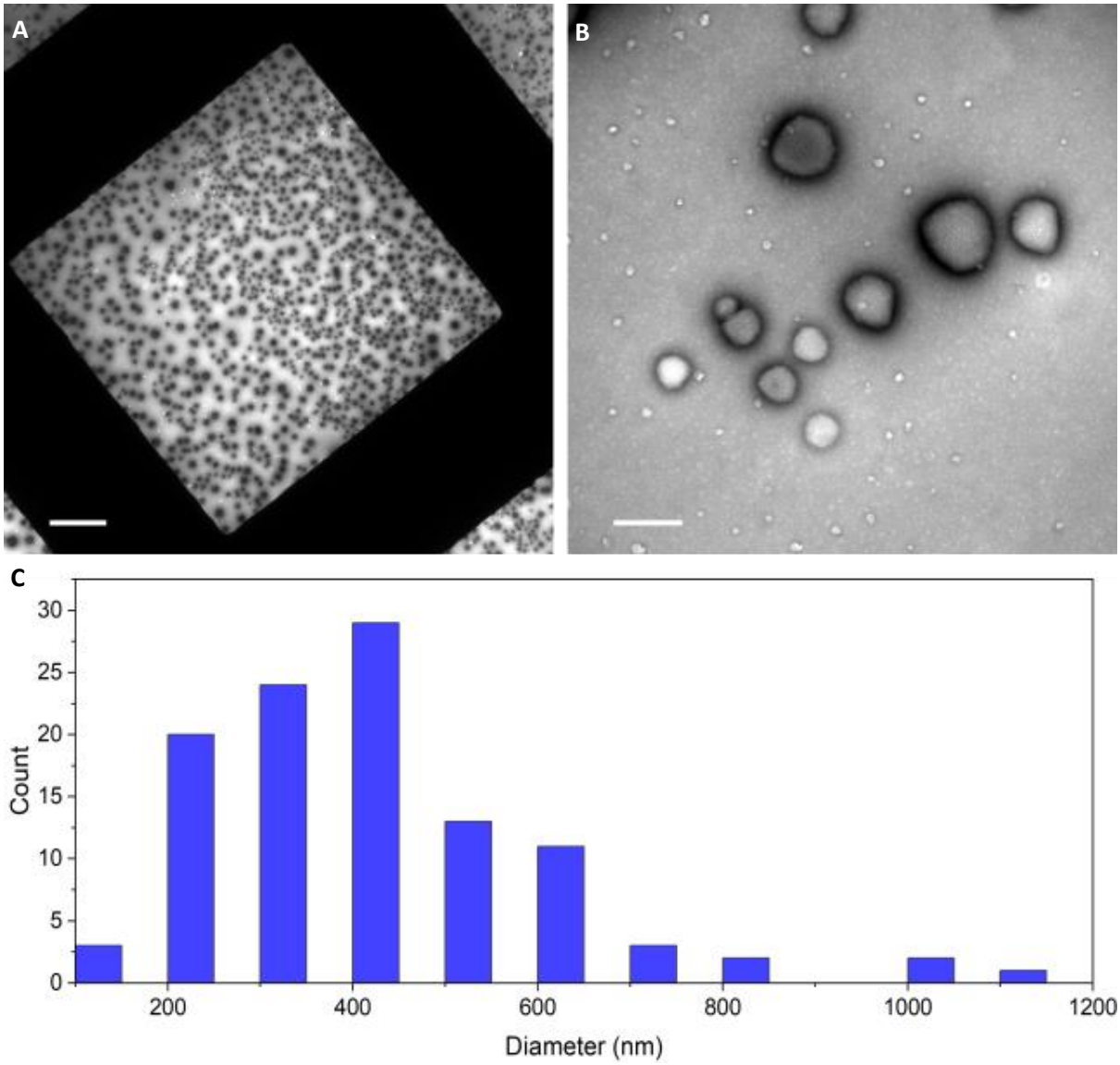

Figure 3.12: Images A and B show liposomes drop deposited onto carbon piolaform coated copper grids and negatively stained with UA. Scale bars on the images represent 10µm and 500nm respectively. Graph C is a histogram of the diameter of liposomes manufactured by this method.

Images A and B (Figure 3.12) show the liposomes drop deposited on carbon piolaform coated copper grids and UA stained for 30 seconds. This staining protocol produced clear high contrast liposomes that were readily resolved while retaining their structural integrity. However during tubulation assays the addition of the protein and a 30 minute incubation severely impacted the clarity and structure of liposomes. This negative staining protocol was therefore substituted for a UA and methylcellulose staining protocol discussed in more detail in section 4.3.

3.9 Discussion

This chapter provides the constituent parts and test bed for further testing of the FKBP-SLF' CLEM probe. Chimera proteins used as part of the CLEM probe system were shown to remain functional, the SLF' ligand was synthesised and successfully tethered to a AuNP probe. In addition liposomes were synthesised with a lipid composition which more closely mimics *in vivo* conditions, with the aim of improving upon existing *in vitro* test models which focused on highly polar lipids to increase tubulation.

ICPM of CLEM probes has provided evidence of fluorescence quenching due to the proximal relationship between fluorophore and AuNP within the label. The probes used in this study contained an AuNP of 10nm which is surface functionalised with Alexa Fluor 633. The fluorescent dye was shown to be quenched by >95% (Miles et al., 2017). Arguably the most widely used probes (Fluoronanogold) feature 1.4nm AuNPs conjugated in close proximity to a fluorescent organic dye. While the quenching effect of these smaller particles is undoubtedly less significant, this thesis does show that AuNPs as small as 2nm have a significant impact on fluorescent signal intensity (section 4.2). The probe designed in this chapter avoids the aforementioned pitfalls by attaching the AuNP portion of the label after FM. While other probe workflows permit labelling in this manner, it is hoped that the small probe size and tight reported binding (Clackson et al., 1998) will give this probe an advantage.

Potentially the addition of FKBP to a protein construct could have impinged on protein function, caused protein aggregation and/or caused the protein of interest to be trafficked incorrectly *in vivo.* For this probe to be successful the protein of interest must be part of a construct containing FKBP as well as EGFP/GFP. The cumulative mass of these two peptide additions is approximately ≈40kDa which is a significant burden. While many proteins remain functional with the addition of EGFP/GFP it was important to investigate the protein of interests function as part of a larger construct. Predicting whether another protein will remain functional under these conditions is difficult and require testing on a case by case basis. Testing of SNX1 function, binding and intracellular trafficking showed promising results and no significant deviations from native behaviour were detected. The EFS1 construct was shown to retain heterodimeric binding to other SNX-BAR (Sorting Nexin BAR) proteins *in vitro* and *in vivo*. Furthermore, laser scanning confocal microscopy revealed healthy protein trafficking, localisation and tubule formation *in vivo*. While it is not possible to say other

tagged proteins would retain function to this extent, it is encouraging that the FKBP tag did not cause significant issues.

A robust synthesis pathway for liposomes was adapted from previous work published by van Weering (van Weering et al., 2012). A freeze-thaw cycling step was added to produce more consistently sized liposomes and minimize multi-vesicular formation. The liposomes were sized using a TEM and found to primarily range between 200-600nm in diameter. Although fairly heterogeneous in diameter, they mirror the size range of endosomes SNXs would commonly interact with. The ligand SLF' was successfully synthesised and a method of AuNP conjugation investigated. When occupying the binding pocket of FKBP, the primary amine contained with the SLF' molecule remains exposed and is not directly involved in the binding process. The conjugation step utilised an electrophilic substitution reaction between the commercially available monovalent NHS 1.4nm AuNP and the primary amine of SLF'. The highest yield achieved using this reaction method was ≈60%. The reaction could have been performed in an alternative anhydrous solvent to help address this. The presence of water triggers hydrolysis of the NHS group, considering both the monovalent NHS 1.4nm AuNP and SLF' molecule were highly miscible in DMSO this may have been a more favourable solvent. However, the removal of DMSO is not trivial and likely necessitated freeze drying to remove it. Ultimately the available quantities of the monovalent NHS 1.4nm were in the nM which proved prohibitive. This method would have guaranteed probes with a stoichiometric ratio of one AuNP per SLF' molecule which could be ideal for quantitative labelling. However insufficient quantity of probes could be produced with this method for rigorous testing. Therefore, this portion of the work was outsourced to an external company (Aurion), who performed the conjugation via a similar NHS-ester based reaction.

Chapter 4

Analysis and Use of the FKBP SLF' CLEM Probe System

4.1 Introduction

This chapter, following on from chapter 3, seeks to further quantify and put into practice the FKBP-SLF' CLEM probe system. This chapter will test the efficacy of the probe in binding affinity assays and in practical labelling applications.

In the context of TEM sample preparation, embedding is the process by which material (typically biological in nature) is set in a resin to preserve the sample. This is paramount for biological structures which would likely be destroyed by the pressure differentials upon exposure to the high vacuum of the TEM. The vast majority of the time, probes function on an antibody or antibody fragment relying on the avidity to localise the probe to the target. Samples can be labelled with both fluorescent and electron dense probes at various points throughout a protocol depending on various factors. However, these can be divided into two main categories: pre-embedding and post-embedding. Pre-embedded labelling tends to favour the preservation of protein antigenicity for superior labelling efficiency over ultrastructural preservation and vice versa for post embedding protocols (Jones, 2016). Labelling pre-embedded samples with antibodies necessitates the use of cell permeabilising agents to allow antibodies access to endogenous proteins which can impinge on the ultrastructure.

Labelling cells before they are embedded allows live cell imaging to track dynamic events. Alternatively, fixed samples can be stained to rapidly screen for cells of interest which would require further investigation using electron microscopy. A protein (CHMP-2A) which was shown to have a pivotal function in the reformation of the nuclear envelope after telophase was labelled with fluoronanogold. The puncta produced by this protein were ephemeral, lasting ≈96s out of an entire 22-hour cell cycle. Very few cells would therefore have this complex present at any given time. Utilising the minimal sample preparation, straight forward identification and wider field of view afforded by FM, cells containing this rare complex could be selected and processed for TEM (Olmos et al., 2015). Another group studying membrane remodelling used live cell CLEM to achieve a similar result. Myotubularin is a 3-phosphoinositide phosphatase that dephosphorylates both PI(3)P and PI(3,5)P_2. When the cell is exposed to hypo-osmotic conditions the myotubularin localises to the cell membrane and after sufficient time forms needle-like structures. Live cell FM was performed and cells forming these structures were monitored. Samples were high pressure frozen at time points between 1.5 and 10 minutes and the previously acquired FM images subsequently informed the

location of these structures of interest (Spiegelhalter et al., 2010). Both chemically fixed and live cell CLEM can utilise FM to identify regions/cells of interest before preparing these samples for EM, streamlining the workflow and increasing TEM throughput.

Both pre-embedding procedures have a niche in the CLEM workflow but for applications requiring a very high precision, post-embedding in-resin fluorescence is preferable. Resins of a less hydrophobic composition such as Lowicryl do not require the sample to be fully dehydrated for optimal polymerisation and sample penetration. This aids in the preservation of fluid filled membrane structures within cells that harsh dehydration would ordinarily collapse or rupture. Post-embedding methods must however be cognisant of the effect of heavy metal stains on the labelling process downstream. Many post-embedding protocols avoid the use of OsO_4 as a fixative and contrast agent. Firstly, OsO_4 has been shown to have a significant deleterious impact on protein antigenicity abolishing antibody labelling. Additionally, avoiding OsO_4 while preserving samples with water content of 5% maintains fluorophore activity in the resin. Dependence on water for fluorescent emission in these conditions was elegantly demonstrated by Peddie et al. HeLa cells expressing a GFP construct were high pressure frozen and freeze substituted into Lowicryl HM20 resin. At high vacuum all fluorescent signal was abolished. Upon reintroduction of water vapour into the SEM chamber, fluorescence remerged as pressure approached one atmosphere (70% relative humidity) (Peddie et al., 2017).

In-resin fluorescence enables EM sections to be imaged by FM. The physical thickness of the sections surpasses the optical sectioning capabilities of even high-end confocal microscopes. Furthermore, visualising the fluorescence in sections leaves very little uncertainty regarding the exact location of the fluorescent object within a volume. Methods performing FM prior to sectioning also have increased uncertainty from the dehydration process during the EM preparation which results in warping/shrinkage. Furthermore, when sectioning the position of the sample in the microtome chuck will very likely be slightly of axis which will subtly alter the depth of the fluorophore within the cellular volume. Although in-resin fluorescence does reduce uncertainty between the position of an object observed in FM and EM, the electron beam incident upon the sample can cause warping. 50% and 80% of structures observed in the FM were shown to shift when observed in the TEM by 40nm and 80nm respectively (Kukulski et al., 2011).

In-resin fluorescence uses FM to identify individual sections containing areas of interest as opposed to pre-embedding workflows where multiple sections need to be screened in the EM before the correct section is found. This aids in the rapid identification of rare events/structures which would take orders of magnitude longer to locate by TEM alone. This technique has enabled high numbers of GFP labelled HIV particles binding to cell membranes of MDCK cells and yeast fission sites to be located with FM and subsequently imaged with TEM (Kukulski et al., 2011). This methodology can also be scaled up to whole organisms which streamlines the identification of sites of interest in a more profound manner than for cells. Whole zebrafish embryos expressing a GFP construct can be viewed in real time, high pressure frozen, sectioned, imaged with FM and further points of interest interrogated in higher detail with EM. The method used to preserve the zebrafish embryos also enables immunolabelling, maximising the amount of information obtainable from a single sample (Nixon et al., 2009).

4.1.1 Objectives

The components of the FKBP SLF' probe system assembled in chapter 3 will be tested as a CLEM probe. The FKBP protein will be expressed as part of a chimera protein with EGFP and act as a targeting site for the binding of the SLF' ligand. The SLF' ligand will be functionalised with an AuNP. The SLF' AuNP conjugate will attach to the chimera protein via FKBP SLF' binding, and localise an electron dense label to it. Therefore, the first objective will be to measure the binding affinity/dissociation constant of the FKBP-SLF' pair and ascertain whether it is as high as the literature reports (94pM) (Clackson et al., 1998). In theory, a higher binding affinity/ lower dissociation constant should translate into a higher labelling efficiency. I will also investigate if the size of the AuNP conjugated to the SLF' impacts the binding affinity.

Subsequently the efficacy of the probes will be assessed *in vitro.* Liposomes tubulated with the construct EFS1 will be tested for labelling efficiency with the ultimate goal of investigating the putative SNX1 helical arrays that support lipid tubules. Quantitative measure of labelling efficiency will be acquired by measuring the distances between gold labels and the lipid membranes in samples with and without the EFS1 protein present.

Finally the FKBP-SLF' CLEM probe will be used in *in vivo* CLEM experiments. As discussed above the two main methods of sample preparation for TEM are: pre-embedding and post embedding. A method that is representative of a "standard protocol" will be used for each one. Firstly, chemically fixed, permeabilised cells expressing an FKBP construct will be labelled with SLF' conjugated AuNP and embedded in epon. The post embedding method will use high pressure freezing, freeze substitution into Lowicryl HM20, sectioning followed by SLF' conjugated AuNP labelling. If this probe is to be widely adopted it must be effective in these ubiquitous protocols.

4.2 Binding Affinity of FKBP and SLF'

The crux of the FKBP-SLF' CLEM probe is how effectively the SLF' can co-localise its conjugated AuNP to the FKBP protein target. Without this, the probe will not function as an effective label for interrogation with TEM. In turn the binding affinity of the system is the primary attribute which determines this efficacy. Binding affinity is defined as the binding strength between a single biomolecule, in this case the FKBP protein, and its complimentary ligand – SLF'.

Isothermal titration calorimetry (ITC) is an effective method to measure the binding affinity of various systems. Most commonly used to probe/test the binding of small molecules/ligands to larger macromolecules such as DNA or protein. Two cells, the first containing the large macromolecule suspended in buffer and the second containing only buffer are enclosed within adiabatic jackets. A solution containing the ligand at a known concentration is titrated in equal volumes into both cells. Binding events have an enthalpic component which can be measured as a difference in temperature between the two cells. Temperature is not measured directly, but rather the power output by the heater to maintain a constant temperature is recorded. After performing the experiment several times using different concentrations of ligand a binding curve can be fitted and the binding affinity calculated. However, this technique has an upper limit, binding partners in excess of µM dissociation constants cannot be accurately measured with this technique. Protein concentrations between 10-1000µM are optimal for the detection of temperature changes, but in order to measure tighter binding pairs, lower concentrations are required (Duff et al., 2011). The reported dissociation constant of FKBP-SLF' is 94pM, far beyond the range measurably with ITC.

Tryptophan is one of three aromatic amino acids. All three of these amino acids are capable of fluorescing but phenylalanine has a very low quantum yield and while tyrosines quantum yield is the highest of the three it is readily quenched (Möller and Denicola, 2002). Tryptophan can be excited at around 295nm. Other residues do not absorb strongly at this wavelength. Subsequent de-excitation gives a peak emission at ≈355nm. However, the peak emission is dependent on the polarity of the local environment surrounding the tryptophan residue. A number of factors including: ligand/partner interactions, protein conformation changes, self-association or protein denaturation can all impact on peak emission. Typically, as the environment directly adjacent to the tryptophan residue increases in hydrophobicity, the corresponding emission will blue shift and decrease in intensity (Yammine et al., 2019).

Since a tryptophan residue is located within the binding pocket of the FKBP protein, it may be possible to utilise it to measure binding affinity. Before SLF' binds to the FKBP, the binding pocket will be occupied by polar molecules provided by the buffer solution. Upon binding of the SLF' ligand the polar molecules/water will be ejected. This ejection coupled with the binding pocket now being occupied by a relatively hydrophobic molecule would likely shift the emission and the calculated binding affinity. This method may have been successful but an alternative method was used. The binding pocket of FKBP is not entirely filled by the SLF' ligand. As a result, polar molecules still present in the binding pocket may have weakened this interaction and the fluorescent shift may have been too weak to elucidate a binding constant.

Fluorescence anisotropy is a very sensitive method capable of measuring high binding affinities which is ideal in the case of FKBP-SLF'. The method revolves around fluorophores not absorbing and emitting light uniformly but rather having an axis about which light is preferentially absorbed and emitted. Fluorophores free in solution will experience Brownian motion as a result of collisions from other molecules in the solution. This motion is defined by:

$$\Phi_r = \frac{nV}{k_B T}$$

Where Φ_r is the rotational time, n is viscosity, V is volume of the particle/molecule, k_B is Boltzmann constant and T is the temperature. Keeping viscosity and temperature constant the volume of a molecule/particle can be inferred by its average rotational time. When fluorophores are illuminated with unidirectional polarised light, only a subset of fluorophores whose fluorescent dipole is

orientated in a narrow range of angles will become excited. If the fluorophores are all stationary, these fluorophores will all re-emit along this same narrow range of angles. When free in solution the molecules are free to tumble. How quickly the molecule is tumbling as a result of Brownian motion will correlate with the time it takes for the emitted fluorescent light to become decorrelated (light is no longer predominantly emitted around the narrow axis of excitation). When a binding event takes place the volume of the molecule/particle will increase with a corresponding reduction in the average rotational time. The fluorescence decorrelation time will increase which is measured and used to calculate the binding affinity.

Fluorescence anisotropy is therefore only effective when the volume of the molecule/particle changes significantly as a result of a binding event. The entity containing the fluorophore should be as small as possible in comparison to its binding partner for an optimal signal. For the CLEM probe system tested in this thesis, the protein containing the fluorophore (EGFP), EFS1 was several orders of magnitude larger than the ligand (SLF'). Therefore, a significant change in rotational time was not observed and a different approach was sort.

Fluorescence/Förster resonance energy transfer (FRET) is a technique commonly used to investigate binding constants and colocalisation of two fluorescent molecules. A pair of fluorophores capable of exhibiting this phenomenon are known collectively as a FRET pair. The emission spectra of the first fluorophore overlaps with the excitation of the second and through non-radiative dipole-dipole coupling energy is transferred from the first to the other (the excitatory wavelength however must not excite the second fluorophore). The strength of this dipole-dipole coupling interaction is inversely proportional to the sixth power of the distance. Therefore, this energy transfer can only occur significantly over very short distances. If the second fluorophore is emitting, the two fluorescent entities must therefore be within very close proximity to one another.

Instead of secondary fluorophore detection, I opted to measure the quenching of the first fluorophore as a function of its proximity to an AuNP. Using the same mechanism detailed above, when a fluorophore comes into very close proximity with an AuNP energy can be transfer to the AuNP where it is radiated away as heat. In addition to FRET, AuNPs exploit another phenomenon known as nanometal surface energy transfer (NSET) to transfer energy. LSPR of an AuNP can be thought of as the collective sympathetic oscillation of many coupled electrons over the surface.

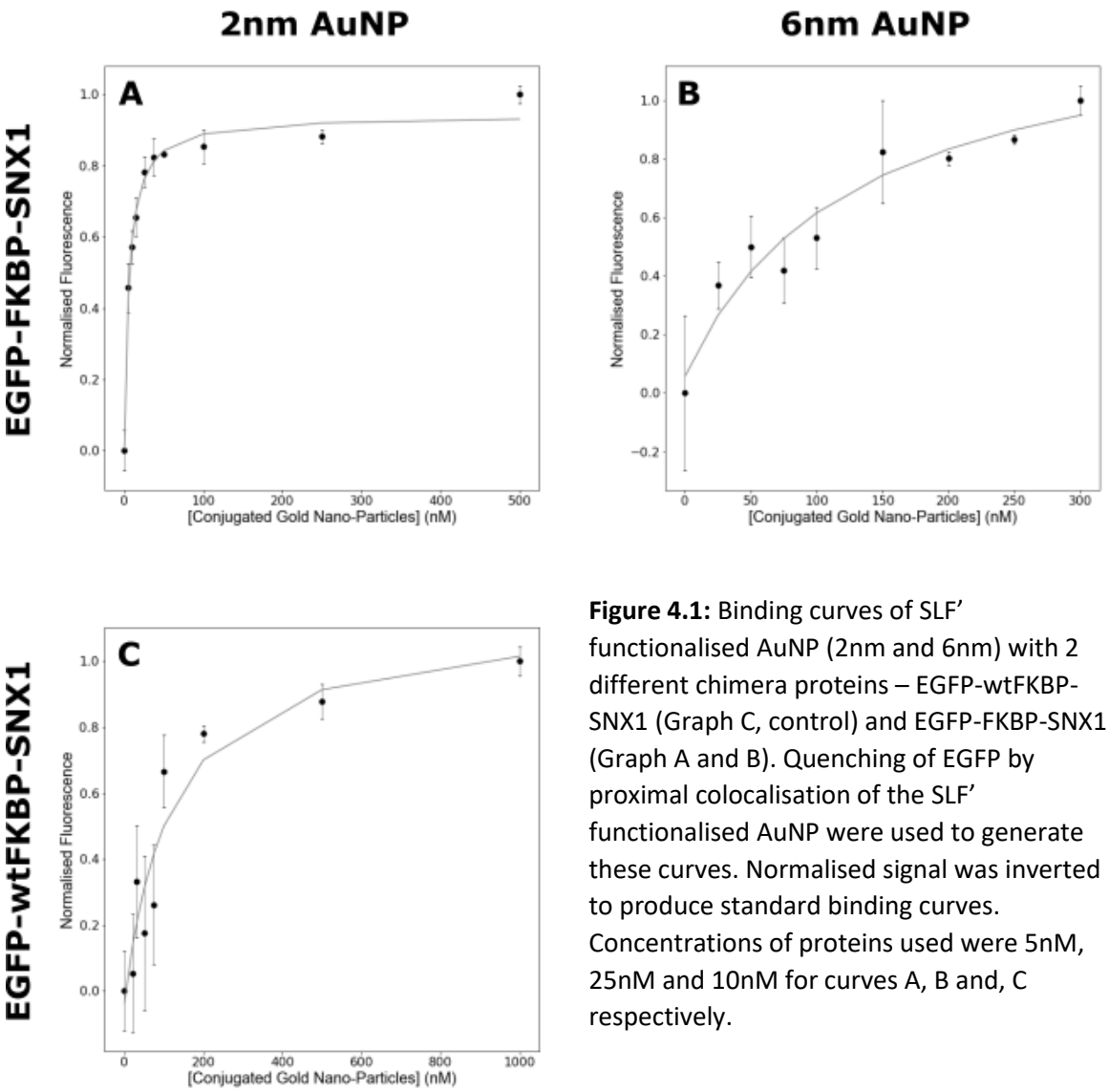

Figure 4.1: Binding curves of SLF' functionalised AuNP (2nm and 6nm) with 2 different chimera proteins – EGFP-wtFKBP-SNX1 (Graph C, control) and EGFP-FKBP-SNX1 (Graph A and B). Quenching of EGFP by proximal colocalisation of the SLF' functionalised AuNP were used to generate these curves. Normalised signal was inverted to produce standard binding curves. Concentrations of proteins used were 5nM, 25nM and 10nM for curves A, B and, C respectively.

Therefore it is useful to conceive NSET as the interaction between a fluorophore (dipole-emitter) with an array of coupled dipoles (Breshike et al., 2013). Furthermore the interaction remains significant over a larger range than FRET (≈15nm), decaying with the inverse of the fourth power as a function of distance.

Binding curves (Figure 4.1) were generated from 8 data points and a control containing only protein and buffer. Each data point represents the average of a quadruplicate measurement and the error bars are two standard deviations of the mean. The dissociation constant is calculated by:

$$K_d = \frac{[SLF'][P]}{[SLF' \cdot P]}$$

Where [P] denotes the concentration of protein, [SLF'] the concentration of SLF' and [SLF' · P] the concentration of the protein ligand complex. The K_d is the concentration of ligand required for the maximum binding capacity (Bmax) of the protein to be 50%. The dissociation constant between 6nm AuNP functionalised with SLF' was calculated to be 127.7nM. However, there was not enough material (6nm AuNP functionalised SLF') to generate data points that fully saturated the protein with ligand. Therefore, to calculate this value the curve was extrapolated and is therefore the dissociation constant is not completely reliable.

The binding curves A and C (figure 4.1) were adequately saturated and show the binding of 2nm AuNP functionalised with SLF' with two proteins EGFP-FKBP-SNX1 and EGFP-wtFKBP-SNX1 (EwtFS1). EwtFS1 contains a point mutation on a prominent residue within the binding pocket of the protein (V36F). With this mutation it is returned to the wild type protein and should have a significantly reduced affinity for the SLF' ligand. A second chimera control protein consisting of EGFP-SNX1 would have been ideal, however difficulty cloning this protein prohibited its inclusion and EwtFS1 was used as the only control. The dissociation constants of 2nm AuNP functionalised with SLF' were calculated to be 5.81nM and 119nM for EGFP-FKBP-SNX1 (EFS1) and EwtFS1 respectively.

4.3 Tubulation Assays and Labelling with FKBP-SLF' Probe

Having demonstrated that SLF' conjugated to a 2nm AuNP retains a dissociation constant of 5.8nM for the FKBP protein, we interpreted this result as a strong binding. The next step was to demonstrate the probe binding process in an *in vitro* model before moving onto *in vivo* systems. The probe was used investigate the structure of SNX1 mediated lipid tubulation *in vitro.* Firstly, acquiring conditions that would produce consistent results and image clarity was imperative. Optimal protein and lipid concentrations were adapted from previous work undertaken by van Weering (van Weering et al., 2012). However, protein concentration used for my own assays were slightly lowered which reduced debris and aggregates on the TEM grids. This previous work used UA negative stain which was abandoned as a method of sample preparation for these studies. UA negative stain is a very robust and straight forward method that produces high contrast with very little time investment. While pure liposomes negatively stained with UA displayed in Images A and B (Figure 4.2) appear clean, upon the addition of protein the negative stain seemed to introduce a very high electron dense background. Images A and B (figure 4.2) were negatively stained with UA and the

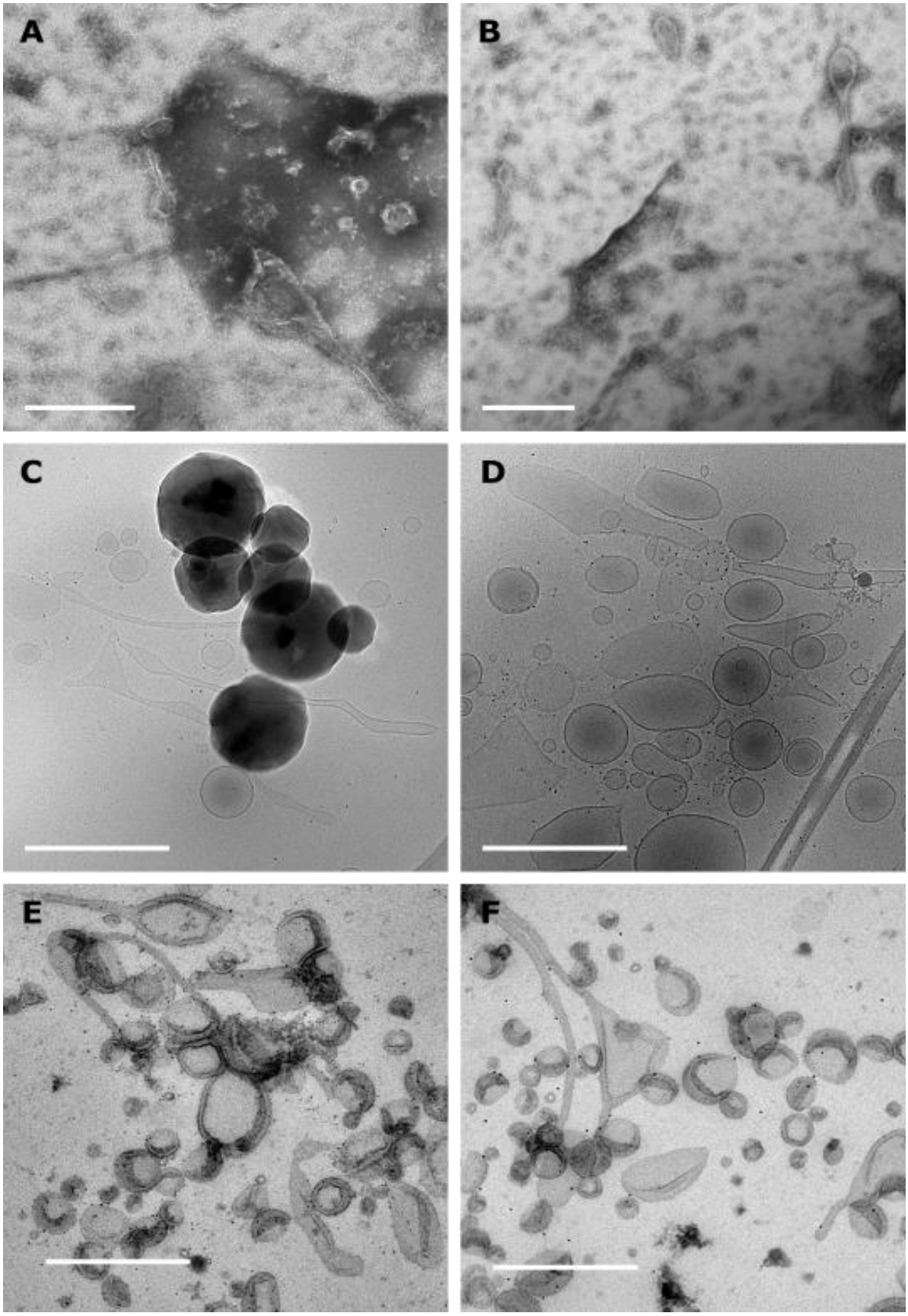

Figure 4.2: Tubulation assays carried out using three different sample preparation methods. Images A and B were performed with a UA negative stain. Images C and D were plunge frozen with no heavy metal staining. Note the dark particles on top of lipid vesicles in image C identified as ice contamination. Images E and F were negatively stained with 0.3% UA in methylcellulose solution.

SNX1 tubules appear jagged and less well defined. This high background/noise did also appear in the aforementioned published work, however in this instance the excessive debris made accurate identification of small AuNP labels significantly more challenging.

To reduce background, two other sample preparation methods were investigated: plunge frozen cryo-EM and UA negative staining with methylcellulose. Plunge freezing a liquid sample in this manner preserves it in a native form in vitreous ice. An incident electron beam will be negligibly scattered by the vitreous ice and significantly more by any other material (including crystalline ice). Therefore, it is not necessary to use any heavy metal stains, minimising artefacts and noise. However, contamination of crystalline ice rendered large portions of the grids unusable and also occlude important areas of the sample (figure 4.2 image C). This technique produced non-spherical liposomes that appeared to have protrusions sometimes similar in nature to a tubule but with a much-increased diameter (figure 4.2 image D). During plunge freezing, excess liquid is removed by blotting to produce a film of liquid suspended over the holey carbon film to ensure the formation of a thin layer of vitreous ice. This process likely imparts a shearing force on the sample. Potentially this force may expand and deform lipid tubules before freezing which produces these structures. This process also has a similar effect to diluting the sample in comparison to a drop deposition technique as excess liquid is blotted away. Therefore, lipid tubules and accompanying AuNP labels were significantly less frequent in cryo-EM. The longer sample preparation time, imaging time and less frequent areas of interest became too prohibitive to use for these samples.

UA negative staining with methylcellulose was the sample preparation method that produced the best results for these *in vitro* assays. This type of negative stain still uses UA but is used one part in nine parts methylcellulose solution (0.3% UA and 2.7% methylcellulose w/v). This produced much cleaner samples than standard negative stain with the added benefit of the methylcellulose stabilising the lipid structures. Samples produced were of a consistent quality and identification of AuNPs in these samples was straightforward due to the low background electron density.

To elucidate whether SLF' functionalised AuNPs would localise to lipid membranes in the presence of EFS1 protein, freshly made liposomes were incubated with SLF'-AuNPs in the presence and absence of purified EFS1 protein. Comparison of images A + B and C + D (Figure 4.3) qualitatively show an increase in AuNP colocalisation with lipid membranes. AuNP labels appear evenly distributed

throughout images A and C whereas B and D appear almost exclusively on or directly adjacent to lipid membranes.

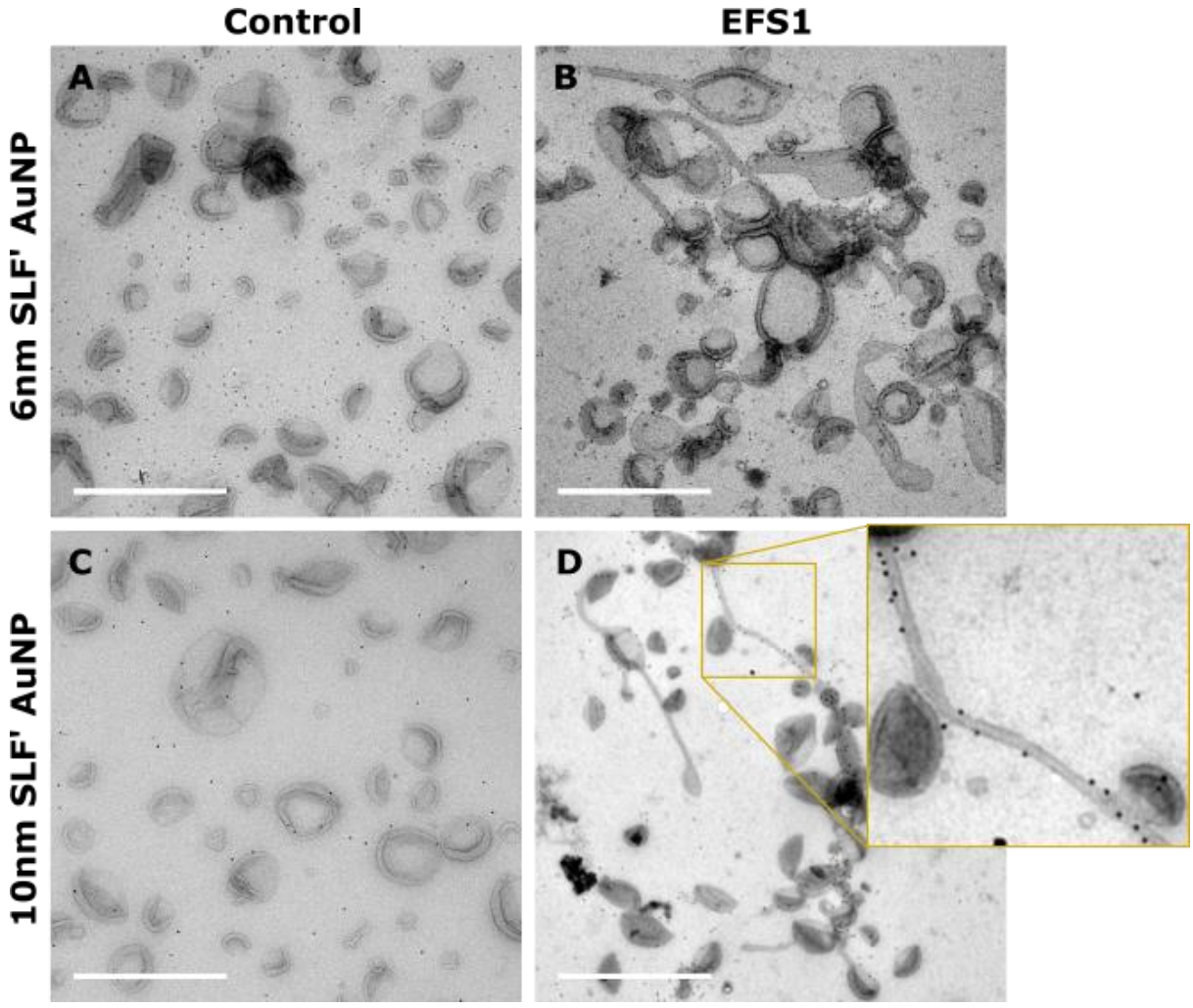

Figure 4.3: Liposomes incubated with two sizes of AuNP 6nm (Images A and B) and 10nm (Images C and D) functionalised with SLF' in the presence and absence of EFS1 protein. Scale bars represent 500nm.

To acquire a quantitative measure of colocalisation between AuNP and lipid membranes many images for each condition were acquired. Representative examples of these images are displayed in Figure 4.3. Each image was then split into quadrants and a random number generator used to select both the image and quadrant to be analysed to eliminate bias. All AuNPs in each randomly selected quadrant would be measured and recorded. Quadrants containing large liposome aggregates were discounted as large numbers of AuNPs co-aggregated or became entangled giving false positives. This was done several times until approximately 100 distances between AuNPs and their nearest lipid membrane were measured for each condition. Liposomes incubated with SLF' functionalised

6nm and 10nm AuNP display an above average propensity for membrane binding likely due to favourable electrostatic interactions with polar lipids (figure 4.3). However in comparison to the two data sets containing protein, a significant increase in lipid membrane localisation of AuNP is observed.

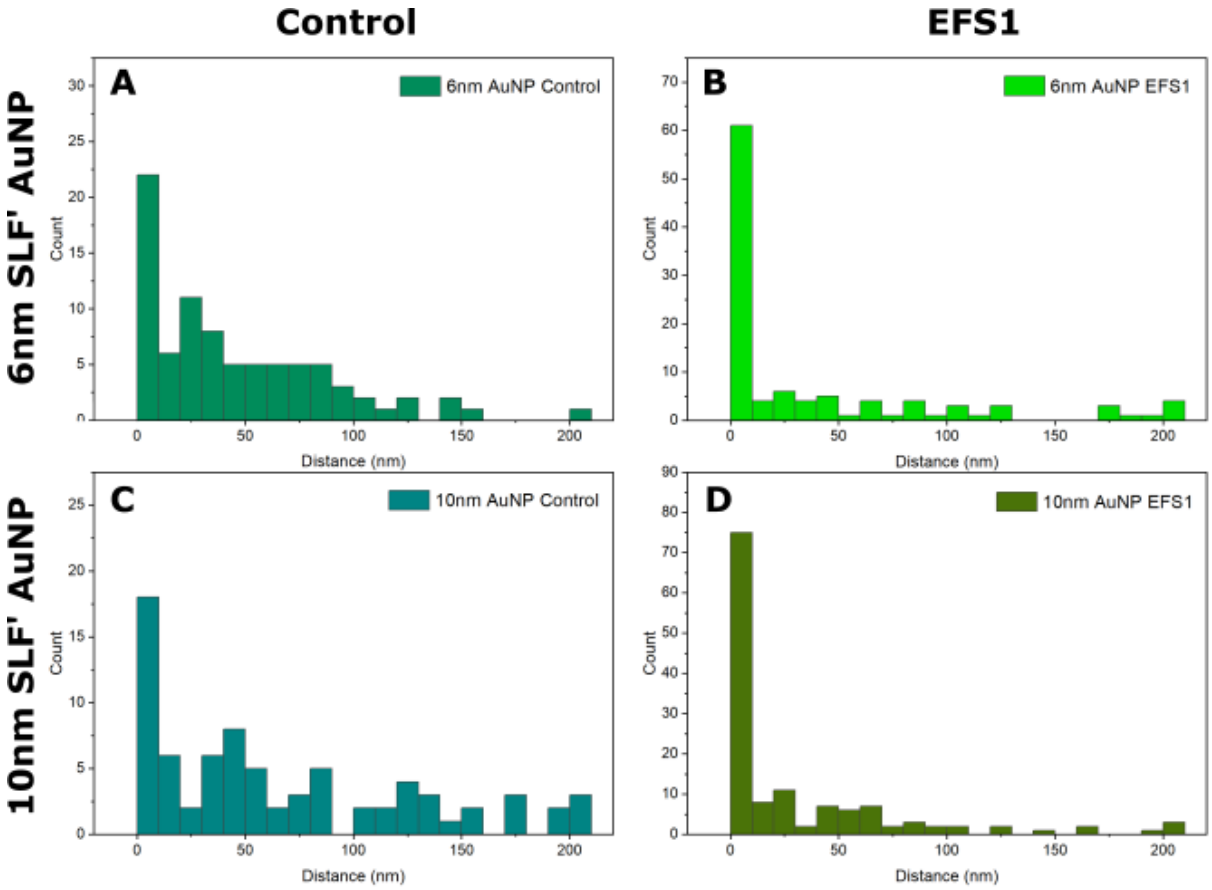

Figure 4.4: Histograms showing the recorded distance between AuNPs functionalised with SLF' and lipid membranes in the presence and absence of EFS1 protein.

The presence of the EFS1 protein decreases the average distance between lipid membranes and AuNPs. Furthermore, if one takes into account the linker length between the AuNP and the SLF' (5nm) and the size of SNX1 (≈3nm monomer, ≈6nm dimer), any AuNP a distance of ≤10nm from a lipid membrane could be considered bound. Assuming this is the case, 57% of 6nm AuNPs are bound to the lipid membrane in the presence of EFS1 compared to the control of 26%. Similarly, when incubated with a protein 56% of 10nm AuNP localise to lipid membranes compared to 23% for the control (Figure 4.4). There is a significant increase in lipid membrane labelling with AuNP functionalised SLF' in the presence of EFS1. However, the background of around 25% is very high. If observations regarding the putative helical arrays formed by SNX1 encasing the lipid tubules are to be interrogated a higher labelling density of AuNPs would be required. Both images B and D show

tubules labelled with AuNPs. The magnified tubule from image D is an example of one of the most densely labelled achieved with this probe.

4.4 *In vivo* CLEM using FKBP-SLF' Probe

4.4.1 Pre-embedded Labelling CLEM using FKBP-SLF' Probe

Labelling fixed and permeabilised cells with immuno-nanogold or fluoronanogold is a ubiquitous method to label proteins of interest with electron density and/or fluorescence. Cells may be fixed a second time with a stronger fixative such as glutaraldehyde before being stained with heavy metals and embedded in a hydrophobic resin. The protocol used here tried to resemble a typical antibody labelling experiment as closely as possible. Concentrations of SLF' conjugated AuNP used were the same as the manufacturers recommended concentration of fluoronanogold to potentially be able compare labelling efficacy.

HeLa cells were seeded in MatTek etched dishes and transfected with an EFS1 and an ES1 (EGFP-SNX1) construct and incubated for 48 hours to allow EGFP expression levels to be readily detectable with FM. Cells were lightly fixed with 4% PFA and imaged with a laser scanning confocal microscope. The cells were subsequently permeabilised and blocked with BSA to reduce non-specific binding before incubating the sample with SLF' conjugated to 2nm AuNP. Samples were fixed again with 2% GA and incubated in silver enhancement solution to increase the visibility of the relatively small 2nm AuNP labels. Samples were then stained with OsO_4 and UA before embedding in epon resin. The epon blocks were trimmed to a small area containing the cell of interest identified previously with FM. Samples were then sectioned and imaged using a Tecnai 12 120kV Bio Twin TEM.

FM images displayed a spread of transfection efficiencies with some cells over-expressing the construct through to cells without any detectable fluorescence. The cells chosen for correlative imaging appeared to display fluorescently labelled punctae typical of SNX1 distribution throughout the cell. Cells with high fluorescent intensity were favoured to aid correlation. As a result these cells contained abnormalities where large "bubbles" in the cytoplasm were visible. These structures

appeared to be a result of protein over-expression and although non-native, did provide strong points of reference to align FM and EM images.

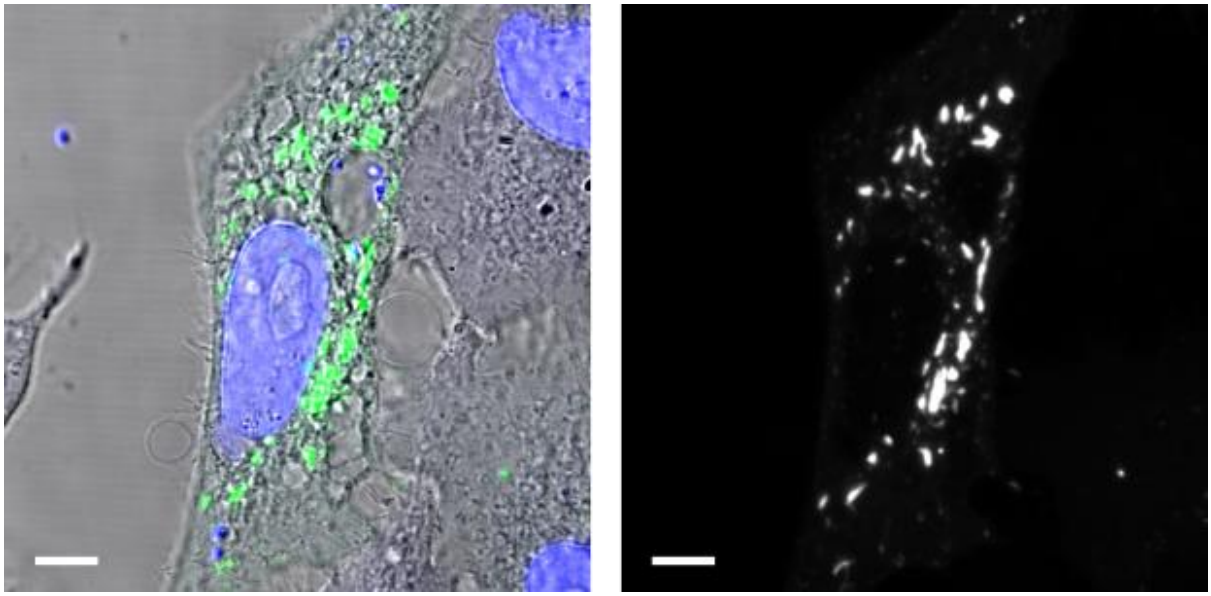

Figure 4.5: HeLa cells transfected with the EFS1 construct and imaged with a laser scanning confocal microscope. The image on the left is a maximum intensity projection of both the EGFP (green) and Hoechst (blue) overlaid with the bright field image. The image on the right is a maximum intensity projection of the EGFP channel in greyscale. Scale bars represent 2µm.

When analysing the TEM images very few AuNPs were visible. Occasionally individual electron dense particles were visible in the sample but almost always removed from any structures previously labelled with EGFP in the FM. Figure 4.5 displays examples of this lack of localisation. Image B shows a large collection of well-defined electron dense particles in the nucleolus. There is no accompanying fluorescent signal in the nucleolus so we would not expect to find an AuNP labels at this location. Likewise, images C and D highlight two areas containing intense fluorescence when investigated by FM. Assuming the SLF' is binding to the FKBP protein within the EFS1 construct one would expect concomitant AuNP labelling in these fluorescent regions. No AuNP labels appeared to correlate with the fluorescent signals in the cells which were analysed. The silver enhancement process or the cell permeabilisation also appears to have had a detrimental impact on the ultrastructural details. It is therefore also not clear if these fluorescent regions correlate with structures one would expect SNX1 to be involved with.

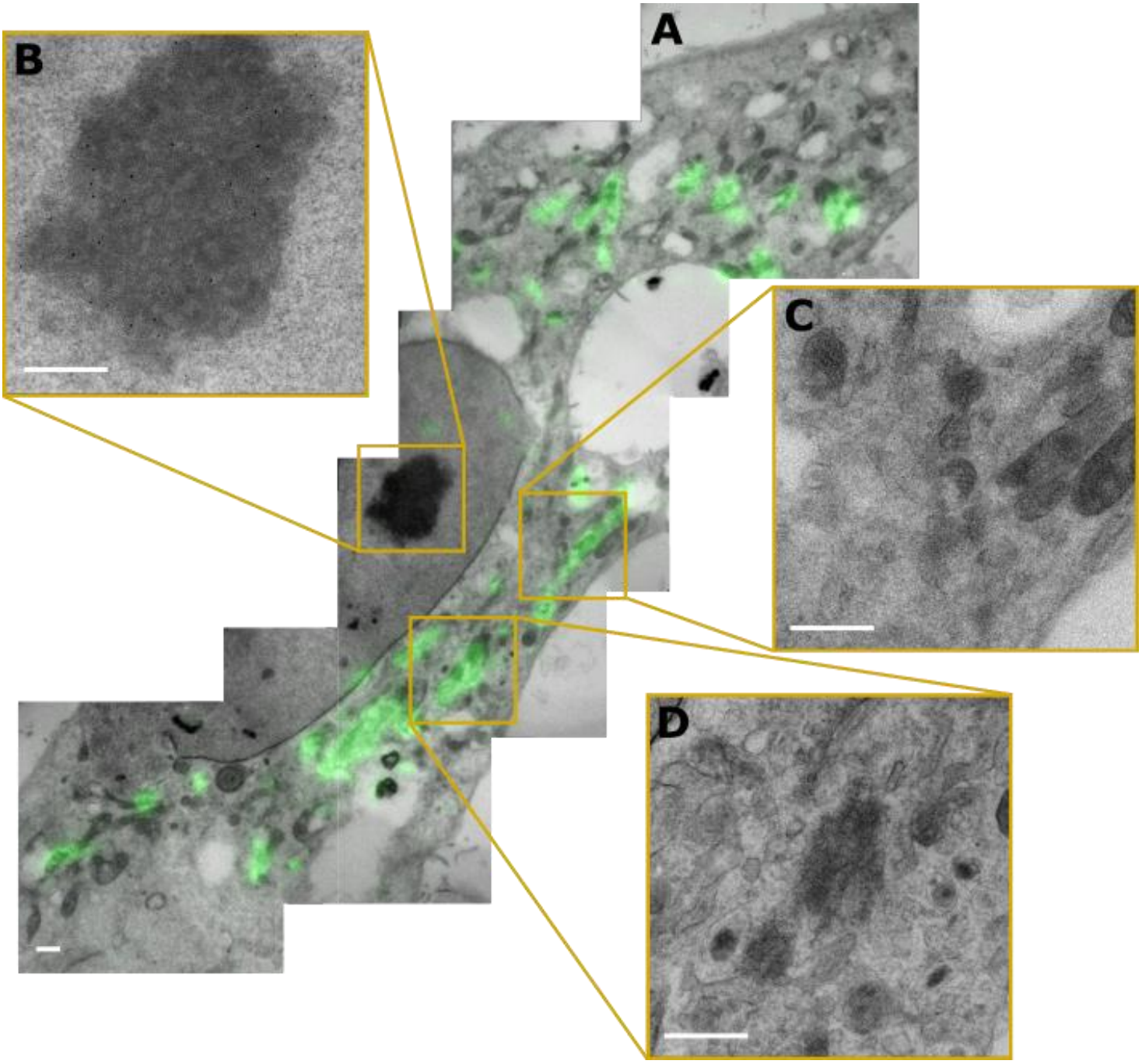

Figure 4.6: HeLa cells transfected with EFS1, labelled with SLF' conjugated to 2nm AuNPs and silver enhanced. Image A is a series of TEM images stitched together overlaid with the previously acquired fluorescent signal. Images B, C and D were taken at higher magnifications and highlight important areas. All scales bars represent 2µm apart from image A where it is 10µm.

4.4.2 Post Embedded Labelling CLEM using FKBP-SLF' Probe

Another very common preparatory technique for TEM samples involves some form of fast freezing, producing vitreous (or near vitreous) ice, before replacing the ice with a polymer resin by means of freeze substitution. This technique favours both ultrastructural preservation and the preservation of the sample's antigenicity. It is possible to retain fluorophore activity within the polymerised resin. Considering individual sections can be imaged with both FM and TEM the degree of certainty with regard to correlating signals is far higher than pre-embedded labelling techniques.

HeLa cells were transfected with both EFS1 and ES1 constructs and incubated for 48 hours to ensure adequate protein expression levels. Cells were then pelleted and high pressure frozen using the EM PACT2. Samples were freeze substituted into a Lowicryl HM20 resin and stained with 0.1% UA. UA is a fixative and damages protein function at high concentrations. Using sufficiently low concentrations can mitigate protein damage and retain fluorophore activity (Kukulski et al. 2011) (Johnson et al., 2015). Lowicryl HM20 blocks were sectioned at a thickness of 150nm and imaged on a wide field fluorescent microscope but initially no fluorescence could be detected. To combat this, thicker sections were created (300nm) which produced a more intense fluorescence. Sections were floated on a solution of SLF' functionalised with 2nm AuNPs followed by a wash before floating on silver enhancement solution. These sections were washed, dried and transferred to the TEM. Acquired FM and TEM images were then overlaid using ecCLEM (Paul-Gilloteauxet al., 2017).

As before with the pre-embedded labelling, no colocalisation of fluorescent signal with AuNPs was detected in either the control or the FKBP containing construct EFS1. Figure4.6 shows the in-resin fluorescent signal of a cell transfected with the control ES1 construct taken through the entire post embedded labelling CLEM workflow. Image B is a high-resolution micrograph overlaid with the in-resin fluorescent signal. Two regions of this cell are then investigated at higher magnifications in images C and D (Figure 4.7). These regions produce an intense fluorescence which corresponds with high concentration of the ES1. In this case the construct does not contain the FKBP protein and therefore we would not expect to see any AuNP labelling in the TEM in these regions. Neither image C or D (Figure 4.7) contain any electron dense punctae which could be considered AuNPs which suggests that at the very least the labelling is not non-specific

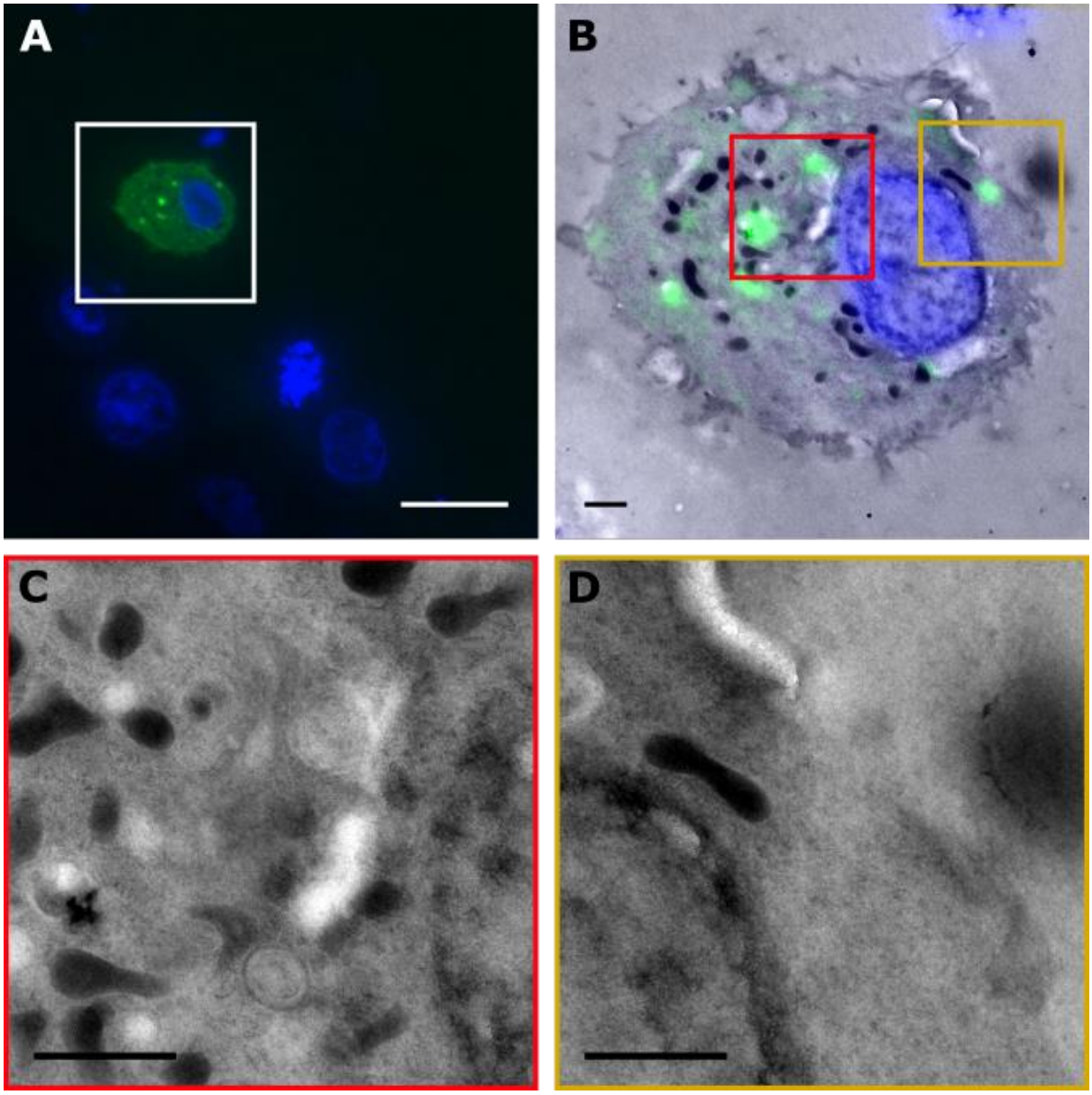

Figure 4.7: HeLa cells transfected with a control ES1 construct, labelled with SLF' conjugated 2nm AuNPs and silver enhanced. Image A is in-resin fluorescence of a 300nm lowicryl section captured on a wide field fluorescent microscope. Image B is an electron micrograph with overlaid fluorescent signal. Images C and D are higher magnification of the two highlighted areas in image B. All scale bars represent 1µm apart from image A were the scale bar is 10µm.

Images obtained from cells endogenously expressing EFS1 and labelled post embedding with SLF' 2nm AuNP appeared similar to the control. Image A (Figure 4.8) shows a very low magnification electron micrograph overlaid with the in-resin fluorescence. The image clearly shows that the section has been ripped and narrowly missed the cell. Image B is a high-resolution electron micrograph with corresponding fluorescence overlaid. Image C is a region containing a very bright fluorescent signal which was further investigated at higher magnification. The FKBP binding protein

is present in this fluorescent protein construct and as such one would expect to see concomitant AuNP labelling in the electron micrograph. However no electron dense punctae which could be considered AuNP labels are visible in this region. Image D is a region containing no significant fluorescent signal but the electron micrograph shows a fairly large aggregate of electron dense particles. SNX1 is not known to interact with the cell membrane directly and so it is likely this interaction is non-specific.

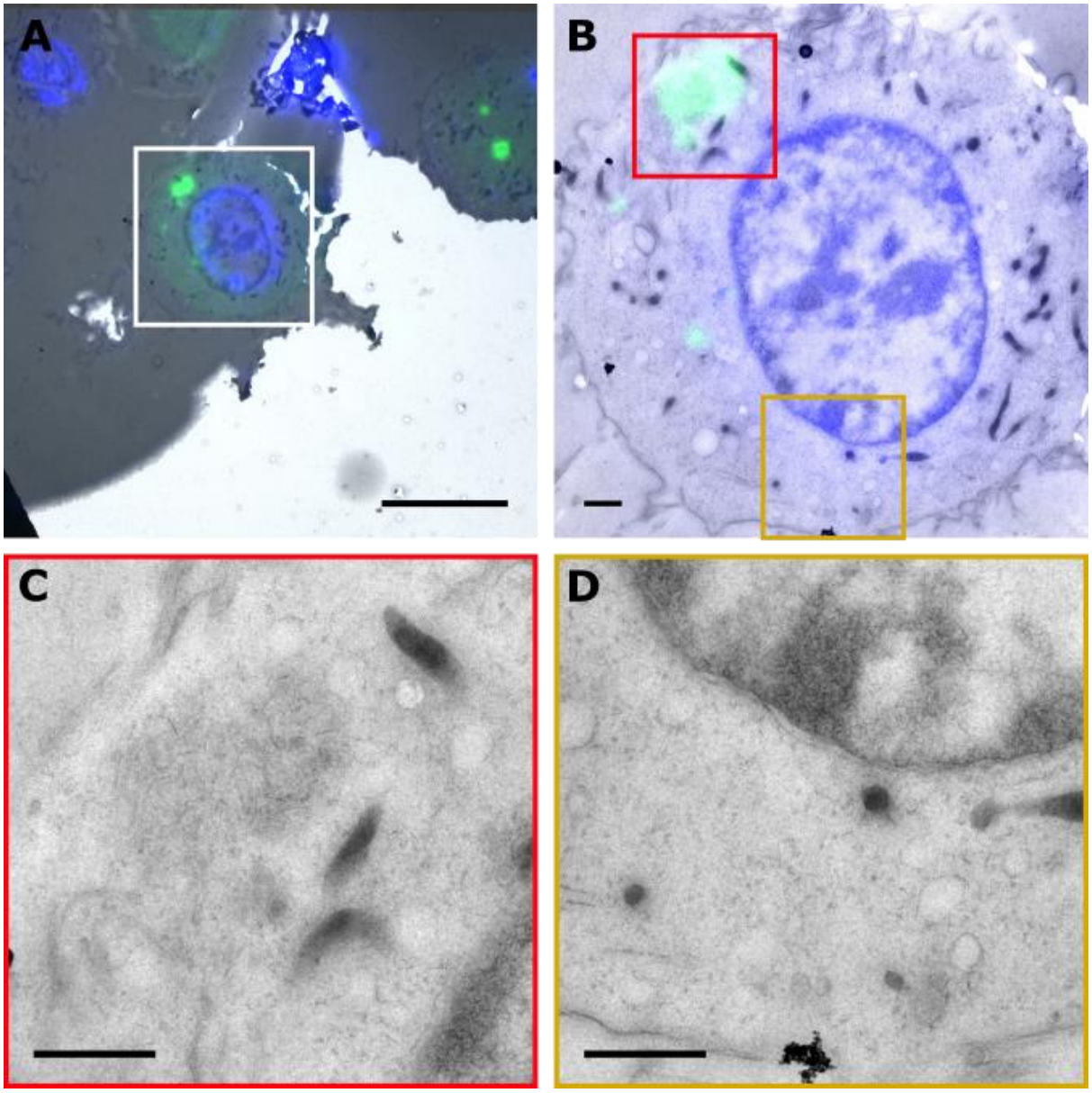

Figure 4.8: HeLa cells transfected with EFS1 construct, labelled with SLF' conjugated 2nm AuNPs and silver enhanced. Image A is in-resin fluorescence of a 300nm lowicryl section imaged on the TEM overlaid with a wide field fluorescent microscope. Image B is an electron micrograph with overlaid fluorescent signal. Images C and D are higher magnification of the two highlighted areas in image B. All scale bars represent 1µm apart from image A were the scale bar is 10µm.

4.5 Discussion

Exogenous probes require a mechanism to localise to a specific target and remain as proximal to the target as possible. Commonly antibodies are used as vehicles to deliver probes/labels to specific intracellular targets in order for them to be vicariously visualised (Takizawa et al., 2015).By opting to replace antibodies for an alternative affinity system, several areas could be improved. Due to their size, antibodies imposed a sizeable distance between the target and label which limits the precision/resolution of acquired images. Furthermore, their size limits both their labelling efficiency and diffusivity through a sample. The size of SLF' 634.77 Au compared to single domain antibodies, fragment antibodies and antibodies which range from 10kDa up to >100kDa is hugely significant. The small size of SLF' confers increased diffusivity and should translate to deeper sample penetration and increased labelling efficiency. The probes design also takes advantage of two endogenously expressed elements: EGFP and FKBP. Since the EGFP and FKBP are expressed with the protein of interest, this ensures strong colocalisation of these three elements. Coupled with the high binding affinity reported in the literature (Clackson et al., 1998) this probe system showed promise.

While the dissociation constants of many antibodies lies in the pM range this is target dependent and the antibody unconjugated. Targets without a complementary antibody or a low affinity primary could benefit from a probe displaying universally high binding. In this chapter, the high binding affinity between the FKBP protein and its ligand SLF' was explored as a possibility for the basis of an affinity base CLEM probe. The binding affinity experiments were successful and showed strong binding even when the SLF' was functionalised with AuNP. The dissociation constant of the FKBP protein for its ligand SLF' was reported to be 94pM in the literature, although the paper does omit any data (Clackson et al., 1998). The dissociation constants acquired in this thesis were 5.8nM and 127.7nM for SLF' functionalised with 2nm and 6nm AuNP respectively. The dissociation constant for the 2nm is within an order of magnitude of the unconjugated ligand. We would expect to see a decrease in dissociation constant due to the steric hindrance induced by the presence of the AuNP. We would also anticipate this steric hindrance to be size dependent so the higher dissociation constant of the SLF' conjugated to the 6nm AuNP is expected. These binding affinities are in the range of many of the antibodies used to label endogenous proteins (Landry et al., 2015) although these data were acquired without any form of conjugated label. Conjugating fluorescent or electron dense labels to an antibody would very likely reduce the avidity in which case the SLF' may still be competitive in this aspect.

Dissociation constants of EFS1 and EwtFS1 were 5.81nM and 119nM. Considering wtFKBP is highly conserved and is expressed in many eukaryotic organisms from plants to humans it is likely that with a 119nM dissociation constant many off-site binding events would occur. For the purposes of *in vitro* and non-eukaryotic labelling this is not an issue but for eukaryotic *in vivo* applications this may not be negligible and may require knockout/knockdown of wtFKBP.

The measured binding affinities did somewhat translate to the *in vitro* labelling model utilising SNX1 lipid tubulation. Liposomes were incubated in the presence and absence of the EFS1 protein construct and labelled with SLF' functionalised 6nm and 10nm AuNPs. The addition of FKBP and EGFP to the SNX1 constuct did not impair the ability of the protein to tubulate *in vitro* or *in vivo*. In the presence of the protein colocalisation between the AuNP and lipid membranes increased by >20%. Despite the high binding affinity between the FKBP and SLF' this did not translate to high density labelling. Many lipid tubules were observed bound to several AuNP labels but never enough to infer a periodic or helical structure. Whether this was due to a discontinuous helical structure along the length of the tubule or inefficient labelling cannot be determined at this point. There was also a high background colocalisation in the control containing no protein. Electrostatics between the AuNP and the lipid membrane are likely responsible for this high background signal. Most, if not all, labelling protocols of this nature will wash excess non-specifically bound probes away. This may have reduced the non-specific interactions and given a higher signal to noise ratio. However, the liposomes and lipid tubules are relatively delicate in nature and washing may have disrupted these structures.

Despite the encouraging data obtained in both the binding affinity experiments and the *in vitro* tests labelling was found to be wholly ineffective *in vivo*. A pre-embedded and post-embedded labelling CLEM workflow was performed with the FKBP-SLF' probe. The pre-embedded labelling lightly fixed cells with 4% PFA before adding the SLF' conjugated AuNP and embedding in epon resin. The post-embedded labelling high pressure froze the cells before staining with 0.1% UA and freeze substituting into Lowicryl HM20. In both cases regions producing fluorescent signal did not correlate with AuNP labelling when imaged with the TEM. In some cases, shown in figure 4.8 electron dense punctae were visible but did not correlate with any fluorescent signal. It may be the case that the FKBP binding pocket is very sensitive to fixatives. In both workflows fixation before labelling was

kept to a minimum but this may have been enough to abolish binding. For the post-embedding protocol specifically, thick sections needed to be cut in order to visualise the fluorescent signal. Ideally these sections should be around 100-150nm in thickness to ensure the probe need only penetrate a small distance before binding. The 300nm sections used in the experiments have detrimentally impacted the SLF' ability to reach its target hence why no colocalisation was observed.

In both CLEM workflows, the SLF' conjugated to 2nm AuNP was used as a label due to its greater measured binding affinity and sample penetration. 2nm AuNPs are not straightforward to visualise in the TEM particularly in a cellular context with additional sources of electron density. This necessitated the use of silver enhancement to increase the particle size and visibility of these AuNP labels. Silver enhancement may have reduced the ultrastructural clarity (saponin permeabilisation may have also contributed to this degradation) impairing the identification of structures that may have been concomitant with SNX1 in the TEM.

In its current iteration the probe is not suitable for protocols which rely on chemical fixation before labelling. This issue is not unique to FKBP-SLF', many antibodies are also unable to recognise epitopes once they have undergone fixation. It does however display a very tight binding which can manifest as target binding which was shown in the *in vitro* tubulation experiments. The FKBP-SLF' probe system has several positive attributes, small size (high sample penetration), tight binding and a large portion of the probe being endogenously expressed.

4.5.1 Future work

First and foremost, re-testing the binding affinity between FKBP containing constructs and the SLF' in the presence of fixatives should be performed. The previously performed binding affinity experiments and *in vitro* labelling of tubules showed SLF' conjugated to AuNP binds to EFS1. The CLEM experiments however showed no colocalisation and therefore likely no binding. It may be that the FKBP binding pocket is highly sensitive and once exposed to fixative, SLF' binding is abolished. This is not uncommon as many antibodies are also unable to recognise epitopes treated with fixative. If several fixatives at varying concentrations were to be tested it may be possible to find a sample preparation method that retains the high affinity of FKBP-SLF' binding.

There are examples of tubulated liposomes labelled with immunogold in the literature (Farsad et al., 2001) (van Weering et al., 2012). Immunolabelling produces very sparse AuNP labelling in both of

these examples, however a direct comparison between standard GFP immunolabelling and FKBP labelled with SLF' AuNP under the same conditions should be performed. This would provide a fixative free model to compare labelling efficiencies. Alternatively, the SLF' molecule could be conjugated with a fluorophore such as Texas Red which has previously been reported by Li Chen Han (Han, 2012). A FRET experiment could then be performed using the EFS1 construct and the SLF' conjugated to Texas Red. This could quantitatively confirm whether the SLF' still binds FKBP in an *in vivo* context.

With regard to the CLEM protocols a myriad of variables could be altered in a bid to improve accuracy of SLF' labelling. Type of resin, fixative, heavy metal stains and section thickness are all candidates to be further investigated. For the post embedded labelling workflow in particular exploration of other resins is particularly relevant. If fixatives do prove to be the limiting factor, it may be wise to alter the workflow to label with the SLF' before fixation. This may not be feasible and result in incredibly poor ultrastructural preservation particularly when factoring in the necessity of permeabilising agents. The Tokuyasu method embeds samples in gelatin and uses a gentler fixation procedure. Immunolabelling is performed while epitopes are still in a hydrated state aiding in antibody recognition (Ripper et al., 2008). Although fixatives are still used in a standard Tokuyasu protocol, more involved methodology combining Tokuyasu and cryo-sections can delay chemical fixation until later in the protocol (Stierhof and Kasmi, 2010). This may a protocol to be fashioned whereby the probe can bind the target prior to fixation. Labelling cell surface proteins is another option for a CLEM workflow that avoids fixatives entirely. To label endogenous proteins, most probes require the cell to be permeabilised in order to gain access to the cytosol. Without prior fixation the cellular contents can extract. Labelling surface proteins would bypass the requirement for fixation but obviously limits the probes wider usage.

All CLEM experiments performed in this chapter used SLF' 2nm AuNP because the higher measured binding affinity and increased diffusivity were thought to be ideal for effective labelling. However repeating the experiments with SLF' 10nm gold would not require silver enhancement in order to visualise the punctae.

The target we had hoped to label was tetherin, a cell surface protein relevant to the cellular response to HIV (Arias et al. 2014). Both the N and C terminus are unsuitable for adding peptide tags.

The N terminus exists in the intracellular lumen and the C-terminus embeds itself into a lipid raft domain of the membrane. Therefore, an internal EGFP-FKBP tag was placed in the extracellular domain of the protein that avoided the termini. Cells expressing this construct could be labelled with SLF' AuNP and either imaged with SEM or TEM. This experiment would avoid many of the potential pitfalls and may establish an effective niche for this probe system.

Chapter 5

Development of Fluorescent Platinum Nanoclusters for use as a CLEM Probe

5.1 Introduction

Recently there has been a huge surge in the development in instrumentation, analysis and specialised workflows for CLEM. Direct electron detectors (McMullan et al., 2016) coupled with hi specification systems such as the Titan Krios (FEI) (Liu et al., 2017) has been termed the resolution revolution (Kühlbrandt, 2014). Likewise, FM has experienced a similar leap forward with the development of several super resolution techniques (Pujals et al., 2019) and deconvolution analysis (Le-Guennec et al., 2020). Probes for these techniques have received comparatively little attention. However, with the improvement of imaging techniques across the board the adoption of CLEM workflows to answer biological questions has become more widespread. CLEM has great potential to capture dynamic and rare biological events but can be somewhat limited by efficacy of the probes. Although not always the case, the main issue often presents itself as lack of co-localisation between fluorescence and electron density. Gold nanoparticles (AuNPs) are widely used labels for electron microscopy due to a number of attributes. High atomic number elements have a large number of electrons generating strong contrast in TEM micrographs. Due to the robust synthesis of AuNPs, it is relatively straightforward to vary their size and morphology based on the demands of the experiment. Furthermore, they can be surface functionalised using the ubiquitous gold-thiol bond. Nevertheless, they are not inherently fluorescent and so in order for them to be visualised with both LM and EM, probes must be coupled to a fluorophore (Alexa dyes etc.). Despite AuNPs outstanding attributes as an EM probe, they are very efficient at quenching fluorophores that are proximal. Instead of energy being emitted from the fluorophore as visible light, it is transferred into the AuNP where the energy is radiated away by lower energy processes/emissions. A catch 22 scenario is reached whereby the origins of the two signals should ideally be as close to one another as possible to produce high accuracy correlation, but higher proximity results in increased quenching of the fluorescence. This presents a significant problem for this kind of dual modality probe.

A paper I made contribution toward showed that AuNP of size 10nm were capable of quenching fluorescence of covalently attached fluorophores (Alexa 633) by >95% (Miles et al., 2017). This level of quenching would render accurate co-localisation between the electron density and fluorescence near impossible. Also, it was shown that 2nm AuNPs binding to a protein adjacent to EGFP were capable of inducing significant quenching (Section 4.2). As the size of AuNP is reduced so too is their quenching efficacy via the FRET mechanism. Metal nanomaterials, such as AuNPs, have a second long-range mechanism of energy transfer which can quench fluorescence termed NSET (discussed in

more detail in section 4.2). Therefore, probes such as fluoronanogold (Takizawa and Robinson, 2000) are still functional but likely operate with a decreased fluorescent signal. Similar to FRET if a fluorophores emission overlaps strongly with the absorbance/LSPR of a nanomaterial it is likely to be quenched more efficiently. However, examples of increased fluorescent output has been observed and modelled in these same circumstances (Breshike et al., 2013).

A CLEM probe that would present a high level of colocalisation would be an electron dense object that is itself fluorescent. At the current time, quantum dots (QDs) do somewhat fulfil this brief (Giepmans et al. 2008) (Killingsworth et al., 2016). QDs have a very wide excitation and narrow emission, high quantum yields and are relatively electron dense. QDs are most often composed of cadmium/selenium or cadmium/tellurium with a zinc sulphide passivating layer. Although they are composed of heavy metals, the contrast conferred in an electron micrograph is significantly less than gold. They can be particularly difficult to identify in a cell prepared for TEM that has undergone heavy metal staining. QDs less electron dense composition can struggle to generate sufficient contrast in an electron micrograph. With the development of silver enhancement protocols for QDs this lack of contrast can be mitigated (Szymanski et al., 2013). However, the persisting issue with QDs is their biocompatibility. QDs leach toxic substances, primarily cadmium and selenium ions which have been shown to have a significant impact on cell viability (Mo et al., 2017) (Oh et al., 2016). The passivating layer, typically composed of zinc-sulphide, can improve biocompatibility in the short term. In the context of a CLEM probe, an additional passivating layer adds to the size of the quantum dot, decreasing sample penetration and labelling efficiency.

5.1.1 Fluorescent Nanoclusters

As previously discussed, a small electron dense structure that is the progenitor of its own fluorescent signal could potentially provide the basis of an effective CLEM probe. Noble metal nanoclusters (NCs) have the potential to fit this niche. NCs are defined as being less than 2nm in size and composed of less than 100 atoms. They are most commonly composed of noble metals: copper, silver, gold and platinum. This composition confers a number of advantageous attributes: high stability, relatively low cytotoxity and high electron density (Shang and Nienhaus, 2012). Synthesising these structures to occupy certain size regimes with a suitable scaffold/stabilising molecule can generate NCs with a large fluorescent output and high quantum yields.

The emergent property of fluorescence in NCs arises as a product of electron confinement due to the particle size. Bulk metals do not display fluorescence, there is no energy gap between the valence and conduction bands and electrons are able to move freely (Wu and Jin, 2010). The size regime occupied by nanoparticles sees the mean free path of the electrons limited by the size of the nanoparticle structure (Zheng et al., 2007). Due to the much-increased surface to volume ratio, the majority of interactions are likely to take place at the surface giving rise to surface plasmon resonance. Particles with a diameter smaller than 1-2nm lose their surface plasmons and due to the Pauli Exclusion Principle the band structure becomes discontinuous and discretised (Zheng et al., 2007). The resulting discretised electron energy levels instead enable the structure to behave similarly to organic fluorescent dyes (although organic fluorescent dyes tend to absorb energy via a conjugated pi bond structures). In both systems, the energy associated with these electronic transitions correspond with specific light absorption and emission. Much like the electronic structure of quantum dots the energy gap between the valence and conduction bands is a size dependent phenomenon (Brown et al., 2017). Smaller particles will have a larger band gap and a blue shifted excitation and emission.

5.1.2 Synthesis of Fluorescent Nanoclusters

There are a wide range of synthetic routes that can be employed to create metal nanoclusters. These range from gas phase synthesis (Huttel et al., 2018), laser ablation (Marine et al., 2000) and organic phase synthesis pathways (Wilcoxon and Abrams, 2006). This thesis will focus on nanoclusters synthesised in biologically viable solution such as water or PBS and from biologically inert materials. Many of these synthetic routes revolve around three key factors: a source of metal ions, a reducing agent and a scaffold/template/stabilising molecule. Metal ions free in solution interact with the scaffold molecule via electrostatics or metal-thiol interactions (typically from cysteine residues). In the presence of a reducing agent the bound metal ion then acts as a nucleation site (Figure 5.1). As more metal ions are reduced in situ the crystal size grows until it becomes sterically hindered by the template molecule. Different scaffolds will impact the final size, morphology and fluorescent characteristics of the nanocluster. In the absence of a scaffold molecule it would be energetically favourable for the nanoclusters to aggregate irreversibly into larger particles to minimize their high surface energy. The secondary function of the scaffold molecules is to stabilize the NCs and prevent this aggregation.

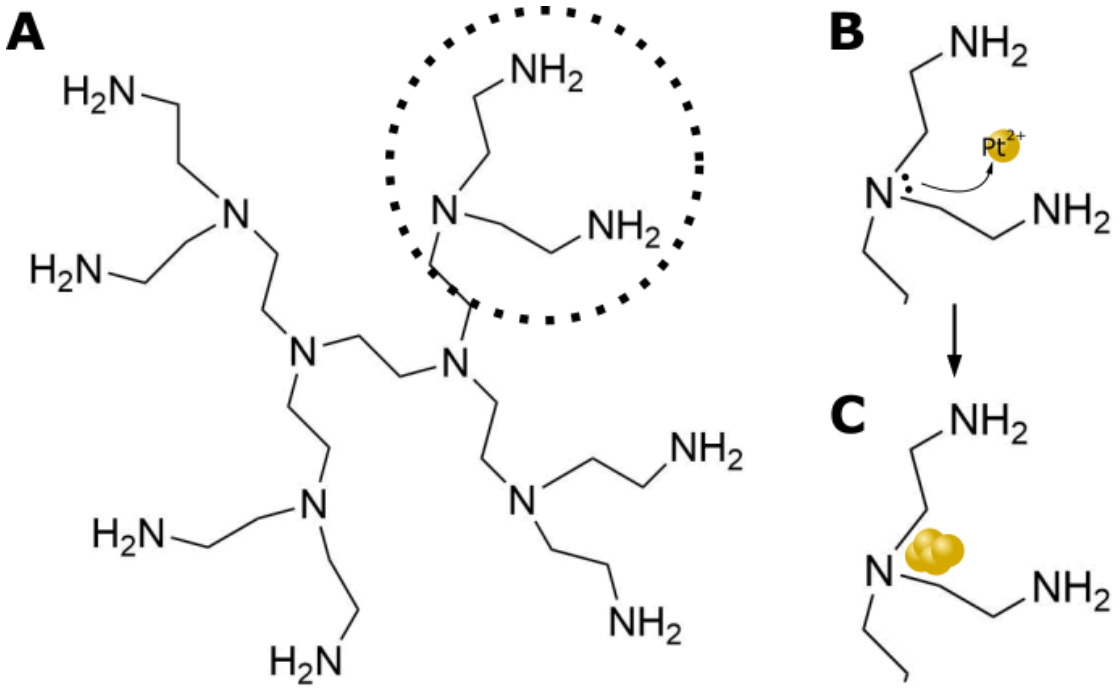

Figure 5.1: Schematic of nanocluster synthesis. Image A shows a 2nd generation PEI dendrimer (Although 4th generation was used in this thesis). Image B shows positively charged metal ions binding to tertiary amines in the PEI. Image C shows the action of the reducing agent forming small clusters sequestered within the PEI molecule.

5.1.3 Nanocluster Scaffold Molecules

5.1.3.1 DNA Scaffolds

DNA oligonucleotides are widely used to synthesise Au (Liu et al., 2012), Ag (Yuan et al., 2015) and Cu nanoclusters (Liu et al. 2013). Oligonucleotides are particularly well suited for the synthesis of Ag nanoclusters (AgNC) as cytosine bases have a high affinity for silver ions. The first reported synthesis of AgNCs used a DNA template was in 2004 by Petty et al (Petty et al., 2004). These nanoclusters boasted a myriad of positive attributes: bright fluorescent output in the near-IR, photo-stable, water soluble and did not blink over experimentally relevant time frames (Li and Xu, 2014). Further investigation in to the optical properties demonstrated the AgNCs were sensitive to the primary and secondary structure of scaffolding oligonucleotides. The AgNCs were reported to only form on single stranded DNA. Single stranded DNA interspersed with regions of double stranded DNA would enable precise positioning at a length scale of around 10nm (Gwinn et al., 2008).

DNA scaffolds are not as widely used with Au nanoclusters (AuNC) as the ion source, $AuCl_4^-$, is negatively charged and repelled from the negatively charged DNA backbone. Despite this weak interaction water soluble red-emitting AuNCs were successfully synthesised after 36 hours with a DNA scaffold, dimethylamine borane as a reductant and $AuCl_4^-$ as the ion source (Liu et al., 2012). More recently a rapid synthetic route was reported using C5 DNA as a template, HEPES was the reductant and $AuCl_4^-$ the ion source. This method produced blue-emitting AuNCs after only five minutes and were also shown to be apt at sensing Hg^{2+} ions in solution (Qing et al., 2016).

5.1.3.2 Protein scaffolds

Proteins and peptides are another viable form of scaffold for nanocluster synthesis. These scaffolds, like the aforementioned DNA scaffolds, electrostatically interact with metal ions, sterically hinder crystal growth beyond a certain size and minimize aggregation of high surface energy particles.

Transferrin is a well-studied protein involved in the transport of extracellular iron ions into the cell. Each transferrin molecule contains 40 cysteine residues which readily bind gold via the gold-thiol interaction which was utilized to begin the nucleation process and act as a scaffold. The gold was reduced using ascorbic acid for 2 hours before AuNCs formation was complete. The authors found that the protein could still perform its native function of iron transport even with AuNCs attached (Guével et al, 2011). Transferrin receptors located on the cell surface membrane were still able to bind and internalise transferrin. Labelling proteins that are readily taken up by cells is interesting as it negates the requirement to permeabilise the cell, leaving the cellular structure in a more native state for subsequent imaging. However even after 4 hours of incubation with cells, the majority of the transferrin remained localised to the surface membrane and very little punctate endocytic labelling was observed (Guével et al, 2011).

A one pot synthesis of AuNC using BSA as a stabilising molecule was reported by Ying's group (Xie et al., 2009). BSA much like transferrin contains a large number (35) of cysteine residues which readily binds gold ions. The large size of BSA also imparts a significant amount of steric protection further increasing AuNC stability. At high pH (pH 12) BSA acts as a reducing agent. Once the gold ions were sequestered in the BSA, the pH of the solution was increased, reducing the gold atoms in situ, forming AuNCs. These AuNCs were composed of 25 gold atoms, displayed a quantum yield of 6%

and a peak emission at 640nm (Xie et al., 2009). The authors did not investigate the AuNCs as a bio-imaging probe, but the large size of BSA (≈66.5kDa) may mean it is unsuitable for this application.

Silver nitrate staining of the nucleolus has long been used by pathologists to highlight nucleolus organising regions and indirectly the nucleolus location (Goodpasture and Bloom, 1975). The protocol produces large metallic silver nanoparticles that produce dark spots under both light and electron microscopy. However, this protocol uses harsh conditions that would likely be unsuitable (5.8M silver nitrate, 60°C) for detailed imaging, particularly live cell imaging. Taking advantage of a specific argyrophilic nuclear protein, nucleolin, Yu et al. used low concentrations of silver nitrate (20mM) and a photo-activation technique to generate fluorescent AgNCs in vivo. The emission spectra of these nanoclusters were quite broad 500-700nm owing to a cluster size range of 2-7 silver atoms. Unfortunately, nucleolin is too large to be utilized as an endogenous protein label. Attempting to use a short peptide containing the prevalent amino acids contained within nucleolin does still enable AgNC formation but with much reduced stability (3 days). These peptide stabilised AuNCs were successfully applied for epifluorescence imaging (Yu et al. 2007).

5.1.3.3 Dendrimers and Polymers

The etymology of the word dendrimer is derived from the Greek word Dendron meaning tree. The iteratively branched structure of these molecules is reminiscent of the structure of tree branches. Dendrimers are usually composed of a single chemical unit known as a core or focal point. The generation number denotes how many times the molecule branches/diverges. The uniform composition and structure lend themselves favourably to nanocluster synthesis. A variety of the core properties can be chemically altered. For example, the charge could be altered to accommodate different metal ions. Furthermore, the terminal ends of the dendrimer can be modified/functionalised to interact and bind with different targets.

Poly(amidoamine) (PAMAM) is the most widely used dendrimer in nanocluster synthesis. One of the earliest examples was in 1998 where PAMAM was used to template the growth of copper nanoclusters (CuNC) with a size range of between 4 and 64 atoms in size (Zhao et al., 1998). A group led by Dickson were the first to create nanoclusters (silver) in a water-soluble form using both G4 and G2 OH terminated PAMAM (Zheng and Dickson, 2002). Continuing to use PAMAM as a template,

the same laboratory led by Dickson went on to synthesise more water soluble fluorescent AuNCs with a very high quantum yield of 41±5% (Zheng et al., 2003).

5.1.3.4 Small Molecule Scaffolds

A prime example of nanoparticle stabilization with small molecules is the ubiquitous gold nanoparticle synthesis with citrate (Al-Johani et al., 2017). The carboxyl groups on the citrate bind to the gold nanoparticle surface and prevent further aggregation. Similarly, small chemical molecules can also be utilized to form NCs. Thiol containing molecules readily bind metal ions and are commonly used as stabilizing agents. 4-*tert*-butylbenzylmercaptan was successfully used to form gold nanoclusters. This synthetic route produced a very homogenous population where each cluster contained 25 gold atoms. This NC population had a quantum yield of 5% and a peak emission at around 620nm (Das et al., 2014).

Small molecule stabilising agents have also been demonstrated with homogenous populations of platinum nanoclusters. The initial synthesis used the PAMAM dendrimer as the scaffold molecule. However, a subsequent process of ligand substitution replaced the dendrimer with the small molecule mercaptoacetic acid. The molecular weight of the PAMAM varies per molecule but with the small molecule stabilising agent accurate mass spectrometry could be performed. Each cluster was found to contain eight platinum atoms stabilised with eight mercaptoacetic acid molecules. These NCs were reported to induce low levels of cytotoxicity, a quantum yield of 28% and a peak emission at around 520nm (Tanaka et al., 2013).

5.1.4 Aim

This chapter explores the potential of using PEI stabilised fluorescent platinum nanoclusters as CLEM probe. Long term stability and straight forward synthesis were key reasons this probe was chosen. Platinum clusters were also particularly useful as the electron dense nature of this element creates a lot of contrast when imaged with TEM. Finally, there was already precedent of using these particles for fluorescent *in vivo* imaging (Huang et al., 2016)

Reliable colocalisation of fluorescence and electron density is the crux of CLEM probes. This can be impacted by linker length separating the two signals or self-quenching. Fluorescent nanoclusters could have the potential to be an exciting novel CLEM probe considering they generate a fluorescent signal from an electron dense core. This would mean the fluorescence and electron density originate from the same point in space increasing the accuracy of correlation. Platinum nanoclusters were chosen for several key reasons. In addition, this chapter explores the prospect of nanocluster silver enhancement. This process uses metal particles as nucleation points for silver crystal growth to further enhance electron density/contrast. Due to the incredibly small cross section of PtNCs it may not be trivial to visualise them under standard TEM, particularly in biological samples with high background noise. This may mean silver enhancement is a requirement in order for PtNCs to be viable as CLEM probes.

5.1 Emission, Excitation and Quantum Yield of PtNCs

As previously described in section 5.1.1 the peak excitation and emission wavelength are a size dependent property of the PtNCs. Since every parameter of the synthesis pathway: concentration of Pt^{2+} ions, concentration of PEI scaffold, concentration of reducing agent etc. is able to impact the size of the nanoclusters in some way it is important to thoroughly characterise each new synthesis. Typically, smaller nanoclusters display blue shifted excitation and emission wavelengths due to the increased band gap. In the context of a CLEM workflow it is preferable for the PtNCs to strongly absorb between 405 and 633 as these wavelengths correspond to excitation lasers of a typical confocal/fluorescence microscope. Using UV-vis spectrometry the excitation and emission maxima of the chosen nanoclusters was found to be 328nm and 461nm respectively. The batch of PtNCs selected did not have an ideal absorbance as its maxima was at 328nm, far below the 405nm UV laser of a confocal microscope. However, of all the reaction conditions used, this batch had the highest fluorescent output when excited with the 405nm laser. Although 405nm excitation is suboptimal, the fluorescent output was still sufficient for the PtNCs to be visualised using hybrid detectors on the confocal microscope. Furthermore, this batch appeared to be homogenous, displaying only a single absorbance and emission maximum (Figure 5.2).

After measuring absorption and emission maxima, the next logical step was to calculate the quantum yield of the PtNCs. Quantum yield describes the efficiency of a fluorophore to convert an excitatory wavelength into a fluorescent emission (Villamena, 2016). It is defined as the ratio

between the number of photons absorbed and the number of photons emitted. In order to calculate the quantum yield the absorbance cross section of a fluorophore must be accounted for. Some fluorophores possess larger chromophores with a larger surface area and therefore absorb more light. Determining this value for PtNCs synthesised in a PEI scaffold is not trivial as each PEI scaffold

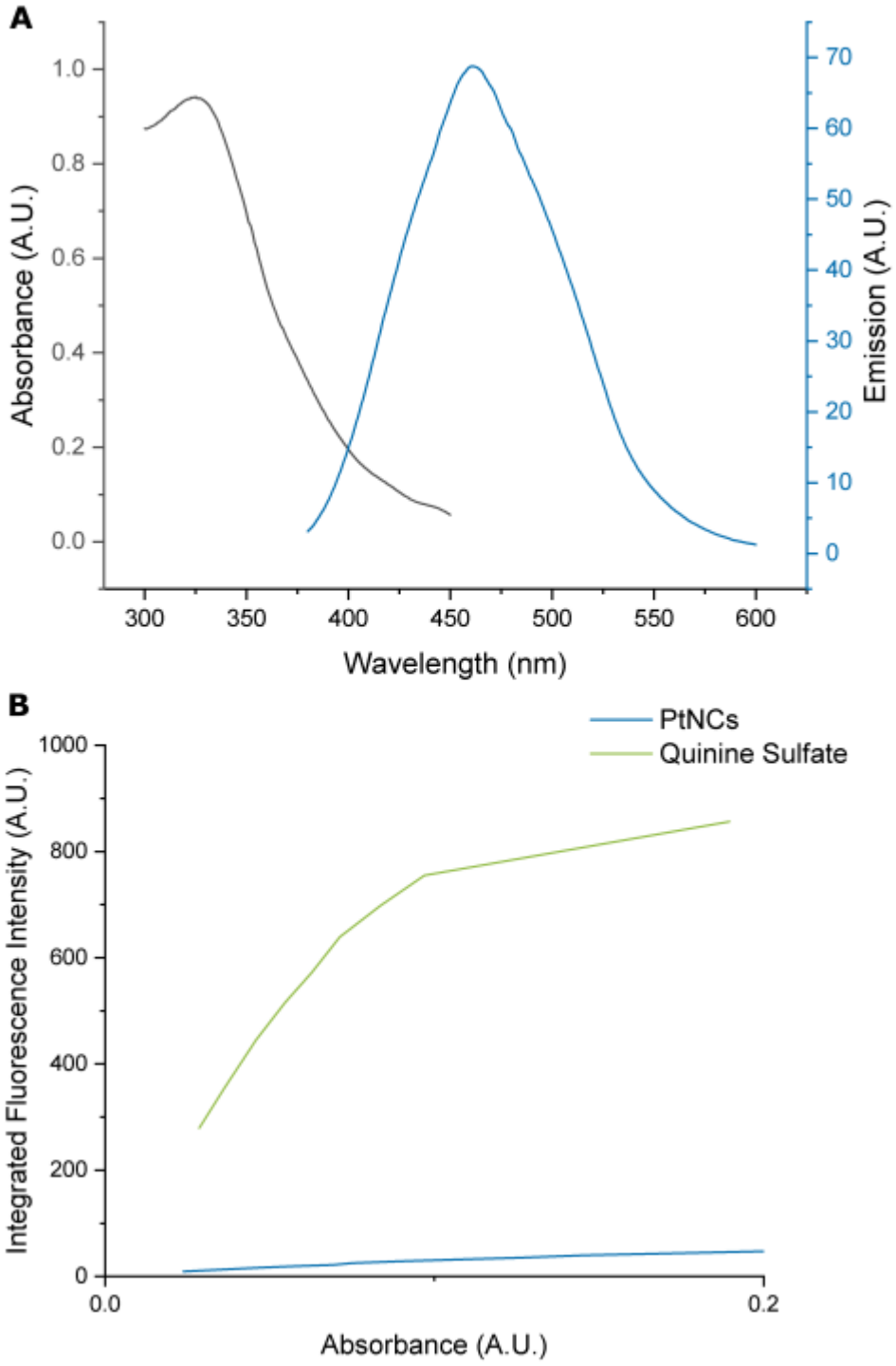

Figure 5.2: Graph A shows the Absorbance and Emission Spectra of PtNCs. Intensity of fluorescent emission is shown in Graph B with respect to the absorbance of the sample. Using Quinine sulfate as a control this data was used to calculate the quantum yield of the PtNCs.

molecule can nucleate multiple clusters. The excitation and emission spectrum of quinine closely resembles that of the PtNCs used. Therefore, quinine sulfate was used as a well-defined standard with which to calculate the quantum yield.

$$\Phi_{PtNC} = \Phi_S \, x \, \frac{F_{PtNC}}{F_S} \, x \, \frac{Abs_S}{Abs_{PtNC}}$$

Where subscripts PtNC and S in the above equation denote platinum nanoclusters and standard respectively. This method of quantum yield measurement does require several conditions and assumptions to be met. To avoid internal filter effects and artefacts of heterogeneously dispersed solute, samples should have an absorbance of <0.1. In addition, having a highly dilute sample also reduces phenomena such as self-quenching. The same sample cell was used for blanks, samples and controls to minimize variance in the interfacial regions and variance in scattering loses. Samples were also blanked against identical solvents to remove any spurious signals generated from impurities. Measurements in the UV regime are particularly sensitive to impurities so this step was particularly relevant.

Quinine sulfate (QS) dissolved in 0.5M H_2SO_4 is a well characterised quantum yield standard in the range of excitations 280-380nm and emission 380-580nm. To minimize internal filter effects further, the emission spectra of a given control sample pair should be as similar as possible. The PtNCs were measured to have an excitation maxima at ≈330nm and a peak emission at ≈460nm (figure 5.1, B). The QS and PtNCs excitation and emission spectra occupied the same spectral region which helped to ensure the quantum yield calculations derived from these measurements would be accurate. Using an absorbance of 0.03 for both the standard and sample the quantum yield of the PtNCs was calculated to be 4.8%. However, this figure is calculated based on an optimal excitation wavelength of 328nm. The absorbance is reduced to only 18% of the maxima when exciting with 405nm meaning the fluorescent output of the PtNCs will be much reduced when visualised using a confocal microscope.

5.2 Characterisation of PtNCs using HAADF-STEM and EDX

The maximum excitation and emission of the PtNCs was found to be 328nm and 461nm respectively (Figure 5.2). Considering the fluorescent emission tends to blue shift as cluster size decreases, it is therefore likely the cluster size is small. This is as much information regarding the physical structure as the fluorescence information can glean. Therefore, more robust morphological characterisation is required. Initially TEM was utilized in an attempt to visualise and size these particles. Unfortunately, the PtNCs, although composed of platinum, were not large/dense enough to generate sufficient contrast to accurately visualise. Due to the contrast generated being weak and diffuse, it was not possible to draw any conclusions using standard TEM.

Selected Area Diffraction Patterns (SADP) were also generated using the TEM. This technique generates a characteristic diffraction pattern specific to the crystalline structure the electron beam passed through. The spacing between atoms in a solid is around 100 times larger than the de Broglie wavelength of these high energy electrons. The crystalline solid behaves like a diffraction grating, diffracting electrons at particular angles determined by the crystal structure. Since the PtNCs were comprised of very small crystalline platinum encasing in a PEI scaffold, it would be expected that a clear diffraction pattern for platinum would be acquired. However, upon exposure to the beam the PtNCs diffraction pattern was immediately destroyed/lost. Melting-point depression is a phenomenon commonly seen in structures such as nanowires. As the diameter of a structure drops below ≈150nm there is an exponential drop in melting temperature (Couchman and Jesser, 1977). It is likely that the large quantity of energy imparted to the nanocluster by the incident beam could cause one of two outcomes: the PtNC melts resulting in the regular spacing between atoms to be lost, or the nanocluster is sublimed/destroyed.

Finally, HAADF-STEM was used in an effort to generate more contrast and better visualise the PtNCs. HAADF-STEM is well suited to this sample due to its high sensitivity to the atomic number (Z) of elements within a sample. Elements with increasing Z also have an increasing electron density, scattering more incident electrons at higher angles due to the increased electrostatic repulsion. This technique uses electron detectors above the objective plane to detect electrons that have undergone Rutherford scattering >5°. Therefore, the annular dark field image produced is the inverse of standard TEM with increasing brightness denoting increasing electron density in the sample. Using HAADF-STEM the electron density of the PtNCs could be more clearly visualised

(Figure 5.3 image A). The PtNCs appeared as diffuse patches of electron density as opposed to the punctate structures reported in the literature (Huang et al., 2016).

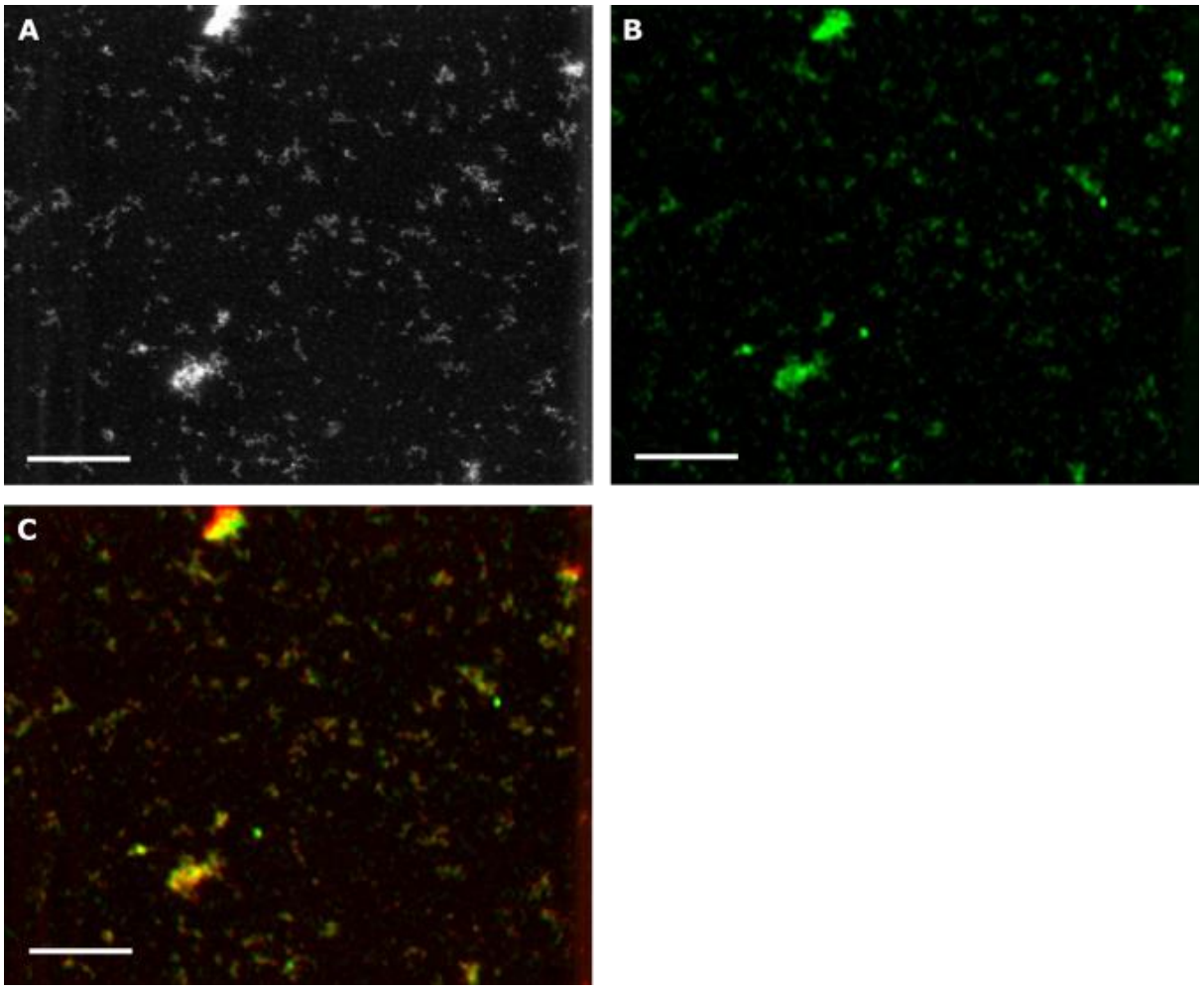

Figure 5.3: PtNCs drop deposited onto carbon-formvar coated copper grids, imaged with HAADF (image A). Image B is an elementary analysis of the same area as image A using EDAX. Image C is an overlay of A and B. Scale bars are 500nm.

With HAADF-STEM alone it was not possible to deduce if the electron density visualised was accurate or merely an artefact/noise. Using energy-dispersive X-ray spectroscopy (EDX) the same area imaged using the HAADF-STEM underwent elemental analysis. Image B (Figure 5.3) shows signal generated from platinum atoms in the sample. A high energy incident beam of charged particles or X-rays (in this case electrons) is directed at the sample. The high incident energy is capable of ejecting low orbital electrons from the atoms leaving an electron hole. An electron from a higher orbital will then fall to fill the hole and as it does so emits an X-ray with characteristic energy enabling elementary detection. Since EDX requires an intense electron beam to be rastered over the

sample, it induces a significant amount of sample warping. Image B (Figure 5.3) has been manually un-warped using a Fiji plugin, MIA (Cross, 2019) (Argandas-Carreras et al. 2006) (Sorzano et al. 2015), by using points of reference in the original HAADF-STEM image. Image C (Figure 5.3) shows an overlay of the two signals, green shows the platinum EDX signal and red the HAADF-STEM. This overlay displays a relatively strong correlation and a Pearson's Correlation of 0.61. Qualitatively the colocalisation of the two signals is in strong agreement even, if the signals do not overlay there is usually a strong complimentary signal directly adjacent. This suggests that EDX introduced significant sample warping and the process to undo this damage was not sufficient to recreate the native arrangement.

5.3 Silver Enhancement of Platinum Nanoclusters

Small gold nanoparticle labels can often be challenging to visualise in TEM. These labels can be easily obscured by other sources of electron density within a sample, particular in a cellular environment stained with heavy metals. The widely used fluoronanogold label (Takizawa and Robinson, 2000) has 1.4nm diameter which although advantageous for membrane and sample penetration is not always trivial to visualise. Therefore, to allow more straightforward visualisation of these small labels, silver or gold enhancement can be employed. This process enables nanoparticles present in a sample (lower in the reactivity series than silver) to act as nucleation sites for silver ions. In a reducing environment, silver ions present in the solution enlarge existing nucleation sites coating them in layers of silver. The additional layers of silver increase the electron density in that immediate loci, increasing the cross section of strong electrostatic force encountered by an incident electron beam, generating more contrast from increased beam occlusion (TEM) or Rutherford scattering (STEM).

As outlined in figure 5.3, the contrast generated by PtNCs in TEM and HAADF-STEM is relatively low resulting in non-trivial visualisation. If PtNCs are to be a robust CLEM probe they must be sufficiently electron dense to readily identify in the context of cells stained with heavy metals. This high background signal would easily obscure the PtNCs without further processing. Silver enhancement may provide PtNCs with sufficient electron density to be readily visualised. Furthermore, the high surface energy of the PtNCs should facilitate a rapid and efficient enhancement. However, the PEI scaffolds function is to limit the crystal growth via steric hindrance. It is therefore likely that the PEI may hinder silver ion access to the PtNC nucleation points or simply block further growth. If this is the case, silver ions may auto-nucleate or nucleate around impurities and create artefacts. To

elucidate whether PtNCs could be specifically and sufficiently silver enhanced, PtNCs were drop deposited onto carbon-formvar coated copper grids and the excess wicked off. For this investigation a commercial silver enhancement kit was used (Aurion, 500.033). Controls (blank grids with no PtNCs) and samples were then floated on silver enhancement solution (as described by the manufacturer) for 1 and 3 hours and imaged by TEM. In the event the silver enhancement was acting as intended, well defined punctate structures should be visible. In addition, if silver growth is triggered by nucleation points of similar sizes, it would be expected that the final size of the punctae would also be with in similar size regime.

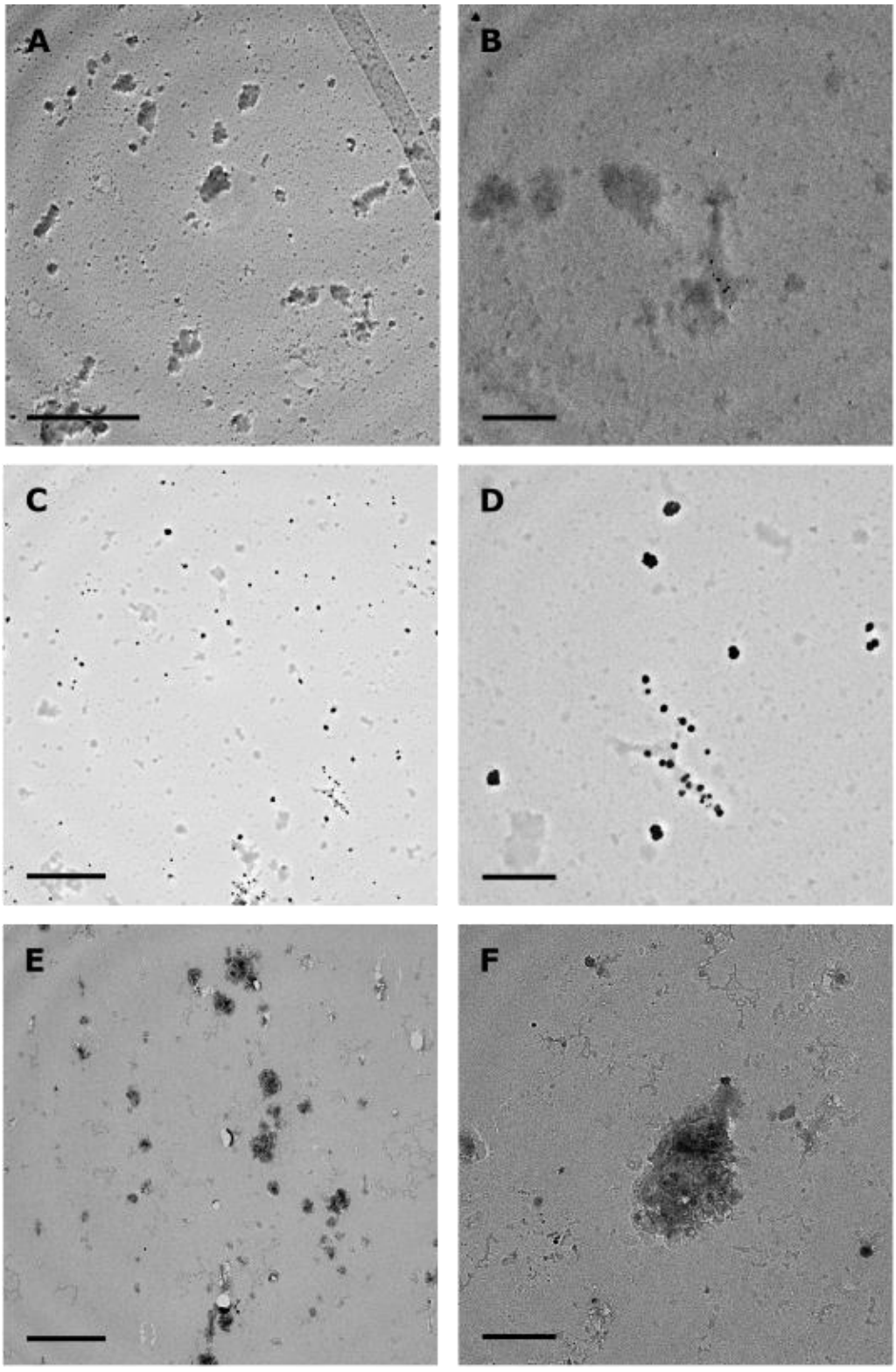

Figure 5.4: Carbon-formvar coated grids were drop deposited with PBS (control) and PtNCs in PBS. Subsequently the grids were floated in silver enhancement solution for 1hr (Images A and B) and 3hrs (Images C, D, E and F). Images E and F show the control grids deposited with PBS only. Scale bars for images A, C and E represent 5µm and images B, D and F represent 1µm.

Figure 5.4 illustrates the difference between samples silver enhanced in the presence (images A, B, C and D) and absence (images E and F) of PtNCs. Images C and D show well-defined punctate structures derived from 3 hours of silver enhancing PtNCs. These structures of a fairly uniform size with a very high electron density. In some cases in the immediate vicinity of these punctae a fainter less electron dense structure can also be visualised which may be the PEI scaffold. In the absence of PtNCs and three hours of silver enhancement images E and F do not show any structures of this nature. Electron density is present in the sample but are not well defined punctae and may be the result of silver ion deposition and/or auto-nucleation.

5.3.1 UV-Vis Spectroscopy of Silver Enhancing PtNCs

When the size of a metallic structure is reduced past a certain threshold, it becomes possible to induce localised surface plasmon resonance (LSPR). LSPR describes the coherent oscillation of electrons at the surface of a metallic structure. When electrons confined within the metallic nanostructure are excited by some incident electromagnetic wave (most commonly within the visible/UV spectrum), energy is transferred to the electrons via sympathetic resonance. This energy transfer via induced electron oscillation corresponds to the absorbance of a nanostructure. Typically, the region of the electro-magnetic spectrum most efficiently absorbed by particles red-shifts with respect to decreasing particle size. This phenomenon has a lower limit with <2nm unable to produce LSPR. Beyond this point the electronic structure becomes too discretised to support LSPR and instead the nanostructure begins to behave more like a molecule.

To more quantitatively measure the silver enhancement of PtNCs UV-vis spectra of PtNCs suspended in silver enhancement solution were recorded at various time points. As the silver enhancement reaction progresses in the presence of PtNCs one would expect to see a defined LSPR peak emerge as the particles enlarge past 2nm in diameter. In the absence of PtNCs to act as nucleation sites it would be expected that significantly fewer particles with a size greater than 2nm should be present in the solution, and the prominence of LSPR much reduced. However, a background LSPR signal in the control would be expected as a result of auto-nucleation but this should be negligible in comparison.

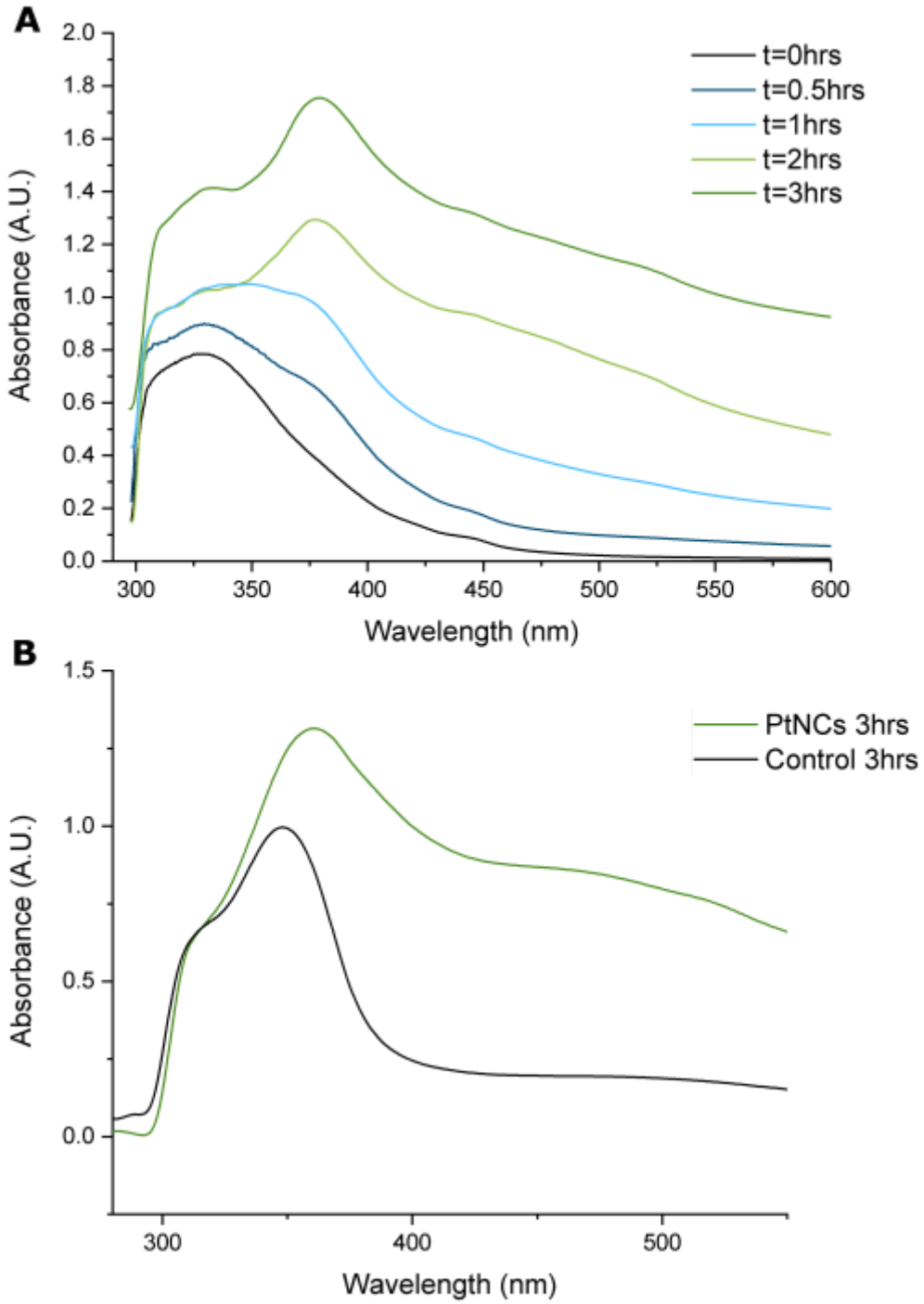

Figure 5.5: UV-vis spectra of PtNCs incubated in silver enhancement solution over a series of time points. Data was normalised against a control at the same incubation time (Graph A). The total change in absorbance of both sample and control incubated for 3 hours in silver enhancement solution. This data was normalised against a control at T=0 (Graph B).

Figure 5.5 (Graph A) shows a time course of PtNCs incubated in silver enhancement solution normalised against a control reaction without PtNCs run in parallel. At each time point the

cumulative absorbance of the sample increases which is likely a result of a general increase in turbidity as particle size increases. After 1 hour a small shoulder becomes visible at ≈375nm. Progression of the reaction to two and three hours, the shoulder develops into a larger and better-defined peak with maxima at ≈380nm and ≈385nm respectively. At each time point (one, two and three hours) the maxima of the LSPR peak progressively blue-shifts. The difference in absorption between the sample containing PtNCs and the control is shown in Figure 5.5 (Graph B). Both of these signals were normalised against the original solution at T=0. The absorbance of sample containing PtNCs is greater than that of the control with peak intensities at ≈1.3 and ≈1.0 respectively. Additionally, the peak intensity is also blue-shifted the PtNC containing solution which suggests the presence of larger particulates.

5.4 Investigation of PtNCs as *In Vivo* Probes

Although PtNCs are capable of displaying high fluorescent outputs/quantum yields, their fluorescence can be sensitive to their environment. Chemical species, particularly metal ions, are able to interact with NCs inducing significant fluorescence quenching. Sensors for metal ions have been developed which utilise NCs as the reporter as very low concentrations ≈nM of metal ions can still induce significant quenching. A variety of chemicals can be detected using this method: Hg^{2+} (Guo et al., 2010), Co^{2+} (Meng et al., 2017), Cu^{2+} (Shang and Dong, 2008) and Cr^{3+} (Xu et al., 2013). Less commonly metal ions in solution can be sensed via an increase in NC fluorescence. In the case of work carried out by the Jin group, it was discovered that the oxidative effect of free Ag^{+} ions lead to a higher charge state on the NC, increasing the fluorescent output (Wu et al., 2012). More biologically relevant molecules can also be detected with this phenomenon including sulphide ions being detected with gold/silver NCs (Chen et al., 2011). An array containing a variety of AuNCs were able to detect specific proteins and bacterial species as a function of global fluorescent response (Wu et al., 2018). NCs could potentially have a high sensitivity to a whole host of chemical species within cells. If NCs are to be used to label endogenous proteins, it is important to study their behaviour and fluorescent response when *in vivo*.

HeLa cells were serum starved for 2 hours before being left to incubate with PtNCs at varying concentrations for 30 minutes. This time point was chosen to maximise the chance of uptake while minimising the likelihood for the cargo to have reached lysosomes and subsequent degradation. Cells were then washed and fixed in 4% PFA. The maximum intensity projection confocal images

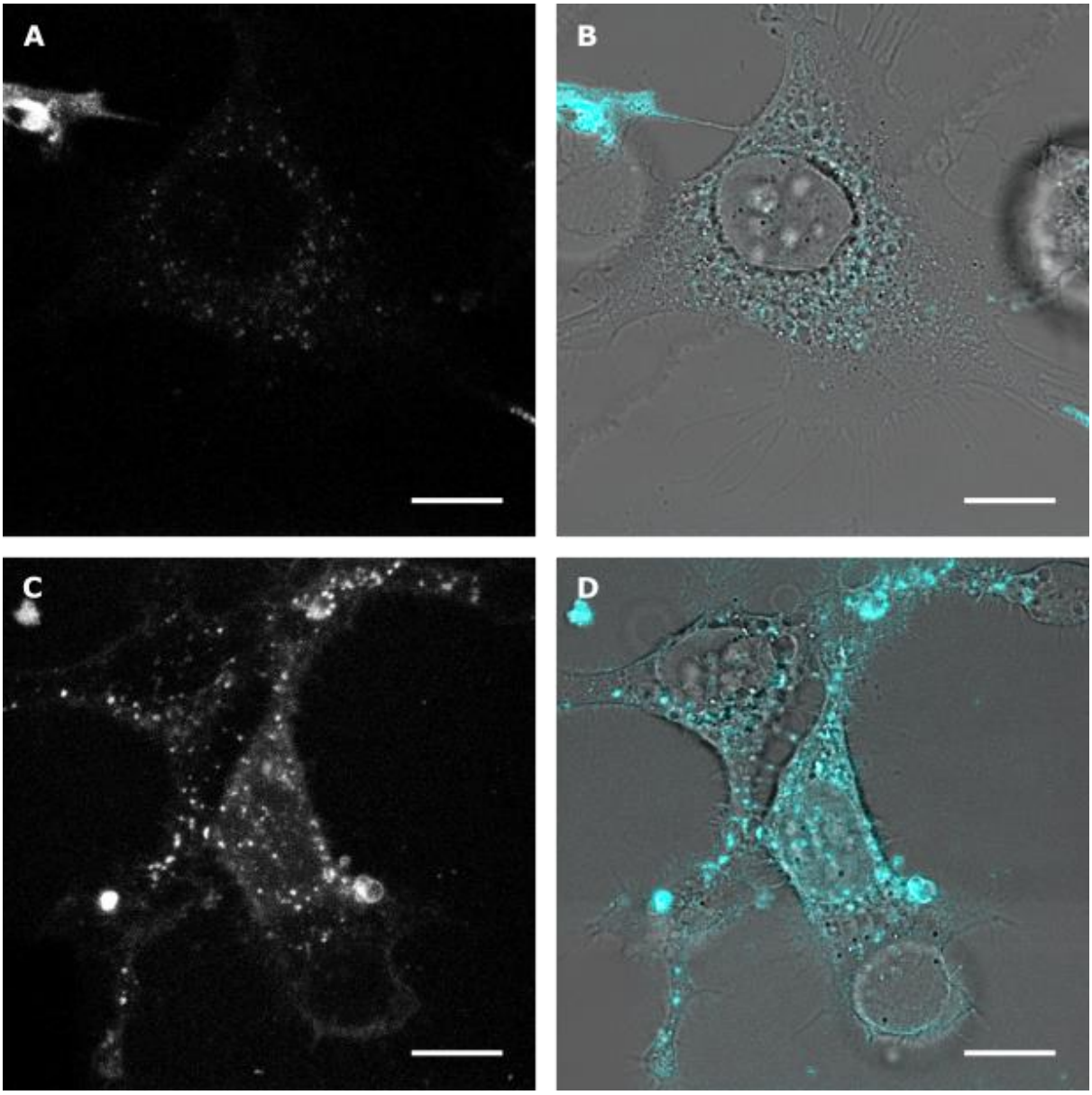

Figure 5.6: HeLa cells incubated with PtNCs for 30 minutes at 37°C and 5% CO_2. Concentration of the PtNC solution was 0.65µg ml^{-1} and 1.3µg ml^{-1} for images A+B and C+D respectively. These confocal images are maximum intensity projections. Scale bars represent 10µm.

displayed (Figure 5.6) punctae clearly show a strong fluorescent signal from subcellular locations. The PtNCs appear capable of entering cells without any assistance, such as membrane permeabilisation. From these data however, PtNCs seem to be denied entry across the nuclear membrane. No significant fluorescent signal from PtNCs originating from the nucleus can be seen (images A+B). At these lower concentrations PtNCs appear to be completely occluded from the nucleus but at higher concentrations some fluorescence is detectable in the nucleus (images C+D). It

is uncertain as to whether the fluorescent signal that appears inside the nucleus originates out of the focal plane.

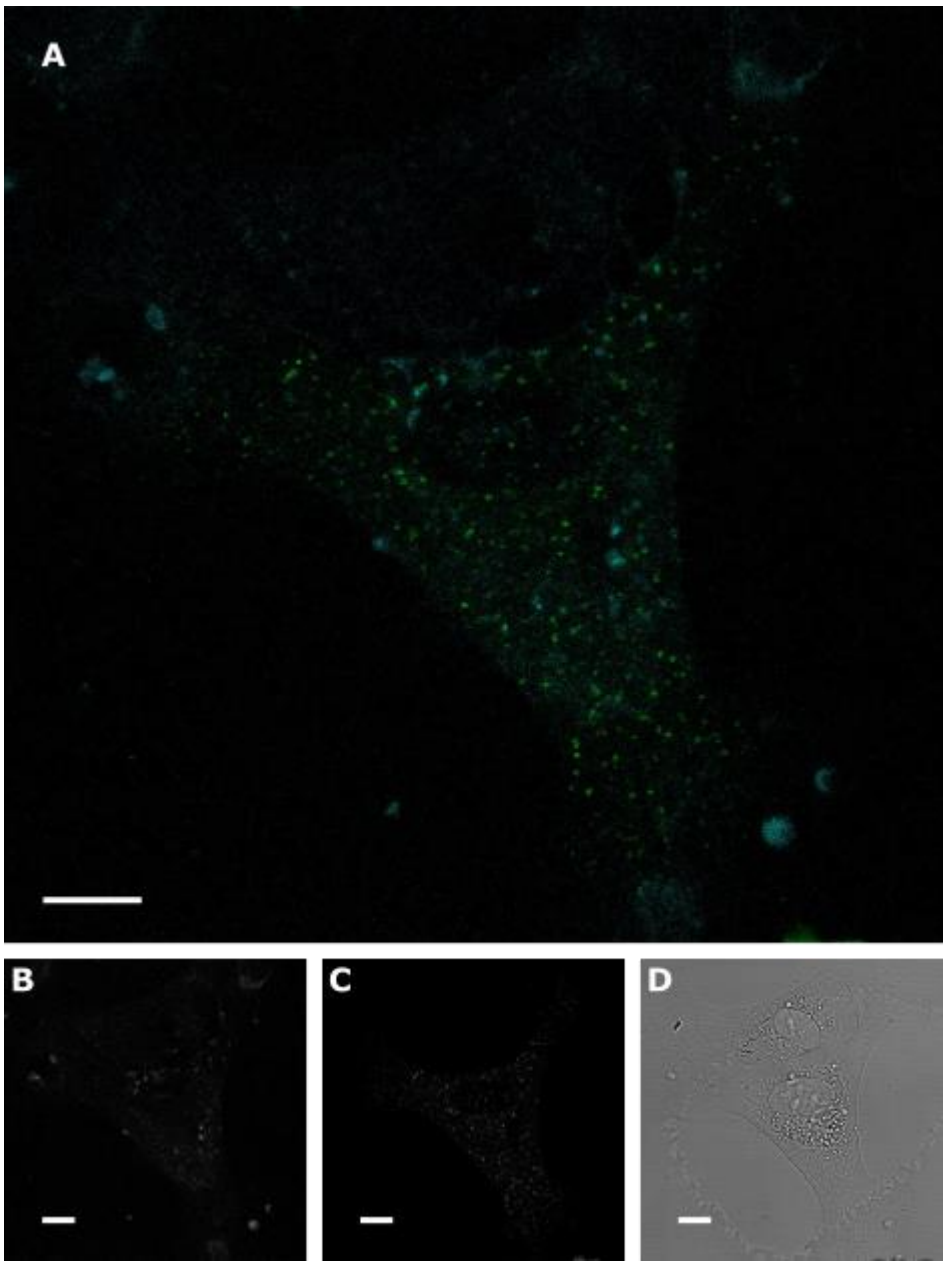

Figure 5.7: HeLa cells transiently transfected with an EGFP-SNX1 construct. Image A was acquired on a scanning confocal microscope and the fluorescence signals are overlaid maximum intensity projections for PtNC signal (cyan) and EGFP (green). Image B and C are greyscale max intensity projections for PtNCs and EGFP respectively. Scale bars represent 10µm.

The PtNCs in this experiment form into small punctate structures within the cell and are evenly distributed throughout the cytosol. The fluorescent distribution of the PtNCs within these cells would suggest that endocytosis is the primary mode of uptake. To lend credibility to this observation

an antibody labelling protocol was utilised to label the endogenous protein EEA1. The primary antibody against EEA1 was then labelled with a secondary fluorescent antibody. If colocalisation between the fluorescent secondary antibody and PtNCs was observed this would provide strong evidence that endocytosis was the primary mechanism of uptake. However, antibodies are unable to innately traverse lipid membranes and therefore required cell permeabilisation with a detergent (Triton) or saponin. Upon permeabilising the cells, all fluorescent signal from the PtNCs was lost when compared to the unpermeabilised control (data not shown). In order to avoid permeabilising the cells a transient transfection protocol was used. EGFP-SNX1 was transfected into HeLa cells using the FuGENE HD protocol (section 2.1.6). SNX1 associates with both early and late endosomes acting as an effective endosomal marker that does not require the use of permeabilising agents. Cells were left to express the transfected gene for 48 hours. Cells were then serum starved for 2 hours, washed with PBS and incubated with PtNCs for 30 minutes. After this time had elapsed cells were washed again with PBS to remove excess PtNCs and fixed for 15 minutes at room temperature with 4% PFA. The PFA was removed, replaced with PBS and the cells were imaged on a scanning confocal microscope. Unlike the previous experiment (Figure 5.6) the PtNCs did not display the same type of distribution. The distribution was far less punctate and instead appeared more diffuse throughout the cytoplasm (5.7). The Pearson's correlation between the PtNCs and EGFP-SNX1 was -0.03. The lack of correlation provides strong evidence that during this particular experiment the PtNCs were not entering the cell via endocytosis.

Between multiple experiments the visual distribution of PtNCs within cells was found to be inconsistent. PtNCs were observed as small punctae, diffuse cytoplasmic fluorescence and also sequestered in much larger structures within cells. This observation was perplexing as the PtNCs and cells were treated in an identical manner each time. Proteins and other biomolecules are known to adsorb to the surface of nanomaterials forming a corona. This can influence and alter the behaviour of nanomaterials as well as how cells interact with them. To investigate if subtle changes in the NCs corona could influence fluorescence and subcellular localisation, HeLa cells were serum starved in serum free media for 2 hours. The cells were washed once more in PBS before adding serum free media or PBS containing a known concentration of PtNCs. The PtNCs were left to incubate with the cells for 30 minutes at 37°C and 5% CO_2. Cells were fixed in 4% PFA and then imaged using a confocal microscope. All samples within a given experiment were imaged using the same microscope with identical settings. Images were also processed in parallel ensuring images were directly comparable. Differences between cells incubated in PBS-PtNCs and Serum Free Media-PtNCs were observed in regard to fluorescent intensity and subcellular localisation of PtNCs.

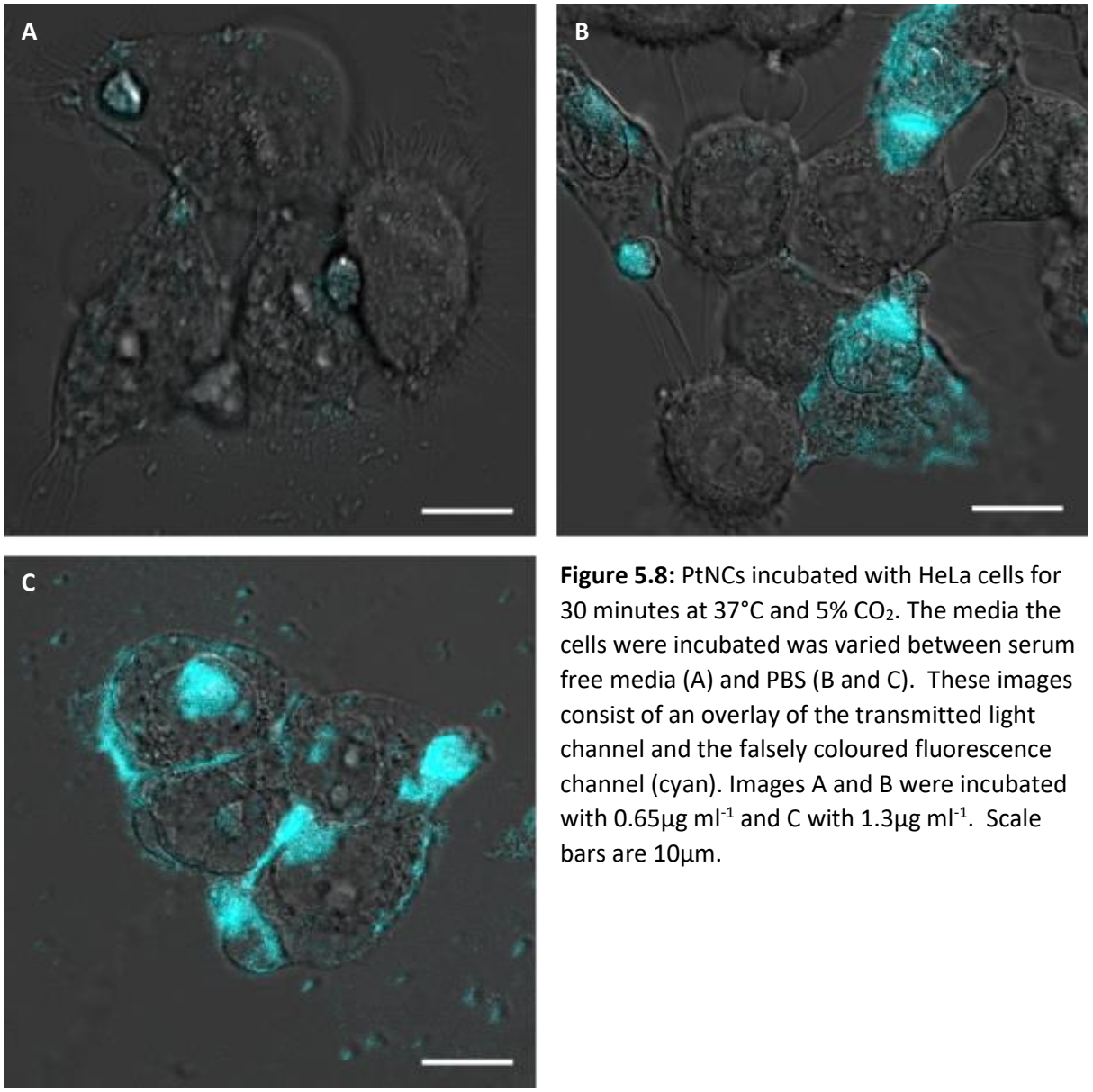

Figure 5.8: PtNCs incubated with HeLa cells for 30 minutes at 37°C and 5% CO_2. The media the cells were incubated was varied between serum free media (A) and PBS (B and C). These images consist of an overlay of the transmitted light channel and the falsely coloured fluorescence channel (cyan). Images A and B were incubated with 0.65µg ml^{-1} and C with 1.3µg ml^{-1}. Scale bars are 10µm.

PtNCs suspended in PBS during cellular incubation appeared to generate a much higher fluorescent signal from intracellular locations than the cells in serum free. Image A and image C (Figure 5.8) were incubated with identical concentrations of PtNCs however the fluorescent intensity between the two samples is vast. From these data it is not possible to say definitively what caused the change in fluorescent intensity. A number of potential mechanisms could be at play: a higher number of PtNCs were able to enter the cell, a component in the serum free media diminished the fluorescence, the PBS enhanced the fluorescence or a combination of the above. The subcellular localisation of the PtNCs changes when incubated with PBS. A larger proportion of the fluorescent signal in these samples was diffuse throughout the cytosol. Although more prominent in the PBS incubated samples, large structures that were microns in diameter, appear to sequester high concentrations of

PtNCs producing high levels of fluorescence. Experiments regarding passive PtNC uptake were always performed in at least duplicate with several concentrations of PtNCs. In addition, experiments were repeated to check variation in experimental setup was not the cause of any observed differences. In the case of the SNX labelling shown in figure 5.7, this was also performed with HeLa cells and RPE1 cells to ensure the cells themselves were not the cause of the inconsistencies. To further investigate the feasibility of using PtNCs as CLEM probes and to more thoroughly elucidate these large micron sized structures TEM was employed.

5.4.1 PtNCs as a CLEM Probe

As previously outlined, CLEM probes must be fluorescent and electron dense entities. Ideally these two attributes must also have a high spatial overlap in order to facilitate accurate correlation of LM and TEM images. As previously shown, the fluorescent signal exhibited by these clusters was detectable with laser scanning confocal microscopy (Section 5.4) and also appeared to enhance with silver (Section 5.3). However, the question still remains if it is possible to correlate the fluorescent signal with electron density as part of a CLEM workflow.

HeLa cells were seeded, serum starved for 2 hours before labelling with PtNCs for 30 minutes. After imaging with confocal microscopy samples were immediately processed for TEM. The cells were firstly more thoroughly fixed with 2% glutaraldehyde before silver enhancing. Silver enhancement of PtNCs was paramount to enable straight forward visualisation. Silver enhancement solution was made up following the manufacturer's instruction and left to incubate for one and a half hours. This is longer than the manufacturer recommends but was performed this way to compensate for any silver stripped away by the osmium tetroxide and the smaller initial nucleation site.

Confocal microscopy revealed large micron sized structures with a high fluorescent signal and therefore sequestering large quantities of PtNCs. CLEM enabled the ultrastructure of these structures to be visualised in high detail. Each structure consisted of a dense overlapping and chaotic network of lipid membranes. This structure did not look native and did not appear in any of the control sections where cells were not exposed to PEI stabilised PtNCs.

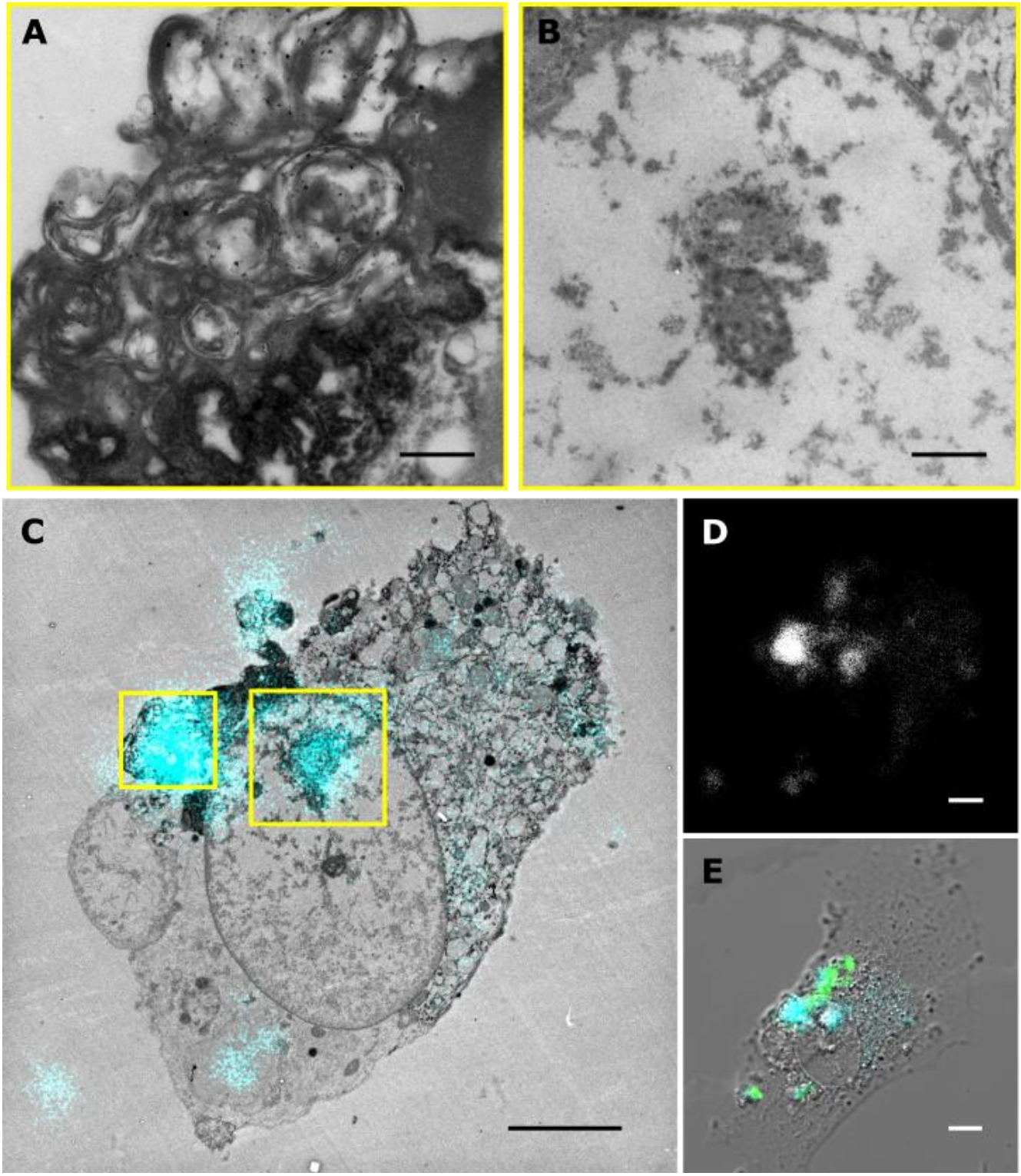

Figure 5.9: A CLEM experiment to correlate confocal and TEM images of PtNCs taken up passively by HeLa cells. Images A and B are electron micrographs of areas of interest containing PtNCs. Image C contains an electron micrograph overlaid with false colour fluorescent signal of the PtNCs. Image D is the raw fluorescent signal of the PtNCs displayed in grayscale. Image E shows PtNC fluorescence (cyan) and SNX1 labelling (green) in a composite image with the transmitted light channel. Scale bars represent 500nm and 5µm in images A and B and C, D and E respectively.

Despite the negative aspects of PEI exposure pertaining to the cytotoxicity and non-native membrane architecture, these large membrane structures enabled relatively straight forward correlation of LM and TEM images. Using etched glass coverslip bottom dishes (MatTek, P35G-1.5-14-CGRD) it was possible to image the exact same cell in both the confocal and TEM microscope. Image C (Figure 5.9) shows the overlay of these two imaging modalities. The fluorescence generated from the PEI-PtNCs correlates neatly with the PEI induced membrane structures. The SNX1 labelling displayed in image E (green) shows very little correlation with the PtNCs (cyan). Using the TEM to achieve higher magnification and resolution, it is possible to resolve very dense punctae, concomitant with areas of high fluorescence (displayed in image A and B to a lesser extent). The similarities between the punctae in this sample and the drop deposited silver enhanced PtNCs (Figure 5.4) is striking with regard to both size and morphology. Furthermore, these small punctae do not appear in areas devoid of fluorescence. If these punctae were merely an artefact or some other unrelated structure they would be visible extracellularly or in other parts of the cell. The tight correlation between these two signals suggests it is highly probable that these punctae are silver enhanced PtNCs. This is an encouraging and provides the first evidence that suggests NCs could potentially be used as CLEM probes

5.5 Discussion

This chapter provided the initial steps that PtNCs are a plausible candidate for the basis of a robust CLEM probe. PtNCs possess many desirable attributes for use as a CLEM probe: small size, high quantum yield and low cytotoxicity (all depending on the scaffold molecule). In particular fluorescence generation by an electron dense body is especially sort after, providing near perfect signal correlation between FM and EM imaging modalities.

The drop deposition and UV-vis experiments provided evidence that PtNCs are the site of silver ion nucleation during the silver enhancement process. There were some initial concerns that silver enhancement may fail due to the PEI ligand inducing excessive steric hindrance upon the cluster. The low pH required for the silver enhancement reaction to progress could have compromised the stabilising effect of the PEI. The attractive interaction between PEI and the sequestered PtNC may have also become weakened, allowing silver ions to gain entry. Being able to silver enhance NCs is paramount, as without it NCs would remain a niche probe as the vast majority of electron microscopes would be unable to visualise them. However, these findings show silver enhanced

PtNCs generated sufficient electron density to be visualised on a TEM micrograph even in the context of a heavy metal stain cellular environment.

The behaviour with regard to subcellular localisation of PtNCs was difficult to predict and was not always reproducible. The unpredictable nature of these particles could at times render the ability to draw meaningful conclusions difficult. The reason for this unpredictable behaviour may be due to the degradation/aggregation of the PtNCs over time. Even with sonication and vortexing it was not possible to consistently reproduce the punctate subcellular localisation shown in Figure 5.6. However, from the data generated small changes in extracellular media and eventual corona did play a role in PtNC uptake and/or fluorescent output.

The abnormal lipid membrane structures formed in response to incubation with PtNCs is likely a result of the PEI scaffolding molecule. A paper which exposed the external membrane of gram negative bacteria (*S. typhimurium*) to PEI generated similar balloon like membrane structures. Some of which contained a high electron density suggesting a similar underlying chaotic membrane system within. The paper demonstrated that PEI exposure to *S. typhimurium* up to a concentration of 10µg ml^{-1} did not have any significant bactericidal effect but did compromise the membrane integrity. This loss of integrity sensitised the bacteria to detergents and hydrophobic molecules that ordinarily would have had a negligible effect (Helander et al., 1998). The bacterial cell wall and additional internal membrane may be responsible for mitigating the toxic effects of PEI, however with fewer protective boundaries mammalian cells are more vulnerable. A paper published by Inoue's group using the same PEI scaffold to grow PtNCs did demonstrate a 10% reduction in cell (HeLa) viability after 48 hours when exposed to 100nM of PEI-PtNCs (Huang et al., 2016). The cytotoxic effect may be elicited by PEI binding to several of the proteins that mediate apoptosis as well as compromising mitochondrial membranes allowing protons to escape (Khansarizadeh et al., 2016).

5.5.1 Future Work

This chapter demonstrates that PtNCs can be taken up by cells, imaged *in vivo* with FM, silver enhanced and finally visualised in TEM. The combination of these attributes provided a proof of concept that PtNCs (as well as fluorescent nanoclusters in general) could be used to fill this brief. Their straightforward and robust synthesis enabled rapid acquisition of samples and minimal

troubleshooting. Their robust nature and high stability enabled them to remain intact during transport from Japan back to the United Kingdom. However, future work should focus on moving away from the current scaffold molecule, PEI. When compared to other scaffold molecules the branched PEI used for these PtNCs is fairly large. Small scaffold molecules such as mercaptoethanoic acid (Tanaka et al., 2013) that minimize steric hindrance are advantageous for use as probes to maximise target binding. Excess sections of scaffold, especially molecular "branches", can interfere and frustrate target binding. Furthermore, a smaller probe is preferable in order to maximise sample penetration, especially in the case of pre-embedded sections. Finally, the variable mass of each PEI molecule means accurate characterisation of cluster size and morphology by mass spectrometry is not possible.

A second argument in favour of changing scaffold molecule is the adverse effects on cells exposed to PEI. Other published work using PEI stabilised PtNCs similar to the ones used in this thesis were shown to be cytotoxic at concentrations as low as 100nM (Huang et al., 2016). In the context of a CLEM experiment a probe impacting cellular function is detrimental. Probes should perturb native cell structure and function as little as possible to ensure any changes measured/observed are purely a result of the variable factors of the experiment. The data shown in figure 5.9 illustrate a non-native membrane architecture induced upon exposure to PEI. This appears to be an artefact induced by the presence of PEI which is supported by the literature (Helander et al., 1998). PEI has also been shown to change membrane permeabilisation further altering native cell behaviour (Khansarizadeh et al., 2016)

The next most important step would be to functionalise the NC with a relevant targeting molecule. Currently the PEI supporting the PtNCs is not conjugated to any other biomolecule and so are passively taken up by the cells. In order to answer biologically relevant questions, the probes need to co-localise with a specific protein/biomolecule. During the course of this work transferrin was conjugated to the PtNCs using a bifunctional linker N-Ɛ-malemidocaproyl-oxysuccinimide ester (ECMS). As expected, this did localise fluorescence to what appeared to be the endocytic network but presented similarly to passive up take. Therefore, no meaningful conclusions can be drawn from this but other targeting methods would be required to ensure PtNCs are a robust and flexible CLEM probe.

Direct EM visualisation of PtNCs may be possible with the aid of specialist EM techniques. Using EDX to image PtNCs taken up by cells may be an alternative way to visualise the PtNCs without requiring silver enhancement. EDX could also be used to lend additional credibility to the idea the PtNCs are the nucleation centre for silver growth. A pre-embedded sample could be imaged with EDX before and after silver enhancement and the colocalisation of Pt and Ag signal could be scrutinised. Finally, super-STEM may also be an exciting technique to utilize to visualise NCs *in vivo.* This technique is known for its incredible resolving power generating super high-quality images. STEM techniques rely on the ability of the sample to scatter. Since PtNCs are composed of an element with a very high Z number, they would be well suited to this imaging modality.

Chapter 6

Final Discussion

6. Final Discussion

Two CLEM probe systems have been designed, synthesised and tested. The affinity CLEM probe system based upon the tight binding of the protein FKBP and its ligand SLF' may require further work before it is a complete and robust label. In an effort to create a robust CLEM probe a EGFP-FKBP tag was genetically fused to the protein of interest SNX1. The tag was then tested in a number of *in vivo* and *in vitro* assays to ensure the protein of interest retained correct native function and intracellular trafficking. The protein tag did not have a detrimental impact and the EFS1 construct was shown to form tubules *in vivo* and *in vitro,* retain accessory protein binding in both *in vivo* and *in vitro* studies and correctly co-localise with intracellular targets *in vivo*.

The binding affinity of FKBP remained high even when the SLF' was conjugated to the AuNP label. *In vitro* experiments labelling SNX1 tubules showed a >20% increase in colocalisation of AuNP labels with lipid membranes and tubules. High AuNP labelling density was observed on lipid tubules *in vitro* but not enough to infer higher order oligomeric states of the SNX1 protein. Unfortunately, this increased labelling efficiency did not translate to *in vivo* experiments, no colocalisation of fluorescent signal and AuNP labels was observed in either pre-embedded or post-embedded labelling protocols. There could be a number of reasons why signal colocalisation was not observed between the fluorescent protein constructs and the SLF' AuNP labels. The most likely is that the binding pocket of the FKBP is very sensitive to fixation. In both pre-embedded and post embedded samples used fixative (PFA and UA) before labelling SLF' AuNP. This fixation step may have already compromised the FKBP binding pocket prior to labelling. However labelling was observed during *in vitro* experiments which avoided fixation. If this is the case the probe may retain some niche usage in live cell imaging and more specialist workflows which can delay fixation post labelling such as Tokuyasu (although PFA is still used as a post fixative). The advantages to this probes system stems from its high binding affinity and small size which may allow targets to be labelled not typically accessible to antibodies or other larger probes.

Fluorescent nanoclusters however have shown promise for use as a CLEM probe. PtNCs produced a readily discernible fluorescent signal *in vivo* despite having a quantum yield of 4.8%. Likewise with the aid of silver enhancement PtNCs were observable and produced high contrast in electron micrographs. Signals acquired in the two imaging modalities were shown to co-localise when

analysed with correlative techniques. These experiments demonstrate a proof of concept that nanocluster based CLEM probes are feasible and opens the door for further exploration. The synthesis of the nanoclusters used in this study was performed in Professor Inoue's Nanobiophotonics Lab in Osaka University, Japan and were brought back to the UK. Therefore the PtNCs were chosen for practical purposes: straight forward synthesis pathway and long-term stability. Favouring these attributes required compromising on others which are arguably more important for use as a CLEM probe.

Further development of fluorescent nanocluster CLEM probes should revolve around the scaffolding molecule and quantum yield. The fluorescent signal was only visible using hybrid detectors on a laser confocal microscope which may limit usage of the probe. Increasing the quantum yield to enable clear visualisation using PMT detectors should be investigated. Altering the scaffolding molecule could address this while also improving biocompatibility and reducing overall probe size. The PEI scaffolding molecule used for these clusters was shown to damage cell membranes and cause formation abhorrent membrane structures *in vivo.* Surprisingly the steric hindrance imposed on the nanocluster by the scaffold molecule did not abolish silver enhancement. Nanocluster based probes can therefore readily be substituted into CLEM workflows without the need for specialist protocols or EM techniques. However, alternative scaffold molecules will likely vary in how much surface area of the nanocluster it occludes and how tightly it binds. Testing therefore will likely be required on a case by case basis. The final consideration would be to identify a method to localise the probe to its target whether that is via antibody conjugation or some other method. As a proof of concept study the data shown here is encouraging and suggests these nanoclusters could make versatile and robust probes. They avoid any signal separation between fluorescence and electron density which could increase the resolution of correlative studies and image registration accuracy which is particularly relevant when considering the rise of super resolution techniques. These PtNCs were also shown to act as nucleation points for silver enhancement protocols. This greatly increases the accessibility/versatility of these probes allowing them to be visualised with the use of standard EM techniques.

7.1 Appendix

7.1.1 Plasmid Sequences

7.1.1.1 pET45b(+) Commercial Vector Sequence

TGGCGAATGGGACGCGCCCTGTAGCGGCGCATTAAGCGCGGCGGGTGTGGTGGTTACGCGCAGCGTGACCGCTACACTTGCCAGCGCCCTAGCGCCCGCTCCTTTCGCTTTCTT
CCCTTCCTTTCTCGCCACGTTCGCCGGCTTTCCCCGTCAAGCTCTAAATCGGGGGCTCCCTTTAGGGTTCCGATTTAGTGCTTTACGGCACCTCGACCCCAAAAAACTTGATTAGGG
TGATGGTTCACGTAGTGGGCCATCGCCCTGATAGACGGTTTTTCGCCCTTTGACGTTGGAGTCCACGTTCTTTAATAGTGGACTCTTGTTCCAAACTGGAACAACACTCAACCCTAT
CTCGGTCTATTCTTTTGATTTATAAGGGATTTTGCCGATTTCGGCCTATTGGTTAAAAAATGAGCTGATTTAACAAAAATTTAACGCGAATTTTAACAAAATATTAACGTTTACAATT
TCTGGCGGCACGATGGCATGAGATTATCAAAAAGGATCTTCACCTAGATCCTTTTAAATTAAAAATGAAGTTTTAAATCAATCTAAAGTATATATGAGTAAACTTGGTCTGACAGT
TACCAATGCTTAATCAGTGAGGCACCTATCTCAGCGATCTGTCTATTTCGTTCATCCATAGTTGCCTGACTCCCCGTCGTGTAGATAACTACGATACGGGAGGGCTTACCATCTGGC
CCCAGTGCTGCAATGATACCGCGAGACCCACGCTCACCGGCTCCAGATTTATCAGCAATAAACCAGCCAGCCGGAAGGGCCGAGCGCAGAAGTGGTCCTGCAACTTTATCCGCC
TCCATCCAGTCTATTAATTGTTGCCGGGAAGCTAGAGTAAGTAGTTCGCCAGTTAATAGTTTGCGCAACGTTGTTGCCATTGCTACAGGCATCGTGGTGTCACGCTCGTCGTTTGG
TATGGCTTCATTCAGCTCCGGTTCCCAACGATCAAGGCGAGTTACATGATCCCCCATGTTGTGCAAAAAAGCGGTTAGCTCCTTCGGTCCTCCGATCGTTGTCAGAAGTAAGTTGG
CCGCAGTGTTATCACTCATGGTTATGGCAGCACTGCATAATTCTCTTACTGTCATGCCATCCGTAAGATGCTTTTCTGTGACTGGTGAGTACTCAACCAAGTCATTCTGAGAATAGT
GTATGCGGCGACCGAGTTGCTCTTGCCCGGCGTCAATACGGGATAATACCGCGCCACATAGCAGAACTTTAAAAGTGCTCATCATTGGAAAACGTTCTTCGGGGCGAAAACTCTC
AAGGATCTTACCGCTGTTGAGATCCAGTTCGATGTAACCCACTCGTGCACCCAACTGATCTTCAGCATCTTTTACTTTCACCAGCGTTTCTGGGTGAGCAAAAACAGGAAGGCAAA
ATGCCGCAAAAAAGGGAATAAGGGCGACACGGAAATGTTGAATACTCATACTCTTCCTTTTTCAATCATGATTGAAGCATTTATCAGGGTTATTGTCTCATGAGCGGATACATATT
TGAATGTATTTAGAAAAATAAACAAATAGGTCATGACCAAAATCCCTTAACGTGAGTTTTCGTTCCACTGAGCGTCAGACCCCGTAGAAAAGATCAAAGGATCTTCTTGAGATCCT
TTTTTTCTGCGCGTAATCTGCTGCTTGCAAACAAAAAAACCACCGCTACCAGCGGTGGTTTGTTTGCCGGATCAAGAGCTACCAACTCTTTTTCCGAAGGTAACTGGCTTCAGCAG
AGCGCAGATACCAAATACTGTCCTTCTAGTGTAGCCGTAGTTAGGCCACCACTTCAAGAACTCTGTAGCACCGCCTACATACCTCGCTCTGCTAATCCTGTTACCAGTGGCTGCTG
CCAGTGGCGATAAGTCGTGTCTTACCGGGTTGGACTCAAGACGATAGTTACCGGATAAGGCGCAGCGGTCGGGCTGAACGGGGGGTTCGTGCACACAGCCCAGCTTGGAGCGA
ACGACCTACACCGAACTGAGATACCTACAGCGTGAGCTATGAGAAAGCGCCACGCTTCCCGAAGGGAGAAAGGCGGACAGGTATCCGGTAAGCGGCAGGGTCGGAACAGGAG
AGCGCACGAGGGAGCTTCCAGGGGGAAACGCCTGGTATCTTTATAGTCCTGTCGGGTTTCGCCACCTCTGACTTGAGCGTCGATTTTTGTGATGCTCGTCAGGGGGGCGGAGCC
TATGGAAAAACGCCAGCAACGCGGCCTTTTTACGGTTCCTGGCCTTTTGCTGGCCTTTTGCTCACATGTTCTTTCCTGCGTTATCCCCTGATTCTGTGGATAACCGTATTACCGCCTT
TGAGTGAGCTGATACCGCTCGCCGCAGCCGAACGACCGAGCGCAGCGAGTCAGTGAGCGAGGAAGCGGAAGAGCGCCTGATGCGGTATTTTCTCCTTACGCATCTGTGCGGTA
TTTCACACCGCATATATGGTGCACTCTCAGTACAATCTGCTCTGATGCCGCATAGTTAAGCCAGTATACACTCCGCTATCGCTACGTGACTGGGTCATGGCTGCGCCCCGACACCC
GCCAACACCCGCTGACGCGCCCTGACGGGCTTGTCTGCTCCCGGCATCCGCTTACAGACAAGCTGTGACCGTCTCCGGGAGCTGCATGTGTCAGAGGTTTTCACCGTCATCACCG
AAACGCGCGAGGCAGCTGCGGTAAAGCTCATCAGCGTGGTCGTGAAGCGATTCACAGATGTCTGCCTGTTCATCCGCGTCCAGCTCGTTGAGTTTCTCCAGAAGCGTTAATGTCT
GGCTTCTGATAAAGCGGGCCATGTTAAGGGCGGTTTTTTCCTGTTTGGTCACTGATGCCTCCGTGTAAGGGGGATTTCTGTTCATGGGGGTAATGATACCGATGAAACGAGAGA
GGATGCTCACGATACGGGTTACTGATGATGAACATGCCCGGTTACTGGAACGTTGTGAGGGTAAACAACTGGCGGTATGGATGCGGCGGGACCAGAGAAAAATCACTCAGGGT
CAATGCCAGCGCTTCGTTAATACAGATGTAGGTGTTCCACAGGGTAGCCAGCAGCATCCTGCGATGCAGATCCGGAACATAATGGTGCAGGGCGCTGACTTCCGCGTTTCCAGA
CTTTACGAAACACGGAAACCGAAGACCATTCATGTTGTTGCTCAGGTCGCAGACGTTTTGCAGCAGCAGTCGCTTCACGTTCGCTCGCGTATCGGTGATTCATTCTGCTAACCAGT
AAGGCAACCCCGCCAGCCTAGCCGGGTCCTCAACGACAGGAGCACGATCATGCTAGTCATGCCCCGCGCCCACCGGAAGGAGCTGACTGGGTTGAAGGCTCTCAAGGGCATCG
GTCGAGATCCCGGTGCCTAATGAGTGAGCTAACTTACATTAATTGCGTTGCGCTCACTGCCCGCTTTCCAGTCGGGAAACCTGTCGTGCCAGCTGCATTAATGAATCGGCCAACG
CGCGGGGAGAGGCGGTTTGCGTATTGGGCGCCAGGGTGGTTTTTCTTTTCACCAGTGAGACGGGCAACAGCTGATTGCCCTTCACCGCCTGGCCCTGAGAGAGTTGCAGCAAGC
GGTCCACGCTGGTTTGCCCCAGCAGGCGAAAATCCTGTTTGATGGTGGTTAACGGCGGGATATAACATGAGCTGTCTTCGGTATCGTCGTATCCCACTACCGAGATGTCCGCACC
AACGCGCAGCCCGGACTCGGTAATGGCGCGCATTGCGCCCAGCGCCATCTGATCGTTGGCAACCAGCATCGCAGTGGGAACGATGCCCTCATTCAGCATTTGCATGGTTTGTTGA
AAACCGGACATGGCACTCCAGTCGCCTTCCCGTTCCGCTATCGGCTGAATTTGATTGCGAGTGAGATATTTATGCCAGCCAGCCAGACGCAGACGCGCCGAGACAGAACTTAATG
GGCCCGCTAACAGCGCGATTTGCTGGTGACCCAATGCGACCAGATGCTCCACGCCCAGTCGCGTACCGTCTTCATGGGAGAAAATAATACTGTTGATGGGTGTCTGGTCAGAGA
CATCAAGAAATAACGCCGGAACATTAGTGCAGGCAGCTTCCACAGCAATGGCATCCTGGTCATCCAGCGGATAGTTAATGATCAGCCCACTGACGCGTTGCGCGAGAAGATTGT
GCACCGCCGCTTTACAGGCTTCGACGCCGCTTCGTTCTACCATCGACACCACCACGCTGGCACCCAGTTGATCGGCGCGAGATTTAATCGCCGCGACAATTTGCGACGGCGCGTG
CAGGGCCAGACTGGAGGTGGCAACGCCAATCAGCAACGACTGTTTGCCCGCCAGTTGTTGTGCCACGCGGTTGGGAATGTAATTCAGCTCCGCCATCGCCGCTTCCACTTTTTCC
CGCGTTTTCGCAGAAACGTGGCTGGCCTGGTTCACCACGCGGGAAACGGTCTGATAAGAGACACCGGCATACTCTGCGACATCGTATAACGTTACTGGTTTCACATTCACCACCC
TGAATTGACTCTCTTCCGGGCGCTATCATGCCATACCGCGAAAGGTTTTGCGCCATTCGATGGTGTCCGGGATCTCGACGCTCTCCCTTATGCGACTCCTGCATTAGGAAGCAGCC
CAGTAGTAGGTTGAGGCCGTTGAGCACCGCCGCCGCAAGGAATGGTGCATGCAAGGAGATGGCGCCCAACAGTCCCCCGGCCACGGGGCCTGCCACCATACCCACGCCGAAAC
AAGCGCTCATGAGCCCGAAGTGGCGAGCCCGATCTTCCCCATCGGTGATGTCGGCGATATAGGCGCCAGCAACCGCACCTGTGGCGCCGGTGATGCCGGCCACGATGCGTCCG
GCGTAGAGGATCGAGATCGATCTCGATCCCGCGAAATTAATACGACTCACTATAGGGGAATTGTGAGCGGATAACAATTCCCCTCTAGAAATAATTTTGTTTAACTTTAAGAAGG
AGATATACCATGGCACATCACCACCACCATCACGTGGGTACCGGTTCGAATGATGACGACGACAAGAGTCCGGATCCCAATTGGGAGCTCGTGTACACGGCGCGCCTGCAGGTC
GACAAGCTTGCGGCCGCACTCGAGTCTGGTAAAGAAACCGCTGCTGCGAAATTTGAACGCCAGCACATGGACTCGTCTACTAGCGCAGCTTAATTAACCTAGGCTGCTGCCACCG
CTGAGCAATAACTAGCATAACCCCTTGGGGCCTCTAAACGGGTCTTGAGGGGTTTTTTGCTGAAAGGAGGAACTATATCCGGAT

7.1.1.2 pET45b(+) EGFP-FKBP-SNX1

TGGCGAATGGGACGCGCCCTGTAGCGGCGCATTAAGCGCGGCGGGTGTGGTGGTTACGCGCAGCGTGACCGCTACACTTGCCAGCGCCCTAGCGCCCGCTCCTTTCGCTTTCTT
CCCTTCCTTTCTCGCCACGTTCGCCGGCTTTCCCCGTCAAGCTCTAAATCGGGGGCTCCCTTTAGGGTTCCGATTTAGTGCTTTACGGCACCTCGACCCCAAAAAACTTGATTAGGG
TGATGGTTCACGTAGTGGGCCATCGCCCTGATAGACGGTTTTTCGCCCTTTGACGTTGGAGTCCACGTTCTTTAATAGTGGACTCTTGTTCCAAACTGGAACAACACTCAACCCTAT
CTCGGTCTATTCTTTTGATTTATAAGGGATTTTGCCGATTTCGGCCTATTGGTTAAAAAATGAGCTGATTTAACAAAAATTTAACGCGAATTTTAACAAAATATTAACGTTTACAATT
TCTGGCGGCACGATGGCATGAGATTATCAAAAAGGATCTTCACCTAGATCCTTTTAAATTAAAAATGAAGTTTTAAATCAATCTAAAGTATATATGAGTAAACTTGGTCTGACAGT
TACCAATGCTTAATCAGTGAGGCACCTATCTCAGCGATCTGTCTATTTCGTTCATCCATAGTTGCCTGACTCCCCGTCGTGTAGATAACTACGATACGGGAGGGCTTACCATCTGGC
CCCAGTGCTGCAATGATACCGCGAGACCCACGCTCACCGGCTCCAGATTTATCAGCAATAAACCAGCCAGCCGGAAGGGCCGAGCGCAGAAGTGGTCCTGCAACTTTATCCGCC
TCCATCCAGTCTATTAATTGTTGCCGGGAAGCTAGAGTAAGTAGTTCGCCAGTTAATAGTTTGCGCAACGTTGTTGCCATTGCTACAGGCATCGTGGTGTCACGCTCGTCGTTTGG

TATGGCTTCATTCAGCTCCGGTTCCCAACGATCAAGGCGAGTTACATGATCCCCCATGTTGTGCAAAAAAGCGGTTAGCTCCTTCGGTCCTCCGATCGTTGTCAGAAGTAAGTTGG
CCGCAGTGTTATCACTCATGGTTATGGCAGCACTGCATAATTCTCTTACTGTCATGCCATCCGTAAGATGCTTTTCTGTGACTGGTGAGTACTCAACCAAGTCATTCTGAGAATAGT
GTATGCGGCGACCGAGTTGCTCTTGCCCGGCGTCAATACGGGATAATACCGCGCCACATAGCAGAACTTTAAAAGTGCTCATCATTGGAAAACGTTCTTCGGGGCGAAAACTCTC
AAGGATCTTACCGCTGTTGAGATCCAGTTCGATGTAACCCACTCGTGCACCCAACTGATCTTCAGCATCTTTTACTTTCACCAGCGTTTCTGGGTGAGCAAAAACAGGAAGGCAAA
ATGCCGCAAAAAAGGGAATAAGGGCGACACGGAAATGTTGAATACTCATACTCTTCCTTTTTCAATCATGATTGAAGCATTTATCAGGGTTATTGTCTCATGAGCGGATACATATT
TGAATGTATTTAGAAAAATAAACAAATAGGTCATGACCAAAATCCCTTAACGTGAGTTTTCGTTCCACTGAGCGTCAGACCCCGTAGAAAAGATCAAAGGATCTTCTTGAGATCCT
TTTTTTCTGCGCGTAATCTGCTGCTTGCAAACAAAAAAACCACCGCTACCAGCGGTGGTTTGTTTGCCGGATCAAGAGCTACCAACTCTTTTTCCGAAGGTAACTGGCTTCAGCAG
AGCGCAGATACCAAATACTGTCCTTCTAGTGTAGCCGTAGTTAGGCCACCACTTCAAGAACTCTGTAGCACCGCCTACATACCTCGCTCTGCTAATCCTGTTACCAGTGGCTGCTG
CCAGTGGCGATAAGTCGTGTCTTACCGGGTTGGACTCAAGACGATAGTTACCGGATAAGGCGCAGCGGTCGGGCTGAACGGGGGGTTCGTGCACACAGCCCAGCTTGGAGCGA
ACGACCTACACCGAACTGAGATACCTACAGCGTGAGCTATGAGAAAGCGCCACGCTTCCCGAAGGGAGAAAGGCGGACAGGTATCCGGTAAGCGGCAGGGTCGGAACAGGAG
AGCGCACGAGGGAGCTTCCAGGGGGAAACGCCTGGTATCTTTATAGTCCTGTCGGGTTTCGCCACCTCTGACTTGAGCGTCGATTTTTGTGATGCTCGTCAGGGGGGCGGAGCC
TATGGAAAAACGCCAGCAACGCGGCCTTTTTACGGTTCCTGGCCTTTTGCTGGCCTTTTGCTCACATGTTCTTTCCTGCGTTATCCCCTGATTCTGTGGATAACCGTATTACCGCCTT
TGAGTGAGCTGATACCGCTCGCCGCAGCCGAACGACCGAGCGCAGCGAGTCAGTGAGCGAGGAAGCGGAAGAGCGCCTGATGCGGTATTTTCTCCTTACGCATCTGTGCGGTA
TTTCACACCGCATATATGGTGCACTCTCAGTACAATCTGCTCTGATGCCGCATAGTTAAGCCAGTATACACTCCGCTATCGCTACGTGACTGGGTCATGGCTGCGCCCCGACACCC
GCCAACACCCGCTGACGCGCCCTGACGGGCTTGTCTGCTCCCGGCATCCGCTTACAGACAAGCTGTGACCGTCTCCGGGAGCTGCATGTGTCAGAGGTTTTCACCGTCATCACCG
AAACGCGCGAGGCAGCTGCGGTAAAGCTCATCAGCGTGGTCGTGAAGCGATTCACAGATGTCTGCCTGTTCATCCGCGTCCAGCTCGTTGAGTTTCTCCAGAAGCGTTAATGTCT
GGCTTCTGATAAAGCGGGCCATGTTAAGGGCGGTTTTTTCCTGTTTGGTCACTGATGCCTCCGTGTAAGGGGGATTTCTGTTCATGGGGGTAATGATACCGATGAAACGAGAGA
GGATGCTCACGATACGGGTTACTGATGATGAACATGCCCGGTTACTGGAACGTTGTGAGGGTAAACAACTGGCGGTATGGATGCGGCGGGACCAGAGAAAAATCACTCAGGGT
CAATGCCAGCGCTTCGTTAATACAGATGTAGGTGTTCCACAGGGTAGCCAGCAGCATCCTGCGATGCAGATCCGGAACATAATGGTGCAGGGCGCTGACTTCCGCGTTTCCAGA
CTTTACGAAACACGGAAACCGAAGACCATTCATGTTGTTGCTCAGGTCGCAGACGTTTTGCAGCAGCAGTCGCTTCACGTTCGCTCGCGTATCGGTGATTCATTCTGCTAACCAGT
AAGGCAACCCCGCCAGCCTAGCCGGGTCCTCAACGACAGGAGCACGATCATGCTAGTCATGCCCCGCGCCCACCGGAAGGAGCTGACTGGGTTGAAGGCTCTCAAGGGCATCG
GTCGAGATCCCGGTGCCTAATGAGTGAGCTAACTTACATTAATTGCGTTGCGCTCACTGCCCGCTTTCCAGTCGGGAAACCTGTCGTGCCAGCTGCATTAATGAATCGGCCAACG
CGCGGGGAGAGGCGGTTTGCGTATTGGGCGCCAGGGTGGTTTTTCTTTTCACCAGTGAGACGGGCAACAGCTGATTGCCCTTCACCGCCTGGCCCTGAGAGAGTTGCAGCAAGC
GGTCCACGCTGGTTTGCCCCAGCAGGCGAAAATCCTGTTTGATGGTGGTTAACGGCGGGATATAACATGAGCTGTCTTCGGTATCGTCGTATCCCACTACCGAGATGTCCGCACC
AACGCGCAGCCCGGACTCGGTAATGGCGCGCATTGCGCCCAGCGCCATCTGATCGTTGGCAACCAGCATCGCAGTGGGAACGATGCCCTCATTCAGCATTTGCATGGTTTGTTGA
AAACCGGACATGGCACTCCAGTCGCCTTCCCGTTCCGCTATCGGCTGAATTTGATTGCGAGTGAGATATTTATGCCAGCCAGCCAGACGCAGACGCGCCGAGACAGAACTTAATG
GGCCCGCTAACAGCGCGATTTGCTGGTGACCCAATGCGACCAGATGCTCCACGCCCAGTCGCGTACCGTCTTCATGGGAGAAAATAATACTGTTGATGGGTGTCTGGTCAGAGA
CATCAAGAAATAACGCCGGAACATTAGTGCAGGCAGCTTCCACAGCAATGGCATCCTGGTCATCCAGCGGATAGTTAATGATCAGCCCACTGACGCGTTGCGCGAGAAGATTGT
GCACCGCCGCTTTACAGGCTTCGACGCCGCTTCGTTCTACCATCGACACCACCACGCTGGCACCCAGTTGATCGGCGCGAGATTTAATCGCCGCGACAATTTGCGACGGCGCGTG
CAGGGCCAGACTGGAGGTGGCAACGCCAATCAGCAACGACTGTTTGCCCGCCAGTTGTTGTGCCACGCGGTTGGGAATGTAATTCAGCTCCGCCATCGCCGCTTCCACTTTTTCC
CGCGTTTTCGCAGAAACGTGGCTGGCCTGGTTCACCACGCGGGAAACGGTCTGATAAGAGACACCGGCATACTCTGCGACATCGTATAACGTTACTGGTTTCACATTCACCACCC
TGAATTGACTCTCTTCCGGGCGCTATCATGCCATACCGCGAAAGGTTTTGCGCCATTCGATGGTGTCCGGGATCTCGACGCTCTCCCTTATGCGACTCCTGCATTAGGAAGCAGCC
CAGTAGTAGGTTGAGGCCGTTGAGCACCGCCGCCGCAAGGAATGGTGCATGCAAGGAGATGGCGCCCAACAGTCCCCCGGCCACGGGGCCTGCCACCATACCCACGCCGAAAC
AAGCGCTCATGAGCCCGAAGTGGCGAGCCCGATCTTCCCCATCGGTGATGTCGGCGATATAGGCGCCAGCAACCGCACCTGTGGCGCCGGTGATGCCGGCCACGATGCGTCCG
GCGTAGAGGATCGAGATCGATCTCGATCCCGCGAAATTAATACGACTCACTATAGGGGAATTGTGAGCGGATAACAATTCCCCTCTAGAAATAATTTTGTTTAACTTTAAGAAGG
AGATATACCATGGCACATCACCACCACCATCACGTGGGTACCGGTTCGAATGATGACGACGACAAGAGTCCGGATCCCAATTGGATGGTGAGCAAGGGCGAGGAGCTGTTCACC
GGGGTGGTGCCCATCCTGGTCGAGCTGGACGGCGACGTAAACGGCCACAAGTTCAGCGTGTCCGGCGAGGGCGAGGGCGATGCCACCTACGGCAAGCTGACCCTGAAGTTCAT
CTGCACCACCGGCAAGCTGCCCGTGCCCTGGCCCACCCTCGTGACCACCCTGACCTACGGCGTGCAGTGCTTCAGCCGCTACCCCGACCACATGAAGCAGCACGACTTCTTCAAG
TCCGCCATGCCCGAAGGCTACGTCCAGGAGCGCACCATCTTCTTCAAGGACGACGGCAACTACAAGACCCGCGCCGAGGTGAAGTTCGAGGGCGACACCCTGGTGAACCGCATC
GAGCTGAAGGGCATCGACTTCAAGGAGGACGGCAACATCCTGGGGCACAAGCTGGAGTACAACTACAACAGCCACAACGTCTATATCATGGCCGACAAGCAGAAGAACGGCAT
CAAGGTGAACTTCAAGATCCGCCACAACATCGAGGACGGCAGCGTGCAGCTCGCCGACCACTACCAGCAGAACACCCCCATCGGCGACGGCCCCGTGCTGCTGCCCGACAACCA
CTACCTGAGCACCCAGTCCGCCCTGAGCAAAGACCCCAACGAGAAGCGCGATCACATGGTCCTGCTGGAGTTCGTGACCGCCGCCGGGATCACTCTCGGCATGGACGAGCTGTA
CGGCACTAGTATGGCTTCTAGAGGAGTGCAGGTGGAGACTATCTCCCCAGGAGACGGGCGCACCTTCCCCAAGCGCGGCCAGACCTGCGTGGTGCACTACACCGGGATGCTTG
AAGATGGAAAGAAAGTTGATTCCTCCCGGGACAGAAACAAGCCCTTTAAGTTTATGCTAGGCAAGCAGGAGGTGATCCGAGGCTGGGAAGAAGGGGTTGCCCAGATGAGTGT
GGGTCAGAGAGCCAAACTGACTATATCTCCAGATTATGCCTATGGTGCCACTGGGCACCCAGGCATCATCCCACCACATGCCACTCTCGTCTTCGATGTGGAGCTTCTAAAACTGG
AATCACCGGCGCTGTACAAGTCCGGACTCAGATCTCGAGCTCAAGCTTCGAATTCTATGGCGTCGGGTGGTGGTGGCTGTAGCGCTTCGGAGAGACTGCCTCCGCCCTTCCCCGG
CCTGGAGCCGGAGTCCGAGGGGGCGGCCGGGGGATCAGAACCCGAGGCTGGGGACAGCGACACCGAGGGGGAGGACATTTTCACCGGCGCCGCGGTGGTCAGTAAACATCA
GTCTCCAAAGATAACTACATCCCTTCTTCCCATCAACAATGGCTCCAAAGAAAATGGGATCCATGAAGAACAAGACCAAGAGCCACAGGATCTCTTTGCAGATGCCACAGTGGAG
CTATCCTTGGACAGCACACAAAATAATCAGAAGAAGGTGCTAGCCAAAACACTCATTTCTCTTCCTCCTCAGGAAGCCACAAATTCTTCGAAGCCCCAGCCAACCTATGAGGAGCT
AGAGGAAGAAGAACAGGAGGATCAATTTGATTTGACAGTCGGTATAACTGATCCTGAGAAGATAGGGGATGGTATGAATGCATATGTAGCCTACAAAGTTACAACACAGACAA
GCTTACCATTGTTCAGAAGCAAACAGTTTGCAGTAAAAAGAAGATTTAGTGACTTTCTGGGTCTTTATGAGAAGCTTTCCGAGAAGCACTCTCAGAATGGCTTCATTGTCCCTCCG
CCCCCGGAGAAGAGCCTCATAGGGATGACAAAAGTGAAAGTTGGGAAGGAAGATTCTTCTTCTGCAGAATTTCTTGAAAAACGGAGGGCCGCTTTAGAAAGGTACCTTCAGAG
GATTGTAAATCATCCTACCATGTTACAGGACCCTGACGTCAGAGAGTTCTTGGAAAAAGAAGAGCTGCCACGTGCCGTGGGTACCCAGACATTGAGTGGTGCTGGTCTCCTCAAG
ATGTTCAACAAAGCCACAGATGCCGTCAGCAAAATGACCATCAAGATGAATGAATCAGACATTTGGTTTGAGGAGAAGCTCCAGGAGGTAGAGTGTGAGGAGCAGCGCTTACG
GAAACTGCATGCTGTTGTAGAAACTCTAGTCAACCATAGGAAAGAGCTAGCGCTGAACACAGCCCAGTTTGCAAAGAGTCTAGCCATGCTTGGGAGCTCTGAGGACAACACGGC
ATTGTCACGGGCACTCTCCCAGCTGGCTGAGGTGGAAGAAAAAATTGAGCAGCTCCACCAGGAACAGGCCAACAATGACTTCTTCCTCCTTGCTGAGCTCCTGAGTGACTACATT
CGCCTCCTGGCCATAGTCCGCGCTGCCTTCGACCAGCGCATGAAGACATGGCAGCGCTGGCAGGATGCCCAAGCCACACTGCAGAAGAAGCGGGAGGCCGAGGCTCGGCTGCT
GTGGGCCAACAAGCCTGATAAGCTGCAGCAGGCCAAGGACGAGATCCTCGAGTGGGAGTCTCGGGTGACTCAATATGAAAGGGACTTCGAGAGGATTTCAACAGTGGTCCGAA
AAGAAGTGATACGGTTTGAGAAAGAGAAATCCAAGGACTTCAAGAACCACGTGATCAAGTACCTTGAGACACTCCTTTACTCACAGCAGCAGCTGGCAAAGTACTGGGAAGCCT
TCCTTCCTGAGGCAAAGGCCATCTCCTAAGTCGAGTCTGGTAAAGAAACCGCTGCTGCGAAATTTGAACGCCAGCACATGGACTCGTCTACTAGCGCAGCTTAATTAACCTAGGC
TGCTGCCACCGCTGAGCAATAACTAGCATAACCCCTTGGGGCCTCTAAACGGGTCTTGAGGGGTTTTTTGCTGAAAGGAGGAACTATATCCGGAT

7.1.1.3 pET45b(+) EGFP-wtFKBP-SNX1

TGGCGAATGGGACGCGCCCTGTAGCGGCGCATTAAGCGCGGCGGGTGTGGTGGTTACGCGCAGCGTGACCGCTACACTTGCCAGCGCCCTAGCGCCCGCTCCTTTCGCTTTCTT
CCCTTCCTTTCTCGCCACGTTCGCCGGCTTTCCCCGTCAAGCTCTAAATCGGGGGCTCCCTTTAGGGTTCCGATTTAGTGCTTTACGGCACCTCGACCCCAAAAAACTTGATTAGGG
TGATGGTTCACGTAGTGGGCCATCGCCCTGATAGACGGTTTTTCGCCCTTTGACGTTGGAGTCCACGTTCTTTAATAGTGGACTCTTGTTCCAAACTGGAACAACACTCAACCCTAT
CTCGGTCTATTCTTTTGATTTATAAGGGATTTTGCCGATTTCGGCCTATTGGTTAAAAAATGAGCTGATTTAACAAAAATTTAACGCGAATTTTAACAAAATATTAACGTTTACAATT
TCTGGCGGCACGATGGCATGAGATTATCAAAAAGGATCTTCACCTAGATCCTTTTAAATTAAAAATGAAGTTTTAAATCAATCTAAAGTATATATGAGTAAACTTGGTCTGACAGT
TACCAATGCTTAATCAGTGAGGCACCTATCTCAGCGATCTGTCTATTTCGTTCATCCATAGTTGCCTGACTCCCCGTCGTGTAGATAACTACGATACGGGAGGGCTTACCATCTGGC

CCCAGTGCTGCAATGATACCGCGAGACCCACGCTCACCGGCTCCAGATTTATCAGCAATAAACCAGCCAGCCGGAAGGGCCGAGCGCAGAAGTGGTCCTGCAACTTTATCCGCC
TCCATCCAGTCTATTAATTGTTGCCGGGAAGCTAGAGTAAGTAGTTCGCCAGTTAATAGTTTGCGCAACGTTGTTGCCATTGCTACAGGCATCGTGGTGTCACGCTCGTCGTTTGG
TATGGCTTCATTCAGCTCCGGTTCCCAACGATCAAGGCGAGTTACATGATCCCCCATGTTGTGCAAAAAAGCGGTTAGCTCCTTCGGTCCTCCGATCGTTGTCAGAAGTAAGTTGG
CCGCAGTGTTATCACTCATGGTTATGGCAGCACTGCATAATTCTCTTACTGTCATGCCATCCGTAAGATGCTTTTCTGTGACTGGTGAGTACTCAACCAAGTCATTCTGAGAATAGT
GTATGCGGCGACCGAGTTGCTCTTGCCCGGCGTCAATACGGGATAATACCGCGCCACATAGCAGAACTTTAAAAGTGCTCATCATTGGAAAACGTTCTTCGGGGCGAAAACTCTC
AAGGATCTTACCGCTGTTGAGATCCAGTTCGATGTAACCCACTCGTGCACCCAACTGATCTTCAGCATCTTTTACTTTCACCAGCGTTTCTGGGTGAGCAAAAACAGGAAGGCAAA
ATGCCGCAAAAAAGGGAATAAGGGCGACACGGAAATGTTGAATACTCATACTCTTCCTTTTTCAATCATGATTGAAGCATTTATCAGGGTTATTGTCTCATGAGCGGATACATATT
TGAATGTATTTAGAAAAATAAACAAATAGGTCATGACCAAAATCCCTTAACGTGAGTTTTCGTTCCACTGAGCGTCAGACCCCGTAGAAAAGATCAAAGGATCTTCTTGAGATCCT
TTTTTTCTGCGCGTAATCTGCTGCTTGCAAACAAAAAAACCACCGCTACCAGCGGTGGTTTGTTTGCCGGATCAAGAGCTACCAACTCTTTTTCCGAAGGTAACTGGCTTCAGCAG
AGCGCAGATACCAAATACTGTCCTTCTAGTGTAGCCGTAGTTAGGCCACCACTTCAAGAACTCTGTAGCACCGCCTACATACCTCGCTCTGCTAATCCTGTTACCAGTGGCTGCTG
CCAGTGGCGATAAGTCGTGTCTTACCGGGTTGGACTCAAGACGATAGTTACCGGATAAGGCGCAGCGGTCGGGCTGAACGGGGGGTTCGTGCACACAGCCCAGCTTGGAGCGA
ACGACCTACACCGAACTGAGATACCTACAGCGTGAGCTATGAGAAAGCGCCACGCTTCCCGAAGGGAGAAAGGCGGACAGGTATCCGGTAAGCGGCAGGGTCGGAACAGGAG
AGCGCACGAGGGAGCTTCCAGGGGGAAACGCCTGGTATCTTTATAGTCCTGTCGGGTTTCGCCACCTCTGACTTGAGCGTCGATTTTTGTGATGCTCGTCAGGGGGGCGGAGCC
TATGGAAAAACGCCAGCAACGCGGCCTTTTTACGGTTCCTGGCCTTTTGCTGGCCTTTTGCTCACATGTTCTTTCCTGCGTTATCCCCTGATTCTGTGGATAACCGTATTACCGCCTT
TGAGTGAGCTGATACCGCTCGCCGCAGCCGAACGACCGAGCGCAGCGAGTCAGTGAGCGAGGAAGCGGAAGAGCGCCTGATGCGGTATTTTCTCCTTACGCATCTGTGCGGTA
TTTCACACCGCATATATGGTGCACTCTCAGTACAATCTGCTCTGATGCCGCATAGTTAAGCCAGTATACACTCCGCTATCGCTACGTGACTGGGTCATGGCTGCGCCCCGACACCC
GCCAACACCCGCTGACGCGCCCTGACGGGCTTGTCTGCTCCCGGCATCCGCTTACAGACAAGCTGTGACCGTCTCCGGGAGCTGCATGTGTCAGAGGTTTTCACCGTCATCACCG
AAACGCGCGAGGCAGCTGCGGTAAAGCTCATCAGCGTGGTCGTGAAGCGATTCACAGATGTCTGCCTGTTCATCCGCGTCCAGCTCGTTGAGTTTCTCCAGAAGCGTTAATGTCT
GGCTTCTGATAAAGCGGGCCATGTTAAGGGCGGTTTTTTCCTGTTTGGTCACTGATGCCTCCGTGTAAGGGGGATTTCTGTTCATGGGGGTAATGATACCGATGAAACGAGAGA
GGATGCTCACGATACGGGTTACTGATGATGAACATGCCCGGTTACTGGAACGTTGTGAGGGTAAACAACTGGCGGTATGGATGCGGCGGGACCAGAGAAAAATCACTCAGGGT
CAATGCCAGCGCTTCGTTAATACAGATGTAGGTGTTCCACAGGGTAGCCAGCAGCATCCTGCGATGCAGATCCGGAACATAATGGTGCAGGGCGCTGACTTCCGCGTTTCCAGA
CTTTACGAAACACGGAAACCGAAGACCATTCATGTTGTTGCTCAGGTCGCAGACGTTTTGCAGCAGCAGTCGCTTCACGTTCGCTCGCGTATCGGTGATTCATTCTGCTAACCAGT
AAGGCAACCCCGCCAGCCTAGCCGGGTCCTCAACGACAGGAGCACGATCATGCTAGTCATGCCCCGCGCCCACCGGAAGGAGCTGACTGGGTTGAAGGCTCTCAAGGGCATCG
GTCGAGATCCCGGTGCCTAATGAGTGAGCTAACTTACATTAATTGCGTTGCGCTCACTGCCCGCTTTCCAGTCGGGAAACCTGTCGTGCCAGCTGCATTAATGAATCGGCCAACG
CGCGGGGAGAGGCGGTTTGCGTATTGGGCGCCAGGGTGGTTTTTCTTTTCACCAGTGAGACGGGCAACAGCTGATTGCCCTTCACCGCCTGGCCCTGAGAGAGTTGCAGCAAGC
GGTCCACGCTGGTTTGCCCCAGCAGGCGAAAATCCTGTTTGATGGTGGTTAACGGCGGGATATAACATGAGCTGTCTTCGGTATCGTCGTATCCCACTACCGAGATGTCCGCACC
AACGCGCAGCCCGGACTCGGTAATGGCGCGCATTGCGCCCAGCGCCATCTGATCGTTGGCAACCAGCATCGCAGTGGGAACGATGCCCTCATTCAGCATTTGCATGGTTTGTTGA
AAACCGGACATGGCACTCCAGTCGCCTTCCCGTTCCGCTATCGGCTGAATTTGATTGCGAGTGAGATATTTATGCCAGCCAGCCAGACGCAGACGCGCCGAGACAGAACTTAATG
GGCCCGCTAACAGCGCGATTTGCTGGTGACCCAATGCGACCAGATGCTCCACGCCCAGTCGCGTACCGTCTTCATGGGAGAAAATAATACTGTTGATGGGTGTCTGGTCAGAGA
CATCAAGAAATAACGCCGGAACATTAGTGCAGGCAGCTTCCACAGCAATGGCATCCTGGTCATCCAGCGGATAGTTAATGATCAGCCCACTGACGCGTTGCGCGAGAAGATTGT
GCACCGCCGCTTTACAGGCTTCGACGCCGCTTCGTTCTACCATCGACACCACCACGCTGGCACCCAGTTGATCGGCGCGAGATTTAATCGCCGCGACAATTTGCGACGGCGCGTG
CAGGGCCAGACTGGAGGTGGCAACGCCAATCAGCAACGACTGTTTGCCCGCCAGTTGTTGTGCCACGCGGTTGGGAATGTAATTCAGCTCCGCCATCGCCGCTTCCACTTTTTCC
CGCGTTTTCGCAGAAACGTGGCTGGCCTGGTTCACCACGCGGGAAACGGTCTGATAAGAGACACCGGCATACTCTGCGACATCGTATAACGTTACTGGTTTCACATTCACCACCC
TGAATTGACTCTCTTCCGGGCGCTATCATGCCATACCGCGAAAGGTTTTGCGCCATTCGATGGTGTCCGGGATCTCGACGCTCTCCCTTATGCGACTCCTGCATTAGGAAGCAGCC
CAGTAGTAGGTTGAGGCCGTTGAGCACCGCCGCCGCAAGGAATGGTGCATGCAAGGAGATGGCGCCCAACAGTCCCCCGGCCACGGGGCCTGCCACCATACCCACGCCGAAAC
AAGCGCTCATGAGCCCGAAGTGGCGAGCCCGATCTTCCCCATCGGTGATGTCGGCGATATAGGCGCCAGCAACCGCACCTGTGGCGCCGGTGATGCCGGCCACGATGCGTCCG
GCGTAGAGGATCGAGATCGATCTCGATCCCGCGAAATTAATACGACTCACTATAGGGGAATTGTGAGCGGATAACAATTCCCCTCTAGAAATAATTTTGTTTAACTTTAAGAAGG
AGATATACCATGGCACATCACCACCACCATCACGTGGGTACCGGTTCGAATGATGACGACGACAAGAGTCCGGATCCCAATTGGATGGTGAGCAAGGGCGAGGAGCTGTTCACC
GGGGTGGTGCCCATCCTGGTCGAGCTGGACGGCGACGTAAACGGCCACAAGTTCAGCGTGTCCGGCGAGGGCGAGGGCGATGCCACCTACGGCAAGCTGACCCTGAAGTTCAT
CTGCACCACCGGCAAGCTGCCCGTGCCCTGGCCCACCCTCGTGACCACCCTGACCTACGGCGTGCAGTGCTTCAGCCGCTACCCCGACCACATGAAGCAGCACGACTTCTTCAAG
TCCGCCATGCCCGAAGGCTACGTCCAGGAGCGCACCATCTTCTTCAAGGACGACGGCAACTACAAGACCCGCGCCGAGGTGAAGTTCGAGGGCGACACCCTGGTGAACCGCATC
GAGCTGAAGGGCATCGACTTCAAGGAGGACGGCAACATCCTGGGGCACAAGCTGGAGTACAACTACAACAGCCACAACGTCTATATCATGGCCGACAAGCAGAAGAACGGCAT
CAAGGTGAACTTCAAGATCCGCCACAACATCGAGGACGGCAGCGTGCAGCTCGCCGACCACTACCAGCAGAACACCCCCATCGGCGACGGCCCCGTGCTGCTGCCCGACAACCA
CTACCTGAGCACCCAGTCCGCCCTGAGCAAAGACCCCAACGAGAAGCGCGATCACATGGTCCTGCTGGAGTTCGTGACCGCCGCCGGGATCACTCTCGGCATGGACGAGCTGTA
CGGCACTAGTATGGCTTCTAGAGGAGTGCAGGTGGAGACTATCTCCCCAGGAGACGGGCGCACCTTCCCCAAGCGCGGCCAGACCTGCGTGGTGCACTACACCGGGATGCTTG
AAGATGGAAAGAAATTTGATTCCTCCCGGGACAGAAACAAGCCCTTTAAGTTTATGCTAGGCAAGCAGGAGGTGATCCGAGGCTGGGAAGAAGGGGTTGCCCAGATGAGTGTG
GGTCAGAGAGCCAAACTGACTATATCTCCAGATTATGCCTATGGTGCCACTGGGCACCCAGGCATCATCCCACCACATGCCACTCTCGTCTTCGATGTGGAGCTTCTAAAACTGGA
ATCACCGGCGCTGTACAAGTCCGGACTCAGATCTCGAGCTCAAGCTTCGAATTCTATGGCGTCGGGTGGTGGTGGCTGTAGCGCTTCGGAGAGACTGCCTCCGCCCTTCCCCGGC
CTGGAGCCGGAGTCCGAGGGGGCGGCCGGGGGATCAGAACCCGAGGCTGGGGACAGCGACACCGAGGGGGAGGACATTTTCACCGGCGCCGCGGTGGTCAGTAAACATCAG
TCTCCAAAGATAACTACATCCCTTCTTCCCATCAACAATGGCTCCAAAGAAAATGGGATCCATGAAGAACAAGACCAAGAGCCACAGGATCTCTTTGCAGATGCCACAGTGGAGC
TATCCTTGGACAGCACACAAAATAATCAGAAGAAGGTGCTAGCCAAAACACTCATTTCTCTTCCTCCTCAGGAAGCCACAAATTCTTCGAAGCCCCAGCCAACCTATGAGGAGCTA
GAGGAAGAAGAACAGGAGGATCAATTTGATTTGACAGTCGGTATAACTGATCCTGAGAAGATAGGGGATGGTATGAATGCATATGTAGCCTACAAAGTTACAACACAGACAAG
CTTACCATTGTTCAGAAGCAAACAGTTTGCAGTAAAAAGAAGATTTAGTGACTTTCTGGGTCTTTATGAGAAGCTTTCCGAGAAGCACTCTCAGAATGGCTTCATTGTCCCTCCGC
CCCCGGAGAAGAGCCTCATAGGGATGACAAAAGTGAAAGTTGGGAAGGAAGATTCTTCTTCTGCAGAATTTCTTGAAAAACGGAGGGCCGCTTTAGAAAGGTACCTTCAGAGG
ATTGTAAATCATCCTACCATGTTACAGGACCCTGACGTCAGAGAGTTCTTGGAAAAAGAAGAGCTGCCACGTGCCGTGGGTACCCAGACATTGAGTGGTGCTGGTCTCCTCAAGA
TGTTCAACAAAGCCACAGATGCCGTCAGCAAAATGACCATCAAGATGAATGAATCAGACATTTGGTTTGAGGAGAAGCTCCAGGAGGTAGAGTGTGAGGAGCAGCGCTTACGG
AAACTGCATGCTGTTGTAGAAACTCTAGTCAACCATAGGAAAGAGCTAGCGCTGAACACAGCCCAGTTTGCAAAGAGTCTAGCCATGCTTGGGAGCTCTGAGGACAACACGGCA
TTGTCACGGGCACTCTCCCAGCTGGCTGAGGTGGAAGAAAAAATTGAGCAGCTCCACCAGGAACAGGCCAACAATGACTTCTTCCTCCTTGCTGAGCTCCTGAGTGACTACATTC
GCCTCCTGGCCATAGTCCGCGCTGCCTTCGACCAGCGCATGAAGACATGGCAGCGCTGGCAGGATGCCCAAGCCACACTGCAGAAGAAGCGGGAGGCCGAGGCTCGGCTGCTG
TGGGCCAACAAGCCTGATAAGCTGCAGCAGGCCAAGGACGAGATCCTCGAGTGGGAGTCTCGGGTGACTCAATATGAAAGGGACTTCGAGAGGATTTCAACAGTGGTCCGAAA
AGAAGTGATACGGTTTGAGAAAGAGAAATCCAAGGACTTCAAGAACCACGTGATCAAGTACCTTGAGACACTCCTTTACTCACAGCAGCAGCTGGCAAAGTACTGGGAAGCCTT
CCTTCCTGAGGCAAAGGCCATCTCCTAAGTCGAGTCTGGTAAAGAAACCGCTGCTGCGAAATTTGAACGCCAGCACATGGACTCGTCTACTAGCGCAGCTTAATTAACCTAGGCT
GCTGCCACCGCTGAGCAATAACTAGCATAACCCCTTGGGGCCTCTAAACGGGTCTTGAGGGGTTTTTTGCTGAAAGGAGGAACTATATCCGGAT

References

Al-Amoudi, A. *et al.* (2003) 'An oscillating cryo-knife reduces cutting-induced deformation of vitreous ultrathin sections', *Journal of Microscopy*. John Wiley & Sons, Ltd (10.1111), 212(1), pp. 26–33. doi: 10.1046/j.1365-2818.2003.01244.x.

Al-Johani, H. *et al.* (2017) 'The structure and binding mode of citrate in the stabilization of gold nanoparticles', *Nature Chemistry*. Nature Publishing Group, 9(9), pp. 890–895. doi: 10.1038/nchem.2752.

Arias, J. F. *et al.* (2014) 'Tetherin antagonism by Vpu protects HIV-infected cells from antibody-dependent cell-mediated cytotoxicity', *Proceedings of the National Academy of Sciences of the United States of America*. National Academy of Sciences, 111(17), pp. 6425–6430. doi: 10.1073/pnas.1321507111.

Ariotti, N., Wu, Y., Okano, S., Gambin, Y., Follett, J., Rae, J., Ferguson, C., Teasdale, R. D., Alexandrov, K., Meunier, F. A., Hill, M. M., & Parton, R. G. (2020). An inverted CAV1 (caveolin 1) topology defines novel autophagy-dependent exosome secretion from prostate cancer cells. *Autophagy*, 15548627.2020.1820787. https://doi.org/10.1080/15548627.2020.1820787

Arribillaga, L. *et al.* (2013) 'A Fusion Protein between Streptavidin and the Endogenous TLR4 Ligand EDA Targets Biotinylated Antigens to Dendritic Cells and Induces T Cell Responses In Vivo', *BioMed Research International*. Hindawi Publishing Corporation, 2013. doi: 10.1155/2013/864720.

Aschenbrenner, L., Lee, T. and Hasson, T. (2003) 'Myo6 facilitates the translocation of endocytic vesicles from cell peripheries.', *Molecular biology of the cell*, 14(7), pp. 2728–43. doi: 10.1091/mbc.e02-11-0767.

Aspect, A. and Villain, J. (2017) 'The birth of wave mechanics (1923–1926)', *Comptes Rendus Physique*. No longer published by Elsevier, 18(9–10), pp. 583–585. doi: 10.1016/J.CRHY.2017.10.007.

Balzarotti, F. *et al.* (2017) 'Nanometer resolution imaging and tracking of fluorescent molecules with minimal photon fluxes', *Science*. American Association for the Advancement of Science, 355(6325), pp. 606–612. doi: 10.1126/science.aak9913.

Barr, F. and Lambright, D. G. (2010) 'Rab GEFs and GAPs', *Current Opinion in Cell Biology*, pp. 461–470. doi: 10.1016/j.ceb.2010.04.007.

Bazett-Jones, D. P., Hendzel, M. J. and Kruhlak, M. J. (1999) 'Stoichiometric analysis of protein- and nucleic acid-based structures in the cell nucleus.', *Micron (Oxford, England : 1993)*, 30(2), pp. 151–7. doi: 10.1016/s0968-4328(99)00019-0.

Beretta, C. A. *et al.* (2016) 'Tracking cells in GFP-transgenic zebrafish using the photoconvertible PSmOrange system', *Journal of Visualized Experiments*. MyJoVE Corporation, 2016(108), p. e53604. doi: 10.3791/53604.

Bhatia, V. K. *et al.* (2009) 'Amphipathic motifs in BAR domains are essential for membrane curvature sensing', *The EMBO Journal*, 28(21), pp. 3303–3314. doi: 10.1038/emboj.2009.261.

Birch-Andersen, A. (1955) 'Reconstruction of the nuclear sites of Salmonella typhimurium from electron micrographs of serial sections.', *Journal of general microbiology*, 13(2), pp. 327–329. doi: 10.1099/00221287-13-2-327.

Botelho, R. J. *et al.* (2008) 'Assembly of a Fab1 phosphoinositide kinase signaling complex requires the Fig4 phosphoinositide phosphatase', *Molecular Biology of the Cell*. American Society for Cell Biology, 19(10), pp. 4273–4286. doi: 10.1091/mbc.E08-04-0405.

Brama, E. *et al.* (2015) 'Standard fluorescent proteins as dual-modality probes for correlative experiments in an integrated light and electron microscope', *Journal of Chemical Biology*, 8(4), pp. 179–188. doi: 10.1007/s12154-015-0143-3.

Breshike, C. J., Riskowski, R. A. and Strouse, G. F. (2013) 'Leaving Förster Resonance Energy Transfer Behind: Nanometal Surface Energy Transfer Predicts the Size-Enhanced Energy Coupling between a Metal Nanoparticle and an Emitting Dipole', *The Journal of Physical Chemistry C*. American Chemical Society, 117(45), pp. 23942–23949. doi: 10.1021/jp407259r.

Brown, E. and Verkade, P. (2010) 'The use of markers for correlative light electron microscopy.', *Protoplasma*, 244(1–4), pp. 91–7. doi: 10.1007/s00709-010-0165-1.

Brown, E. *et al.* (2012) 'Capturing Endocytic Segregation Events with HPF-CLEM', in *Methods in Cell Biology*. Academic Press Inc., pp. 175–201. doi: 10.1016/B978-0-12-416026-2.00010-8.

Brown, S. L. *et al.* (2017) 'First-Principles Study of Fluorescence in Silver Nanoclusters', *Journal of Physical Chemistry C*. American Chemical Society, 121(43), pp. 23875–23885. doi: 10.1021/acs.jpcc.7b04870.

Carlton, J. *et al.* (2004) 'Sorting Nexin-1 Mediates Tubular Endosome-to-TGN Transport through Coincidence Sensing of High- Curvature Membranes and 3-Phosphoinositides', *Current Biology*, 14(20), pp. 1791–1800. doi: 10.1016/j.cub.2004.09.077.

Chen, B.-C. *et al.* (2014) 'Lattice light-sheet microscopy: Imaging molecules to embryos at high spatiotemporal resolution', *Science*, 346(6208), p. 1257998. doi: 10.1126/science.1257998.

Chen, W.-Y., Lan, G.-Y. and Chang, H.-T. (2011) 'Use of Fluorescent DNA-Templated Gold/Silver Nanoclusters for the Detection of Sulfide Ions', *Analytical Chemistry*. American Chemical Society, 83(24), pp. 9450–9455. doi: 10.1021/ac202162u.

Chen, Z. *et al.* (2016) 'The N-Terminal Amphipathic Helix of Endophilin Does Not Contribute to Its Molecular Curvature Generation Capacity', *Journal of the American Chemical Society*, 138(44), pp. 14616–14622. doi: 10.1021/jacs.6b06820.

Chung, K. *et al.* (2013) 'Structural and molecular interrogation of intact biological systems', *Nature*, 497(7449), pp. 332–337. doi: 10.1038/nature12107.

Clackson, T. *et al.* (1998) 'Redesigning an FKBP-ligand interface to generate chemical dimerizers with novel specificity.', *Proceedings of the National Academy of Sciences of the United States of America*, 95(18), pp. 10437–42. doi: 10.1073/pnas.95.18.10437.

Connor, E. E. *et al.* (2005) 'Gold nanoparticles are taken up by human cells but do not cause acute cytotoxicity', *Small*, 1(3), pp. 325–327. doi: 10.1002/smll.200400093.

Couchman, P. R. and Jesser, W. A. (1977) 'Thermodynamic theory of size dependence of melting temperature in metals', *Nature*. Nature Publishing Group, 269(5628), pp. 481–483. doi: 10.1038/269481a0.

Coutinho, M. F., Prata, M. J. and Alves, S. (2012) 'A shortcut to the lysosome: The mannose-6-phosphate-independent pathway', *Molecular Genetics and Metabolism*, pp. 257–266. doi: 10.1016/j.ymgme.2012.07.012.

Cross. S. (2019, May 10). SJCross/MIA: Version 0.9.30 (Version v0.9.30). Zenodo. http://doi.org/10.5281/zenodo.2712750

Cullen, P. J. (2008) 'Endosomal sorting and signalling: an emerging role for sorting nexins', *Nature Reviews Molecular Cell Biology*, 9(7), pp. 574–582. doi: 10.1038/nrm2427.

Cullen, P. J. and Korswagen, H. C. (2012) 'Sorting nexins provide diversity for retromer-dependent trafficking events', *Nature Publishing Group*. Nature Publishing Group, 14(1), pp. 29–37. doi: 10.1038/ncb2374.

Das, A. *et al.* (2014) 'Crystal structure and electronic properties of a thiolate-protected Au24 nanocluster', *Nanoscale*. The Royal Society of Chemistry, 6(12), p. 6458. doi: 10.1039/c4nr01350f.

Dempsey, G. T. *et al.* (2011) 'Evaluation of fluorophores for optimal performance in localization-based super-resolution imaging', *Nature Methods*. Nature Publishing Group, 8(12), pp. 1027–1036. doi: 10.1038/nmeth.1768.

Diestra, E. *et al.* (2009a) 'Visualization of proteins in intact cells with a clonable tag for electron microscopy', *Journal of Structural Biology*, 165(3), pp. 157–168. doi: 10.1016/j.jsb.2008.11.009.

Diestra, E. *et al.* (2009b) 'Cellular Electron Microscopy Imaging Reveals the Localization of the Hfq Protein Close to the Bacterial Membrane', *PLoS ONE*. Edited by C. Mayer. Public Library of Science, 4(12), p. e8301. doi: 10.1371/journal.pone.0008301.

Dislich, B., Than, M. E. and Lichtenthaler, S. F. (2011) 'Specific amino acids in the BAR domain allow homodimerization and prevent heterodimerization of sorting nexin 33', *Biochemical Journal*, 433(1), pp. 75–83. doi: 10.1042/BJ20100709.

Duff, M. R. *et al.* (2011) 'Isothermal titration calorimetry for measuring macromolecule-ligand affinity.' *Journal of visualized experiments : JoVE*. MyJoVE Corporation, (55). doi: 10.3791/2796.

Dyve, A. B. *et al.* (2009) 'Sorting nexin 8 regulates endosome-to-Golgi transport', *Biochemical and Biophysical Research Communications*, 390(1), pp. 109–114. doi: 10.1016/j.bbrc.2009.09.076.

Fabig, G. *et al.* (2012) 'Labeling of Ultrathin Resin Sections for Correlative Light and Electron Microscopy', in *Methods in Cell Biology*. Academic Press Inc., pp. 75–93. doi: 10.1016/B978-0-12-416026-2.00005-4.

Fallon, P. J. and Brown, L. M. (1993) 'Analysis of chemical-vapour-deposited diamond grain boundaries using transmission electron microscopy and parallel electron energy loss spectroscopy in a scanning transmission electron microscope', *Diamond and Related Materials*. Elsevier, 2(5–7), pp. 1004–1011. doi: 10.1016/0925-9635(93)90265-4.

Farsad, K. *et al.* (2001) 'Generation of high curvature membranes mediated by direct endophilin bilayer interactions', *The Journal of Cell Biology*, 155(2), pp. 193–200. doi: 10.1083/jcb.200107075.

Ford, M. G. J. *et al.* (2002) 'Curvature of clathrin-coated pits driven by epsin', *Nature*. Nature Publishing Group, 419(6905), pp. 361–366. doi: 10.1038/nature01020.

Freundlich, M. M. (1963) 'Origin of the Electron Microscope', *Science*, 142(3589), pp. 185–188. doi: 10.1126/science.142.3589.185.

Frost, A. *et al.* (2008) 'Structural Basis of Membrane Invagination by F-BAR Domains', *Cell*, 132(5), pp. 807–817. doi: 10.1016/j.cell.2007.12.041.

Gaietta, G. *et al.* (2002) 'Multicolor and electron microscopic imaging of connexin trafficking', *Science*, 296(5567), pp. 503–507. doi: 10.1126/science.1068793.

Gallop, J. L. *et al.* (2006) 'Mechanism of endophilin N-BAR domain-mediated membrane curvature', *The EMBO Journal*, 25(12), pp. 2898–2910. doi: 10.1038/sj.emboj.7601174.

Gammons, C. H., Yu, Y. and Williams-Jones, A. E. (1997) 'The disproportionation of gold(I) chloride complexes at 25 to 200°C', *Geochimica et Cosmochimica Acta*. Pergamon, 61(10), pp. 1971–1983. doi: 10.1016/S0016-7037(97)00060-4.

Gaullier, J. M. *et al.* (1999) 'FYVE finger proteins as effectors of phosphatidylinositol 3-phosphate', in *Chemistry and Physics of Lipids*, pp. 87–94. doi: 10.1016/S0009-3084(99)00021-3.

Giepmans, B. N. G. (2008) 'Bridging fluorescence microscopy and electron microscopy', *Histochemistry and Cell Biology*. Springer, pp. 211–217. doi: 10.1007/s00418-008-0460-5.

Giepmans, B. N. G. *et al.* (2005) 'Correlated light and electron microscopic imaging of multiple endogenous proteins using Quantum dots.', *Nature methods*, 2(10), pp. 743–9. doi: 10.1038/nmeth791.

Goodpasture, C. and Bloom, S. E. (1975) 'Visualization of nucleolar organizer regions in mammalian chromosomes using silver staining', *Chromosoma*. Springer-Verlag, 53(1), pp. 37–50. doi: 10.1007/BF00329389.

Göttfert, F. *et al.* (2013) 'Coaligned dual-channel STED nanoscopy and molecular diffusion analysis at 20 nm resolution.', *Biophysical journal*. The Biophysical Society, 105(1), pp. L01-3. doi: 10.1016/j.bpj.2013.05.029.

Gross, J. B. *et al.* (2006) 'Use of a ROSA26:GFP transgenic line for long-term Xenopus fate-mapping studies.', *Journal of anatomy*. Wiley-Blackwell, 209(3), pp. 401–13. doi: 10.1111/j.1469-7580.2006.00608.x.

Gruenberg, J., Griffiths, G. and Howell, K. E. (1989) 'Characterization of the early endosome and putative endocytic carrier vesicles in vivo and with an assay of vesicle fusion in vitro.', *The Journal of cell biology*. The Rockefeller University Press, 108(4), pp. 1301–16. doi: 10.1083/jcb.108.4.1301.

Guével, X. Le, Daum, N. and Schneider, M. (2011) 'Synthesis and characterization of human transferrin-stabilized gold nanoclusters', *Nanotechnology*. IOP Publishing, 22(27), p. 275103. doi: 10.1088/0957-4484/22/27/275103.

Guo, W. *et al.* (2010) 'Highly Sequence-Dependent Formation of Fluorescent Silver Nanoclusters in Hybridized DNA Duplexes for Single Nucleotide Mutation Identification', *Journal of the American Chemical Society*. American Chemical Society, 132(3), pp. 932–934. doi: 10.1021/ja907075s.

Gwinn, E. G. *et al.* (2008) 'Sequence-Dependent Fluorescence of DNA-Hosted Silver Nanoclusters', *Advanced Materials*. John Wiley & Sons, Ltd, 20(2), pp. 279–283. doi: 10.1002/adma.200702380.

Hagen, C. and Grünewald, K. (2008) 'Microcarriers for high-pressure freezing and cryosectioning of adherent cells', *Journal of Microscopy*, 230(2), pp. 288–296. doi: 10.1111/j.1365-2818.2008.01987.x.

Han, L (2012) 'Synthetic and Biosynthetic Studies on Polyketide Derived Natural Products', PhD thesis, University of Bristol, Bristol.

Han, S. *et al.* (2017) 'Proximity Biotinylation as a Method for Mapping Proteins Associated with mtDNA in Living Cells', *Cell Chemical Biology*. Elsevier Ltd, 24(3), pp. 404–414. doi: 10.1016/j.chembiol.2017.02.002.

Hatteland, R. - Own work, Public Domain, https://commons.wikimedia.org/w/index.php?curid=8675960

Heiligenstein, X. *et al.* (2017) 'The HPM Live µ–From Live Cell Imaging to High Pressure Freezing in Less than 2 Seconds for Correlative Microscopy Approaches', *Microscopy and Microanalysis*. Cambridge University Press, 23(S1), pp. 1276–1277. doi: 10.1017/S1431927617007048.

Helander, I. M., Latva-Kala, K. and Lounatmaa, K. (1998) 'Permeabilizing action of polyethyleneimine on Salmonella typhimurium involves disruption of the outer membrane and interactions with lipopolysaccharide', *Microbiology*. Microbiology Society, 144(2), pp. 385–390. doi: 10.1099/00221287-144-2-385.

Helfer, E. *et al.* (2013) 'Endosomal recruitment of the WASH complex: Active sequences and mutations impairing interaction with the retromer', *Biology of the Cell*. John Wiley & Sons, Ltd, 105(5), pp. 191–207. doi: 10.1111/boc.201200038.

Helmchen, F. and Denk, W. (2005) 'Deep tissue two-photon microscopy', *Nature Methods*, pp. 932–940. doi: 10.1038/nmeth818.

Henne, W. M. *et al.* (2007) 'Structure and Analysis of FCHo2 F-BAR Domain: A Dimerizing and Membrane Recruitment Module that Effects Membrane Curvature', *Structure*. Cell Press, 15(7), pp. 839–852. doi: 10.1016/J.STR.2007.05.002.

Holmberg, A. *et al.* (2005) 'The biotin-streptavidin interaction can be reversibly broken using water at elevated temperatures', *ELECTROPHORESIS*, 26(3), pp. 501–510. doi: 10.1002/elps.200410070.

Horiuchi, H. *et al.* (1997) 'A novel Rab5 GDP/GTP exchange factor complexed to Rabaptin-5 links nucleotide exchange to effector recruitment and function.', *Cell*, 90(6), pp. 1149–59. doi: 10.1016/s0092-8674(00)80380-3.

Howarth, M. *et al.* (2008) 'Monovalent, reduced-size quantum dots for imaging receptors on living cells', *Nature Methods*, 5(5), pp. 397–399. doi: 10.1038/nmeth.1206.

Huang, B. *et al.* (2008) 'Whole-cell 3D STORM reveals interactions between cellular structures with nanometer-scale resolution', *Nature Methods*, 5(12), pp. 1047–1052. doi: 10.1038/nmeth.1274.

Huang, X., Ishitobi, H. and Inouye, Y. (2016) 'Formation of fluorescent platinum nanoclusters using hyper-branched polyethylenimine and their conjugation to antibodies for bio-imaging', *RSC Advances*. The Royal Society of Chemistry, 6(12), pp. 9709–9716. doi: 10.1039/C5RA24522B.

Huttel, Y. *et al.* (2018) 'Gas-Phase Synthesis of Nanoparticles: present status and perspectives', *MRS communications*. Europe PMC Funders, 8(3), p. 947. doi: 10.1557/MRC.2018.169.

Jin, N., Lang, M. J. and Weisman, L. S. (2016) 'Phosphatidylinositol 3,5-bisphosphate: Regulation of cellular events in space and time', *Biochemical Society Transactions*. Portland Press Ltd, 44(1), pp. 177–184. doi: 10.1042/BST20150174.

Johnson, E. *et al.* (2015) 'Correlative in-resin super-resolution and electron microscopy using standard fluorescent proteins', *Scientific Reports*. Nature Publishing Group, 5. doi: 10.1038/srep09583.

Jones, J. C. R. (2016) 'Pre- and post-embedding immunogold labelingof tissue sections', in *Methods in Molecular Biology*. Humana Press Inc., pp. 291–307. doi: 10.1007/978-1-4939-6352-2_19.

Jovic, M. *et al.* (2010) 'The early endosome: A busy sorting station for proteins at the crossroads', *Histology and Histopathology*, pp. 99–112. doi: 10.14670/HH-25.99.

Kägi, J. H. and Schäffer, A. (1988) 'Biochemistry of metallothionein.', *Biochemistry*, 27(23), pp. 8509–15. Available at: http://www.ncbi.nlm.nih.gov/pubmed/3064814 (Accessed: 2 January 2017).

Kanaya, K. and Okayama, S. (1972) 'Penetration and energy-loss theory of electrons in solid targets', *Journal of Physics D: Applied Physics*, 5(1), p. 308. doi: 10.1088/0022-3727/5/1/308.

Kane, P. M. (2006) 'The Where, When, and How of Organelle Acidification by the Yeast Vacuolar H+-ATPase', *Microbiology and Molecular Biology Reviews*. American Society for Microbiology, 70(1), pp. 177–191. doi: 10.1128/mmbr.70.1.177-191.2006.

Keller, P. J. *et al.* (2008) 'Reconstruction of Zebrafish Early Embryonic Development by Scanned Light Sheet Microscopy', *Science*, 322(5904), pp. 1065–1069. doi: 10.1126/science.1162493.

Khansarizadeh, M. *et al.* (2016) 'Identification of possible cytotoxicity mechanism of polyethylenimine by proteomics analysis', *Human & Experimental Toxicology*, 35(4), pp. 377–387. doi: 10.1177/0960327115591371.

Kirchhausen, T. (2009). Imaging endocytic clathrin structures in living cells. In *Trends in Cell Biology* (Vol. 19, Issue 11, pp. 596–605). Elsevier Ltd. https://doi.org/10.1016/j.tcb.2009.09.002

Killingsworth, M. C. and Bobryshev, Y. V. (2016) 'Correlative light- and electron microscopy using quantum dot nanoparticles', *Journal of Visualized Experiments*. Journal of Visualized Experiments, 2016(114). doi: 10.3791/54307.

Kovtun, O. *et al.* (2018) 'Structure of the membrane-assembled retromer coat determined by cryo-electron tomography.', *Nature*. Europe PMC Funders, 561(7724), pp. 561–564. doi: 10.1038/s41586-018-0526-z.

Kühlbrandt, W. (2014) 'The resolution revolution', *Science*. American Association for the Advancement of Science, pp. 1443–1444. doi: 10.1126/science.1251652.

Kuipers, J. *et al.* (2015) 'FLIPPER, a combinatorial probe for correlated live imaging and electron microscopy, allows identification and quantitative analysis of various cells and organelles', *Cell and Tissue Research*, 360(1), pp. 61–70. doi: 10.1007/s00441-015-2142-7.

Kukulski, W. *et al.* (2011) 'Correlated fluorescence and 3D electron microscopy with high sensitivity and spatial precision', *The Journal of Cell Biology*. Rockefeller University Press, 192(1), pp. 111–119. doi: 10.1083/jcb.201009037.

Kutateladze, T. G. (2010) 'Translation of the phosphoinositide code by PI effectors', *Nature Chemical Biology*, 6(7), pp. 507–513. doi: 10.1038/nchembio.390.

Kvainickas, A. *et al.* (2017) 'Cargo-selective SNX-BAR proteins mediate retromer trimer independent retrograde transport', *The Journal of Cell Biology*, 216(11), pp. 3677–3693. doi: 10.1083/jcb.201702137.

Landry, J. P. *et al.* (2015) 'Measuring affinity constants of 1450 monoclonal antibodies to peptide targets with a microarray-based label-free assay platform', *Journal of Immunological Methods*. Elsevier, 417, pp. 86–96. doi: 10.1016/j.jim.2014.12.011.

Le Guennec, M. *et al.* (2020) 'A helical inner scaffold provides a structural basis for centriole cohesion', *Science Advances*. American Association for the Advancement of Science, 6(7), p. eaaz4137. doi: 10.1126/sciadv.aaz4137.

Leapman, R. D. and Rizzo, N. W. (1999) 'Towards single atom analysis of biological structures.', *Ultramicroscopy*, 78(1–4), pp. 251–68. doi: 10.1016/s0304-3991(99)00031-5.

Lee, J. O. *et al.* (2008) 'Aptamers as molecular recognition elements for electrical nanobiosensors', *Analytical and Bioanalytical Chemistry*, 390(4), pp. 1023–1032. doi: 10.1007/s00216-007-1643-y.

Lee, K. *et al.* (2013) 'Autofluorescence generation and elimination: a lesson from glutaraldehyde', *Chemical Communications*. Royal Society of Chemistry, 49(29), p. 3028. doi: 10.1039/c3cc40799c.

Li (2010) 'Membrane targeted horseradish peroxidase as a marker for correlative fluorescence and electron microscopy studies', *Frontiers in Neural Circuits*, 4(February), pp. 1–10. doi: 10.3389/neuro.04.006.2010.

Li, J., Zhu, J.-J. and Xu, K. (2014) 'Fluorescent metal nanoclusters: From synthesis to applications', *TrAC Trends in Analytical Chemistry*. Elsevier, 58, pp. 90–98. doi: 10.1016/J.TRAC.2014.02.011.

Lim, K. H. *et al.* (2013) 'Stable, high-affinity streptavidin monomer for protein labeling and monovalent biotin detection', *Biotechnology and Bioengineering*, 110(1), pp. 57–67. doi: 10.1002/bit.24605.

Linkner, J. *et al.* (2014) 'The inverse BAR domain protein IBARa drives membrane remodeling to control osmoregulation, phagocytosis and cytokinesis.', *Journal of cell science*. The Company of Biologists Ltd, 127(Pt 6), pp. 1279–92. doi: 10.1242/jcs.140756.

Liu, F., Zhang, J. Z. H. and Mei, Y. (2016) 'The origin of the cooperativity in the streptavidin-biotin system: A computational investigation through molecular dynamics simulations', *Scientific Reports*. Nature Publishing Group, 6(1), p. 27190. doi: 10.1038/srep27190.

Liu, G. *et al.* (2012) 'Synthesis of DNA-templated fluorescent gold nanoclusters', *Gold Bulletin*. Springer-Verlag, 45(2), pp. 69–74. doi: 10.1007/s13404-012-0049-6.

Liu, G. *et al.* (2013) 'Highly thymine-dependent formation of fluorescent copper nanoparticles templated by ss-DNA.', *Nanotechnology*, 24(34), p. 345502. doi: 10.1088/0957-4484/24/34/345502.

Liu, Z. *et al.* (2017) 'Determination of the ribosome structure to a resolution of 2.5 Å by single-particle cryo-EM', *Protein Science*. Blackwell Publishing Ltd, 26(1), pp. 82–92. doi: 10.1002/pro.3068.

Lu, X. *et al.* (2008) 'Facile Synthesis of Gold Nanoparticles with Narrow Size Distribution by Using AuCl or AuBr as the Precursor', *Chemistry - A European Journal*. John Wiley & Sons, Ltd, 14(5), pp. 1584–1591. doi: 10.1002/chem.200701570.

Luzio, J. P., Pryor, P. R. and Bright, N. A. (2007) 'Lysosomes: Fusion and function', *Nature Reviews Molecular Cell Biology*, pp. 622–632. doi: 10.1038/nrm2217.

Machleidt, T., Robers, M. and Hanson, G. T. (2007) 'Protein Labeling With FlAsH and ReAsH', in *High Content Screening*. New Jersey: Humana Press, pp. 209–220. doi: 10.1385/1-59745-217-3:209.

Mari, M. *et al.* (2008) 'SNX1 defines an early endosomal recycling exit for sortilin and mannose 6-phosphate receptors', *Traffic*, 9(3), pp. 380–393. doi: 10.1111/j.1600-0854.2007.00686.x.

Marine, W. *et al.* (2000) 'Strategy of nanocluster and nanostructure synthesis by conventional pulsed laser ablation', *Applied Surface Science*. North-Holland, 154–155, pp. 345–352. doi: 10.1016/S0169-4332(99)00450-X.

Martell, J. D. *et al.* (2012) 'Engineered ascorbate peroxidase as a genetically encoded reporter for electron microscopy.', *Nature biotechnology*. NIH Public Access, 30(11), pp. 1143–8. doi: 10.1038/nbt.2375.

Mattila, P. K. *et al.* (2007) 'Missing-in-metastasis and IRSp53 deform PI(4,5)P2-rich membranes by an inverse BAR domain–like mechanism', *The Journal of Cell Biology*, 176(7), pp. 953–964. doi: 10.1083/jcb.200609176.

Maunsbach, A. B. and Afzelius, B. A. (2001) 'Biomedical Electron Microscopy: Illustrated Methods and Interpretations, Academic Press, San Diego, London. https://doi.org/10.1046/j.1365-2818.1999.00605.x

McMullan, G., Faruqi, A. R. and Henderson, R. (2016) 'Direct Electron Detectors', in *Methods in Enzymology*. Academic Press Inc., pp. 1–17. doi: 10.1016/bs.mie.2016.05.056.

McNally, K. E. *et al.* (2017) 'Retriever is a multiprotein complex for retromer-independent endosomal cargo recycling', *Nature Cell Biology*, 19(10), pp. 1214–1225. doi: 10.1038/ncb3610.

Meng, L. *et al.* (2017) 'Polyethyleneimine protected silver nanoclusters luminescence probe for sensitive detection of cobalt (II) in living cells', *Journal of Photochemistry and Photobiology B: Biology*, 173, pp. 508–513. doi: 10.1016/j.jphotobiol.2017.06.033.

Mercogliano, C. P. and DeRosier, D. J. (2007) 'Concatenated Metallothionein as a Clonable Gold Label for Electron Microscopy', *Journal of structural biology*. NIH Public Access, 160(1), p. 70. doi: 10.1016/J.JSB.2007.06.010.

Meresse, S., Gorvel, J. P. and Chavrier, P. (1995) 'The rab7 GTPase resides on a vesicular compartment connected to lysosomes', *Journal of Cell Science*, 108(11), pp. 3349–3358.

Mihelc, E. M., Angel, S., Stahelin, R. V, & Mattoo, S. (2020). The CryoAPEX Method for Electron Microscopy Analysis of Membrane Protein Localization Within Ultrastructurally-Preserved Cells. *Journal of Visualized Experiments : JoVE*, *156*. https://doi.org/10.3791/60677

Michell, R. H. *et al.* (2006) 'Phosphatidylinositol 3,5-bisphosphate: metabolism and cellular functions', *Trends in Biochemical Sciences*. Elsevier Current Trends, 31(1), pp. 52–63. doi: 10.1016/J.TIBS.2005.11.013.

Miles, B. T. *et al.* (2017) 'Direct Evidence of Lack of Colocalisation of Fluorescently Labelled Gold Labels Used in Correlative Light Electron Microscopy', *Nature Publishing Group*. Nature Publishing Group, (Lm), pp. 1–15. doi: 10.1038/srep44666.

Miles, B. T., Hong, X. and Gersen, H. (2015) 'On the complex point spread function in interferometric cross-polarisation microscopy.', *Optics express*, 23(2), pp. 1232–9. Available at: http://www.ncbi.nlm.nih.gov/pubmed/25835881 (Accessed: 8 July 2016).

Mim, C. and Unger, V. M. (2012) 'Membrane curvature and its generation by BAR proteins.', *Trends in biochemical sciences*. NIH Public Access, 37(12), pp. 526–33. doi: 10.1016/j.tibs.2012.09.001.

Mo, D. *et al.* (2017) 'Cadmium-containing quantum dots: properties, applications, and toxicity', *Applied Microbiology and Biotechnology*. Springer Verlag, pp. 2713–2733. doi: 10.1007/s00253-017-8140-9.

Möller, M. and Denicola, A. (2002) 'Study of protein-ligand binding by fluorescence', *Biochemistry and Molecular Biology Education*. John Wiley & Sons, Ltd, 30(5), pp. 309–312. doi: 10.1002/bmb.2002.494030050089.

Morphew, M. K. *et al.* (2015) 'Metallothionein as a clonable tag for protein localization by electron microscopy of cells.', *Journal of microscopy*. NIH Public Access, 260(1), pp. 20–9. doi: 10.1111/jmi.12262.

Nielson, K. B., Atkin, C. L. and Winge, D. R. (1985) 'Distinct metal-binding configurations in metallothionein', *Journal of Biological Chemistry*, 260(9), pp. 5342–5350.

Nixon, S. J. *et al.* (2009) 'A Single Method for Cryofixation and Correlative Light, Electron Microscopy and Tomography of Zebrafish Embryos', *Traffic*. Blackwell Publishing Ltd, 10(2), pp. 131–136. doi: 10.1111/j.1600-0854.2008.00859.x.

Nordmann, M. *et al.* (2010) 'The Mon1-Ccz1 complex is the GEF of the late endosomal Rab7 homolog Ypt7', *Current Biology*, 20(18), pp. 1654–1659. doi: 10.1016/j.cub.2010.08.002.

Oh, E. *et al.* (2016) 'Meta-analysis of cellular toxicity for cadmium-containing quantum dots', *Nature Nanotechnology*. Nature Publishing Group, 11(5), pp. 479–486. doi: 10.1038/nnano.2015.338.

Olivier, N. *et al.* (2013) 'Simple buffers for 3D STORM microscopy', *Biomedical Optics Express*. The Optical Society, 4(6), p. 885. doi: 10.1364/boe.4.000885.

Olmos, Y. *et al.* (2015) 'ESCRT-III controls nuclear envelope reformation', *Nature*. Nature Publishing Group, 522(7555), pp. 236–239. doi: 10.1038/nature14503.

Ormö, M. *et al.* (1996) 'Crystal structure of the Aequorea victoria green fluorescent protein', *Science.* AAAS, 273(5280), pp. 1392-1395. DOI: 10.1126/science.273.5280.1392

Pang, X. *et al.* (2014) 'A PH Domain in ACAP1 Possesses Key Features of the BAR Domain in Promoting Membrane Curvature', *Developmental Cell*. Cell Press, 31(1), pp. 73–86. doi: 10.1016/J.DEVCEL.2014.08.020.

Patterson, W. R. and Poulos, T. L. (1995) 'Crystal Structure of Recombinant Pea Cytosolic Ascorbate Peroxidase', *Biochemistry*, 34, pp. 4331–4341.

Paul-Gilloteaux, P. *et al.* (2017) 'EC-CLEM: Flexible multidimensional registration software for correlative microscopies', *Nature Methods*. Nature Publishing Group, pp. 102–103. doi: 10.1038/nmeth.4170.

Peddie, C. J. *et al.* (2017) 'Correlative super-resolution fluorescence and electron microscopy using conventional fluorescent proteins in vacuo', *Journal of Structural Biology*. Academic Press Inc., 199(2), pp. 120–131. doi: 10.1016/j.jsb.2017.05.013.

Peter, B. J. *et al.* (2004) 'BAR Domains as Sensors of Membrane Curvature: The Amphiphysin BAR Structure', *Science*, 303(5657), pp. 495–499. doi: 10.1126/science.1092586.

Petty, J. T. *et al.* (2004) 'DNA-Templated Ag Nanocluster Formation'. American Chemical Society. doi: 10.1021/JA031931O.

Polishchuk, R. S. *et al.* (2000) 'Correlative Light-Electron Microscopy Reveals the Tubular-Saccular Ultrastructure of Carriers Operating between Golgi Apparatus and Plasma Membrane', *The Journal of Cell Biology*, 148(1), pp. 45–58. doi: 10.1083/jcb.148.1.45.

Pujals, S. *et al.* (2019) 'Super-resolution microscopy as a powerful tool to study complex synthetic materials', *Nature Reviews Chemistry*. Nature Publishing Group, pp. 68–84. doi: 10.1038/s41570-018-0070-2.

Pylypenko, O. *et al.* (2007) 'The PX-BAR membrane-remodeling unit of sorting nexin 9', *The EMBO Journal*, 26(22), pp. 4788–4800. doi: 10.1038/sj.emboj.7601889.

Qing, T. *et al.* (2016) 'Oligonucleotide-templated rapid formation of fluorescent gold nanoclusters and its application for Hg2+ ions sensing', *Talanta*. Elsevier, 161, pp. 170–176. doi: 10.1016/J.TALANTA.2016.08.045.

Riedl, T. *et al.* (2007) 'Determination of manganese valency in La1-xSrxMnO3 using ELNES in the (S)TEM', *Micron*. Pergamon, 38(3), pp. 224–230. doi: 10.1016/j.micron.2006.06.017.

Ripper, D., Schwarz, H. and Stierhof, Y.-D. (2008) 'Cryo-section immunolabelling of difficult to preserve specimens: advantages of cryofixation, freeze-substitution and rehydration', *Biology of the Cell*. Wiley-Blackwell, 100(2), pp. 109–123. doi: 10.1042/bc20070106.

Robinson, J. M. *et al.* (2001) 'Correlative fluorescence and electron microscopy on ultrathin cryosections: Bridging the resolution gap', *Journal of Histochemistry and Cytochemistry*. Histochemical Society Inc., pp. 803–808. doi: 10.1177/002215540104900701.

Robinson, J. M., Takizawa, T. and Vandré, D. D. (2000) 'Enhanced labeling efficiency using ultrasmall immunogold probes: Immunocytochemistry', in *Journal of Histochemistry and Cytochemistry*. Histochemical Society Inc., pp. 487–492. doi: 10.1177/002215540004800406.

Rodriguez, E. A. *et al.* (2016) 'A far-red fluorescent protein evolved from a cyanobacterial phycobiliprotein', *Nature Methods*. Nature Publishing Group, 13(9), pp. 763–769. doi: 10.1038/nmeth.3935.

Rudge, S. A., Anderson, D. M. and Emr, S. D. (2004) 'Vacuole size control: regulation of PtdIns(3,5)P2 levels by the vacuole-associated Vac14-Fig4 complex, a PtdIns(3,5)P2-specific phosphatase.', *Molecular biology of the cell*, 15(1), pp. 24–36. doi: 10.1091/mbc.e03-05-0297.

Rueden, C. T. *et al.* (2017) 'ImageJ2: ImageJ for the next generation of scientific image data', *BMC Bioinformatics*. BioMed Central Ltd., 18(1), pp. 1–26. doi: 10.1186/s12859-017-1934-z.

Sánchez Sorzano, C. O., Thévenaz, P., Unser, M. "Elastic Registration of Biological Images Using Vector-Spline Regularization", IEEE Transactions on Biomedical Engineering, vol. 52, no. 4, pp. 652-663, April 2005.

Sbrissa, D. and Shisheva, A. (2005) 'Acquisition of unprecedented phosphatidylinositol 3,5-bisphosphate rise in hyperosmotically stressed 3T3-L1 adipocytes, mediated by ArPIKfyve-PIKfyve pathway', *Journal of Biological Chemistry*, 280(9), pp. 7883–7889. doi: 10.1074/jbc.M412729200.

Seaman, M. N. J. (2012) 'The retromer complex – endosomal protein recycling and beyond', *Journal of Cell Science*. Company of Biologists, 125(20), p. 4693. doi: 10.1242/JCS.103440.

Shang, L. and Dong, S. (2008) 'Silver nanocluster-based fluorescent sensors for sensitive detection of Cu(ii)', *Journal of Materials Chemistry*. The Royal Society of Chemistry, 18(39), p. 4636. doi: 10.1039/b810409c.

Shang, L. and Nienhaus, G. U. (2012) 'Gold nanoclusters as novel optical probes for in vitro and in vivo fluorescence imaging', *Biophysical Reviews*. Springer, pp. 313–322. doi: 10.1007/s12551-012-0076-9.

Shearer, L. J. and Petersen, N. O. (2019) 'Distribution and Co-localization of endosome markers in cells', *Heliyon*. Elsevier Ltd, 5(9). doi: 10.1016/j.heliyon.2019.e02375.

Shimada, A. *et al.* (2007) 'Curved EFC/F-BAR-Domain Dimers Are Joined End to End into a Filament for Membrane Invagination in Endocytosis', *Cell*, 129(4), pp. 761–772. doi: 10.1016/j.cell.2007.03.040.

Shu, X. *et al.* (2011) 'A Genetically Encoded Tag for Correlated Light and Electron Microscopy of Intact Cells, Tissues, and Organisms', *PLoS Biology*. Edited by J. R. McIntosh. Public Library of Science, 9(4), p. e1001041. doi: 10.1371/journal.pbio.1001041.

Simonetti, B. *et al.* (2017) 'Sequence-dependent cargo recognition by SNX-BARs mediates retromer-independent transport of CI-MPR', *Journal of Cell Biology*. Rockefeller University Press, 216(11), pp. 3695–3712. doi: 10.1083/jcb.201703015.

Simunovic, M. *et al.* (2013) 'Protein-Mediated Transformation of Lipid Vesicles into Tubular Networks', *Biophysical Journal*, 105(3), pp. 711–719. doi: 10.1016/j.bpj.2013.06.039.

Sorre, B. *et al.* (2012) 'Nature of curvature coupling of amphiphysin with membranes depends on its bound density', *Proceedings of the National Academy of Sciences*, 109(1), pp. 173–178. doi: 10.1073/pnas.1103594108.

Spiegelhalter, C. *et al.* (2010) 'From dynamic live cell imaging to 3D ultrastructure: Novel integrated methods for high pressure freezing and correlative light-electron microscopy', *PLoS ONE*. Public Library of Science, 5(2). doi: 10.1371/journal.pone.0009014.

Steinman, R. M., Silver, J. M. and Cohn, Z. A. (1974) 'PINOCYTOSIS IN FIBROBLASTS', *The Journal of Cell Biology*, 63(3), pp. 949–969. doi: 10.1083/jcb.63.3.949.

Stierhof, Y. D. and El Kasmi, F. (2010) 'Strategies to improve the antigenicity, ultrastructure preservation and visibility of trafficking compartments in Arabidopsis tissue', *European Journal of Cell Biology*, 89(2–3), pp. 285–297. doi: 10.1016/j.ejcb.2009.12.003.

Subach, O. M. *et al.* (2011) 'An Enhanced Monomeric Blue Fluorescent Protein with the High Chemical Stability of the Chromophore', *PLoS ONE*. Edited by J. Rao. Public Library of Science, 6(12), p. e28674. doi: 10.1371/journal.pone.0028674.

Szymanski, C. J. *et al.* (2013) 'Imaging Intracellular Quantum Dots: Fluorescence Microscopy and Transmission Electron Microscopy', in. Humana Press, Totowa, NJ, pp. 21–33. doi: 10.1007/978-1-62703-468-5_2.

Takei, K. *et al.* (1999) 'Functional partnership between amphiphysin and dynamin in clathrin-mediated endocytosis', *Nature Cell Biology*, 1(1), pp. 33–39. doi: 10.1038/9004.

Takizawa, T. and Robinson, J. M. (1994) 'Use of 1.4-nm immunogold particles for immunocytochemistry on ultra-thin cryosections.', *The journal of histochemistry and cytochemistry : official journal of the Histochemistry Society*, 42(12), pp. 1615–23.

Takizawa, T. and Robinson, J. M. (2000) 'FluoroNanogold Is a Bifunctional Immunoprobe for Correlative Fluorescence and Electron Microscopy', *Journal of Histochemistry & Cytochemistry*, 48(4), pp. 481–485. doi: 10.1177/002215540004800405.

Takizawa, T. *et al.* (2015) 'FluoroNanogold: an important probe for correlative microscopy', *Journal of Chemical Biology*. Springer Verlag, pp. 129–142. doi: 10.1007/s12154-015-0145-1.

Tanaka, S. *et al.* (2013) 'Synthesis of green-emitting Pt_8 nanoclusters for biomedical imaging by pre-equilibrated Pt/PAMAM (G4-OH) and mild reduction', *Optical Materials Express*. The Optical Society, 3(2), p. 157. doi: 10.1364/ome.3.000157.

Titze, B. and Genoud, C. (2016) 'Volume scanning electron microscopy for imaging biological ultrastructure', *Biol. Cell*, 108, pp. 307–323. doi: 10.1111/boc.201600024.

Tortarolo, G. *et al.* (2018) 'Evaluating image resolution in stimulated emission depletion microscopy', *Optica*. Optical Society of America, 5(1), p. 32. doi: 10.1364/OPTICA.5.000032.

Tuijtel, M. W. *et al.* (2017) 'Inducing fluorescence of uranyl acetate as a dual-purpose contrast agent for correlative light-electron microscopy with nanometre precision', *Scientific Reports*. Nature Publishing Group, 7(1), pp. 1–12. doi: 10.1038/s41598-017-10905-x.

Valnes, K. and Brandtzaeg, P. (1984) 'Paired indirect immunoenzyme staining with primary antibodies from the same species. Application of horseradish peroxidase and alkaline phosphatase as sequential labels', *The Histochemical Journal*. Kluwer Academic Publishers, 16(5), pp. 477–487. doi: 10.1007/BF01041348.

Van Meel, E. and Klumperman, J. (2008) 'Imaging and imagination: Understanding the endo-lysosomal system', *Histochemistry and Cell Biology*, 129(3), pp. 253–266. doi: 10.1007/s00418-008-0384-0.

van Weering, J. R. T. *et al.* (2010b) *Intracellular membrane traffic at high resolution*, *Methods in Cell Biology*. doi: 10.1016/S0091-679X(10)96026-3.

van Weering, J. R. T., Verkade, P. and Cullen, P. J. (2010a) 'SNX-BAR proteins in phosphoinositide-mediated, tubular-based endosomal sorting', *Seminars in Cell and Developmental Biology*. Elsevier Ltd, pp. 371–380. doi: 10.1016/j.semcdb.2009.11.009.

van Weering, J. R. T. Van *et al.* (2012) 'Molecular basis for SNX-BAR-mediated assembly of distinct endosomal sorting tubules', *The EMBO Journal*. Nature Publishing Group, 31(23), pp. 4466–4480. doi: 10.1038/emboj.2012.283.

Villamena F. A.*'Reactive Species Detection in Biology: From Fluorescence to Electron Paramagnetic Resonance Spectroscopy'* 1st Edition. Amsterdam, Netherlands: Elsevier, 2016

Wei, D. *et al.* (2012) 'High-resolution three-dimensional reconstruction of a whole yeast cell using focused-ion beam scanning electron microscopy', *BioTechniques*, 53(1), pp. 41–48. doi: 10.2144/000113850.

Wilcoxon, J. P. and Abrams, B. L. (2006) 'Synthesis, structure and properties of metal nanoclusters', *Chemical Society Reviews*. The Royal Society of Chemistry, 35(11), p. 1162. doi: 10.1039/b517312b.

Woehl, T. J. *et al.* (2014) 'Correlative electron and fluorescence microscopy of magnetotactic bacteria in liquid: Toward in vivo imaging', *Scientific Reports*. Nature Publishing Group, 4(1), pp. 1–8. doi: 10.1038/srep06854.

Wu, J. S. *et al.* (2013) 'Imaging and elemental mapping of biological specimens with a dual-EDS dedicated scanning transmission electron microscope', *Ultramicroscopy*. NIH Public Access, 128, pp. 24–31. doi: 10.1016/j.ultramic.2013.01.004.

Wu, Y. *et al.* (2018) 'Identification of proteins and bacteria based on a metal ion–gold nanocluster sensor array', *Analytical Methods*. The Royal Society of Chemistry, 10(32), pp. 3939–3944. doi: 10.1039/C8AY00558C.

Wu, Z. and Jin, R. (2010) 'On the ligand's role in the fluorescence of gold nanoclusters', *Nano Letters*. American Chemical Society, 10(7), pp. 2568–2573. doi: 10.1021/nl101225f.

Wu, Z. *et al.* (2012) 'Well-Defined Nanoclusters as Fluorescent Nanosensors: A Case Study on Au25(SG)18', *Small*. John Wiley & Sons, Ltd, 8(13), pp. 2028–2035. doi: 10.1002/smll.201102590.

Xie, J., Zheng, Y. and Ying, J. Y. (2009) 'Protein-Directed Synthesis of Highly Fluorescent Gold Nanoclusters', *Journal of the American Chemical Society*. American Chemical Society, 131(3), pp. 888–889. doi: 10.1021/ja806804u.

Xie, J., Zheng, Y. and Ying, J. Y. (2009) 'Protein-Directed Synthesis of Highly Fluorescent Gold Nanoclusters', *Journal of the American Chemical Society*. American Chemical Society, 131(3), pp. 888–889. doi: 10.1021/ja806804u.

Xu, Y. *et al.* (2013) 'Colorimetric Detection of Trivalent Chromium in Aqueous Solution Using Tartrate-Capped Silver Nanoparticles as Probe', *Journal of Nanoscience and Nanotechnology*, 13(10), pp. 6820–6825. doi: 10.1166/jnn.2013.7785.

Yamashiro, D. J. and Maxfield, F. R. (1987) 'Acidification of morphologically distinct endosomes in mutant and wild-type Chinese hamster ovary cells', *Journal of Cell Biology*, 105(6 I), pp. 2723–2733. doi: 10.1083/jcb.105.6.2723.

Yammine, A., Gao, J. and Kwan, A. (2019) 'Tryptophan Fluorescence Quenching Assays for Measuring Protein-ligand Binding Affinities: Principles and a Practical Guide', *BIO-PROTOCOL*, 9(11). doi: 10.21769/BioProtoc.3253.

Yang, F., Moss, L. G. and Phillips, G. N. (1996a) 'The Molecular Structure of Green Fluorescent Protein', *Nature Biotechnology*. Nature Publishing Group, 14(10), pp. 1246–1251. doi: 10.1038/nbt1096-1246.

Yang, H. N. *et al.* (2009) 'The use of green fluorescence gene (GFP)-modified rabbit mesenchymal stem cells (rMSCs) co-cultured with chondrocytes in hydrogel constructs to reveal the chondrogenesis of MSCs', *Biomaterials*. Elsevier, 30(31), pp. 6374–6385. doi: 10.1016/J.BIOMATERIALS.2009.07.062.

Yang, T.-T., Cheng, L. and Kain, S. R. (1996b) 'Optimized Codon Usage and Chromophore Mutations Provide Enhanced Sensitivity with the Green Fluorescent Protein', *Nucleic Acids Research*, 24(22), pp. 4592–4593. doi: 10.1093/nar/24.22.4592.

Yildiz, A. *et al.* (2003) 'Myosin V walks hand-over-hand: Single fluorophore imaging with 1.5-nm localization', *Science*, 300(5628), pp. 2061–2065. doi: 10.1126/science.1084398.

Yu, J., Patel, S. A. and Dickson, R. M. (2007) 'In Vitro and Intracellular Production of Peptide-Encapsulated Fluorescent Silver Nanoclusters', *Angewandte Chemie International Edition*. John Wiley & Sons, Ltd, 46(12), pp. 2028–2030. doi: 10.1002/anie.200604253.

Yuan, Z. *et al.* (2014) 'Fluorescent silver nanoclusters stabilized by DNA scaffolds', *Chemical Communications*. Royal Society of Chemistry, 50(69), pp. 9800–9815. doi: 10.1039/c4cc02981j.

Zhao, M., Sun, L., Crooks, R. M. (1998) 'Preparation of Cu Nanoclusters within Dendrimer Templates'. American Chemical Society . doi: 10.1021/JA980438N.

Zheng, J., Nicovich, P. R. and Dickson, R. M. (2007) 'Highly Fluorescent Noble-Metal Quantum Dots', *Annual Review of Physical Chemistry*. Annual Reviews, 58(1), pp. 409–431. doi: 10.1146/annurev.physchem.58.032806.104546.

Zheng, J., Petty, J. T., Dickson, R. M. (2003) 'High Quantum Yield Blue Emission from Water-Soluble Au8 Nanodots'. American Chemical Society . doi: 10.1021/JA035473V.

Zimmerberg, J. and McLaughlin, S. (2004) 'Membrane Curvature: How BAR Domains Bend Bilayers', *Current Biology*. Cell Press, 14(6), pp. R250–R252. doi: 10.1016/J.CUB.2004.02.060.